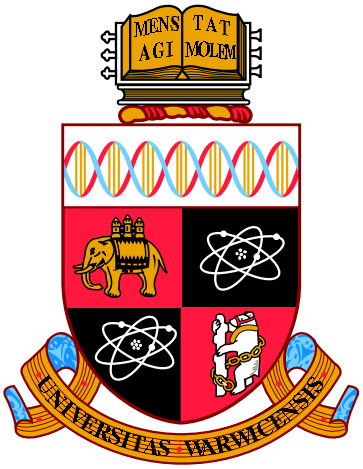

Detection and Characterisation of Transiting Exoplanets with *TESS* across Populations and Orbital Periods

by

Faith Hawthorn

Thesis

Submitted to the University of Warwick

for the degree of

Doctor of Philosophy

Department of Physics

April 2024

THE UNIVERSITY OF WARWICK

Contents

List of Tables

List of Figures

Acknowledgments

I would firstly like to thank my supervisor, Daniel Bayliss, for his constant invaluable guidance and advice over the past 4 years - I will be forever grateful that I was chosen to undertake what has been a fascinating, challenging and rewarding PhD. It has been an honour to be guided down the first chapter of the rest of my academic career by such a brilliant, and exceptionally kind and patient, supervisor and mentor.

I would also like to extend heartfelt thanks to everyone in the Warwick Astro group, particularly my PhD 'brother' Ed for dealing with my incessant questions at all hours of the day; Sam for his guidance, helpfulness and dealing with the questions I didn't ask Ed; Sean, Cait, Toby and Yoshi (my MSc 'children') and my PhD 'cousins' Gareth, Jorge, Ares, Ioannis, Anwesha and Emily for their continual kindness and friendship - plus many more, you know who you are...!

More thanks must go to those who I have made music with over the past few years, especially my Sermon bandmates - Tudor, Luke and Rachel. Thanks are also extended to my friends from back home for their support and understanding of my busy schedule, including Ruzi (17 years and counting!), Erin, Nina, Amy, Chris, Lisa, Matt, Tash, Callum, Jake, Vas and Izzie.

I am enormously grateful to my counsellor Vicky Putt for her gentle support, guidance and kindness during some of my most difficult times throughout the past few years.

Immense thanks go to my partner Ben, without whom I likely would have never gotten through the last couple of years with my sanity (mostly) intact, and never made it to all those conferences... in a racecar no less!

Finally, huge thanks go to my parents Iain and Julie, and my brother Benedict, for keeping me going with nothing but love, understanding and encouragement throughout my entire academic life (and reminders that sometimes I do actually know what I'm doing). It's still on my bucket list to take you to a rocket launch Dad, don't worry!

This thesis is dedicated to the memories of:

John Thomas Edwards, *beloved Grandfather, 1929–2010*

Sylvia Edna Eunice Edwards, *beloved Grandmother, 1940–2016*

Keith Albert Blanchard, *beloved Uncle, 1948–2018*

Professor Thomas Marsh, *founder of the Warwick Astronomy & Astrophysics group, 1961–2022*

For small creatures such as we, the vastness is bearable only through love.

Carl Sagan

Declarations

I declare that this thesis is my own work except where explicitly stated otherwise. This thesis has not been submitted to this or any other academic institution for any other degree or qualification.
Science chapters 3, 4, 5 and 6 are reproductions of peer-reviewed publications or publications in preparation, and contributions from collaborators are stated at the beginning of each chapter.

Chapter 3 - 'TOI-836: a super-Earth and mini-Neptune transiting a nearby K-dwarf' - Hawthorn et al. [2023a]
The majority of the writing and analysis of the paper was performed by the author, with contributions to observational data and sections of analysis made by external collaborators. Sections 3.2.2, 3.2.3, 3.2.3, 3.2.3, 3.2.3, 3.2.4, 3.2.5, 3.3.1 and 3.4.2 were written by co-authors; and Sections 3.2.3, 3.2.4 and 3.4.3 include contributions by co-authors.

Chapter 4 - 'TOI-908: a planet at the edge of the Neptune desert transiting a G-type star' - Hawthorn et al. [2023b]
The majority of the writing and analysis of the paper was performed by the author, with contributions to observational data and sections of analysis made by external collaborators. Sections 4.4.4 and 4.4.5 were written by co-authors, and Sections 4.2.2, 4.2.3, 4.2.4 and 4.3.1 include contributions by co-authors.

Chapter 5 - 'TESS Duotransit Candidates from the Southern Ecliptic Hemisphere' - Hawthorn et al. [2024]
The majority of the writing and analysis of the paper was performed by the author,

with contributions to observational data and sections of analysis made by external collaborators. Section 5.3.3 was written by a co-author, and sections 5.3.1, 5.3.2, 5.4.1, 5.4.2 and 5.5 include contributions by co-authors.

Chapter 6 - 'Statistical analysis of seven TESS duotransit exoplanet candidates' - in preparation

The writing and analysis of the paper was performed in entirety by the author. The paper is currently still in preparation for submission to Monthly Notices of the Royal Astronomical Society.

Abstract

Since the discovery of the very first exoplanets approximately thirty years ago there has been enormous growth in exoplanet research, and currently over 5000 exoplanets have been discovered. The transit method of finding exoplanets has by far been the most successful, accounting for approximately 75% of the known population. Transiting exoplanets are also the most amenable to techniques such as radial velocity monitoring and transmission spectroscopy. In this work, I use data from the Transiting Exoplanet Survey Satellite (TESS) in order to confirm and characterise a set of transiting exoplanets across different populations and orbital periods. I combine this with radial velocity measurements to derive their masses and bulk densities.

In Chapter 3 I present the discovery of two planets in the TOI-836 system. TOI-836 b has a radius of $1.70 \pm 0.07\,R_\oplus$ and a mass of $4.5 \pm 0.9\,M_\oplus$, and orbits its host K-dwarf star on an orbital period of 3.82 days. Its properties place it in the region of parameter space known as the 'radius valley'. The outer planet, TOI-836 c, has a radius of $2.59 \pm 0.09\,R_\oplus$, a mass of $9.6 \pm 2.6\,M_\oplus$, and an orbital period of 8.60 days.

In Chapter 4 I detail the discovery and characterisation of a planet in the TOI-908 system, which resides in the 'Neptune desert' parameter space. TOI-908 b has a radius of $3.18 \pm 0.16\,R_\oplus$, a mass of $16.1 \pm 4.1\,M_\oplus$, and an orbital period of 3.18 days. I found that it may have originally been around the size of Saturn before undergoing photoevaporation of its atmosphere due to extreme XUV flux from its host star.

In Chapter 5, I present 85 candidate planets that are 'duotransiting' in the TESS data, 60 of which were previously unknown. They transit once in Cycle 1, and once in Cycle 3, meaning that their orbital periods range from approximately 20-700 days, typically longer than the minimum period determined by the length of a single TESS Sector. A novel search method was employed to find and match transit events, and a rigorous vetting process was conducted in order to remove false-positive scenarios mimicking exoplanet transits.

In Chapter 6 I analyse seven of our duotransit candidates from TESS that have since had their orbital periods solved with NGTS. I use the statistical validation package `TRICERATOPS` to help determine the true nature of the systems. We find that five are classified as 'likely planets', and two are classified as 'likely false-positives'.

Finally, in Chapter 7 I discuss potential future directions associated with the results from each science chapter and publication, and the overall future of exoplanet discovery and characterisation across different populations and orbital periods.

Abbreviations and quantities

Abbreviations

2MASS Two Micron All-Sky Survey

ARES Automated Routine for line Equivalent widths in stellar Spectra

BIC Bayesian Information Criterion

BJD Barycentric Julian Date

BLS Box-fitting Least Squares

CBV Cotrending Basis Vector

CCD Charge-Coupled Device

CCF Cross-Correlation Function

CHEOPS CHaracterising ExOPlanet Satellite

CMOS Complementary Metal-Oxide Semiconductor

CoRoT Convection, Rotation, and planetary Transits

CTL Candidate Target List

CTOI Community TESS Object of Interest

CVZ Continuous Viewing Zone

DACE Data Analysis Center for Exoplanets

DVR Data Validation Report

EB Eclipsing Binary

EDR Early Data Release

ESA European Space Agency

ESO European Southern Observatory

ESPRESSO Echelle SPectrograph for Rocky Exoplanets and Stable Spectroscopic Observations

ExoFOP Exoplanet Follow-up Observing Program

FAP False Alarm Probability

FFI Full Frame Image

FPP False Positive Probability

FWHM Full-Width Half Maximum

HARPS High Accuracy Radial velocity Planet Searcher

JWST James Webb Space Telescope

NGTS Next Generation Transit Survey

PDC(SAP) Pre-search Data Conditioning (Simple Aperture Photometry)

PLATO PLAnetary Transits and Oscillations of stars

PSF Point Spread Function

RM Rossiter-McLaughlin effect

RV Radial Velocity

SAP Simple Aperture Photometry

SPOC Science Processing Operations Centre

TBJD TESS Barycentric Julian Date

TCE Threshold Crossing Event

TESS Transiting Exoplanet Survey Satellite

TDV Transit Duration Variation

TFOP TESS Follow-up Observing Program

TIC TESS Input Catalog

TOI TESS Object of Interest

TPF Target Pixel File

TRICERATOPS Tool for Rating Interesting Candidate Exoplanets and Reliability Analysis of Transits Originating from Proximate Stars

TSM Transmission Spectroscopy Metric

TTV Transit Timing Variation

WASP Wide-Angle Search for Planets

Quantities

$\mathbf{R}_\oplus$ Earth radius: 6371 km

$\mathbf{M}_\oplus$ Earth mass: 5.972×10^{24} kg

$\mathbf{R}_J$ Jupiter radius: 71,492 km

$\mathbf{M}_J$ Jupiter mass: 1.898×10^{27} kg

$\mathbf{R}_\odot$ Solar radius: 695,000 km

$\mathbf{M}_\odot$ Solar mass: 1.988×10^{30} kg

$\mathbf{L}_\odot$ Solar luminosity: 3.846×10^{26} W

$\mathbf{S}_\odot$ Solar insolation: 1360 Wm^{-2}

AU Astronomical unit: 1.496×10^{8} km

pc Parsec: 3.086×10^{13} km

Chapter 1

Introduction

"Watcher of the skies, watcher of all / His is a world alone, no world is his own / He whom life can no longer surprise / Raising his eyes beholds a planet unknown."

'Watcher of the Skies', Genesis, 1972, Gabriel/Hackett/Rutherford/Banks/Collins

Exoplanet *noun* a planet that orbits a star outside the solar system.

Astronomers have accepted the idea of other planets orbiting the Sun since early times - our five closest neighbours Mercury, Venus, Mars, Jupiter and Saturn were observed and documented by Babylonian astronomers since circa 2000 BC (Swerdlow 1998), and the outer planets of Uranus (initially believed to be a comet according to Herschel & Watson 1781) and Neptune (Galle 1846) following many years later. The Italian philosopher Giordano Bruno suggested as far back as 1584 in *'De l'Infinito Universo e Mondi'* ('On the Infinite Universe and Worlds', Bruno & Maddamma 2013) that other stars outside the Solar system may host their own planets - but it was not until 1988 that the first exoplanet, Gamma Cephei A b (Campbell et al. 1988), was seemingly detected by the radial velocity technique. Due to poor data quality at the time of the original observations, this discovery was not confirmed until 2003 (Hatzes et al. 2003). However, it set a precedent for exoplanet discovery that would eventually lead to the confirmation of the hot Jupiter 51 Pegasi b in 1995 (Mayor & Queloz 1995), and the first detection of an extrasolar planet using the transit method would soon follow in 1999 in the form of HD 209458 b (Charbonneau et al. 2000).

As of 18 April 2024, a total of 5609 planets have been confirmed, and a further 10,098

are unconfirmed candidates according to the NASA Exoplanet Archive (Akeson et al. 2013). Searches for exoplanets are ongoing, and planets that have been discovered now span a wide range of masses, radii and sub-types (including terrestrial planets, ice giants and gas giants) as the capabilities of telescopes, instruments and data analysis techniques have developed over time. As a result of flagship missions, particularly *Kepler* (Koch et al. 2004) and TESS (Ricker et al. 2015), the catalog of exoplanets continues to grow at a considerable rate in recent years. Characterisation of these exoplanets is an important aspect of discovering how these systems form and evolve over time. Furthermore, comparative planetology involving these extrasolar systems is able to contextualise the structure and evolution of our own Solar system; and ultimately, aid in answering the naturally human question of whether or not we are alone in the universe.

1.1 Planets

1.1.1 The Solar System

The Earth resides in the Solar system, a group of eight planets orbiting the Sun, a G2V-type Main Sequence star in the Milky Way galaxy. The planets of the Solar system show a wide diversity of sizes, masses and subtypes; from the inner rocky and terrestrial planets of Mercury, Venus, Earth and Mars; the gas giants Jupiter and Saturn; out to the ice giants of Uranus and Neptune, beyond which lies the circumstellar Kuiper belt of smaller icy objects at the very edge containing the 'dwarf planet' population and small icy bodies. The orbits of the planets are aligned co-planar to the rotational motion of the Sun, meaning they were likely forming around the same time as the Sun, the remaining mass from the collapse of the progenitor gas cloud forming a protoplanetary disk (Shu et al. 1987; Williams & Cieza 2011) in which smaller clumps of material coalesced into planets (Goldreich & Ward 1973; Pollack et al. 1996). There exists a dramatic temperature gradient the further from the Sun the planets reside, meaning that the average temperatures at the closest planet Mercury and the furthest planet Neptune range from 440 K to 72 K respectively. Earth resides in the 'Habitable Zone' (HZ) of the Sun, the region of distances at which surface water is in a liquid state (Kasting et al. 1993; Kopparapu et al. 2013). The HZ region can change depending on the host's stellar properties, and the Solar system is not the only system of planets within the galaxy.

1.1.2 Exoplanets

The IAU (International Astronomical Union) working definition (Lecavelier des Etangs & Lissauer 2022) defines an exoplanet as an object orbiting a star or stellar remnant with a mass below $\approx 13\,\mathrm{M}_J$ (and massive enough for the object to be in hydrostatic equilibrium and broadly spherical). $13\,\mathrm{M}_J$ was selected as it is the mass at which the fusion of hydrogen into deuterium begins in the core of the object. Objects above this mass limit but below $\approx 70\,\mathrm{M}_J$ still do not have enough mass to trigger this hydrogen fusion reaction, and are referred to as 'brown dwarfs'. Exoplanets exist on a wide range of masses, radii, densities, internal structures and sub-types (see Section 1.8.2); many of which are unlike any of the planets of the Solar system, in particular the population of hot Jupiters, super-Earths and sub-Neptunes found in abundance orbiting a multitude of host stars of different spectral types and evolutionary stages unlike our Sun.

1.1.3 Planet Formation

Current theories surrounding the formation of planets interpret the process as being 'bottom-up' (Safronov [1972]). Planets are initially formed from microscopic material in protoplanetary disks remaining from star formation, and clump together under the influence of gravity to form small planetesimals (Youdin & Goodman 2005). These objects continue to accrete mass, and may form an atmosphere dependent on the amount of leftover material; and the ability to retain that material around the planet under the influence of gravity. Larger cores may hold onto larger amounts of gaseous material and become giant planets, and smaller cores may retain less of an atmosphere (or no atmosphere at all) and become terrestrial rocky planets (Bodenheimer & Pollack [1986]).

The two leading theories of planet formation include core accretion (described in Pollack et al. 1996), and gravitational instability (Boss 1997). Core accretion involves the repeated coagulation of rocky planetesimals until a 'critical mass' is reached, beyond which the object will accrete a gaseous envelope and form a giant planet. However, some early models predicted that the formation timescale of such a planet may exceed the lifetime of the gas disk from which it accretes material, and so the theory of gravitational instability may help to overcome this limitation. During the early stages of stellar formation, the surrounding mass of the gas disk may contain as much material as the protostar itself, and gravitationally unstable regions within this disk may fragment and coalesce into bound clumps of material that contract to form giant planets.

Figure 1.1 from Mordasini & Burn [2024] shows a schematic of planet formation and evolution processes, along with their typical timescales.

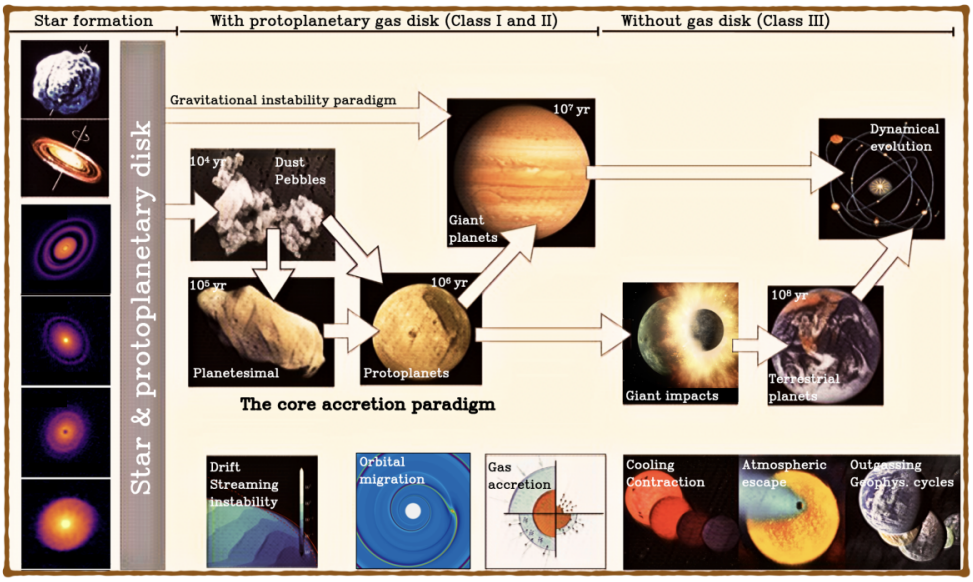

Figure 1.1: Diagram of planet formation and evolution theories from Mordasini & Burn [2024], including the stellar formation process and typical timescales on which each planetary process occurs. Subfigures are from Andrews et al. [2018], Baruteau et al. [2014], Birnstiel et al. [2012], NASA, NASA/JPL, ESA, A. Vijal-Madjar (IAP, CNRS).

1.1.4 Planet Evolution

Various environmental effects can cause planets' properties and orbits to evolve over time. Host stars undergo a well-understood process of evolution depending on their mass, and as their size and luminosity change, they can affect an orbiting planet. For example, as a Main Sequence (MS) star swells to the size of a red giant towards the end of its MS lifetime, it may engulf any close-orbiting planets (O'Connor et al. 2023). Dynamical interactions can also cause changes in planetary orbits and properties, e.g. through interactions with remnant planetesimals not fully accreted by a larger planet, tidal interactions with the host star, and interactions with a stellar companion in the case of bound or binary stellar systems (Deeg & Belmonte 2018). Planetary migration in the gas disk may also occur due to gravitational interactions between an exoplanet and the disk (Goldreich & Tremaine 1979), and the sub-type of type II migration can lead to orbital resonances forming in multi-planet systems (Goldreich 1965).

One example of evolution is the photoevaporation of exoplanet atmospheres due

to high levels of incident radiation from their host stars, usually in the X-ray and extreme ultra-violet (XUV) regimes. The Neptune desert, an observed dearth of Neptune-sized planets at short orbital periods (see Section 1.9.2) provides possible evidence for this process.

1.1.5 Motivation

In order to better understand the processes of planetary formation, and their subsequent evolution, a wide sample of planets across a range of sub-types and host stars must be observed, modelled and studied. The transit method (Section 1.2.2) and the Radial Velocity (RV, Section 1.2.3) allow for a determination of exoplanetary properties such as mass, radius and bulk density, leading to a classification of the planet as one of a number of types (see Section 1.8.2). Transmission spectroscopy (Section 1.2.2) further allows for measurements of the chemical compositions of exoplanet atmospheres, which can reveal ongoing processes and dynamics of individual planets and the wider implications for the systems they reside in, such as their potential formation pathways and eventual fates.

Certain regions of parameter space when examining populations of exoplanets reveal distinct dearths of planets in particular areas - for example, the radius valley, which describes the bimodal distribution of planets at two peaks either side of $1.6 R_\oplus$, below which planets are categorised as 'super-Earths', and above $2\,R_\oplus$, where they are categorised as 'sub-Neptunes' (see Section 1.9.1). The TOI-836 system described in Chapter 3 details the analysis of a multi-planet system where the inner planet b resides inside this valley, and the outer planet c is a larger sub-Neptune. Another relatively sparse region of mass-period space is the Neptune desert, an area where there is a lack of planets around the size of Neptune on close orbits to their stars (see Section 4). It is currently theorised that a number of mechanisms cause these planets to lose their atmospheres at such separations, and efforts are ongoing to discover and characterise such systems.

The transit and RV methods are typically well-suited to finding large planets residing on relatively short orbital periods around 3-10 days, due to the fact that they exert large and observable signals on their host stars, and their orbits cause regular transits and a fully-covered RV phase curve in which an orbital period can be determined in a short space of time. However, there exists a dearth of well-characterised transiting planets on orbital periods above ~ 20 days - the TESS mission in particular imposes this soft limit due to its observing strategy (see Section 1.4.1). The shortest-period planet in the Solar system, Mercury, has an orbital period of 88 days, and the Earth's period is 365 days, significantly longer than most detections of transiting

exoplanets, and the giant planet population have orbits considerably further from their stars than this. Therefore, we focus part of this work on detecting a set of new relatively long-period planets from TESS in a novel way, with the aim of enabling the community to confirm these planets and study a population much similar to the planets of our own Solar system (Chapter 2.5).
Transiting exoplanets as seen from Earth require the specific geometric alignment of their orbits to be edge-on relative to the observer, and so they are relatively rare. Discovery and characterisation of such systems is challenging, but in recent times has become possible and is improving with the deployment of state-of-the-art instruments and facilities such as TESS (Ricker et al. [2015]), NGTS (Wheatley et al. 2018), and HARPS (Mayor et al. [2003]). This thesis details work done using these facilities and more to discover new worlds in sparsely-populated regions of parameter space, and help us to further understand exoplanets and their host systems.

1.2 Discovery methods

1.2.1 Photometry

Photometry is a technique that relies on measurements of incident light from astronomical objects in terms of its intensity or brightness ('flux') using a detector system. Monitoring changes in the brightness of an object can reveal the presence of stellar variability and/or companion objects, including transiting exoplanets (Deeg & Alonso 2018). This is often done through the use of CCDs (Charge-Coupled Devices, Howell 2000) or, in more recent times, CMOS (Complementary Metal-Oxide Semiconductor, Waltham 2010) detectors. CCDs collect and store electronic charge in response to incident photons on individual pixels of the detector, and these pixel charges are read out at the end of each exposure period to produce an array of pixel values corresponding to the collected charge. Various processes of image calibration and reduction are performed in order to reduce noise effects that affect CCD operation, and extract time-series photometric light curves. In order to reduce the effects of thermal noise, CCDs are often cooled to sub-zero Celsius temperatures, and three types of calibration frames are taken and combined to offset the inherent noise properties of the CCD, described below (Davenhall et al. 2001).

- **Bias frames** - bias frames are taken with the shortest possible exposure time, typically sub-second, with the shutter closed to encapsulate the electronic noise of the detector when no light is incident upon it.

- **Dark frames** - dark frames are designed to correct for thermal noise causing

the generation of electrons (dark current), and are taken at the same exposure time as the planned observations with the shutter closed.

- **Flat field frames** - flat field frames correct for non-uniform pixel-to-pixel variations on the CCD array by uniformly illuminating it with a flat light source, such as the twilight sky or a flat field lamp, at the same exposure time as the planned observations.

One technique used for extracting photometric information about a point-source target is aperture photometry (Howell 1989). An aperture is a defined region large enough to encapsulate the target in the image and measure its total flux, but not so large that it begins to incorporate a significant amount of background or contaminating sources. A second annulus can be placed around the target to incorporate the average background flux, and the median of the pixel values in this annulus is subtracted from the target aperture to correct for the background.
Differential photometry involves further corrections to the extracted flux and time-series light curve, in order to remove effects of instrumental or atmospheric noise, as identical variations in flux across multiple targets are unlikely to be astrophysical in nature (Young et al. 1991). Identical apertures to that on the target are placed on similar 'reference stars' in the same image, and the target flux is divided by the resulting light curves of the reference stars to ensure that the final light curve is free of external non-astrophysical sources of variability.
Pipelines associated with missions and instruments such as TESS (Section 1.4, Ricker et al. 2015) and NGTS (Section 1.3.4, Wheatley et al. 2018) employ aperture photometry in order to extract light curves from their time-series frame observations. TESS in particular has two main data products from these pipelines: SPOC (Science Processing Operations Centre, Jenkins et al. 2016) and QLP (Quick-Look Pipeline, Huang et al. 2020a,b).

1.2.2 Transit photometry

As an exoplanet passes between its host star and an observer on Earth, it blocks some of the star's light and causes a 'transit'(Winn 2014). This technique relies on the system being edge-on relative to the observer, and it is therefore not possible to find exoplanets that may be on highly-inclined orbits that do not pass in front of the stellar disk with this method. Transits can be observed multiple times over many orbital periods of the planet (dependent on the lengths of time of the planet's period and the observational baseline), and various properties can be resolved from the transit shape. However, whilst this method is able to recover exoplanet radii

(the effectiveness of this is of course dependent on the size of the planet and the amount of light blocked), it cannot be used to recover the planetary mass. It should be noted that the transit method alone is usually not enough to fully confirm the existence of an exoplanet - it is often combined with other methods, particularly the radial velocity method as described in Section 1.2.3, in order to further constrain system parameters and provide a full characterisation of the system. Furthermore, multiple transits of a planet are often required in order to confirm its orbital period from the time difference between the events.

Transit geometry

Information about the planetary system parameters is encoded within the shapes of individual and phase-folded transit events, between the points of ingress when an exoplanet first makes contact with the stellar disk, and the point of egress where it leaves the stellar disk. The equations below, from Sackett [1999], Murray & Correia [2010] and Winn [2014], describe how certain parameters can be calculated from transit features.

$$\delta = \frac{\Delta F}{F} = \left(\frac{R_p}{R_*}\right)^2 \tag{1.1}$$

If the radius of the star (R_*) is a known quantity, along with the change in the apparent stellar flux (ΔF), the radius of the planet (R_p) can be obtained from Equation 1.1, where δ represents the transit depth and F the baseline stellar flux (assuming the transit is non-grazing).

$$b = \frac{a\cos(i)}{R_*} \tag{1.2}$$

The impact parameter b is the sky-projected perpendicular distance at conjunction between the centre of the stellar disk and the centre of the exoplanet, shown in Equation 1.2, where a is the semi-major axis of the planet's orbit, i is the orbital inclination and R_* is the stellar radius, and assuming a circular orbit where eccentricity $e = 0$.

$$b = \frac{a\cos(i)}{R_*}\left(\frac{1-e^2}{1+e\sin\omega}\right) \tag{1.3}$$

Adapting this equation for a non-circular orbit where eccentricity $e > 0$ we find Equation 1.3, where ω represents the longitude of periastron.

$$T_{dur} = \frac{P}{\pi} \sin^{-1} \left(\frac{\sqrt{(R_p + R_*) - (bR_*)^2}}{a} \right). \tag{1.4}$$

With knowledge of each of these geometric quantities and the orbital period of the planet P, the full transit duration T_{dur} can be calculated as in Equation 1.4.

$$p = \frac{R_*}{a}. \tag{1.5}$$

We turn to Equation 1.5 from Borucki & Summers [1984] to calculate the probability of a transit occurring in a system, where p is the transit probability and the quantities R_* and a are as described previously, and the orbit is circular.
A diagram of a transit event is shown in Figure 1.2 (from figure 2 of Winn 2010) showing the described quantities of transit depth δ, impact parameter b, the transit duration (T or T_{dur} for our purposes), and the individual contact points t_I and t_{II} at ingress and t_{III} and t_{IV} at egress.

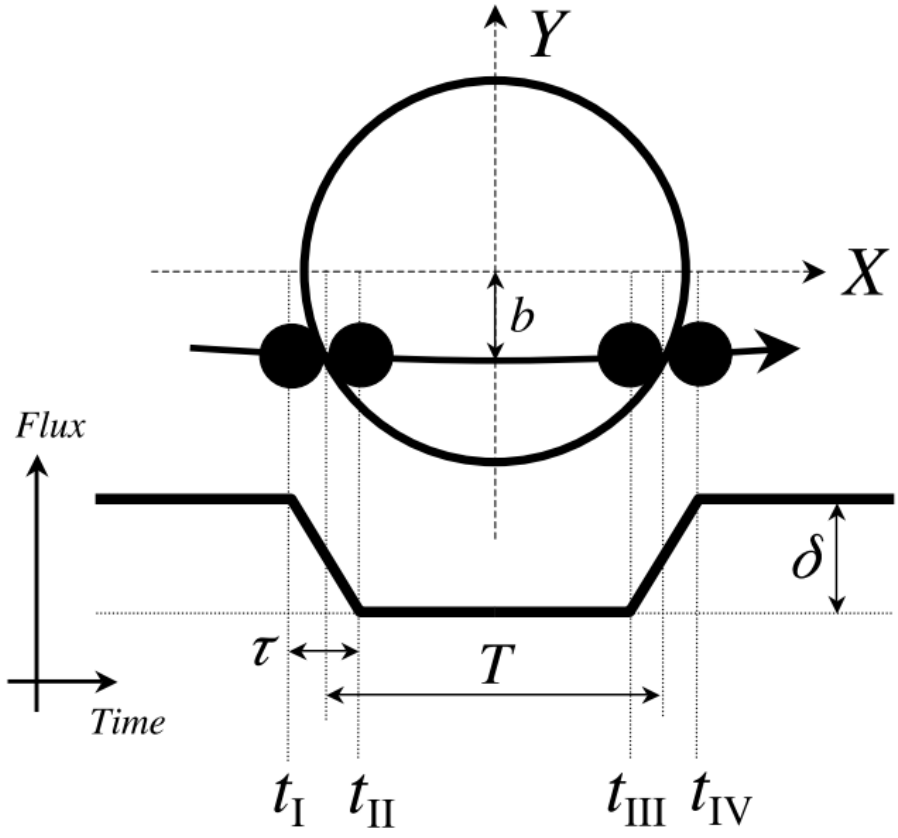

Figure 1.2: Diagram of a transit event from Winn [2010], showing the depth δ, impact parameter b, the full transit duration T and the ingress and egress contact points.

Transit light curves

Figure 1.3 shows a transit of WASP-44 b (Anderson et al. 2012) as an example with data from TESS, phase-folded to a transit ephemeris (central timestamp) of 2458338.102 TBJD and an orbital period of 2.424 days. Note that drops in fluxes are typically measured in $e^{-}s^{-1}$ (electrons per second, as in the case of the TESS raw light curves) or difference in magnitude Δmag. Transit light curves at high cadences are also often binned for clarity of interpretation, and overlaid with a best-fitting transit model from which system parameters can be drawn.

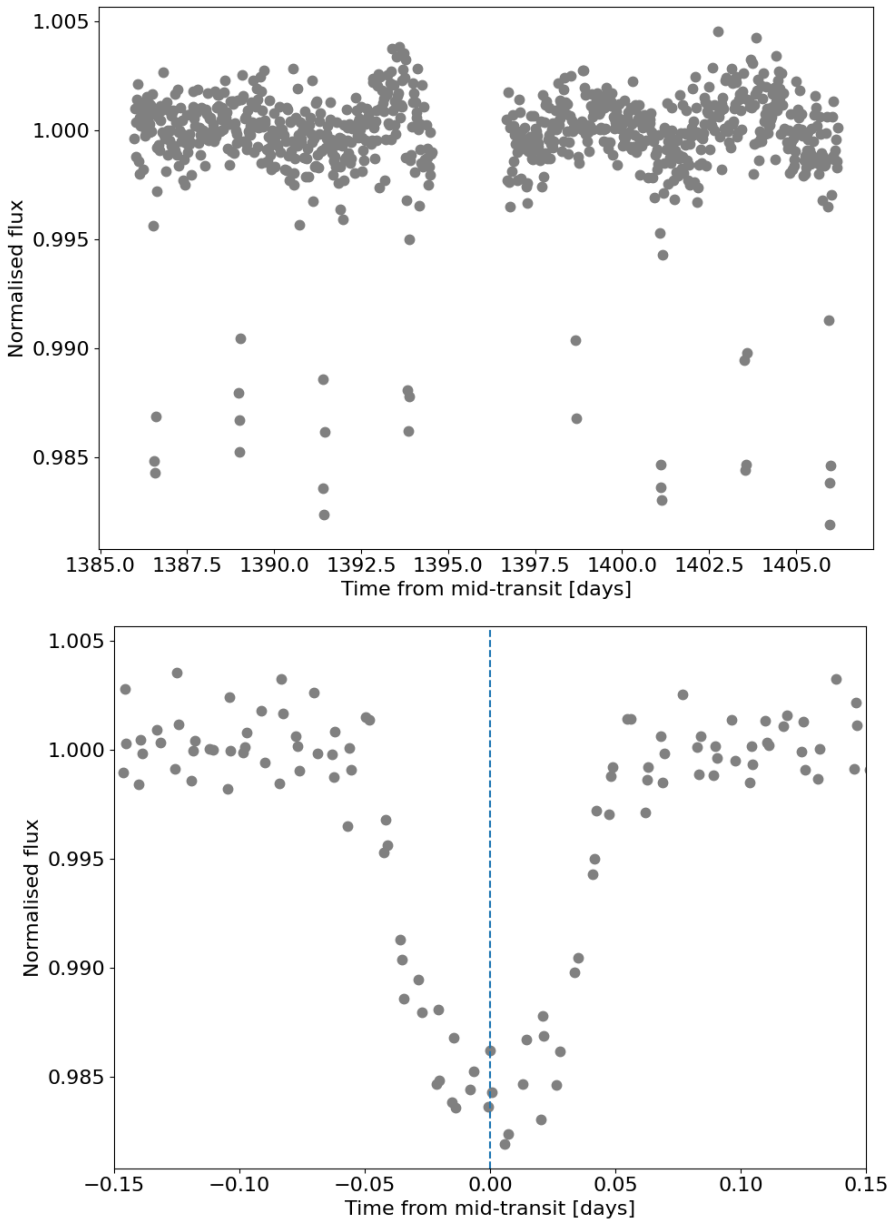

Figure 1.3: WASP-44 b (Anderson et al. 2012) photometry from the TESS mission. **Top panel:** TESS light curve from Sector 3 (2018 Sep 21 - 2018 Oct 17). **Bottom panel:** The TESS data phase folded to an ephemeris of 2458338.102 TBJD and an orbital period of 2.424 days. The blue dashed line marks the centre of the transit.

Transit model parameters are often assessed for goodness-of-fit using the χ^2 statistic, given by Equation 1.6, where x_i represents the set of individual measurements, μ_i is the set of predicted values, and σ_i is the set of uncertainties on the individual measurements. Values of μ_i are often generated from physical models and a set of

given parameters, and the value of χ^2 is ideally reduced to a minimum value after testing all combinations of input parameters.

$$\chi^2 = \sum_i \left(\frac{x_i - \mu_i}{\sigma_i} \right)^2 \tag{1.6}$$

The shape of a transit light curve is also affected by the phenomenon of 'limb darkening', which is a result of the fact that stars are not uniformly bright across the stellar disk - they exhibit variations in brightness, being brighter at the centre, and dimmer at the outer edges. This is illustrated in Figure 1.4 from Strøm [2016], where it can be seen that emitted photons at the edge of the star must follow an oblique path towards the observer through the star's atmosphere compared to those leaving and following the same path length L from a region of the stellar disk at the centre. Limb darkening effects are often modelled using parametric laws with fitted coefficients (e.g. u_0 and u_1 for a quadratic law), which can either be derived from prior knowledge of the host star (as in the Python package `LDTK`, Parviainen & Aigrain 2015) or through alternate parameterisations that are not informed by host star characterisation (as in Kipping 2013b).

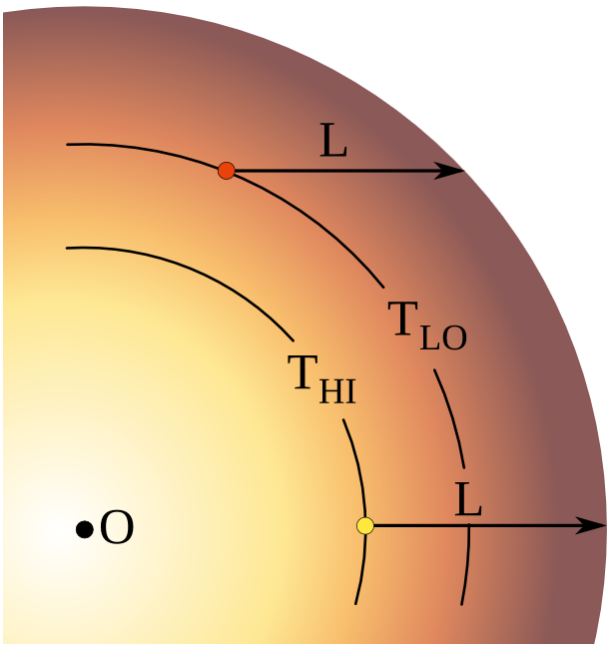

Figure 1.4: Diagram of the effects of limb darkening, showing how light propagates through more oblique paths towards the edge of the star (the 'limb') across a distance L towards an observer at the right side of the diagram.

Figure 1.5 shows observations from the Hubble Space Telescope (*HST*) at multiple

wavelengths of HD 209458 b from 300-1000 nm (from Knutson et al. 2007), in which the effects of limb darkening are apparent in the shape of the curves, being more pronounced at shorter wavelengths. This is due to the fact that the opacity of stellar atmospheres varies with wavelength - at shorter wavelengths the opacity is higher, allowing us to probe only the upper, cooler layers of the atmosphere where there is a higher contrast between the centre of the disk and the limb; at longer wavelengths the opacity decreases which allows the lower, hotter layers of the atmosphere to be probed, and the overall effect of limb darkening is less pronounced. Accurately modelling limb darkening effects of an exoplanet transit is crucial for obtaining and interpreting the transit shape, and the derived properties of the exoplanet itself. Limb darkening effects also come into play when studying the transmission spectra of exoplanet atmospheres (see Section 1.2.2) to more accurately determine their chemical composition. Correct interpretation of limb darkening during a secondary eclipse also helps to determine the planetary albedo and its thermal emission and reflection properties (e.g. Snellen & Covino 2007).

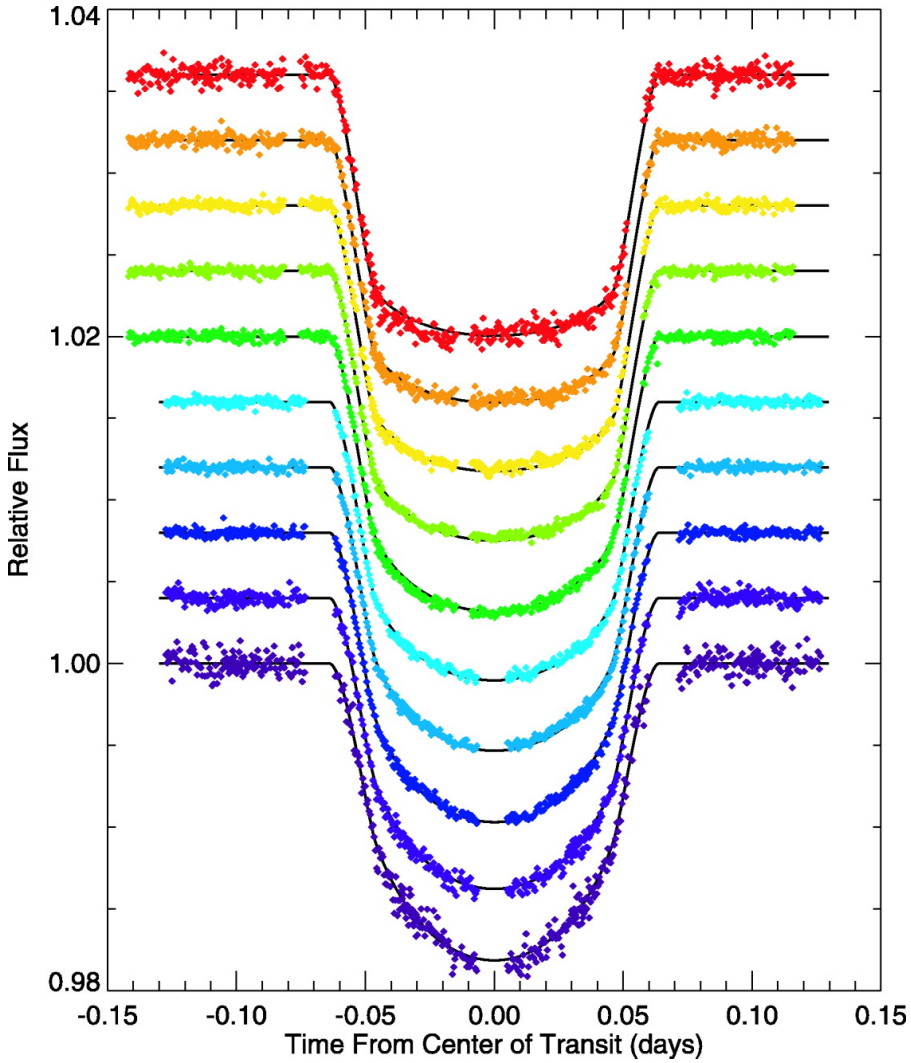

Figure 1.5: Transit events of HD 209458 b from Knutson et al. [2007] observed with *HST* at wavelengths varying from 920-1000 nm (top, red) to 300-350 nm (bottom, purple).

As of 18 April 2024, 4168 planets have been discovered using the transit method (NASA Exoplanet Archive, Akeson et al. 2013), making it the most successful method to date amongst the techniques presented here.

Transit timing variations

On occasion, deviations in the timing of individual transit events from their predicted ephemerides may be observed in some systems (e.g. Kepler-9, Holman et al. 2010). These 'transit timing variations' (TTVs) typically arise from the presence

of an additional planet in the system, as it acts to gravitationally interact with the planet exhibiting TTVs during close approaches. The effect is often particularly pronounced for planets residing in first-order mean motion resonance orbits (1:2, 2:3 etc.). The additional planet may be unseen in transit photometry but visible in radial velocity observations, however from long-term and frequent monitoring of the TTVs it is possible to extract the masses of these unseen planets, as in e.g. Barros et al. [2015]. Figure 1.6 from Ballard et al. [2011] shows TTVs of the planet Kepler-19 b, which were seen to have a super-period of $\sim$ 316 days and an approximate TTV amplitude of $\sim$ 5 minutes. This allowed for the discovery of a companion planet, *Kepler*-19 c, which was fully characterised in Malavolta et al. [2017] and given a mass of $13.1 \pm 2.7\,M_\oplus$ following TTV analysis.

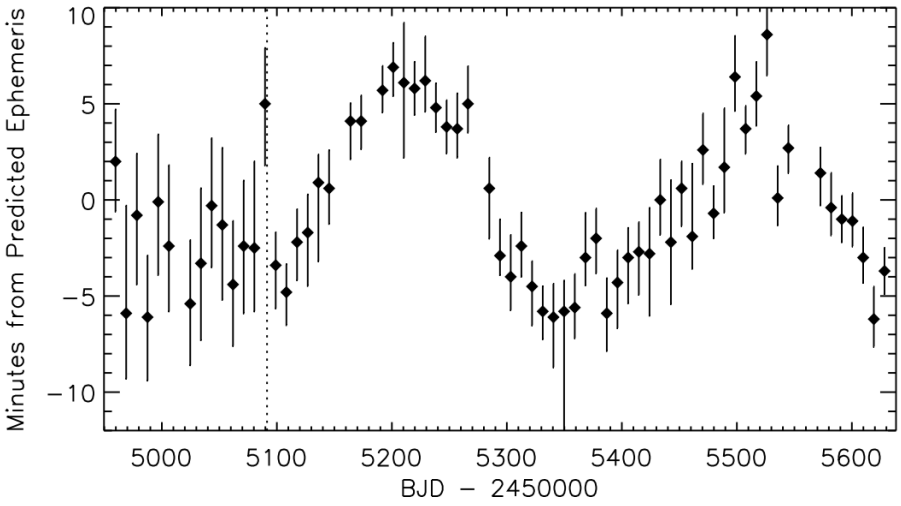

Figure 1.6: Transit timing variations of *Kepler*-19 b from Ballard et al. [2011], measured in minutes from the predicted transit ephemeris. A clear periodicity can be seen, corresponding to a super-period of $\sim$ 316 days and amplitude of $\sim$ 5 minutes.

As of 18 April 2024, 29 planets have been discovered using TTVs (NASA Exoplanet Archive, Akeson et al. 2013).

Transit depth variations

In cases where multiple transits of a planet are seen, individual transits may exhibit variations in depth (if it is known that the transits are caused by the same object and not planets with different radii). One such example is TOI-216 b, light curves of which from Cycle 1 and Cycles 3 and 5 combined are shown in Figure 1.7 from McKee & Montet [2023]. In this case, the transit of the planet was originally grazing in Year 1 (i.e. not all of the planetary disk occults the star), but due to orbital precession

the planet eventually transits the star in full during Cycles 3 and 5 as the impact parameter b decreases from ~ 0.98 to ~ 0.88 over a period of ~ 1500 days, enabling a robust measurement of the planetary radius. This particular system also exhibits mutual TTVs between the two planets , TOI-216 b and c, with a super-period of ~ 1500 days.

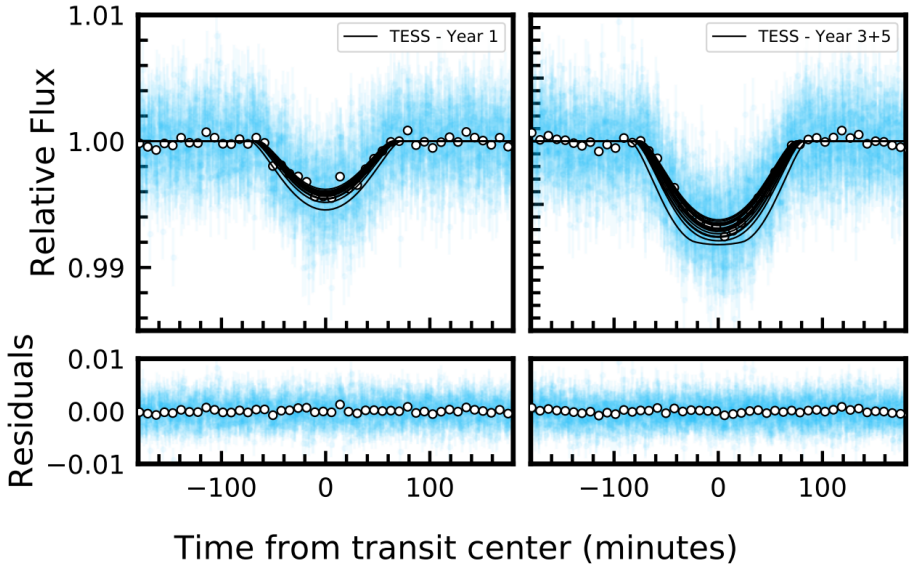

Figure 1.7: Transit depth variations of TOI-216 b from Cycle 1 (left panels), Cycle 3 (right panels) and Cycle 5 (right panels) of TESS observations, from McKee & Montet [2023]. A clear difference in the depth of the transits can be seen, in this case due to orbital precession of the planet over time.

Another potential source of variations in the depth of an individual transit event is starspot crossings - where a planet will transit regions of lower temperatures on the stellar surface ('starspots'), leading to a decrease in the depth of the transit relative to the rest of the stellar disk. An example of this is TOI-3884 b, a super-Neptune that transits the starspots of an M4 dwarf star. Two possible starspot configurations (assuming starspot temperature of 2900 K and photospheric temperature of 3200 K) and transit data (ARC 3.5 m telescope, Apache Point Observatory) for this system is shown in Figure 1.8 from Libby-Roberts et al. [2023].

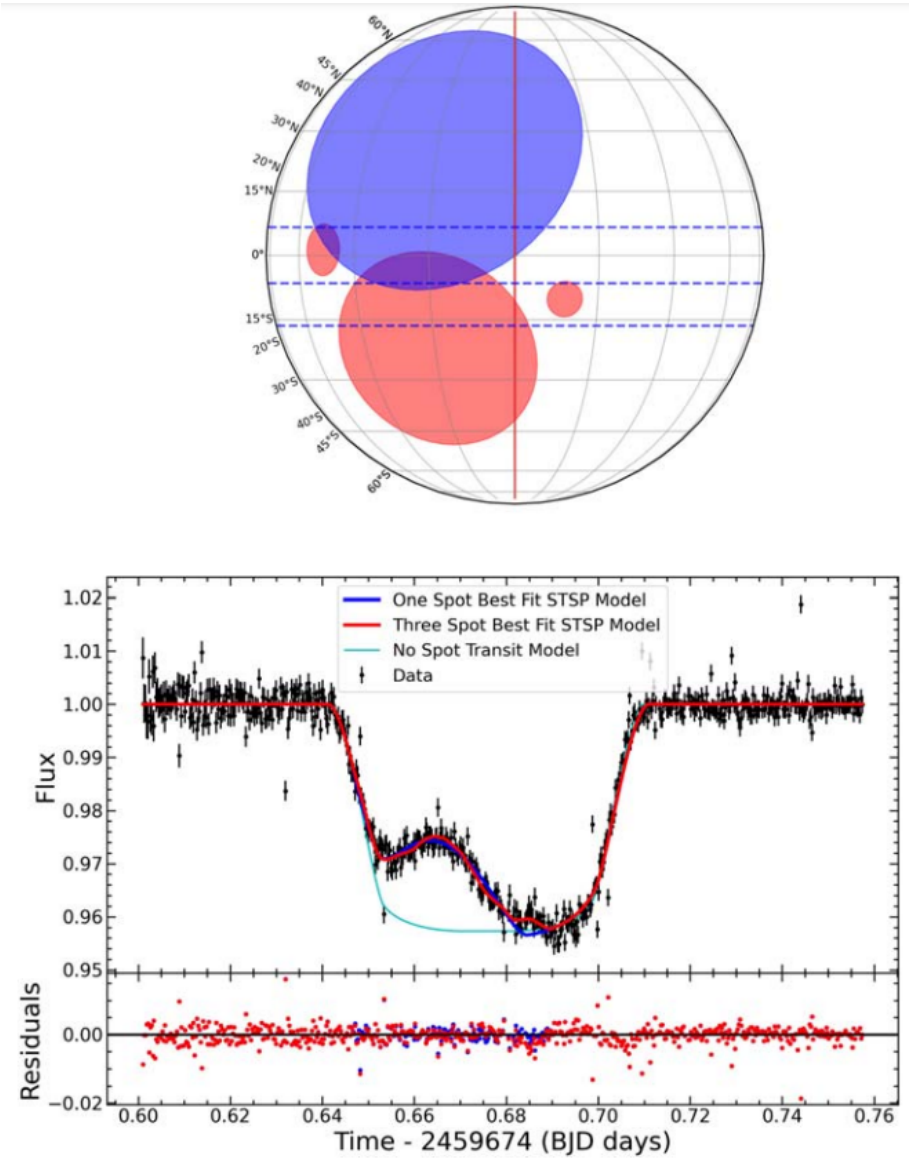

Figure 1.8: Figure from Libby-Roberts et al. [2023]. **Top panel:** Two starspot configurations for TOI-8334 (one-spot model in blue, three-spot model in red). **Bottom panel:** Transit data from APO on 5 April 2022 (black points), overplotted with the best-fit models for the one-spot system (blue line), three-spot system (red line) and the transit model assuming no starspots (cyan line). Clear depth variations spanning the transit can be seen.

Transmission spectroscopy

Transmission spectroscopy is the process by which we are able to observe variations in the depth of planetary transits when measured at different wavelengths. As individual atmospheric atomic and molecular constituents display different absorption

properties, we can read a transmission spectrum's absorption features to gain a characteristic signature of the planet's atmospheric composition. However, atmospheres are more dynamically complicated than the individual constituents would imply. Figure 1.9 from Madhusudhan [2019] shows various additional atmospheric processes in different atmospheric layers, from the planetary surface through to cloud layers and the very top of the atmosphere, where escape may occur.

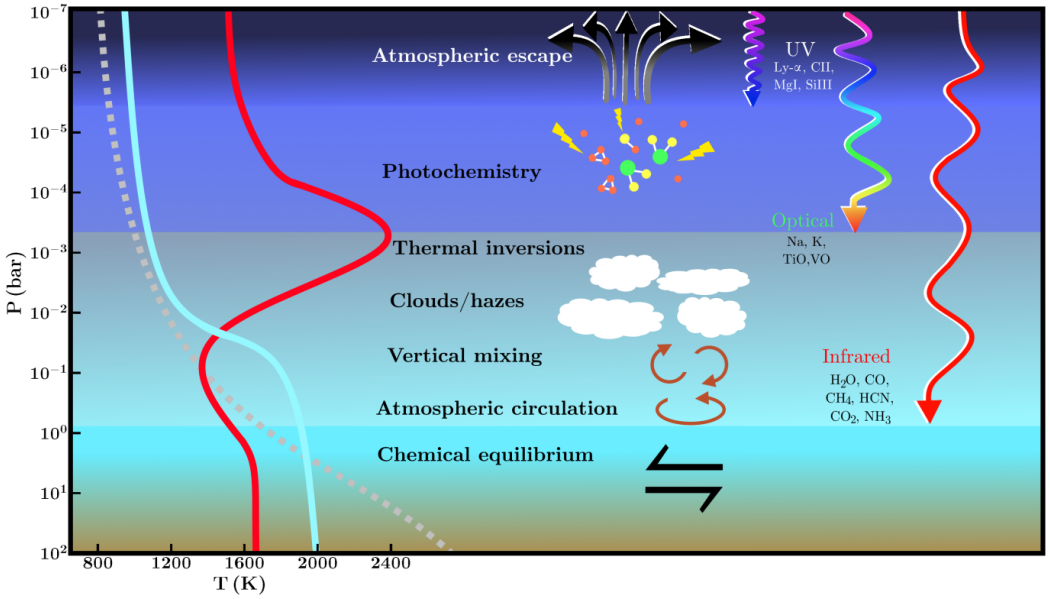

Figure 1.9: Figure from Madhusudhan [2019], showing different dynamic processes in planetary atmospheres in varying layers.

Figure 1.10 from Feinstein et al. [2023] is an example of a transmission spectrum derived from observations with the NIRISS instrument of JWST (James Webb Space Telescope; Gardner et al. 2006) and HST of WASP-39 b from three different data reduction pipelines. Multiple broad absorption features of H_2O can be seen.

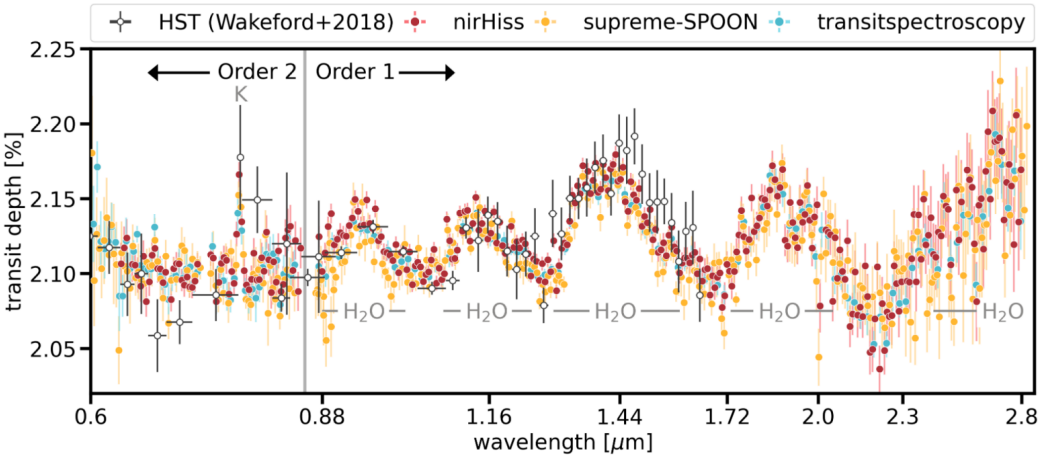

Figure 1.10: Transmission spectrum of WASP-39 b from *HST* and JWST, from Feinstein et al. [2023], reduced with the `nirHiss`, `supreme-SPOON` and `transitspectroscopy` data reduction pipelines. Transmission spectrum features characteristic of H_2O are present and labelled in grey.

1.2.3 Radial velocity

The radial velocity (RV) method is an exoplanet detection method that is often complementary to the transit detection technique, as it is able to reveal the mass of an orbiting exoplanet (Lovis & Fischer 2010), provided that the system is relatively edge-on to an observer and the signal is not sufficiently small as to be masked completely by stellar activity effects (see Section 1.2.3). This method relies on a system being observed relatively edge-on to an observer, as the effect relies on observing both the exoplanet and the star orbiting a common centre of mass (the barycentre) due to the effect of mutual gravitational forces. The star appears to move towards and away from the observer as it periodically orbits the barycentre, usually under the surface of the star, and over time the spectrum of the star will be Doppler shifted. As the star moves towards the observer, a blue-shift will be observed, and a red-shift as the star moves away. Equation 1.7 relates the observed and emitted wavelengths, λ_o and λ_e respectively, to the change in wavelength λ_0 (deviation from a template spectra):

$$V_{RV} = c\left(\frac{\lambda_o - \lambda_e}{\lambda_e}\right) \tag{1.7}$$

A larger Doppler shift corresponds to a higher velocity and vice-versa, allowing us to measure the star's radial velocity. High precision is necessary in order to see small radial velocities due to the large differences in mass between stars and their planets -

the HARPS spectrograph (described in brief in Section 1.5.1) is capable of resolving radial velocities as low as 1 $\mathrm{m\,s^{-1}}$ according to Pepe et al. [2000]. Until around 2012, this was the most successful method for exoplanet detection, but it has since been surpassed by transit photometry (see Section 1.2.2) due to the advent of the *Kepler* mission and the subsequent successes of TESS. 51 Pegasi b, was confirmed by this technique by Mayor & Queloz [1995] as the first planet to be found orbiting a Sun-like star, for which the Nobel Prize in Physics was awarded in 2019. A plot of the radial velocity curve of 51 Pegasi from Mayor & Queloz [1995] is shown in Figure 1.11.

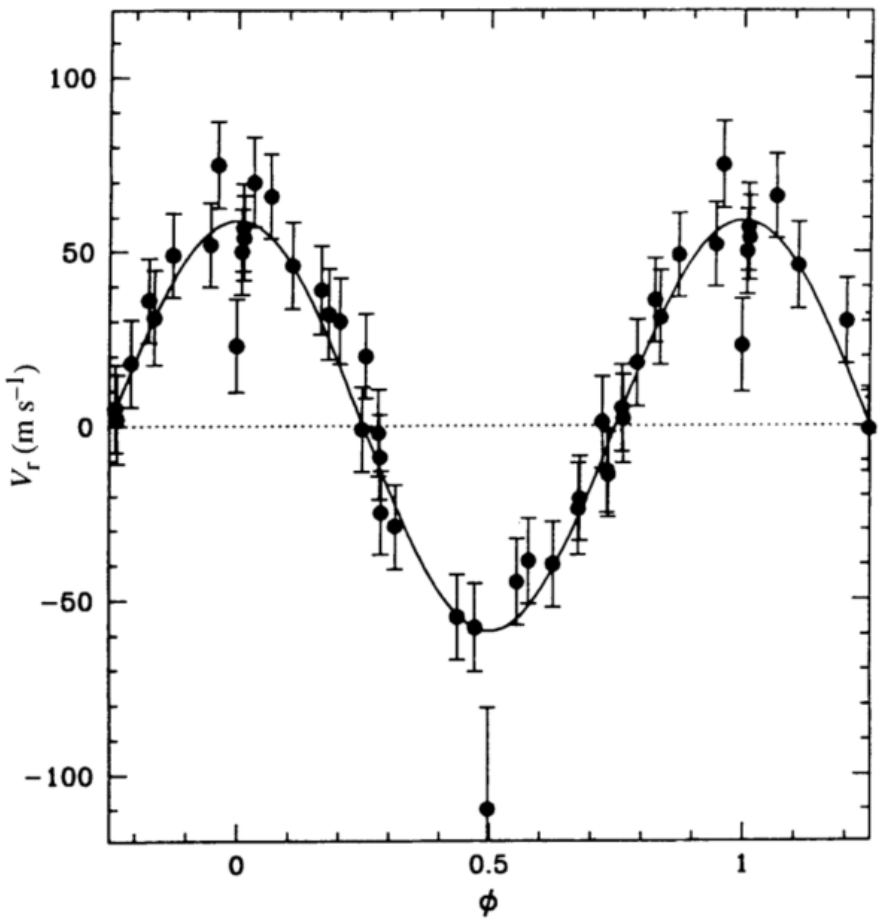

Figure 1.11: Orbital motion of 51 Pegasi - data from the *ELODIE* spectrograph, with the best-fitting orbital motion as the solid line computed from orbital parameters - retrieved from Mayor & Queloz [1995].

The amplitude of a planet's radial velocity K can be determined from Equation 1.8 (Lovis & Fischer 2010), where M_* is the mass of the host star and M_p the mass of

the orbiting planet, P is the orbital period and e is the orbital eccentricity. It can be seen that K increases with diminishing orbital period and increasing planetary mass, as the effect of the stellar reflex motion is more pronounced:

$$K_{RV} = \left(\frac{2\pi\, G}{P}\right)^{1/3} \left(\frac{\mathrm{M}_p \sin i}{(\mathrm{M}_* + \mathrm{M}_p)^{2/3}}\right) \left(\frac{1}{(1-e^2)^{1/2}}\right). \tag{1.8}$$

Figure 1.12 from Kuntzer [2013] shows how radial velocity modelling can reveal the eccentricity of a planet's orbit, i.e. how elliptical it is where $e = 0$ corresponds to a perfectly circular orbit. High eccentricity values modify the shape of the radial velocity curve, along with variations in the true anomaly ω (the angle between the direction of the orbital perigee and the position of the planet). All models presented incorporate uniform values of RV amplitude K, orbital period P and ephemeris T_0.

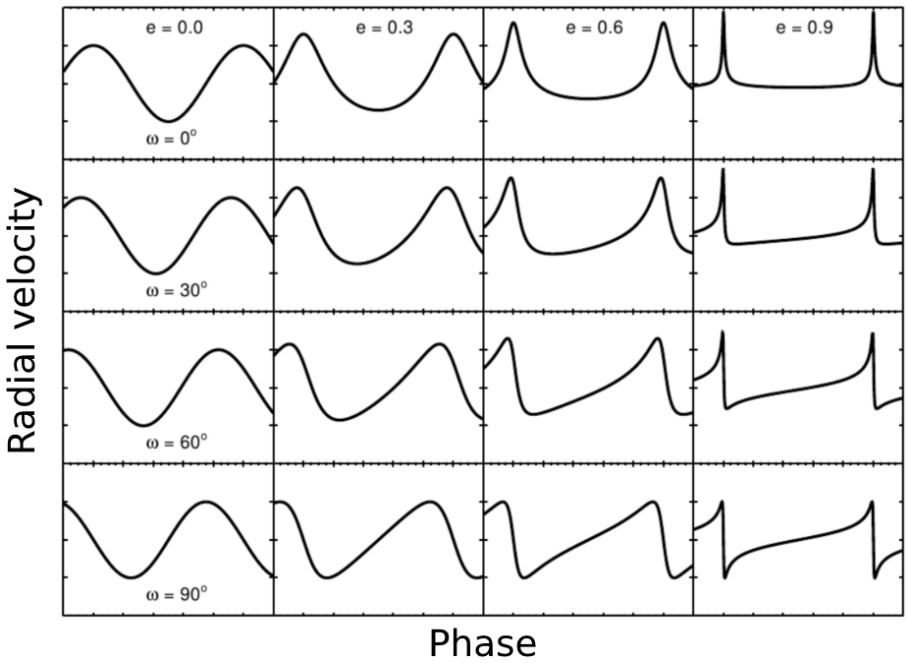

Figure 1.12: Figure from Kuntzer [2013] showing the variation in radial velocity phase curve shapes with increasing eccentricity (e) and a range of true anomaly values (ω).

As of 18 April 2024, a total of 1089 planets have been discovered using the radial velocity method.

Rossiter-McLaughlin effect

Radial velocity observations of transiting exoplanets may occasionally display additional shapes within their phase curves due to the planet occulting part of the star's rotating surface. From analysis of this 'Rossiter-McLaughlin effect' (Rossiter 1924, McLaughlin 1924) we are able to measure the approximate obliquity angle of a transiting planet relative to the spin axis of its host star. Figure 1.13 from Gaudi & Winn [2007] illustrates the shape of the resultant radial velocity curve during transits across a range of spin-orbit angles. Studying the spin-orbit alignments of exoplanets also acts as a probe of their possible formation and eventual migration pathways (Triaud 2018).

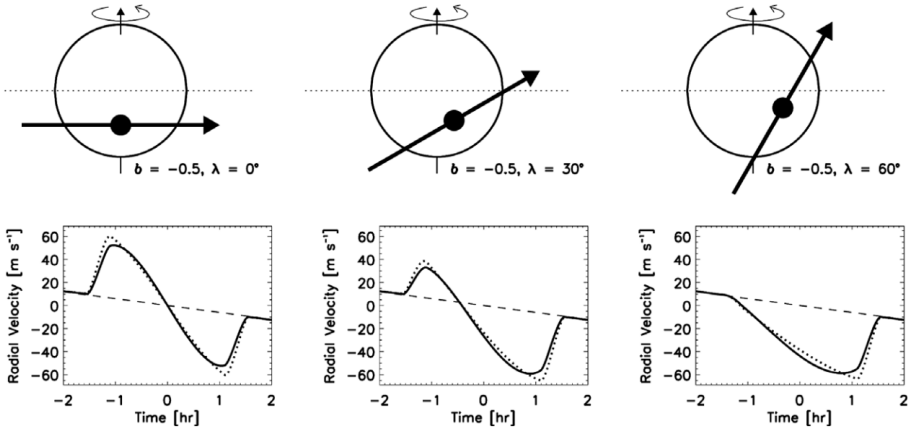

Figure 1.13: Figure from Gaudi & Winn [2007] illustrating the Rossiter-McLaughlin effect for a range of spin-orbit angles (λ) of a transiting planet and its host star, and the observed effect on the radial velocity phase curve during transit. These systems would produce identical light curves and have the same impact parameter (b). The solid line indicates the case for no limb darkening (LD coefficient $\epsilon = 0$) and the dashed line for limb darkening included ($\epsilon = 0.6$).

Stellar activity

Stars in general are not uniformly-bright disks - they have surface features that contaminate radial velocity measurements, often on scales down to tens of cms^{-1}, similar to true RV signals caused by small terrestrial planets (Cegla et al. 2019). Disentangling these signals is no simple feat, as there are many sources of stellar activity that must be taken into consideration. For example, granulation features are caused by bubbles of plasma rising through the outer layers of a star, which cool and sink down, causing an overall net convective blueshift effect (Cegla et al. 2019). Regions of varying magnetic activity also produce areas on the stellar surface

such as spots (e.g., Lagrange et al. 2010) and faculae/plages (e.g., Meunier et al. 2010). A set of spectral 'indicators' of these stellar activity features can help with this disentanglement and recovery of a clearer planetary Doppler signal. These indicators include (but are not limited to):

- **S-index and $\log \mathbf{R}'_{\mathrm{HK}}$** - magnetic activity causes an increase in the overall emission in the chromosphere and corona of the star (e.g., Duncan et al. 1991).
- **Hα-index** - faculae on the stellar surface emit Hα photons and cause a change in the depth of the Hα absorption line in the spectra (e.g. Gomes da Silva et al. 2022).
- **CCF shape changes** - changes in the FWHM (Full-Width Half Maximum), bisector span and contrast (depth) can reflect other features of stellar atmospheric variations over time or the presence of companion stars (Costes et al. 2021).

1.2.4 Joint analysis of transit photometry and RV spectroscopy

Often we will have obtained a combination of transit photometry, radial velocity and spectroscopic observations of a star hosting an exoplanet, along with parameters of the star from Gaia and other surveys. Each of these discovery methods and sets of information provide different contributions to the understanding of the system as a whole, and can be analysed jointly to provide a global model of an exoplanet system. Photometry data allows us to determine the planetary radius from the transit depth, as long as the radius of the star is known and the planet is inclined relatively edge-on to the observer. This inclination can also be derived from the impact parameter (Winn 2010).
Analysis of radial velocity data also allows for the measurement of $v \sin i_*$, where v represents the rotational velocity of the star and i can also be inferred from the transit. When combined with transit photometry as part of a joint model, RV measurements allow the exoplanet's mass to be derived, which can be converted to an approximate bulk density along with the radius. Matching of high S/N spectra with templates can allow for a determination of the star's spectral type, and analysis of the spectral energy distribution (SED) of the star. The logarithmic surface gravity $\log g$ and the density of the host star can also be determined from the planetary transit and the radial velocity data (Seager & Mallén-Ornelas 2003).

1.2.5 Other discovery methods

Astrometry

Similar to the radial velocity method of exoplanet discovery, the astrometry method relies on the reflex motion of a planet-hosting star around the system barycentre in response to the gravitational interaction with its planet (Black & Scargle 1982). However, the astrometric method aims to detect the angular displacement (β) of the star as it moves in the plane of the sky.

$$\beta = \frac{\mathrm{M}_p \, a_p}{\mathrm{M}_* \, d}. \tag{1.9}$$

This value is obtained with Equation 1.9 and is reliant on the masses of the host star and planet M_* and M_p respectively, and the semi-major axis of the planet a_p and distance from the observer to the object d. Astrometric detections are particularly sensitive to planets on orbits at large distances from their stars, and one such example is GJ 896 A b (Curiel et al. 2022) - a planet of 2.3 M_J orbiting the primary star of a low-mass binary system on an orbital period of 284.4 days. Figure 1.14 from Curiel et al. [2022] shows the motion of the primary star across the sky plane due to the gravitational interaction with the planet.

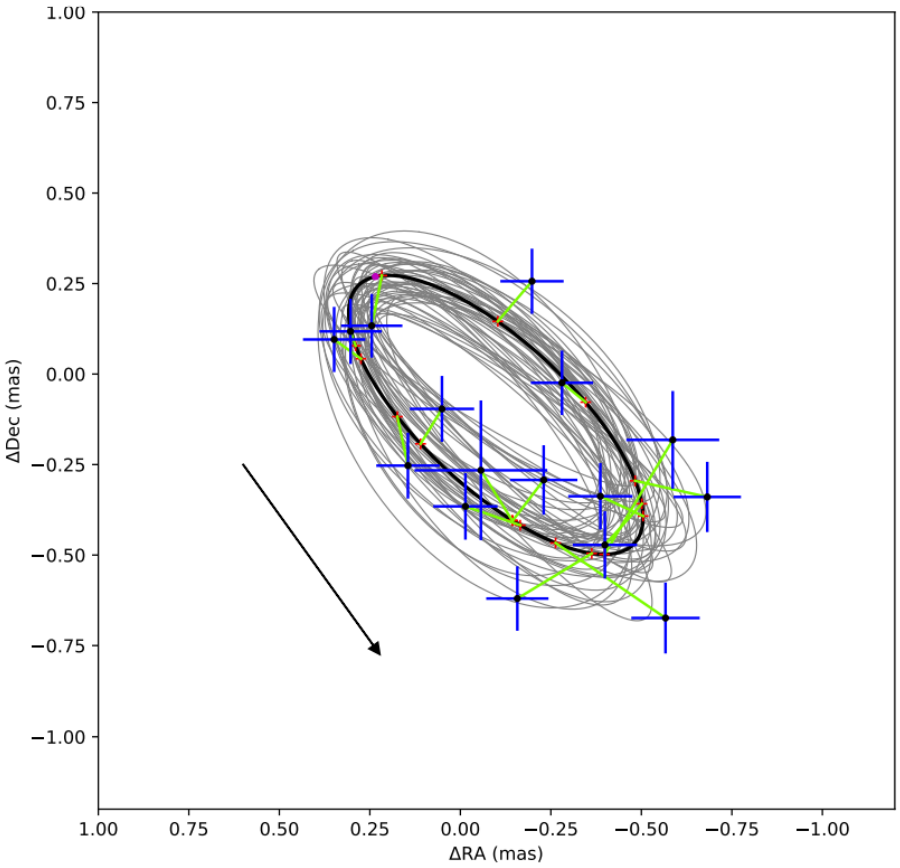

Figure 1.14: Astrometric motion of GJ 896 A from Curiel et al. [2022] due to gravitational interaction with its companion planet GJ 896 A b. The blue crosses represent the observational datapoints, connected to the positions of the star on the expected orbital location at the observation epoch (red crosses). Overplotted are are 50 randomly-generated orbits based on system parameters (grey ellipses), and the direction of orbital motion (black arrow).

It should be noted that while current exoplanet discoveries by this method are extremely limited, the European Space Agency's *Gaia* mission (Gaia Collaboration et al. 2016a) is expected to yield over 21,000 new exoplanet detections via this method over the lifetime of the nominal 5-year mission (Perryman et al. 2014). As of 18 April 2024, only 3 planets have been discovered using astrometry - DENIS-P J082303.1-491201 b (Sahlmann et al. 2013), GJ 896 A b (Curiel et al. 2022), and HIP 66074 b (Sozzetti et al. 2023).

Gravitational microlensing

Gravitational microlensing relies on the effect of general relativity (Einstein 1916), whereby a massive body will bend light around it. In the context of exoplanet discovery, a foreground star acts as a lens, which passes in front of a background source star and distorts its light. A star hosting a planet will cause an overall brightening in intensity of the observed star, and a second lensing peak can be seen in the brightness profile due to the planet perturbing the overall lensing effect and producing characteristic signatures in the light curve. In order for this effect to occur, the lensing and source stars and the observer must be precisely aligned - making such microlensing events relatively rare. Figure 1.15, originally from the discovery publication of MOA-2016-BLG-227L b by Koshimoto et al. [2017], illustrates this phenomenon.

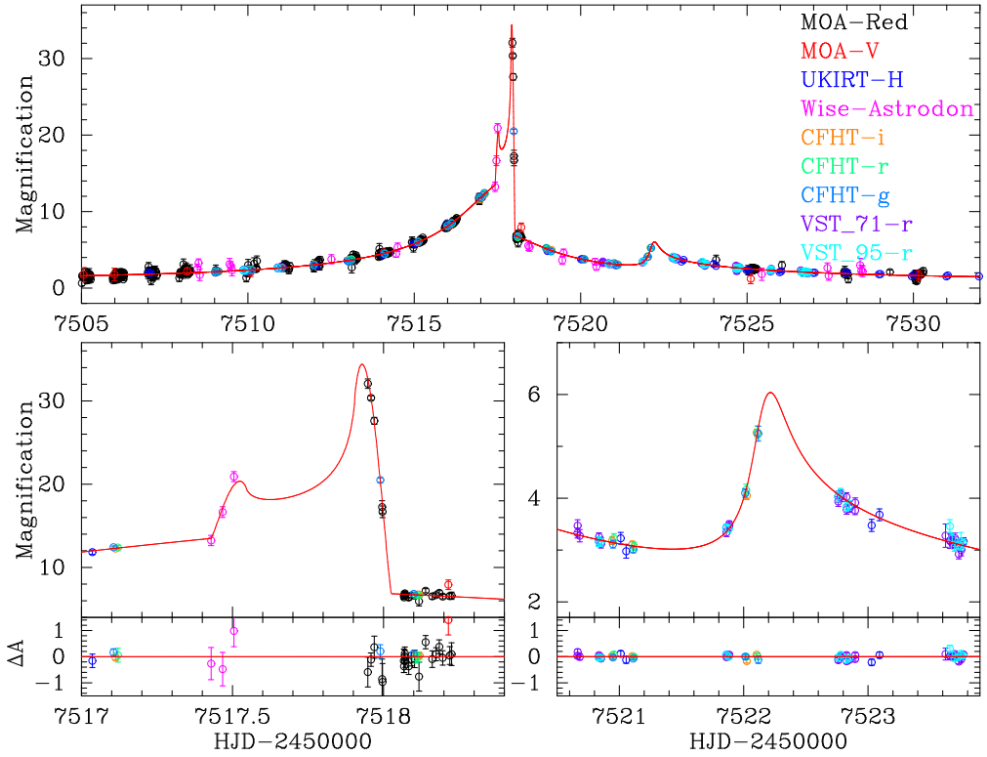

Figure 1.15: **Top panel:** Light curve of MOA-2016-BLG-227L from Koshimoto et al. [2017]. Sources are colour-coded, and overplotted with the best-fitting model (red line). **Bottom panels:** Highlights of the individual peak features and residuals, overplotted with the best-fitting model (red line).

As of 18 April 2024, a total of 214 planets have been discovered using gravitational microlensing observations.

Direct imaging

In particular cases, exoplanets can be directly imaged orbiting their host stars. This requires certain conditions to be met, such as the planet itself being sufficiently bright, and the planet having a large angular separation such that its image is not completely engulfed by that of the host star. In order to overcome the issues caused by host stars blotting out the light from their planets, coronagraphs are used to block out the stellar light so that individual nearby objects can be resolved (e.g. *Gemini* Planet Imager; Macintosh et al. 2014). Young planets are particularly amenable to direct imaging, as the latent heat from recent formation makes them bright in the infrared, producing increased planet-star contrast ratios (Bowler 2016). An example of the use of direct imaging to discover a multi-planet system is that of TYC 8998-760-1, a Solar analogue hosting two giant planets in the Lower Centaurus Crux subgroup of the Scorpius-Centaurus association (Bohn et al. 2020). Figure 1.16 from this publication shows imaging data from multiple filters of the *SPHERE* and *NACO* facilities.

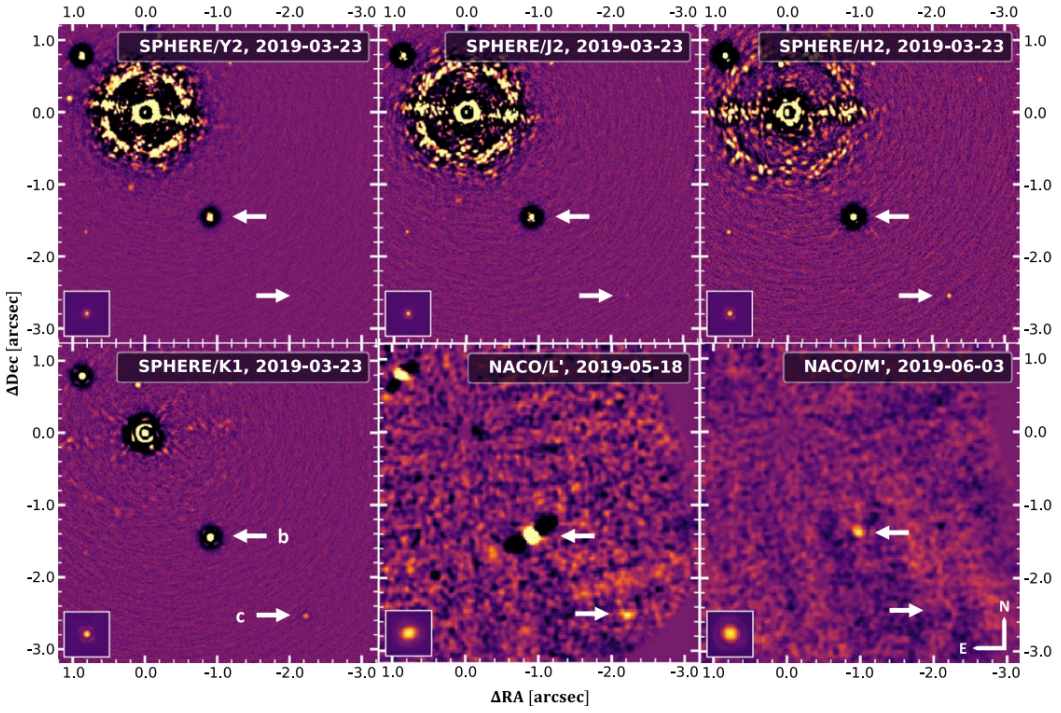

Figure 1.16: Imaging data of TYC 8998-760-1 from *SPHERE* and *NACO* at multiple wavelength filters from Bohn et al. [2020]. The two giant companion planets are labelled b and c, and the stellar host is positioned in the top left of each panel at the origin relative to the declination and right ascension axes.

As of 18 April 2024, 69 planets have been discovered through direct imaging methods.

1.3 Transit surveys

This section details the specifications and key discoveries from a selection of ground and space-based transit surveys that are most relevant to this work. This is not an exhaustive list; other surveys not discussed here include *MEarth* (Irwin et al. 2015a,b, see Section 1.6.3), KELT (Pepper et al. 2007), and CoRoT (Auvergne et al. 2009) amongst others. CoRoT in particular, launched in 2006, was the first space mission to search for exoplanets, and was responsible for the discovery of the first rocky planet CoRoT-7 b (Queloz et al. 2009) (before the first rocky planet from *Kepler*, *Kepler*-10 b, Batalha et al. [2011]).

1.3.1 WASP

WASP (*Wide Angle Search for Planets*, Pollacco et al. 2006) was a ground-based telescope facility located at the sites of Roque de los Muchachos Observatory (*SuperWASP North*) and the South African Astronomical Observatory (*WASP-South*), with each version housing eight 20 cm individual wide-angle cameras for simultaneous monitoring of a 482 square degree FOV (Field Of View), each with a CCD array of 2048×2048 pixels. It was a photometric survey of the entire sky that focused on the detection of transiting exoplanets, particularly those amenable to radial velocity follow-up observations (e.g. Wilson et al. 2020; Nikolov et al. 2021; Spyratos et al. 2021). At the time of writing, WASP has been responsible for the discovery of 189 planetary systems, many of which are Jupiter-size exoplanets orbiting main-sequence host stars in the range of visual magnitudes 9–13. Key discoveries include the first planet found to have a retrograde orbit, WASP-17 b (Anderson et al. 2010); and the low-Albedo Jupiter WASP-12 b (Hebb et al. 2009) experiencing elongation due to its proximity to the host star, stretching it into an 'egg' shape. Subsequent monitoring of WASP targets with RV spectrographs and *Kepler*/K2 have revealed additional planets in some systems, including WASP-8 c (Knutson et al. 2014), WASP-47 d and e (Becker et al. 2015); and two potential planets from TTVs in TESS data in the WASP-18 and WASP-126 systems (Pearson 2019).

1.3.2 HATNet

HATNet (*Hungarian-made Automated Telescope Network*, Bakos et al. 2004) is a ground-based facility of transiting exoplanets consisting of seven 11 cm telescopes each equipped with 2000×2000 pixel CCDs for a wide FOV of 8×8 square degrees, situated between the sites of Fred Lawrence Whipple Observatory in Arizona (5 telescopes), and the Mauna Kea Observatory in Hawaii (2 telescopes). To date it has discovered a total of 72 exoplanets since its first light in 2003, operating in a similar magnitude regime to WASP of visual magnitudes 9–14. Key discoveries include HAT-P-7 b (Pál et al. 2008), a short-period hot Jupiter falling in the field of *Kepler*, and HAT-P-11 b (Bakos et al. 2010), the first transiting Neptune-sized planet discovered by a ground-based survey.

1.3.3 HATSouth

HAT-South (*Hungarian-made Automated Telescope South*, Bakos et al. 2013) is a wide-field telescope facility consisting of 24 telescopes spread evenly across three continents - Las Campanas Observatory in Chile, HESS Observatory in Namibia, and in Siding Spring Observatory Australia. Each telescope is a 18 cm Takahashi coupled to a 4000×4000 pixel Apogee CCD with an R-band filter. To date HAT-South has discovered a total of 74 exoplanets. Notable discoveries include HATS-6 b, one of the first transiting giant planets confirmed around an M dwarf star (Hartman et al. 2015); and HATS-17 b, which has an orbital period of 16.3 days, making it the longest period transiting exoplanet discovered by a ground-based transit survey to date (Brahm et al. 2016).

1.3.4 NGTS

NGTS (*Next Generation Transit Survey*, Wheatley et al. 2018) is a ground-based telescope facility situated at Paranal Observatory, Chile, a site associated with the European Southern Observatory (ESO). It is a wide-field photometric survey, comprised of twelve 20 cm telescopes, that mainly focuses on the detection and characterisation of exoplanets within the Neptune-size and super-Earth regimes transiting bright stars (V > 13 mag). It operates in a wavelength range of 520–890 nm (red-optical), and is capable of achieving a photometric precision of 150 ppm. This enables planets as small as 3 $R_\oplus$ to be detected, such as NGTS-4 b as described in West et al. [2019]. The facility is also noted for its discovery of a planet on an extremely short orbital period of 18 hours, NGTS-10 b (McCormac et al. 2020). NGTS is now primarily monitoring TOIs (TESS Objects of Interest) as detailed in Bayliss

et al. [2020].

1.3.5 Kepler and K2

The *Kepler* (Borucki et al. 2010) satellite was launched into an Earth-trailing orbit in 2009 by NASA, and was a flagship space mission with the goal of determining an occurrence rate for Earth-sized exoplanets in the habitable zones (HZs) of Sun-like stars. *Kepler* observed a single patch of sky with an area of 115 square degrees (0.25% of the sky) from an array of 42 CCDs and a primary mirror of diameter 1.4 m, providing continuous photometric monitoring of a sample of approximately 150,000 stars. Data was available at both long and short cadences of approximately 30 minutes and 1 minute respectively (Christiansen et al. 2010). *Kepler* operated for a total of 4 years, during which time it was responsible for the detection of 2778 exoplanets, 2708 of which have been confirmed and published (Akeson et al. 2013). *Kepler* was able to discover many small planets, including the smallest planet orbiting a main-sequence star *Kepler*-37 b (Barclay et al. 2013), being smaller than Mercury. The continuous monitoring of a single field also allowed *Kepler* to find long-period planets, including *Kepler*-88 d (Weiss et al. 2020) on a period of 1403 ± 14 days, one of numerous multi-planet systems discovered during the survey. Due to the nature of *Kepler* target stars being observationally faint from the ground, radial velocity confirmations of their planet candidates were challenging - and as of 18 April 2024, only 311 planets have an associated mass measurement (excluding candidates with an upper mass limit only, of which there are 83). As a result, statistical validation techniques (see Section 2.6 for more information) were developed (e.g. VESPA, Morton et al. 2016) in order to provide probabilities that *Kepler* candidates are planetary in nature for the cases where a mass measurement remained elusive. The number of *Kepler* discoveries additionally enabled the study of a wider population of exoplanets and their occurrence rates (Batalha 2014), including those in Habitable Zones (Traub 2012; Gaidos 2013), planets within 0.25 AU of their stars (Howard et al. 2012), small planets (Dressing & Charbonneau 2013), and overall false-positive detection rates (Fressin et al. 2013).

In 2013, two of the reaction wheels on the *Kepler* satellite failed, leading to a change in observing strategy as the field-of-view (and thus the photometric observations) could no longer remain stable. The mission was reformed into K2 (Howell et al. 2014), and instead focused on observing stars along the ecliptic plane for 80 days at a time before the field-of-view moved, beginning in 2014 after initial testing. Additional methods were implemented in order to detrend out new systematics caused by the spacecraft movement, and provide new photometry with quality comparable to

that of the *Kepler* primary mission. K2 provided a further sample of 596 exoplanet candidates as of 18 April 2024, 127 of which have either a confirmed mass or upper mass limit (Akeson et al. 2013).

1.3.6 CHEOPS

CHEOPS (*CHaracterising ExOPlanet Satellite*, Benz et al. 2020) is a space telescope launched in 2019 by the European Space Agency (ESA) as part of the Cosmic Vision program, designed for the characterisation of transiting exoplanets. CHEOPS is equipped with a primary mirror of diameter 320 mm, and its camera system is comprised of a single 30 cm aperture and a single CCD of size 1024×1024 pixels to provide a total FOV of approximately 19×19 arcminutes. Its main aim is to determine the radii of exoplanets with associated mass measurements from spectroscopic radial velocity observations, to determine the density and bulk composition of those planets. It is in a low-Earth orbit which is in a Sun-synchronous, dusk-dawn configuration at an altitude of 700 km. This means that observations are often interrupted when the spacecraft passes behind the Earth relative to the target; this effect can be seen in Figure 3.4. CHEOPS has made significant contributions to exoplanet follow-up; for example in studying the hot dayside of WASP-189 b (Lendl et al. 2020b), the detection of the long-period planet ν^2 Lupi d (Delrez et al. 2021), and the near-polar orbit of MASCARA-1 b (Hooton et al. 2022).

1.4 TESS

TESS (*Transiting Exoplanet Survey Satellite*, Ricker et al. 2015) is a NASA mission launched in 2018 with the goal of surveying the brightest nearby stars to search for exoplanet transits (Stassun et al. 2019). One of the primary aims is to discover many thousands of exoplanet candidates across populations and subtypes, and determine the masses of > 50 small planets with radii $< 4\,R_\oplus$.
The spacecraft, a schematic of which is shown in Figure 1.17 from the NASA Goddard Space Flight Center[1], was launched into an eccentric, inclined orbit in a 2:1 resonance with the Moon (shown in Figure 1.18 from Ricker et al. 2015).

[1] `https://tess.mit.edu/science/`, NASA Goddard Space Flight Center, accessed 20 February 2024

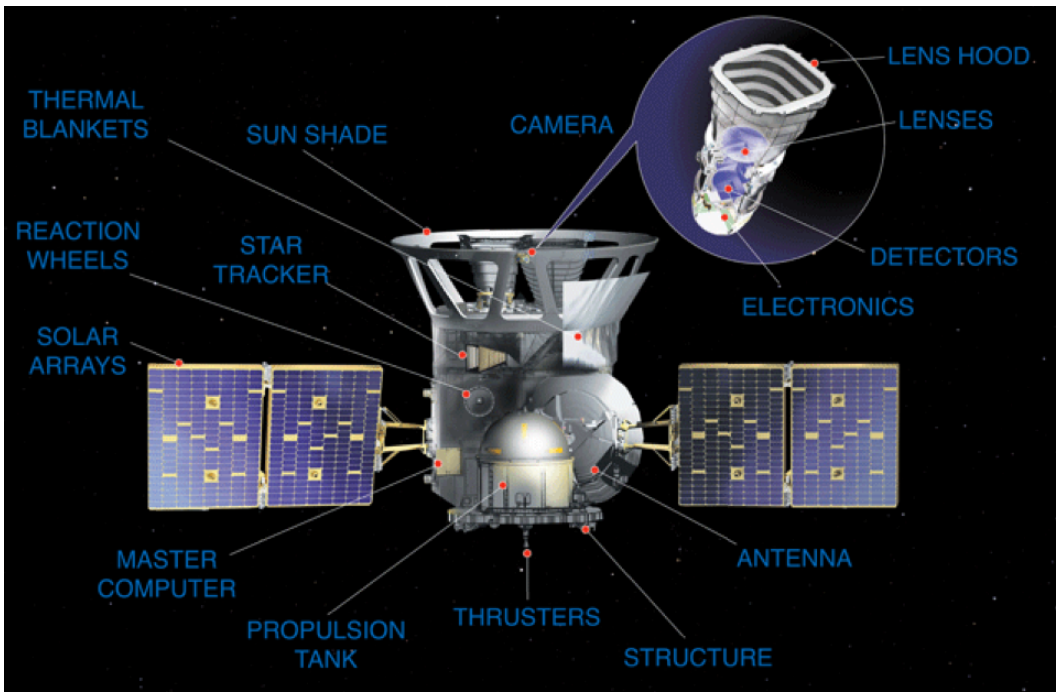

Figure 1.17: Schematic of the TESS spacecraft, showing the individual components of the spacecraft and the internal structure of the camera. Figure from the NASA Goddard Space Flight Center.

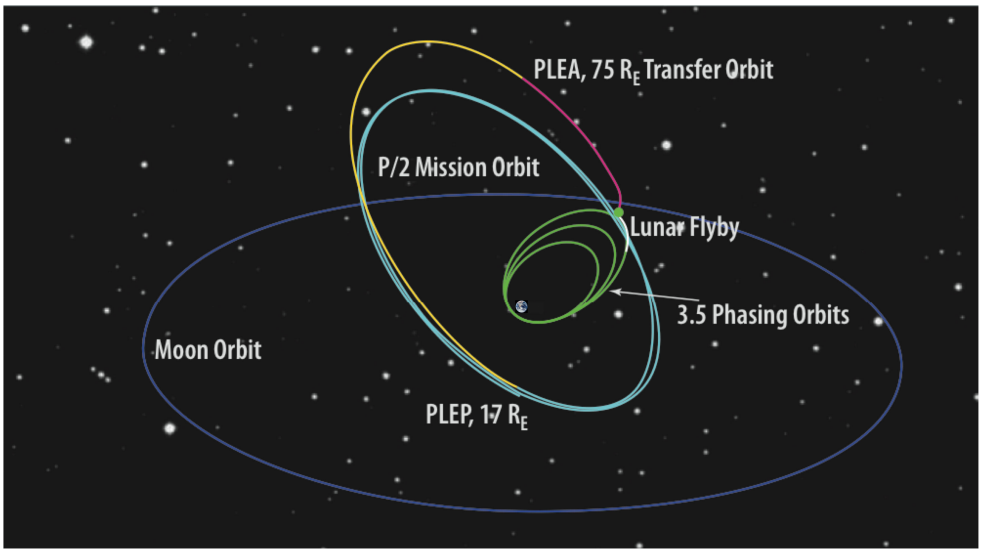

Figure 1.18: Schematic of the TESS orbit (light blue), with the 3.5 phasing orbits in green, the points of PLEA (Post-Lunar Encounter Apogee) and PLEP (Post-Lunar Encounter Perigee), and the Moon's orbit in dark blue. Figure from Ricker et al. [2015].

TESS is particularly well-suited for discovering short-period planets (typically P < 10 days) transiting bright stars, as its continuous monitoring for 27 days per Sector allows it to detect multiple transits during this time period.
A summary of the technical specifications and orbital parameters of TESS are shown in Table 1.1, reproduced in part from NASA HEASARC documentation[2] and Ricker et al. [2015].

Feature	**Value**
Single camera FOV (deg)	24 × 24
Combined FOV (deg^2)	3200
Entrance pupil diameter (cm)	10.5
Focal ratio (f/n)	f/1.4
Wavelength range (nm)	600–1000
Dimensions (m)	3.7 × 1.2 × 1.5
Power (W)	530
Perigee altitude (km)	108,000
Apogee altitude (km)	375,000
Inclination (deg)	37.00
Period (d)	13.70

Table 1.1: Technical specifications and orbital parameters of the TESS camera and spacecraft, from NASA HEASARC documentation and Ricker et al. [2015].

1.4.1 Observing strategy

TESS splits the sky into 26 Sectors, each with dimensions of 24×96 degrees (made up of 4×10 cm observation cameras and CCDs of 4096×4096 pixels), surveying each sector for approximately 27 days across a total sky view of 300 square degrees, which is 400 times that of the *Kepler* mission. Each alternating Cycle observes a different hemisphere of the sky, beginning in the Southern Ecliptic hemisphere in Cycles 1 and 3, and the Northern Ecliptic Hemisphere in Cycles 2, 4 and 6, with extra coverage of the Ecliptic provided in Cycles 4, 6 and 7 (coverage by Sector is shown in Figure 1.19[3]). Minor adjustments are made to the pointing of TESS between similar Cycles in order to cover areas not previously within the detection range due to the rectangular shape of individual Sectors. At the time of writing, TESS was in the process of Cycle 5 observations. Cycle dates are listed in Table 1.2.

[2] `https://heasarc.gsfc.nasa.gov/docs/tess/the-tess-space-telescope.html`, accessed 20 February 2024

[3] `https://tess.mit.edu/observations/`, accessed 20 February 2024

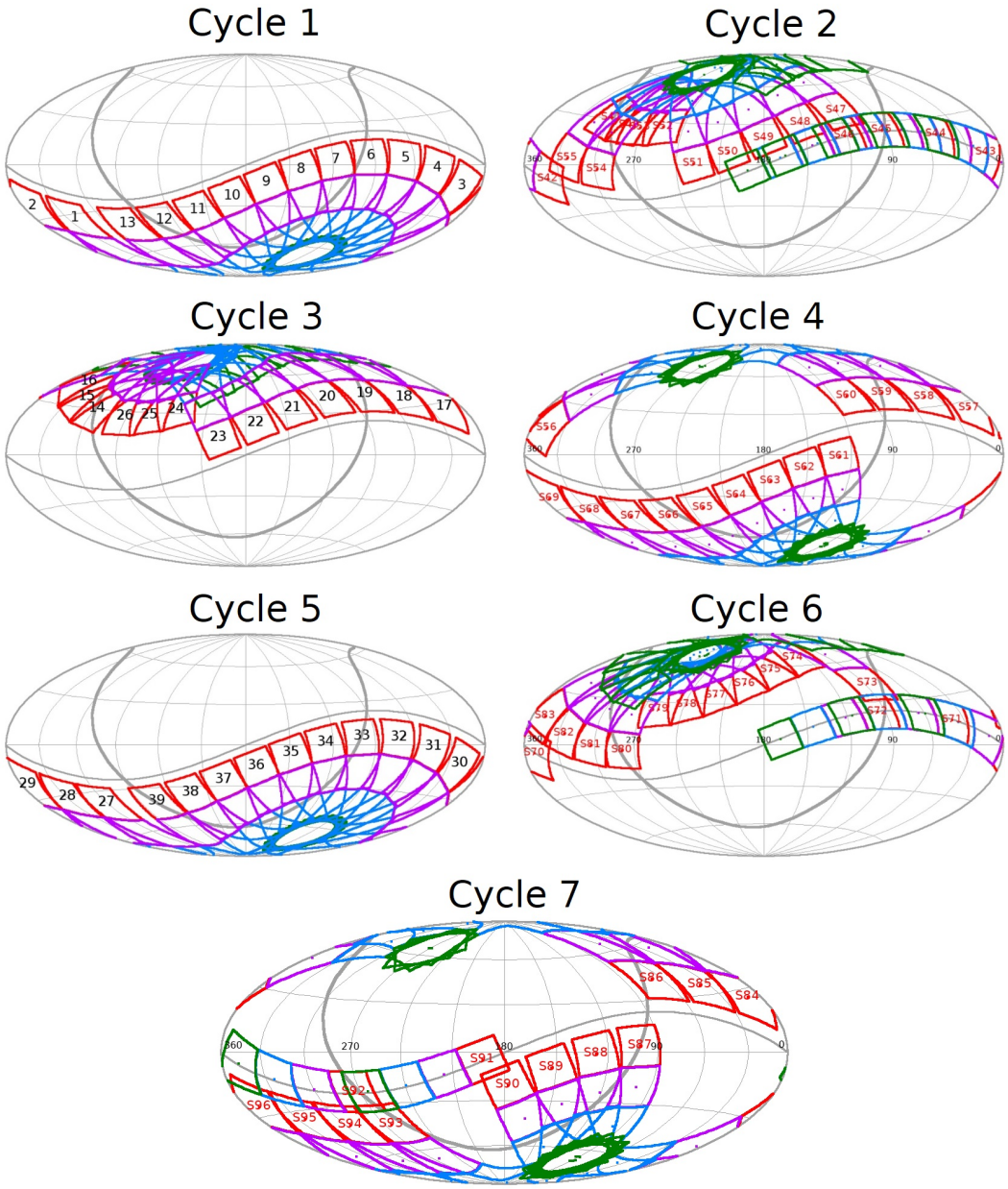

Figure 1.19: Pointings for TESS Cycles 1-7, showing the position of the Sectors on the sky for each Cycle; dates are in Table 1.2. Figures are from the TESS observations webpage (see footnote).

Figure 1.20, adapted from Ricker et al. [2015], shows a more general overview of the TESS observing strategy in relation to the individual Sectors and the overlaps between them providing different temporal coverage, including the Continuous Viewing Zones (CVZs) at the poles.

TESS Cycle number	Start date	End date	Sectors
1	2018 Jul 25	2019 Jul 17	1-13
2	2019 Jul 18	2020 Jul 04	14-26
3	2020 Jul 05	2021 Jun 24	27-39
4	2021 Jun 24	2022 Sep 01	40-55
5	2022 Sep 01	2023 Sep 20	56-69
6	2023 Sep 20	2024 Oct 01	70-83
7	2024 Oct	2025 Sep	84-96

Table 1.2: Observation dates for each Cycle of TESS (see Figure 1.19) and the associated Sectors. The exact dates of Cycle 7 had not yet been confirmed at the time of writing.

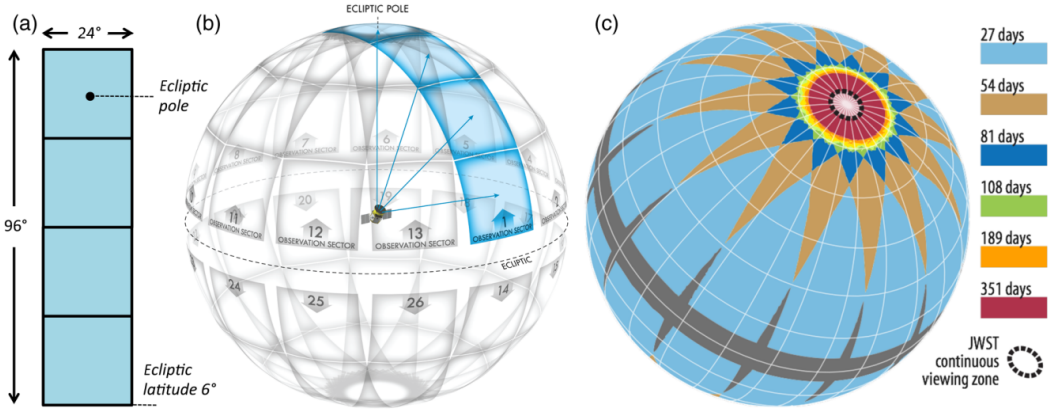

Figure 1.20: Schematic from Ricker et al. [2015]. **(a)** The four individual TESS cameras and the provided FOV. **(b)**The sky hemispheres showing the full observing strategy and approximate positioning of 13 Sectors per hemisphere. **(c)** The durations of TESS observations, ranging from a single Sector (27 days) to areas of overlap between Sectors (54-189 days), and the Continuous Viewing Zones at the poles ($\sim$ 351 days), which aligns with the JWST CVZ.

1.4.2 Data products

TESS obtains a wealth of different data products at varying cadences, formats and outputs (Stassun et al. 2019). These are described in more detail below.

- **Full Frame Images (FFIs)** - the full area of the CCDs, observed at cadences of 30 minutes (Cycles 1 and 2), 10 minutes (Cycle 3 onwards), 200 seconds (Cycle 4 onwards), 2 minutes (high priority stars) and 20 seconds (high priority stars from Cycle 3 onwards). The FFIs are available in both calibrated and uncalibrated formats.

- **Target Pixel Files (TPFs)** - groups of pixels are downloaded at cadences of 2 minutes and 20 seconds for selected higher priority targets.
- **Light Curve (LC) files** - flux time series data extracted with aperture photometry for the calibrated 2 minute and 20 second TPFs, produced by the Science Processing Operations Centre pipeline (SPOC; Jenkins et al. 2016). The raw aperture photometry is labelled as SAP (Simple Aperture Photometry), and the resulting flux from removal of systematics and contaminating effects using the CBVs is labelled as PDCSAP (Pre-Search Data Conditioning SAP).
- **Cotrending Basis Vectors (CBV)** - the set of systematic trends present in all light curve data from each CCD, used in removing instrumental systematics from the data to produce the PDCSAP light curves. These are not produced for the 20 second cadence targets.

- **TESS Input Catalog (TIC)** - the full catalog of sky sources observed by TESS, from which individual targets are selected for higher priority, shorter cadence observations.
- **Candidate Target List (CTL)** - the set of individual TIC objects selected for shorter cadence observations, for varying science purposes.
- **TESS Objects of Interest (TOIs)** - objects displaying signals of Threshold Crossing Events (TCEs) found in the TESS data are subjected to further vetting, and promoted to TOI status if the signal is determined to likely be associated with a transit or eclipse event.
- **Community TESS Objects of Interest (CTOIs)** - additional transit search projects conducted by the community may reveal potential transiting exoplanets previously missed by other detection processes, and once additional vetting has occurred they may be promoted to TOI status.

An example light curve from TESS of WASP-132 with data from Sectors 11 and 38 is shown in Figure 1.21, and the phase-folded transit of WASP-132 b is shown in Figure 1.22, folded onto the transit epoch value of 2459337.608 BJD, and the orbital period of 7.133514 days (Hellier et al. 2017).

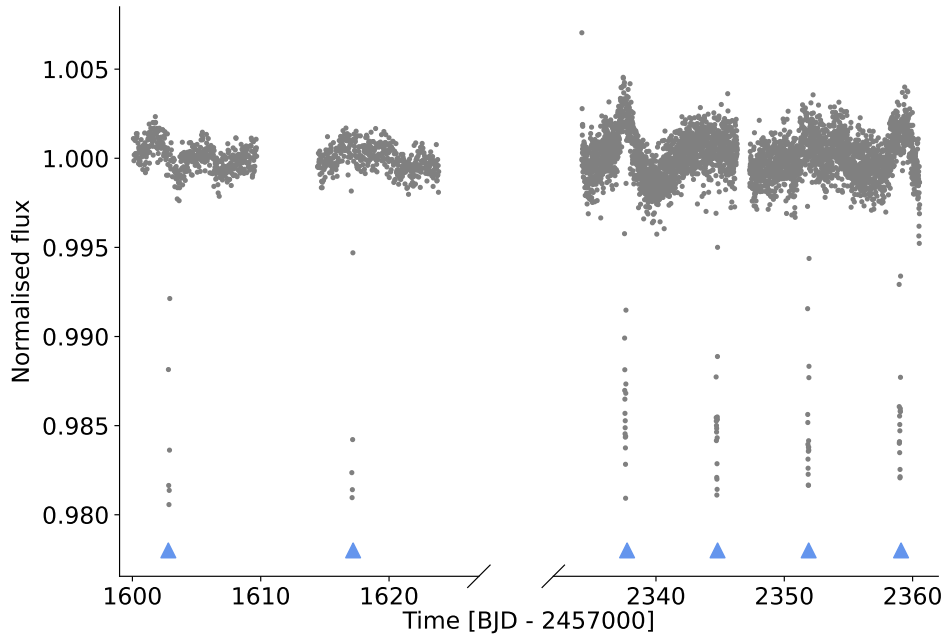

Figure 1.21: TESS SPOC PDCSAP light curve of WASP-132 ($V = 11.938$ mag), observed in Sectors 11 (2019 Apr 23 - 2019 May 20), 38 (2021 Apr 29 - 2021 May 26) of TESS at 30 minute and 10 minute cadence respectively. Individual transits of WASP-132 b are marked with blue triangles.

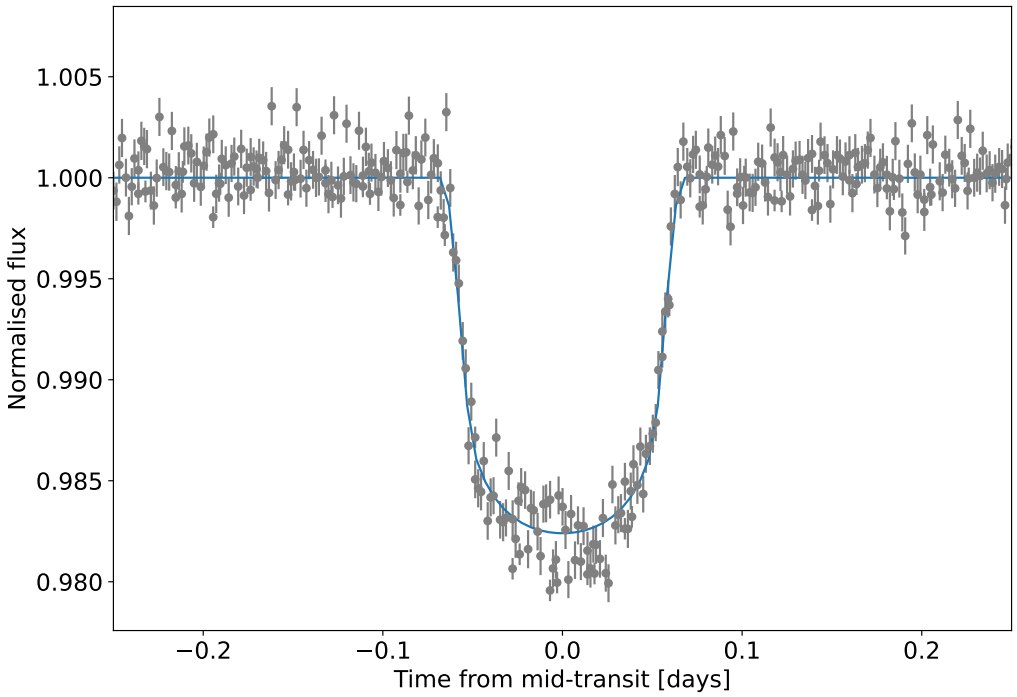

Figure 1.22: TESS light curve of WASP-132, phase-folded on the orbital period and transit epoch of WASP-132 b from Hellier et al. [2017] containing 6 full transits, overplotted with a transit model using parameters from Hellier et al. [2017] in blue.

1.4.3 Follow-up observations

Follow-up analysis is organised and coordinated by the TFOP (*TESS Follow-up Observing Program*) using ground-based facilities. TFOP further examines potential targets with a view to more robustly characterising planets in terms of their masses, radii, density, composition and other parameters. A level 1 mission goal of TFOP is to measure the masses of 50 transiting planets with radii smaller than $4\,R_\oplus$, with the follow-up work split into five sub-groups[4]:

- **SG1** - Seeing-Limited Photometry
- **SG2** - Recon Spectroscopy
- **SG3** - High-resolution Imaging
- **SG4** - Precise Radial Velocity
- **SG5** - Space-based Photometry

[4] `https://tess.mit.edu/followup/`, accessed 20 February 2024

TESS observations are still ongoing, and as of 18 September 2023 there are 385 confirmed and published exoplanets (Exoplanet Archive, Akeson et al. 2013; accessed 18 September 2023), with a further 7138 awaiting confirmation and designated either 'TOIs' (TESS Object of Interest) or 'CTOIs' (Community TOIs). CTOIs may come from a variety of sources, including citizen science initiatives such as the Planet Hunters TESS (PHT) project (Eisner et al. 2021), the TESS Single Transit Finder (STF) project and the Warm gIaNts with *tEss* (WINE) project (e.g. Schlecker et al. 2020; Jordán et al. 2020). CTOIs undergo a vetting process before being promoted to TOI status, upon which community efforts begin in order to confirm and publish the candidate planet.

1.5 Follow-up spectroscopy

Typically, a determination of planetary mass is required in order for an exoplanet candidate to be 'confirmed' as real, and not caused by an alternative scenario mimicking the presence of a planet. Follow-up spectroscopy utilising the radial velocity method (see Section 1.2.3) can provide this mass determination or an estimation of the upper limit of planetary mass, and this data is combined with the transit photometry (see Section 1.2.1) to fully characterise the bulk properties of an exoplanet system.

RV spectrographs work by observing a single target, the light from which is focused onto the entrance slit of the instrument and separated into its constituent wavelengths by a diffraction grating or prism. The spectrograph then records the position of selected spectral absorption lines over time (the Doppler shift), allowing for the derivation of the target's radial velocity compared to template spectra at rest. Spectrographs are often calibrated using e.g. thorium lamps (Coffinet et al. 2019) that produce known spectral lines, which are compared to laboratory-produced wavelength values. The value of $R = \lambda \,/\, \Delta\,\lambda$ represents the ability of an instrument to distinguish between two neighbouring spectral lines at a separation of $\Delta\,\lambda$, measured at a particular wavelength λ, and this value increases at higher resolutions.

Some key facilities that provide this RV data and that are most relevant to this work are described below.

1.5.1 HARPS

HARPS (*High Accuracy Radial velocity Planet Searcher*, Mayor et al. 2003) is a high-precision spectrograph mounted on ESO's 3.6 m telescope at La Silla Observatory,

Chile, based on the CORALIE and ELODIE instruments. It is able to obtain radial velocity data in the visible spectrum (380–690 nm) at a precision of $0.97\,\mathrm{m\,s^{-1}}$ and a resolution of R∼120,000, enabling the detection of habitable super-Earths (e.g. Gliese 581, Udry et al. 2007). HARPS-North (Cosentino et al. 2012) is the Northern hemisphere equivalent of HARPS, and is currently installed on the 3.58 m TNG (Telescopio Nazionale Galileo) at Roque de los Muchachos Observatory on La Palma.

1.5.2 ESPRESSO

ESPRESSO (*Echelle SPectrograph for Rocky Exoplanets and Stable Spectroscopic Observations*, Pepe et al. 2021) is a high-precision spectrograph situated at the 8 m VLT's (Very Large Telescope) Coudé facility at Paranal Observatory, Chile. It operates at resolutions from R∼70,000–190,000 at a wavelength range of 378.2–788.7 nm to provide an ideal radial velocity precision of $10\,\mathrm{cms^{-1}}$, comparable to an RV signature caused by that of an Earth-sized exoplanet (e.g. TOI-700 e, Gilbert et al. 2023).

1.5.3 CORALIE

CORALIE (Queloz et al. 1999) is an Echelle spectrograph currently mounted on the 1.2 m Leonhard Euler telescope at La Silla Observatory, Chile. It operates at a spectral resolution of R∼60,000 to provide radial velocity measurements down to a precision of $3\,\mathrm{ms^{-1}}$, and is a copy of the original *ELODIE* spectrograph that was used in the discovery of 51 Pegasi b in 1995 (Mayor & Queloz 1995).

1.5.4 PFS

PFS (*Planet Finder Spectrograph*, Crane et al. 2006) is a spectrograph installed on the 6.5 m Magellan II telescope at the Las Campanas Observatory, Chile. It observes in wavelengths from 391–734 nm and provides spectral resolutions of R∼38,000–190,000.

1.6 Follow-up photometry

Due to the limited observations that most targets receive from TESS (see Section 1.4.1), individual targets deemed to be of interest in detecting exoplanets are often followed-up from the ground using additional photometric telescope observations. These observations may allow for the collection of additional information, such as extra transit events to further refine the event parameters (see Section 1.2.2),

particularly in the cases of mono- and duotransiting planets (Sections 2.4 and 2.5, e.g. Gill et al. [2020c])); determine the presence of and monitor TTVs and TDVs (see Sections 1.2.2 and 1.2.2); and monitor stellar activity trends and features for detrending of data sets (Section 1.2.3) to name a few. Some of the facilities performing this photometric follow-up that are relevant to this work are described below.

1.6.1 LCOGT

LCOGT (Las Cumbres Observatory Global Telescope network, Brown et al. 2013) is a suite of observatory facilities comprised of a total of 18 telescopes spread across six locations in the Northern and Southern hemispheres (listed below). Owing to its potential for wide spatial and temporal coverage across multiple sites, LCOGT has contributed data to projects studying exoplanet transits and microlensing events, explosive transients and asteroids. LCOGT is used extensively in following up on exoplanet candidates from TESS.

- **CTIO** - Cerro Tololo Inter-American Observatory, Chile
- **SAAO** - South African Astronomical Observatory, South Africa
- **SSO** - Siding Spring Observatory, Australia
- **McDonald Observatory** - Fort Davis, Texas
- **Haleakala Observatory** - Maui, Hawaii
- **Teide Observatory** - Tenerife, Canary Islands

1.6.2 ASTEP

ASTEP (*Antarctic Search for Transiting ExoPlanets*, Crouzet et al. 2010, 2018) is a 40 cm optical telescope situated at Concordia Research Station, Dome C, on the Antarctic plateau, designed for detections of exoplanet transits. It experiences 4 months of continuous night during the Antarctic winter, and favourable weather conditions for observing owing to the low temperatures and relatively low levels of atmospheric scintillation noise at the site.

1.6.3 MEarth

The *MEarth* Project (Nutzman & Charbonneau 2008) is a robotic telescope observatory stationed at Fred Lawrence Whipple Observatory, Arizona. It focuses on monitoring small red M-dwarf stars for photometric transits of exoplanets, and is further separated into *MEarth*-North, and *MEarth*-South.

1.7 Future exoplanet studies

In addition to the TESS mission, a number of other space missions will change the landscape of our understanding of exoplanets. This section details the most important of these current and future space-based missions that are dedicated to or include detection and characterisation of exoplanets: the *Gaia* mission, JWST and the the PLATO mission.

1.7.1 Gaia

Gaia (Gaia Collaboration et al. 2016a) is an ESA space telescope launched in 2013, focusing on the creation of the largest and most precise 3-dimensional map of the Milky Way galaxy using properties derived from astrometric motion (see Section 1.2.5). It is estimated that *Gaia* will also provide up to an additional 10,000 new exoplanets to the catalog as a result of astrometric detections (Perryman et al. 2014), along with a census of non-stellar objects such as comets and asteroids. At the time of writing, *Gaia* has had four individual Data Releases: DR1 (Gaia Collaboration et al. 2016b), DR2 (Gaia Collaboration et al. 2018), and DR3 (Gaia Collaboration 2022) along with Early Data Release 3 (Gaia Collaboration et al. 2021). The first *Gaia* detections of transiting planets were *Gaia*-1 b and *Gaia*-2 b (Panahi et al. 2022).

1.7.2 JWST

JWST (*James Webb Space Telescope*, Gardner et al. 2006) is a NASA/ESA satellite launched in 2021 to the L2 Lagrange point, designed for a broad range of astronomical applications in the long-range-visible to mid-infrared range from 0.6–28.3 μm. The primary mirror of JWST is 6.5 m, which is 6 times that of the Hubble Space Telescope (*HST*). It is comprised of 18 individual hexagonal segments, creating a total light-collecting area of 25 m^2. It is able to observe some of the most distant objects in the universe up to redshift $z \approx 20$, and is equipped with four instruments: *NIRCam* (Rieke et al. 2005, 2023), *NIRSpec* (Jakobsen et al. 2022), *MIRI* (Rieke et al. 2015) and *NIRISS* (Doyon et al. 2023). JWST is able to provide high-precision transmission spectra of exoplanet atmospheres, allowing for improved detections of individual molecular and atomic species and potential biomarkers. Some examples of successful studies of exoplanet atmospheres include the detection of carbon dioxide on WASP-39 b (JWST Transiting Exoplanet Community Early Release Science Team et al. 2023), and the detection of methane on WASP-80 b (Bell et al. 2023).

1.7.3 PLATO

PLATO (*PLAnetary Transits and Oscillations of stars*, Rauer et al. 2014) is a future space telescope expected to be launched at the end of 2026 (Rauer et al. 2024) as part of the ESA Cosmic Vision program. It is designed to detect a large number of Earth-sized exoplanets within the habitable zones (HZs) of their stars, and provide precise characterisation of planet-hosting stars through asteroseismology. Its hardware consists of 26 12 cm aperture telescopes, 24 of which are designed for normal operation at a cadence of 25 s for objects with an apparent magnitude > 8, and 2 fast cameras with a shorter cadence of 2.5 s for brighter stars between magnitude 4 and 8. The first field for PLATO has been selected (Nascimbeni et al. 2022) and an input catalogue has been defined (Montalto et al. 2021).

1.8 Exoplanet demographics

1.8.1 Discoveries to date

In Figure 1.23 using data from the NASA Exoplanet Archive (Akeson et al. 2013), a cumulative histogram of exoplanet detections through various methods is shown, colourised by the primary discovery method and annotated with the first detection using each method. It should be noted that the sharp rise in detections through the transit method between 2010-2016 is largely due to the launch and operation of the *Kepler* mission (see Section 1.3.5), with the TESS mission following in 2018 (see Section 1.4). Radial velocity detections continue to steadily increase with the continual development of ever more stable and precise spectrographs such as HARPS and *ESPRESSO*, whilst detections through microlensing, direct imaging and TTVs only remain small in number. It should be noted that the *Gaia* mission is expected to drastically increase the number of astrometric exoplanet detections in the coming years.

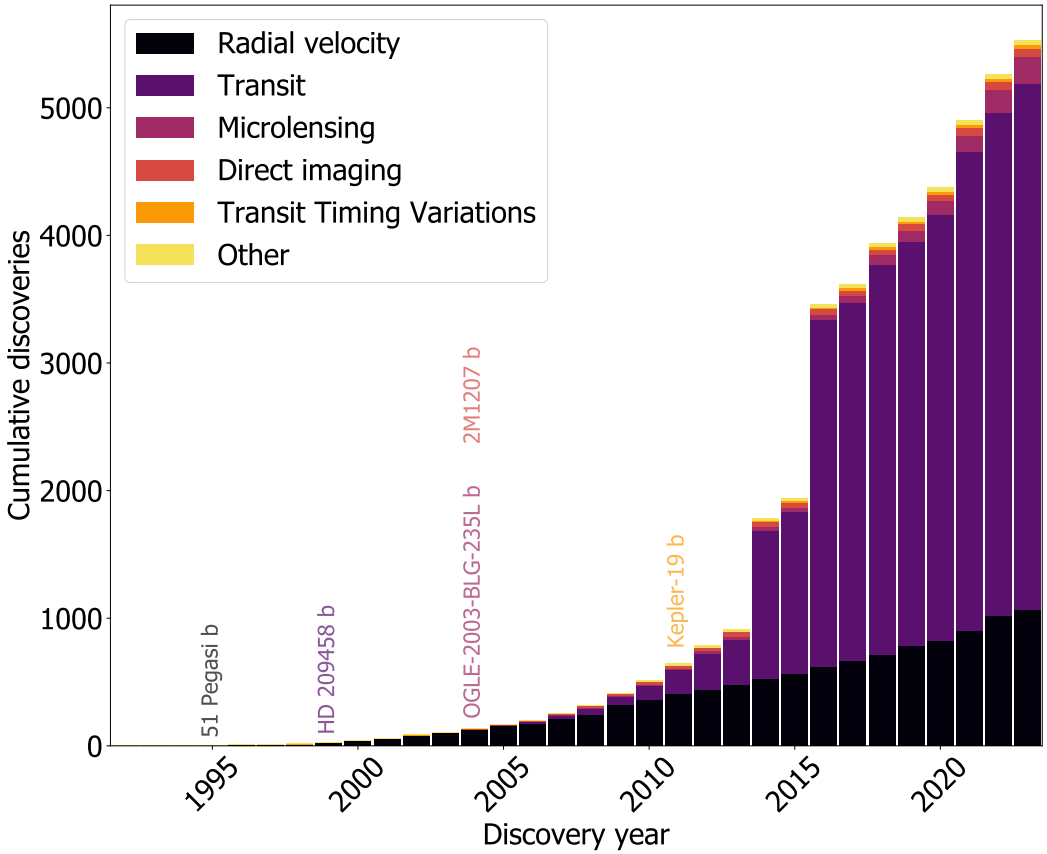

Figure 1.23: Cumulative histogram of exoplanet detections from the NASA exoplanet archive (Akeson et al. 2013). Annotated planetary discoveries are as follows: **51 Pegasi b** - Mayor & Queloz [1995], **HD 209458 b** - Charbonneau et al. [2000], **OGLE-2003-BLG-235L b** - Bond et al. [2004], **2M1207 b** - Chauvin et al. [2004], **Kepler-19 b** - Ballard et al. [2011]

Figure 1.24 (also created with the NASA Exoplanet Archive) shows exoplanet detections colourised by discovery method in terms of their orbital period in days and planetary mass in Jupiter masses. It can be seen that most detections of transiting exoplanets lie below approximately 100–200 days in orbital period, but reside across a range of radii; whereas detections via radial velocity extend further into long-period space but are limited for smaller-mass planets. The longest-period planetary detections are consistently from direct imaging observations, as a wide planet-star separation is required in order to disentangle the visible signature of an exoplanet.

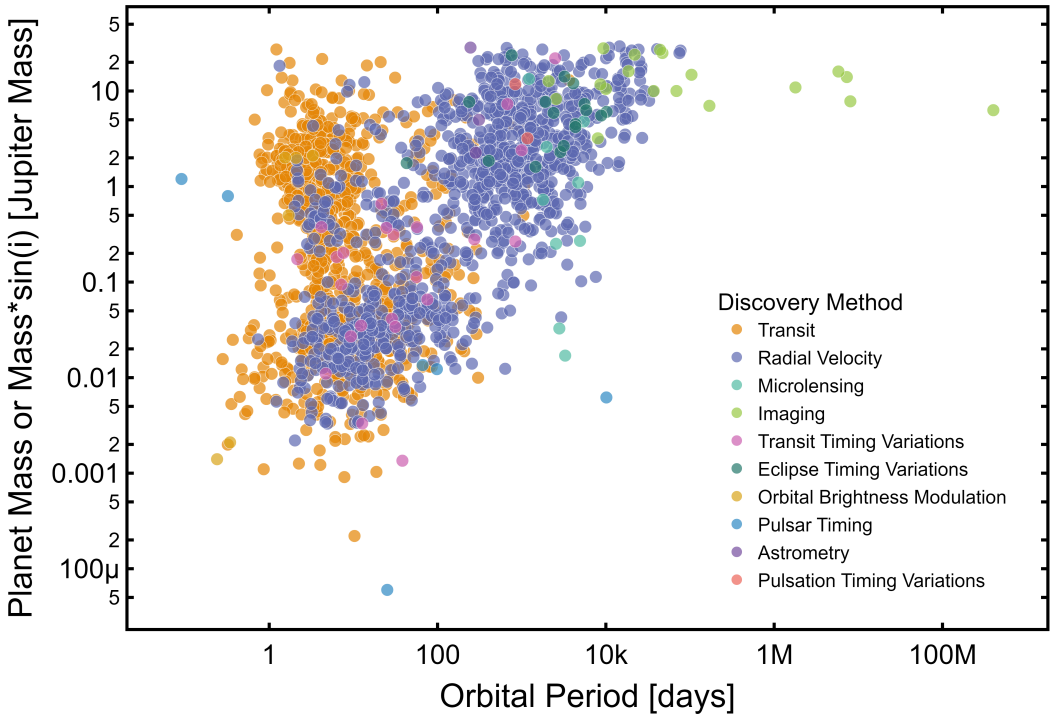

Figure 1.24: Exoplanet detections from the NASA Exoplanet Archive (Akeson et al. 2013) as of 5 February 2024, colourised by detection technique and in period-planetary mass space.

1.8.2 Classes of exoplanet

Figure 1.25, shows the distribution of exoplanet detections in period-mass space, approximately grouped into categories of planetary characterisations based on their observed properties and positions on the diagram.

Classification	Radius ($R_\oplus$)	Mass ($M_\oplus$)
Earths	< 1.25	$0.1 - 2$
Super-Earths	$1.25 - 2$	$2 - 10$
Neptunes	$2 - 6$	$10 - 100$
Jupiters	$6 - 15$	$100 - 4100$

Table 1.3: Categorisation of exoplanet types, based on radius boundaries from Borucki et al. [2011] and mass boundaries from Stevens & Gaudi [2013]. The upper limit on planetary mass for Jupiters at $4100\,M_\oplus$ is equivalent to $13\,M_J$, the deuterium burning limit for brown dwarfs.

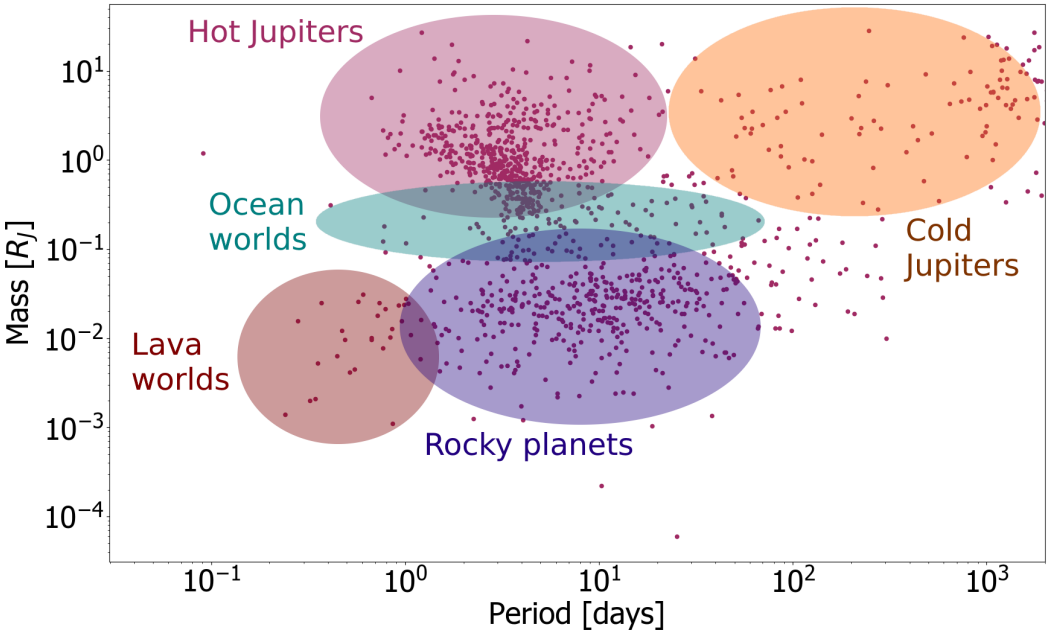

Figure 1.25: Exoplanet detections from the NASA Exoplanet Archive (Akeson et al. 2013), with approximate locations of exoplanet populations and types overplotted in the following colours: **Hot Jupiters** - magenta, **Ocean worlds** - blue, **Cold Jupiters** - orange, **Lava worlds** - red, **Rocky planets** - purple. Ellipses are not representative of exact population locations and are for illustrative purposes only.

Table 1.3, adapted from radius categories given in Borucki et al. [2011] and mass categories from Stevens & Gaudi [2013] respectively, separates the exoplanet population into four non-exhaustive groups.

Lava worlds

Lava worlds are a subclass of exoplanet which may have surfaces of entirely or partially lava (Chao et al. 2021), due to their extremely close proximities to their

host stars (often within 0.02 AU). Such planets on very short orbital periods (<1 day) may be tidally locked, the case in which one hemisphere of the exoplanet constantly faces the star and the other is in perpetual darkness, producing a large surface temperature differential. Lava worlds may also arise due to extremely variable tidal forces producing internal heating if the planet is on a highly eccentric orbit, and volcanic activity on their surfaces may serve to continually replenish the molten surface. Examples of such lava worlds include CoRoT-7 b (Queloz et al. 2009), *Kepler*-10 b (Batalha et al. 2011) and *Kepler*-78 b (Sanchis-Ojeda et al. 2013).

Rocky planets

Typically, Earth analogues and their larger counterparts, super-Earths, are considered to be terrestrial or rocky planets. Their assumed structure based on studies of the four terrestrial Solar system planets (Mercury, Venus, Earth and Mars) is that of an iron core surrounded by a mantle of rock and silicate material, and potentially a gaseous atmosphere and/or liquid water depending on their proximity to their host stars and the composition of the available constituents during the planet formation process. Secondary atmospheres may be formed after the initial accretion phase in which the primordial H/He atmosphere is created, through outgassing of volatile compounds (e.g. Swain et al. 2021), impact events depositing volatiles onto planetary surfaces (e.g. Kral et al. 2018), or biological processes as on Earth. The first rocky planet to be discovered and have determined values for both mass and radius was the aforementioned *Kepler*-10 b, categorised as a super-Earth with a radius of $1.4\,R_\oplus$. Super-Earths have no counterpart in the Solar system, however Petigura et al. [2013] found that approximately 15% of Solar-type stars in the galaxy host terrestrial planets with radii between 1–2 $R_\oplus$ and orbital periods between 5 and 50 days.

Ocean worlds

Ocean or water worlds are usually considered to be planets that have retained a significant fraction of their mass in the form of water and/or water ice in various states (defined and explored in Léger et al. 2004). This water may be in the form of considerable amounts of atmospheric water vapour, subsurface oceans beneath icy crusts (as is the case for some moons of the Solar system, e.g. Enceladus, Zolotov 2007), or a fully liquid surface ocean. Ocean worlds are of considerable interest in terms of planetary habitability, as liquid water provides a medium for biochemical reactions that provide the precursors to extraterrestrial life (Lammer et al. 2009).

Examples of discovered and confirmed ocean worlds include TOI-1452 b (Cadieux et al. 2022), and *Kepler*-138 c and d (Piaulet et al. 2023).

Neptunian planets

Neptunian planets (3.5 $R_\oplus$ and larger) and their smaller counterparts, sub- or mini-Neptunes (1.7–3.5 $R_\oplus$), are theorised to be composed of a rocky or metallic core with a large atmospheric envelope of primarily H and He of up to 20% of their total mass. Ice giants are a subset of these planets, such as Neptune itself and Uranus in the Solar system, that contain a substantial fraction of their mass in the form of ices (including water, methane and ammonia - Podolak et al. 1995). The structure of sub-Neptunes is often variable, as the same measurements of mass, radius and bulk density may arise from different models of interior structure (Dorn et al. 2017). An example of a confirmed sub-Neptune is TOI-836 c, described in Hawthorn et al. [2023a], which forms Chapter 3 of this work. Two features of the Neptune and sub-Neptune population are also described: the 'radius valley' in Section 1.9.1 and the 'Neptune desert' in Section 1.9.2.

Gas giants

Gas giant planets (those above 6–7 $R_\oplus$) are named as such for their large extended gaseous envelopes. The upper mass limit at 13 M_J is given as the boundary after which objects are able to fuse deuterium and become known as 'brown dwarfs'. Contrary to the gas giants in the Solar system (Jupiter and Saturn), the exoplanet population in the early days of the field was dominated by 'hot Jupiters' - gas giant planets residing on extremely short orbital periods of less than 10 days. They are often relatively easy to detect, as they induce large transit depths due to their larger radius, and induce larger variations in radial velocity due to their larger mass and larger gravitational effect on their host stars. As a result of their proximity to their stars, they can often reach much higher temperatures of thousands of K - one of the most irradiated being KELT-9 b, an ultra-short period (1.5 day) hot Jupiter with a temperature of ~ 4600 K that orbits an A-type star (Gaudi et al. 2017). Their ease of observation also makes them amenable to transmission spectroscopy studies to uncover their compositions, and this has been successfully done for hot Jupiters such as HD 209549 b (Xue et al. 2024) using JWST, which was found to have significant fractions of water and carbon dioxide.

However, as new studies of long-period transiting planets have emerged, we are also beginning to uncover the population of 'warm' and 'cold' Jupiters that reside on

longer orbital periods and at larger distances from their host stars. These planets would be more similar to Jupiter and Saturn, which themselves reside on orbital periods of ~ 4332 and $\sim 10,759$ days respectively. Warm (or 'temperate') Jupiters are a loosely-defined subclass; literature such as Fleming et al. [2008] define boundaries of orbital period from 4–150 days, whereas Encrenaz et al. [2018] defines boundaries of temperature from 350–500 K.

Unlike hot Jupiters, warm and cold Jupiters are more challenging to detect using transit and radial velocity observations, as extended monitoring campaigns are often required to recover even a single transit, or constrain the entire RV phase curve over their long orbital periods - however, detections using other methods such as direct imaging are more conducive to long-period planet detection, as they require larger orbital separations between star and planet.

1.8.3 Occurrence rates

Obtaining large numbers of well-characterised exoplanets allows for a determination of the approximate occurrence rates of certain planet demographics; i.e. the average number of planets per star. However, individual catalogues of exoplanets are often either incomplete or still contain a number of false-positive detections, in which case we must consider the completeness of the sample; and different discovery methods are biased towards particular system configurations (for example, the transit and radial velocity methods in particular require planets to be reasonably well-aligned). Mayor et al. [2011] made use of 8 years' worth of HARPS and *CORALIE* data on 376 stars to provide the first estimations of exoplanet occurrence rates, and found that over 50% of Solar-type stars are orbited by a planet with mass $< 30\,M_\oplus$ on a period of up to 100 days, and around 14% host a planet with mass $> 50\,M_\oplus$ on orbital periods of less than 10 years. The *Kepler* mission data and subsequent analyses of planetary occurrence rates (e.g. Fressin et al. [2013]) uncovered an average rate of false-positive detections of 9.4%, and a giant planet frequency of $\sim 5.24\%$ around stars of all spectral types. This work was updated by Hsu et al. [2019] using data from Data Release 25 of *Kepler* and stellar parameters from Data Release 2 of *Gaia*, and their results as a function of planetary radius and orbital period are shown in Figure 1.26.

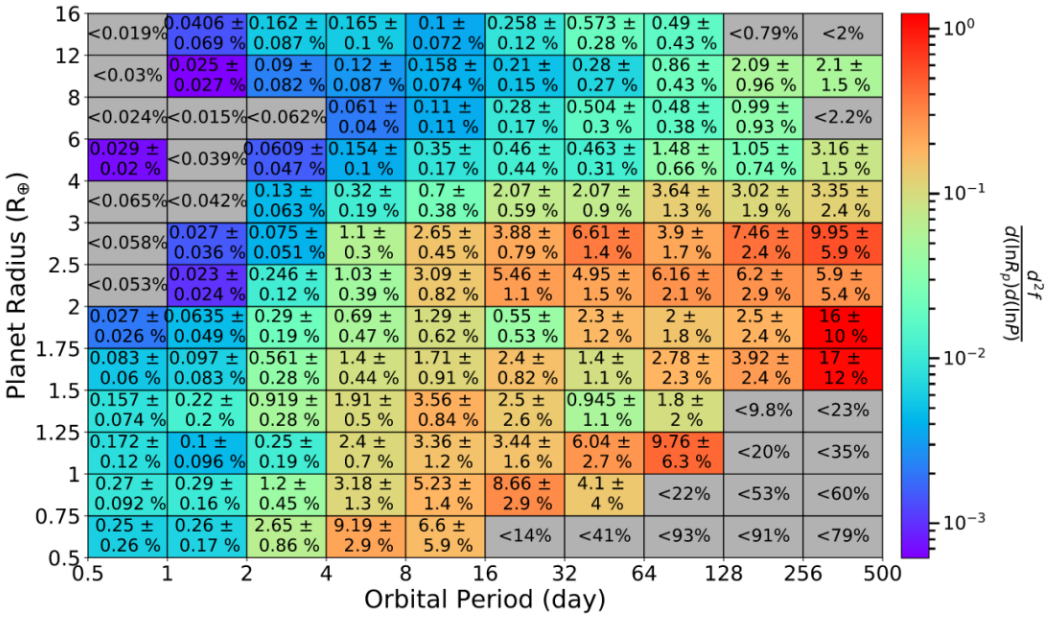

Figure 1.26: Occurrence rates from Hsu et al. [2019], from a combination of *Kepler* and *Gaia* data, in radius-period space.

1.9 Exoplanet population features

1.9.1 Radius valley

The 'radius valley' describes a distinct bimodal shape in the population of well-characterised exoplanets: the population appears to show a dearth of planets of radii between approximately 1.3–2.6 $R_\oplus$ (Van Eylen et al. 2018; Fulton & Petigura 2018). This was first seen in Youdin [2011] when examining the planetary distribution function of the discovered planets from the *Kepler* mission at that time. Owen & Wu [2013] further explored this phenomenon and was theorised to be the result of close-in Neptune-radius planets being unable to retain their atmospheres beyond the first ~ 100 Myr of the host stellar lifetime; the atmosphere undergoes photoevaporation as the result of intense X-ray and EUV (Extreme Ultra-Violet) radiation from the star. It has also been interpreted as the result of core mass loss (Ginzburg et al. 2016) or the impact of planetesimals onto planetary surfaces (Schlichting et al. 2015). The population is divided into the two categories, that of the stripped super-Earths on the left and the mini-Neptune population to the right, which was also seen by Fulton et al. [2017] in the California-*Kepler* survey. Figure 1.27 from Fulton & Petigura [2018] illustrates the position of the radius valley within the population of discovered exoplanets with orbital periods < 100 days.

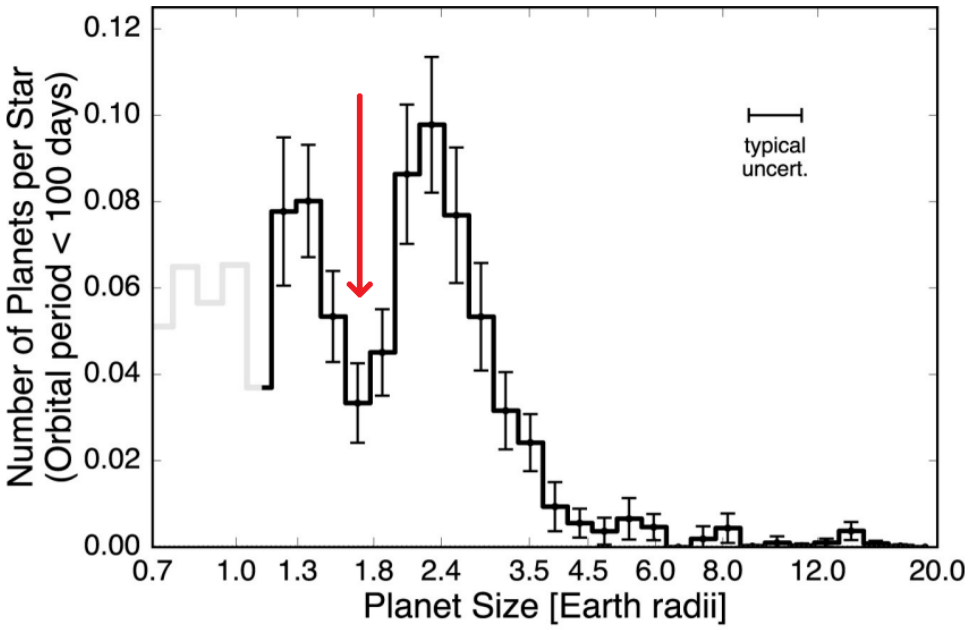

Figure 1.27: Figure reproduced from Fulton & Petigura [2018] illustrating the position of the radius gap (red arrow) at $\sim 1.8\,R_\oplus$, in relation to the population of exoplanets with orbital periods < 100 days.

1.9.2 Neptune desert

Both transit and radial velocity surveys are readily able to detect Neptunian planets - however, when examining the wider exoplanet population, there is a distinct dearth of planets with radii between 3–4 $R_\oplus$ residing on relatively short orbital periods < 5 days. The lack of discovered planets in this part of parameter space was first noted in Szabó & Kiss [2011], but boundaries were not prescribed to it until Mazeh et al. [2016] (shown in Figure 1.28) - and it has since been referred to as the 'Neptune desert', 'sub-Jovian desert' or 'evaporation desert'. Such planets may have had their atmospheric H/He envelopes stripped away by the intense X-ray and EUV radiation of their host stars through photoevaporation (Kurokawa & Nakamoto 2014; Mazeh et al. 2016), as is the case for TOI-849 b (Armstrong et al. 2019) that has left behind a very dense planetary core. Some planets may be currently undergoing this process - e.g. TOI-908 (Hawthorn et al. 2023b), presented in Chapter 4 of this work. Matsakos & Königl [2016] proposed that the desert is the result of high-eccentricity tidal migration that transports planets to within the Roche limit of their stars, and their orbits become circularised. In recent times the desert has become more populated with discoveries such as LTT-977 b (Jenkins et al. 2020), NGTS-4 b (West et al. 2019), the aforementioned TOI-849 b (Armstrong et al. 2019), and TOI-969 b

(Lillo-Box et al. 2022) - see Figure 4.9 for the placements of these discoveries relative to the Mazeh et al. [2016] desert boundaries.

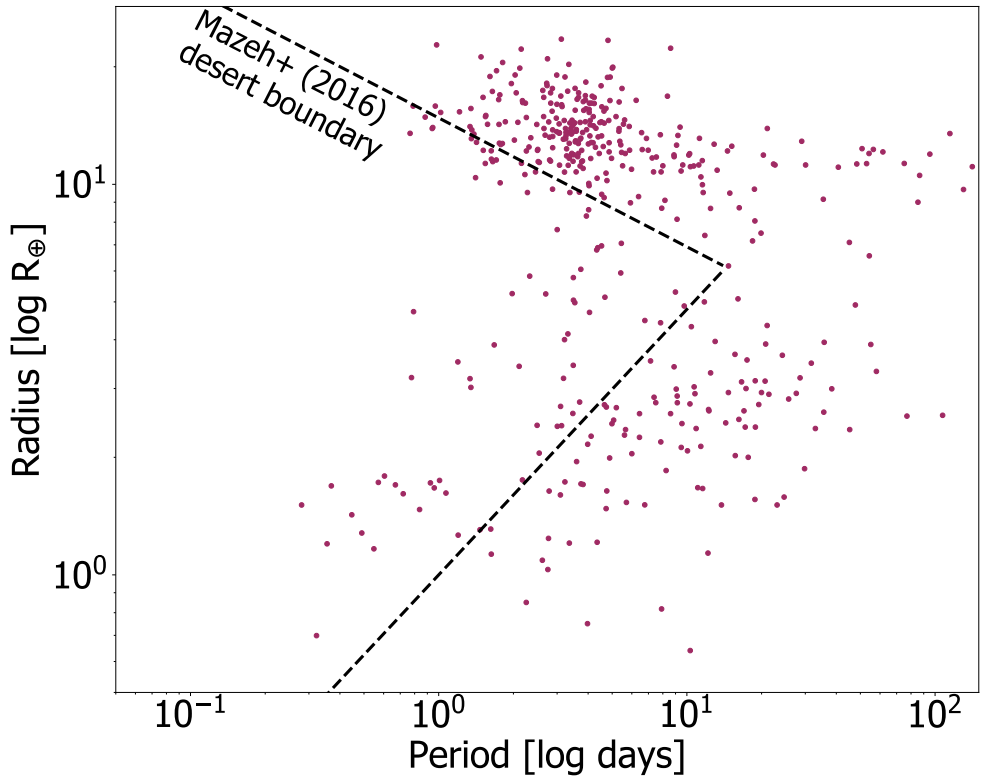

Figure 1.28: The position of the Neptune desert boundaries from Mazeh et al. [2016] in period-radius space relative to the population of discovered exoplanets as of 12 November 2023, obtained from the NASA Exoplanet Archive (Akeson et al. 2013).

1.10 Thesis outline

This thesis is comprised of work conducted to discover and characterise transiting exoplanets, primarily with TESS mission data, and aided by the observations and working groups of NGTS and multiple other photometric and spectroscopic facilities. Chapter 2 details various methods used in initial discoveries and further characterisation of exoplanets, including sources of potential false-positive signals, details of how mono- and duotransiting exoplanets are found and followed-up on, and a discussion of independent methods of validating exoplanet candidates from transit photometry alone.

Chapter 3 (Hawthorn et al. 2023a) presents the discovery of the two-planet system TOI-836, of which the inner planet is inside the radius valley parameter space. Chap-

ter 4 (Hawthorn et al. 2023b) presents the discovery of TOI-908 b, a planet in the Neptune desert parameter space, found to have originally been approximately the size of Saturn before experiencing significant photoevaporation of its atmospheric envelope. Chapter 5 (Hawthorn et al. 2024) presents the detection of 85 duotransiting exoplanet candidates in TESS data, 60 of which are previously unknown candidates. Chapter 6 presents statistical validation of seven duotransit candidates that have had their orbital periods solved with NGTS observations. Finally, chapter 7 presents the conclusions and future outlook of this research.

Chapter 2

Methodologies

"Tell me, what did you see there? / In the darkness of the past?"

'From the Dark Past', Mayhem, 1994, Ohlin/Aarseth/Stubberud/Blomberg

2.1 Planet search methods

This chapter sets out methods used in the thesis for photometric and spectroscopic detection, modelling, characterisation, manual vetting and statistical validation of transiting exoplanets. Chapters 3 and 4 use the `exoplanet` package (Foreman-Mackey et al. 2021a) in presenting the discovery and characterisation of the TOI-836 and TOI-908 systems. Chapter 5 includes the detection of 85 'duotransit' exoplanets, search and vetting methods for which are discussed in Sections 2.4 and 2.5. Section 2.2 discusses the various scenarios that can cause false-positive transit events, which were used in the manual vetting of the duotransit candidates. Chapter 6 makes use of an independent statistical vetting tool, `TRICERATOPS` (discussed in Section 2.6) in evaluating seven potential duotransiting exoplanet systems as false-positives or true transiting planets.

2.1.1 BLS and TLS

The Box-fitting Least Squared algorithm (BLS; Kovács et al. 2002) is a method commonly used to detect the transit of an exoplanet in photometric time-series data. It firstly assumes that the transits are strictly periodic in nature (period

P), and that they vary only between the out-of-transit flux and the in-transit flux, starting at the transit epoch t_0 and spending a fraction of the phase q in transit - i.e. the transit is purely box-shaped in nature. The algorithm then tests a variety of possible periods after performing a phase-fold on the data according to $\phi = (t_0 \mod P) \,/\, P$, and considers a range of bins and the maximum allowed value of q, before computing the least-squares best-fit values from which a periodogram can be created. The input data is often binned for increased computational efficiency. If a periodic signal of a transit is present in the light curve data, a peak at the corresponding value of P will be seen in the BLS periodogram, along with peaks at aliases such as $P/2$, $2 \times P$, $3 \times P$ and so forth. Figure 2.1 from Kovács et al. [2002] shows an example application of the BLS technique as used on photometric time-series data in the detection of a potential exoplanet transit in low-SNR data.

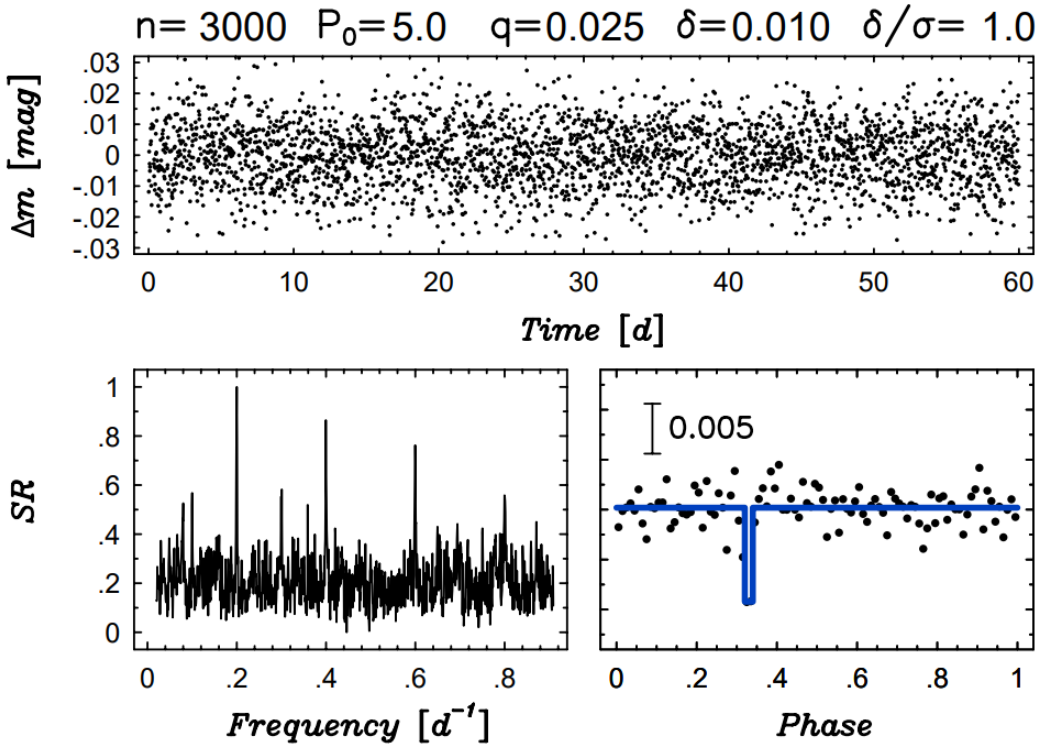

Figure 2.1: Figure from Kovács et al. [2002]. **Top panel:** The original generated time-series photometry of a test object with a low SNR. **Bottom left panel:** The normalised BLS (Kovács et al. 2002) frequency spectrum of the test object, showing the true signal and its period aliases. **Bottom right panel:** The time-series data phase-folded based on the results of the BLS analysis.

Equation 2.1[1] describes the overall calculated BLS power, equivalent to the log-likelihood of a particular transit model $\log \mathcal{L}(P, d, t_0)$ at an orbital period P, duration d, and central transit time t_0. y_{in} represents the maximum likelihood in-transit flux, y_{out} the maximum likelihood out-of-transit flux, y_n the individual flux measurements and associated uncertainties σ_n, and c a constant.

$$\log \mathcal{L}(P, d, t_0) = -\frac{1}{2} \sum_{in} \frac{(y_n - y_{in})^2}{{\sigma_n}^2} - \frac{1}{2} \sum_{out} \frac{(y_n - y_{out})^2}{{\sigma_n}^2} + c \tag{2.1}$$

An example of a BLS application to TESS photometry data for WASP-132 is presented in Figure 2.2. The photometry data is shown in Figures 1.21 and 1.22.

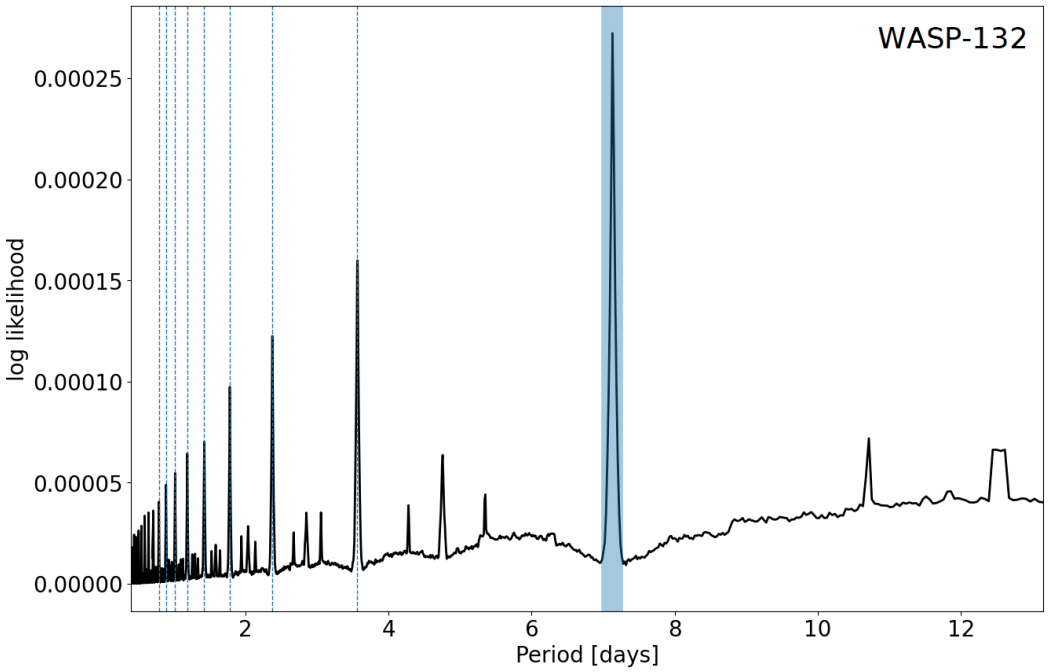

Figure 2.2: An example of the BLS periodogram method described in Kovács et al. [2002] applied to TESS photometry data from Sectors 11 and 38 for WASP-132 (see Figures 1.21 and 1.22). The corresponding peak at the orbital period of WASP-132 b of 7.133514 days (Hellier et al. 2017) is shaded blue; aliases of this period are marked with blue dashed lines. Test parameters used were a period range of 0.5–20 days, and a duration range of 0.05–0.2 days.

The box-shaped model of BLS is computationally efficient and generally appropriate for low-SNR data, however at higher SNR a more realistic model can be used that incorporates the ingress and egress of the transit and the stellar limb darkening (see

[1] `astropy` documentation, `https://docs.astropy.org/en/stable/timeseries/bls.html`, accessed 26 February 2024

Section 1.2.2 and Figure 1.4). The Transit Least Squares (TLS; Hippke & Heller 2019) algorithm is a development of BLS that incorporates the parameterisation of these effects, and has been shown to achieve increased recovery rates of transiting exoplanets of up to ∼93%, compared to that of ∼76% for BLS when tested on identical data sets (Hippke & Heller 2019).

2.1.2 Lomb-Scargle RV periodograms

Lomb-Scargle periodograms (Lomb 1976; Scargle 1982) are an efficient way of searching for periodic signals from radial velocity data, as typically a full RV data set will show signals from any planets in the system as well as the rotation period of the host star, and other periodic components of stellar activity (see Section 1.2.3). Each of these can be modelled as a sinusoidal curve, with data points typically spread unevenly in time due to observational constraints, and it will search for periodicities that induce particularly high Fourier powers. However, it will also spuriously detect periods at 'aliases' (multiples or divisions) of the true planetary period, and 'daily aliases' often around the timescale of 1 day, due to the fact observations are often taken on consecutive nights (Dawson & Fabrycky 2010). In order to evaluate the most likely true signals in the data, False Alarm Probabilities (FAPs) are calculated (e.g. Cumming 2004; Baluev 2008). Equation 2.2 is used to calculate the Lomb-Scargle power from radial velocity points, where $P(f)$ is the power at frequency f, N is the number of data points, t_i are the data timestamps, y_i are the radial velocity measurements at each timestamp, $\bar{y}$ is the mean of the radial velocity values, σ is the standard deviation of the radial velocity measurements used to normalise the dataset and τ is a time offset.

$$P(f) = \frac{1}{2\sigma^2}\left[\frac{\left[\sum_{i=1}^{N}(y_i-\bar{y})\cos(2\pi f(t_i-\tau))\right]^2}{\sum_{i=1}^{N}\cos^2(2\pi f(t_i-\tau))} + \frac{\left[\sum_{i=1}^{N}(y_i-\bar{y})\sin(2\pi f(t_i-\tau))\right]^2}{\sum_{i=1}^{N}\sin^2(2\pi f(t_i-\tau))}\right] \tag{2.2}$$

Figures 2.3 and 2.4 show data from the APF-Levy spectrograph (Vogt et al. 2014) for 51 Pegasi presented in Rosenthal et al. [2021], the discovery of which was originally published in Mayor & Queloz [1995]. The Lomb-Scargle periodogram for this data set is shown in Figure 2.4, where the highest normalised power peak corresponds to the orbital period of the planet at 4.230785 days, and lies above the FAPs at 0.1, 1 and 10%.

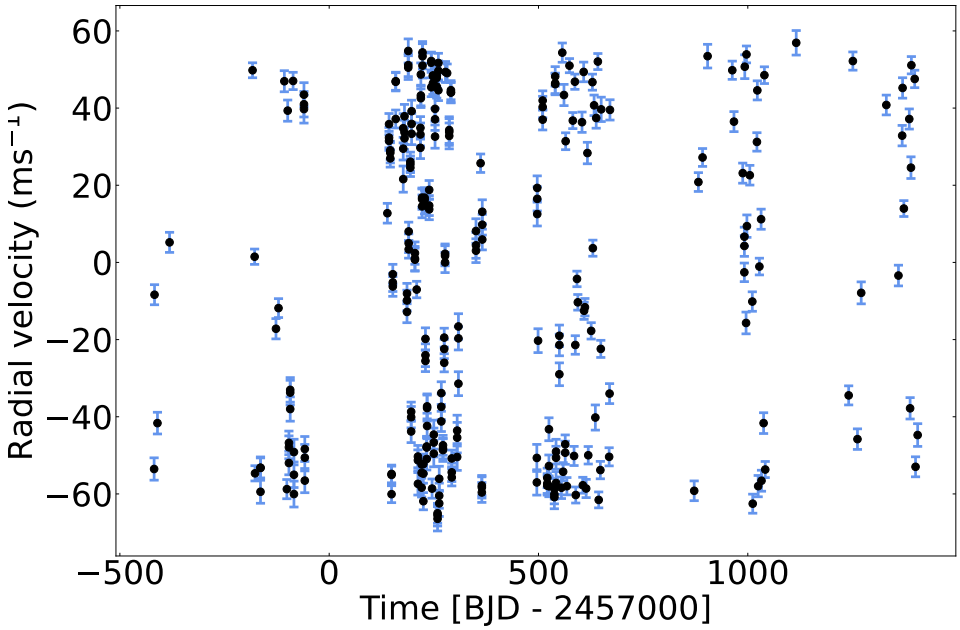

Figure 2.3: Radial velocity data from APF-Levy for 51 Pegasi, from Rosenthal et al. [2021].

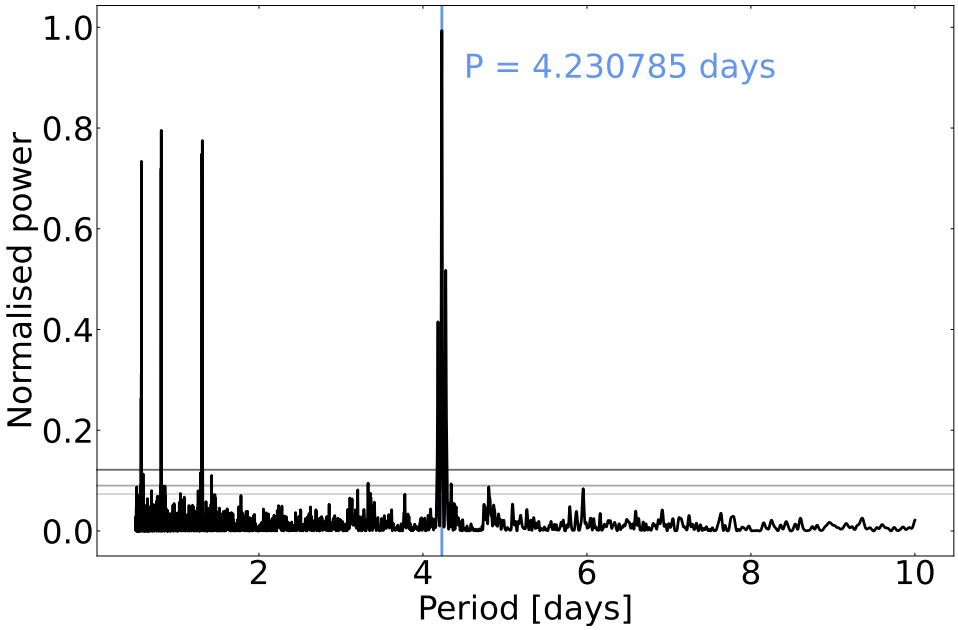

Figure 2.4: Lomb-Scargle periodogram for the APF-Levy radial velocity data shown in Figure 2.3. The highest peak corresponds to the planetary orbital period of 4.230785 days, and is marked with a blue vertical line. The FAPs are marked as the horizontal grey lines at 0.1, 1 and 10% from top to bottom. Parameters used include a period range from 0.5-10 days across 30,000 bins. The peaks at lower periods are caused by instrumental noise.

The Generalised Lomb-Scargle periodogram method (GLS, Zechmeister & Kürster 2009) is an adaptation that allows for more flexible and accurate analysis of unevenly-spaced data, where baselines may vary (by adding a floating mean rather than a fixed value) and non-sinusoidal trends due to stellar activity effects may exist. It can also detect eccentric orbits, and is generally well-suited to more complex signals.

2.2 False positive vetting

When studying transiting exoplanet candidates for the purposes of confirming a discovery, it is often necessary to consider the possibility that the transit signal is caused by a false-positive scenario. Automated detection pipelines are often affected by these signals when searching for true planetary candidates, and often individual studies will consider alternative explanations for the retrieved signal alongside their confirmation of its planetary nature. Different system architectures and spurious features in photometric data can effectively mimic a signal of a transiting planet, and below are described some possible sources of false-positive transit signal detections,

explored in the context of TESS observations and data (see Section 1.4).

2.2.1 Eclipsing binaries

Eclipsing binary systems are often similar to planetary systems in that they are comprised of two bodies orbiting a common centre of mass, and if they are sufficiently aligned along the line-of-sight relative to the observer, the passing of a companion star in front of a host (and vice-versa) can produce the same dips in brightness that a planet would cause, with some additional features (Fressin et al. 2013). A 'primary eclipse' refers to the smaller of the two objects eclipsing the primary component of the binary (typically the larger or brighter of the two), and a 'secondary eclipse' refers to the opposite case, when the primary component passes in front of the secondary - both will cause decreases in the flux of the system (Santerne et al. 2013). Primary eclipses can be relatively deep, V-shaped compared to the shallow flat-bottomed transits of a planet. However, some eclipsing binaries will display shallow, U-shaped troughs and do not display a secondary eclipse feature in the light curve (e.g. TOI-222, Lendl et al. 2020a).
An example of TESS photometric time-series data for a probable eclipsing binary system, TIC-372909068, with a visible secondary eclipse is shown in Figure 2.5.

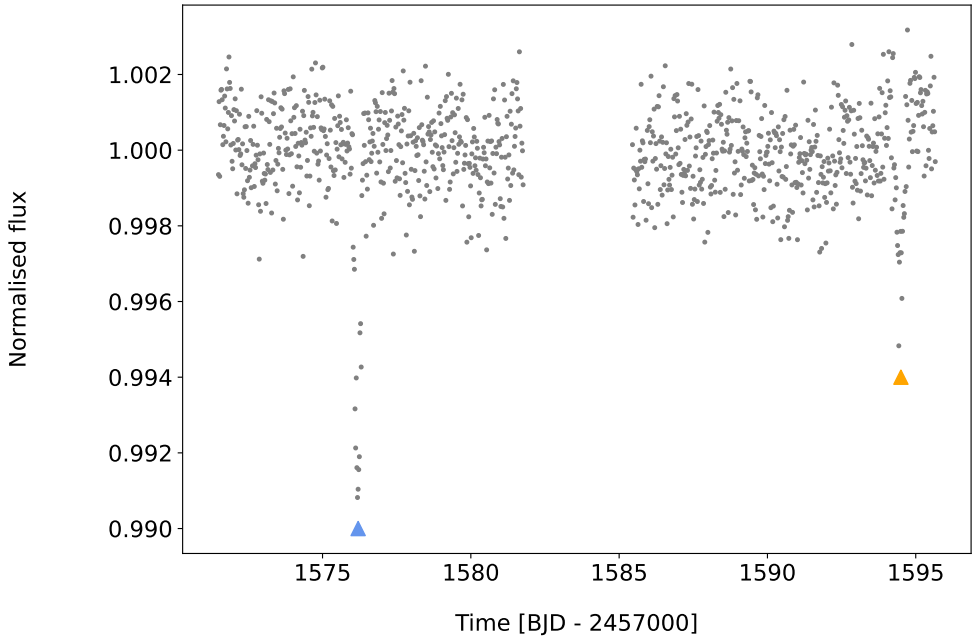

Figure 2.5: TESS photometry of TIC-372909068 from TESS Sector 10. The primary eclipse is marked with a blue triangle and the secondary eclipse with an orange triangle.

2.2.2 Solar system asteroid crossings

Occasionally, asteroids within the Solar system itself will pass near the photometric aperture used to create a stellar light curve. If the asteroid passes through the pixels used to estimate the background level for the light curve, this effect can cause a dip in the light curve, appearing much like an exoplanet transit, and so it is necessary to remove these events as potential candidates (e.g. Hawthorn et al. 2024, Chapter 5 of this work). However, asteroids are relatively easily identified in pixel data as they cause an increase in flux in the background of full-frame images at the same timestamp as the 'transit' event. Their 'transit' events can also have variations in shape, due to the speed and direction of movement across the pixels used to target background photometric levels. An example of a false-positive asteroid crossing event identified in Hawthorn et al. [2024] is shown in Figure 2.6 for TIC-32087566 from Sector 10 of TESS.

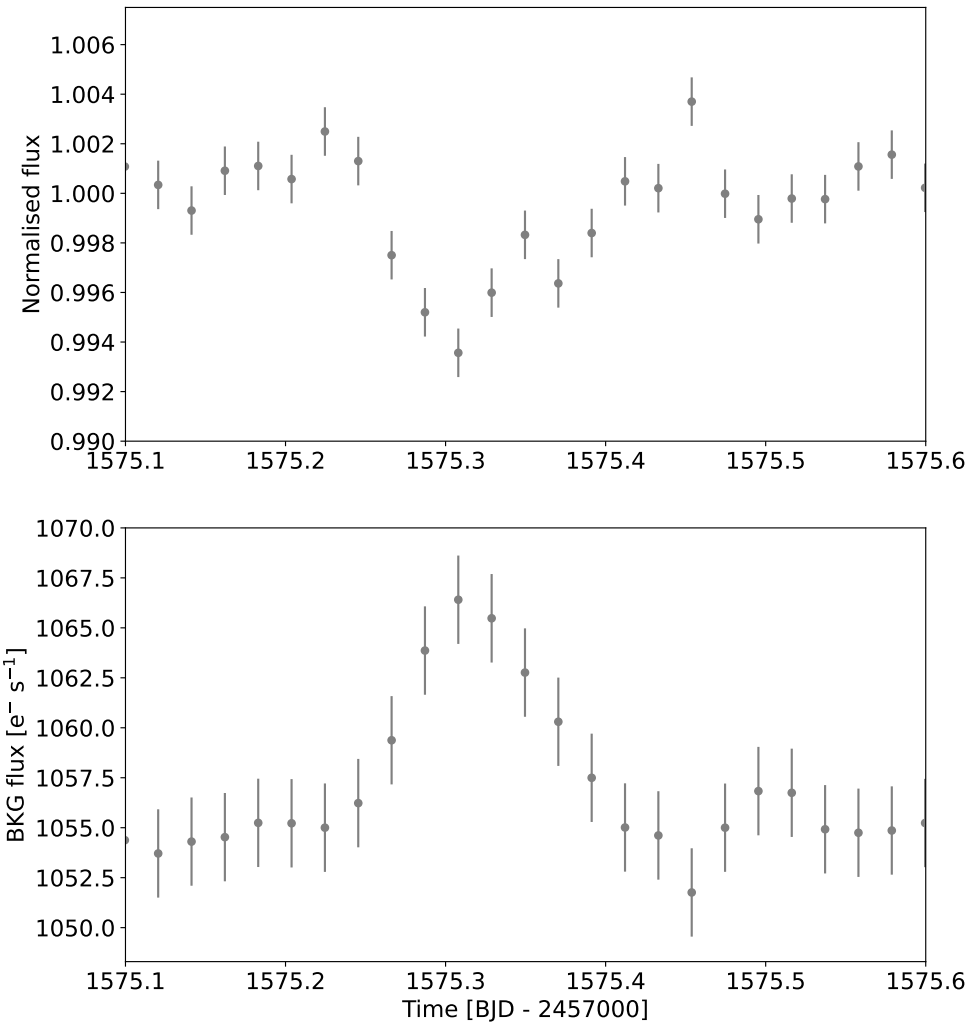

Figure 2.6: TESS photometry of TIC-32087566 from Sector 10. **Top panel:** Normalised SPOC PDCSAP flux centered around the asteroid crossing event. The uneven shape of the 'transit' is apparent. **Bottom panel:** Background flux as measured by TESS, centered around the same timestamps. The peak caused by the asteroid reflecting Solar light can be clearly seen to correlate with the false 'transit' event in the panel above.

Figure 2.7 shows the contamination of TESS Sector 35 TPF data for TIC-133027879, where an asteroid appears from the top right and moves through the image, causing a dip in the light curve of the target star and an increase in the background flux, before leaving the frame.

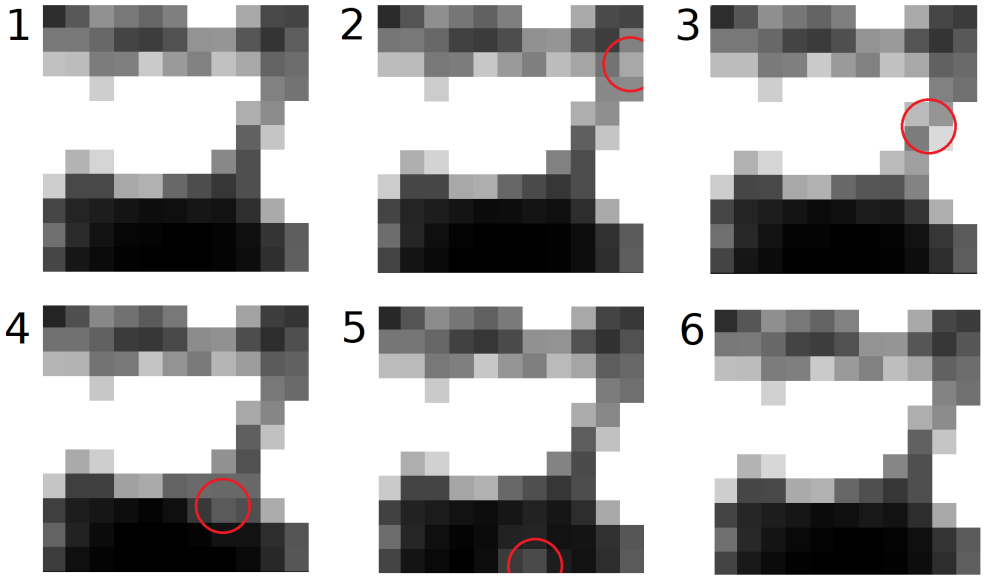

Figure 2.7: TESS Target Pixel File (TPF) of TIC-133027879 from Sector 35 through time, showing the appearance and movement of a Solar system asteroid through the image from the top right, marked with a red circle. **Panel 1:** The TPF immediately before the asteroid enters the frame. **Panels 2-5:** The movement of the asteroid from the top right to the bottom centre of the frames through time. **Panel 6**: The TPF immediately after the asteroid has left the frame.

2.2.3 Stellar variability

Stellar variability can present itself in photometric light curves as peaks and troughs of differing timescales and amplitudes of the stellar flux (e.g. Pojmanski 2002), and on occasion, a decrease in this flux causing a trough will be falsely identified by automated pipelines as an exoplanet transit event (Hawthorn et al. 2024). An example is shown in Figure 2.8 for TIC-317603510 from Sector 6 of TESS, where it can be seen in the un-corrected SPOC SAP flux that the identified 'transit' event is part of the overall stellar variability, and was not sufficiently removed by the PDC algorithm (top panel).

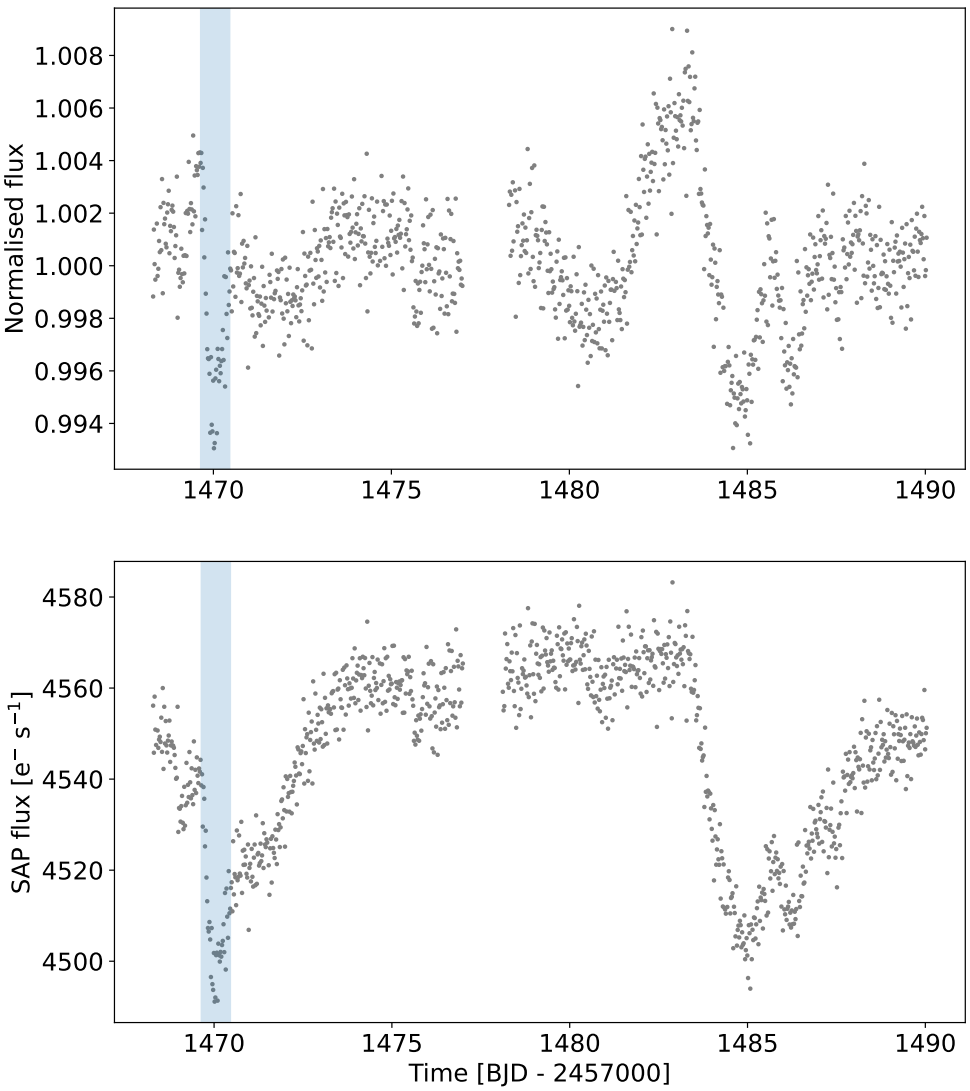

Figure 2.8: **Top panel:** Normalised SPOC PDCSAP flux from TESS photometry of TIC-317603510 from Sector 6, showing the identified trough causing a false transit detection marked with the shaded blue box. **Bottom panel:** Un-normalised and un-corrected SPOC SAP flux of the same object, showing that the false-positive 'transit' event is part of the overall stellar variability.

2.2.4 Centroid shifts

Nearby eclipsing binaries can cause brightness dips in photometric time-series data that can mimic transit signals (Hedges 2021), which is a particular issue for TESS due to its relatively large pixel scale (21"/pixel). In the TESS data, this can be detected in visible centroid shifts in pixels in the x- and y-directions, which correspond to the same timestamp as transit events. This is shown in Figure 2.9 for

TIC-111637732 from TESS sector 7, showing the false-positive 'transit' event in the SPOC PDCSAP data and the corresponding centroid shift in the y-direction in pixels at the same timestamp.

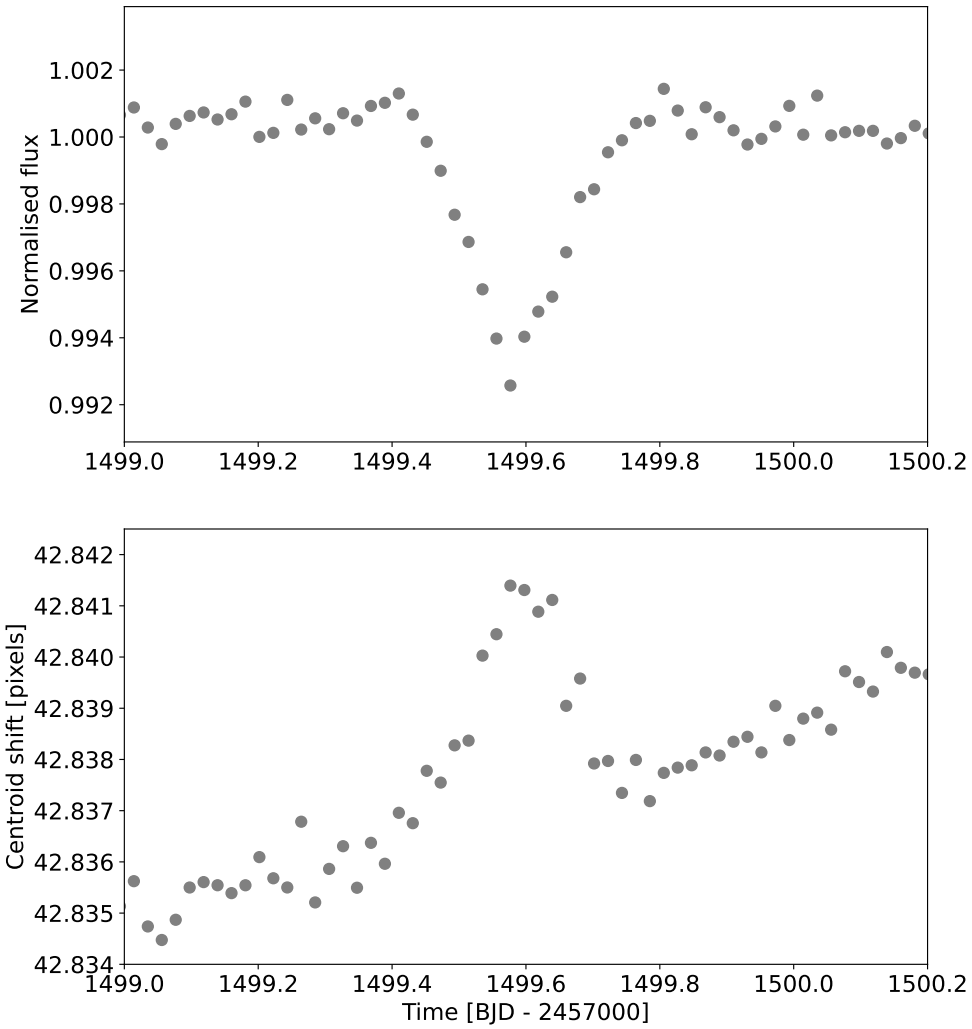

Figure 2.9: **Top panel:** Normalised SPOC PDCSAP flux from TESS photometry of TIC-111637732 from Sector 7, centered around the detected false-positive 'transit' event. **Bottom panel:** Centroid shift in the y-direction (FITS keyword MOMCENTR2 in the TESS data) of the same object, showing a peak at the same timestamp as the event.

Figure 2.10 shows the Target Pixel File (TPF) from TESS centred on TIC-111637732, with nearby sources from *Gaia* DR3 up to a magnitude difference of 4 mag. The source causing the blend and resulting centroid shift in the y-direction is TIC-1057264202.

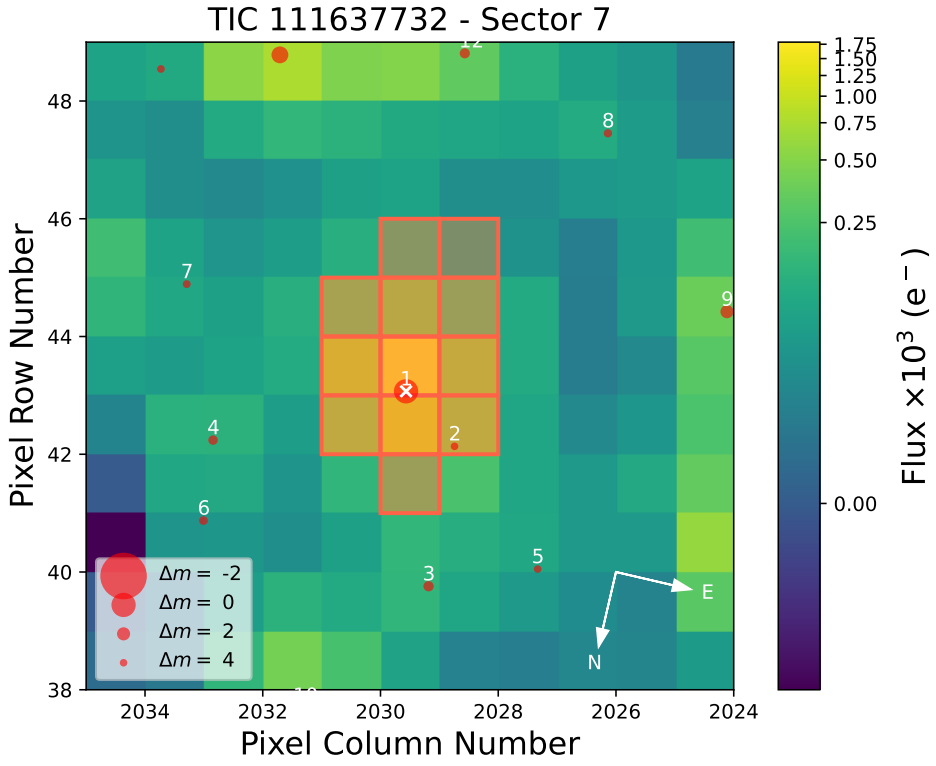

Figure 2.10: Target Pixel File (TPF) from TESS centered on TIC-111637732 from the *Gaia* catalog, with *Gaia* DR3 sources indicated by red circles with scaled magnitudes. Numbers indicate ranked distance from the target represented by a white cross. The object causing the centroid shift is TIC-1057264202, marked with a 2.

2.3 Analysis with `exoplanet`

Simultaneous fitting of both transit photometry data (see Sections 1.2.2 and 1.2.1) and radial velocity data (see Section 1.2.3) allows for the parameters of an exoplanet system to be derived. `exoplanet` (Foreman-Mackey et al. 2021a) is one of a number of available tools used for this purpose. Other popular fitting packages include `EXOFAST` (Eastman et al. [2013]), `juliet` (Espinoza et al. 2019) and `allesfitter` (Günther & Daylan 2019, 2021). These packages bring together a number of aspects of exoplanet system processes and dynamics such as the properties that can be obtained from the transit light curves and geometry (Section 1.2.2), properties from RV spectroscopy, and disentangling the effects of stellar activity (Section 1.2.3) using Gaussian process models. `exoplanet` incorporates the `PyMC3` (Salvatier et al. 2016) toolkit for the fitting of parameters using Markov Chain Monte Carlo (MCMC) methods, described here in Section 2.3.2. Joint modelling of data for the TOI-836

and TOI-908 systems was done using `exoplanet` as part of Chapters 3 and 4 of this work respectively.

2.3.1 Modelling

`exoplanet` is built on the `PyMC3` statistical Python library, which allows for flexible and scalable fitting of multiple parameters, and combines it with other custom applications specific to the modelling of exoplanet data. Each component is described below.

- `exoplanet` (Foreman-Mackey et al. 2021a) - the primary package that includes functionality for Keplerian orbit calculation, eccentricity distributions from Kipping [2013b]; Van Eylen et al. [2019], and parameterisations of limb darkening effects from Kipping [2013a].
- `celerite2` (Foreman-Mackey et al. 2017b) - package built upon the original `celerite` algorithm for fast and scalable Gaussian Process (GP) modelling, that allows for the fitting of periodic stellar activity effects when using both photometric and spectroscopic time-series data.
- `starry` (Luger et al. 2019) - incorporation of limb-darkened light curves using surface brightness distributions of exoplanet host stars.
- `PyMC3` (Salvatier et al. 2016) - a probabilistic programming library that allows the user to perform Bayesian inference on statistical models using sampling methods such as MCMC (Section 2.3.2).

2.3.2 Markov chain Monte Carlo

Monte Carlo (MC) is a class of methods that uses repeated random sampling of a variable to obtain numerical results, where direct calculation may be difficult. It is often used in optimisation, numerical integration or generating draws from probability distributions, and is particularly useful for the simulation of systems with many sources of uncertainty.
Markov chain Monte Carlo (MCMC) is a subset of these methods that employs Bayesian statistics to approximate the posterior distributions of parameters by random sampling in a probabilistic space until a stationary distribution is reached, using a set of 'walkers' that explore the parameter space. The Metropolis-Hastings algorithm (Metropolis et al. 1953; Hastings 1970; Mackay 2003) is a commonly used method that involves starting at a set of model parameter values, generating the

next set, computing the acceptance ratio R of the posteriors of both and deciding to accept or reject the new set of values based on the value of R. If R is ≥ 1, i.e. the new set of values is more likely than the previous, it is accepted and becomes the new starting point in the chain. If R is < 1, i.e. the new set of values is less likely than the previous, it is not accepted and a new set is generated until it is accepted and the chain continues. The new parameter values are often bounded by a step parameter that prevents the chain from exploring extremely small or extremely wide parameter spaces. Additionally, a number of samples are discarded at the beginning of the chain ('burn-in') to allow the walkers to explore the most optimal regions of the parameter spaces, especially if they started in a low-probability region, and converge on a solution. The solution for each parameter is output as a posterior distribution function with a median value, and the 1-σ uncertainties either side are the 16th and 84th percentiles.

The Hamiltonian Monte Carlo (HMC) (Neal 2011) is a variation of MCMC used in the analysis presented in Chapters 3 and 4 of this work, implemented in the `PyMC3` package as part of the modelling of exoplanet systems using the `exoplanet` package framework. HMC incorporates gradient-based sampling (the slope of the probability distribution) and Hamiltonian dynamics to guide the sampling process and add more informed steps to the MCMC chains. It generally converges faster than the standard Metropolis-Hastings algorithm and gives a greater effective sample size, as it leads to more samples that are likely to be accepted as the next step in the chain and explores the parameter space more efficiently.

2.4 Detecting single-transit events

In an ideal scenario, multiple individual transits of an exoplanet across the stellar disk will be seen within a single TESS sector, allowing for detection via BLS (see Section 2.1.1), and the determination of the planet's orbital period. However, for planets on longer periods, many will only exhibit a single transit within a given observation time (often depending on the number of TESS sectors it is observed in). We henceforth refer to this phenomenon as a 'monotransit'. Determination of the planetary orbital period with only a single TESS transit is considerably more difficult, but some inferences can be drawn with knowledge of the host star (eg. Osborn et al. 2016). Independent search methods have uncovered numerous planet candidates displaying these monotransit events in the TESS data set. One such example is `monofind` (also described in chapter 5). `monofind` reads in and normalises the TESS-SPOC light curve data for a selected target, and smoothes it using an

iterative Savitzky-Golay (SG) filter (Savitzky & Golay [1964]) to remove effects of stellar activity but maintain the presence of any possible transit signals. This corrected light curve is then passed to the monotransit search algorithm, which searches for single events in the light curve that show three or more consecutive points that fall at least 3 median absolute deviations below the normalised light curve, and flags it as a potential transit event (Hawthorn et al. 2024). Manual vetting of the event is then done on the target according to the processes described in section 2.2.

TIC-257527578/TOI-5152 from Ulmer-Moll et al. [2022] is shown in Figure 2.11. The individual transit is shown in Figure 2.12.

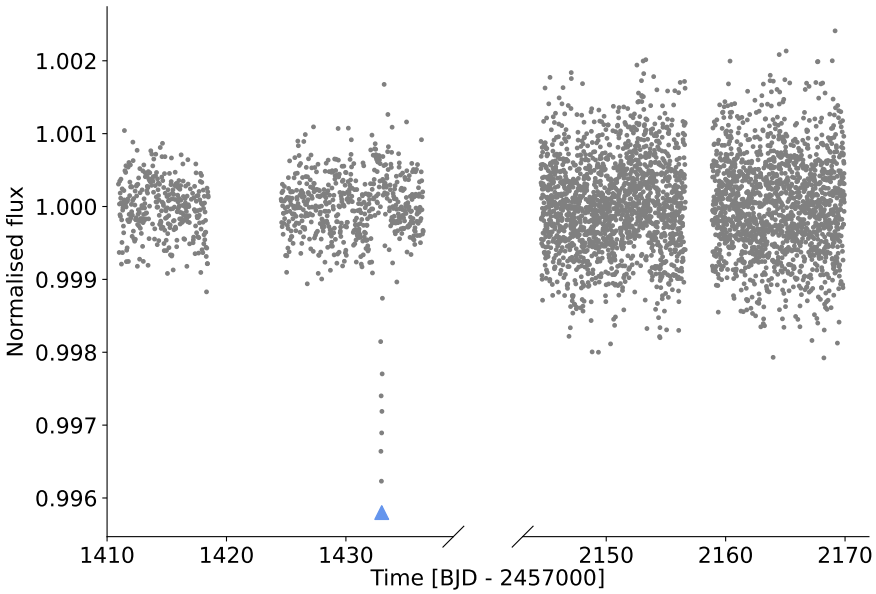

Figure 2.11: TESS light curve of TIC-257527578/TOI-5152 from Ulmer-Moll et al. [2022], observed in Sectors 4 and 31. The monotransit of TOI-5152 b is marked with a blue triangle.

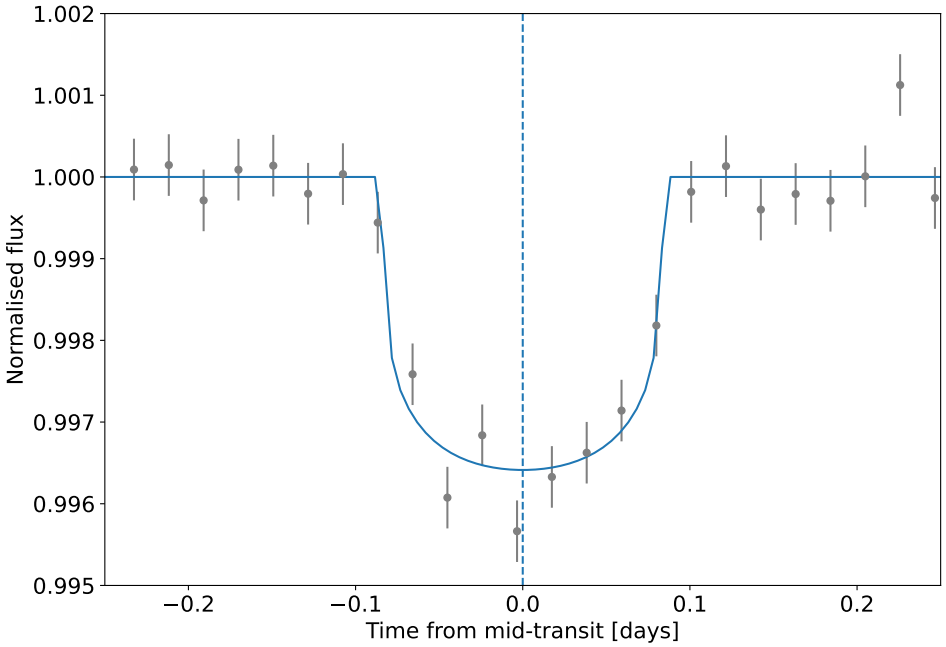

Figure 2.12: TESS light curve of TIC-257527578/TOI-5152, phase-folded on the orbital period and transit epoch of TOI-5152 b and overplotted with an approximate transit model (blue) using parameters from Ulmer-Moll et al. [2022]. The blue dotted line marks the centre of the transit event.

2.5 Duotransit events

Similarly to monotransits, sometimes a system will display two transit events instead of one throughout TESS observations - we refer to this phenomenon as 'duotransits'. If the planet transits once in Cycle 1 and Cycle 3, these are 'biennial' duotransits (see Chapter 5, Hawthorn et al. 2024 and Rodel et al. 2024). The presence of two transits means that we are able to find a set of possible periods ('aliases'), given by integer divisions of the separation between the two transit events. This is shown in Equation 2.3, where P_n denotes the possible set of period aliases, ΔT is the separation between the two events, and n is an integer from $n = 1$ at the longest period to n_{max} at the shortest possible period, often bounded by the duration of a single TESS Sector (20–27 days).

$$P_n \in \left(\frac{\Delta T}{n} \right), n = 1, ..., n_{max} \tag{2.3}$$

A discussion of duotransits is also presented in Chapter 5 of this work. The `monofind` algorithm (section 2.4) was adapted to find two transits occurring in the data, by

cross-matching between events in Cycle 1 and Cycle 3. Figure 2.13 shows an example duotransiting exoplanet candidate from TESS, TIC-70561926. In Figure 2.14 these observations are phase-folded onto the most probable orbital period calculated using the `MonoTools` package (Osborn [2022]).

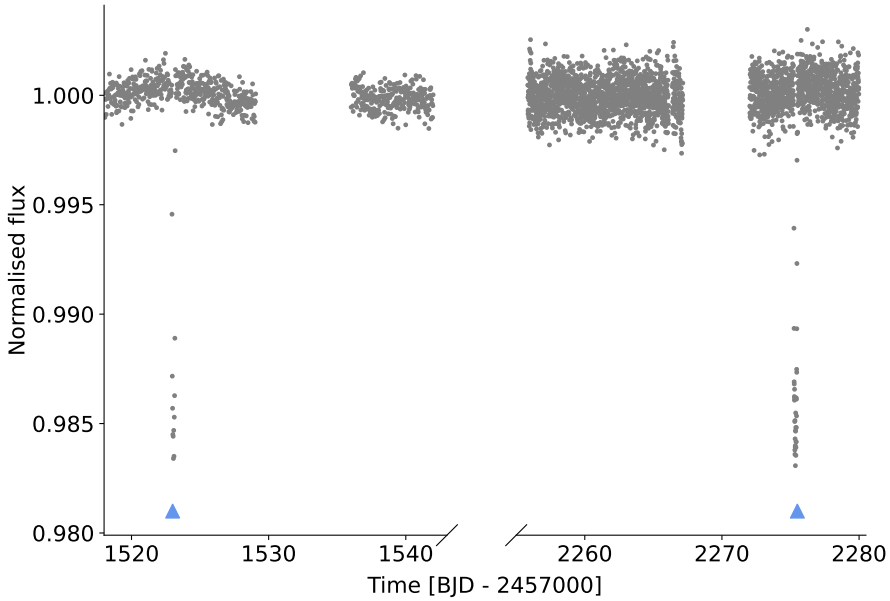

Figure 2.13: TESS light curve of TIC-70561926 from Hawthorn et al. [2024], observed in Sectors 8 and 35. The transits of the planetary candidate TIC-70561926 b are marked with blue triangles. The approximate separation of the two events is ~ 752.296 days.

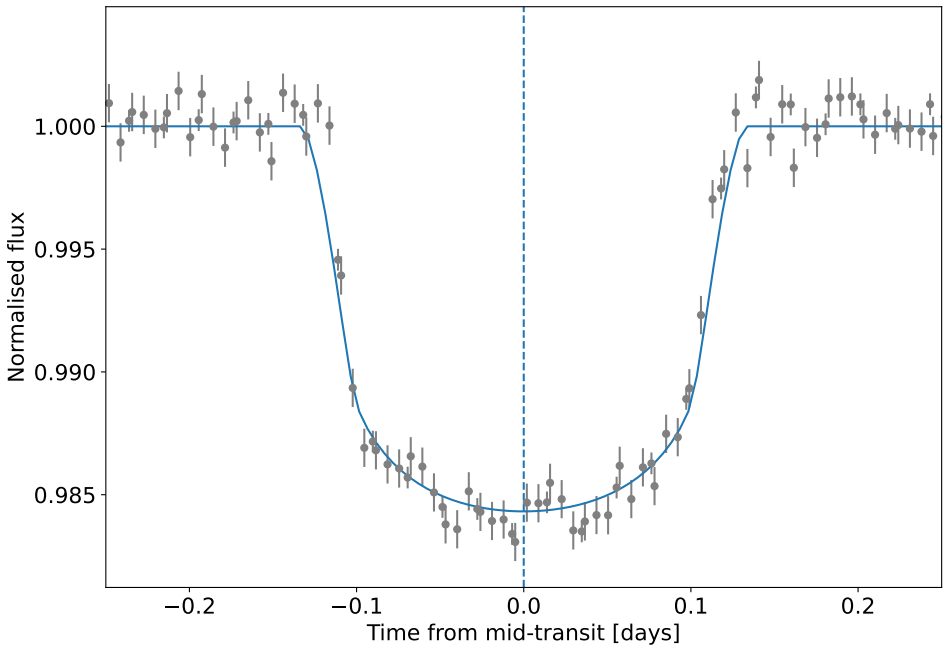

Figure 2.14: TESS light curve of TIC-70561926, phase-folded on the most probable orbital period and transit epoch of TIC-70561926 b and overplotted with an approximate transit model (blue) using parameters from Hawthorn et al. [2024]. The blue dotted line marks the centre of the transit events.

`MonoTools`[2] (Osborn 2022) is a Python package designed to model and analyse transit light curves and radial velocity data sets, particularly for mono- and duotransiting systems as it is agnostic of the true orbital period, and calculate marginalised probabilities for sets of possible period aliases of a duotransiting system (see section 5.3.3). It uses the transit parameters of impact parameter, R_p/R_* and duration to calculate the orbital velocity of the system. `MonoTools` was used successfully in predicting the potential transit times of both TOI-2076 c and d (Osborn et al. 2022) to allow for follow-up with *CHEOPS*, observations from which found the true orbital periods of both planets. Figure 2.15 from Osborn et al. [2022] shows the marginalised probabilities of each period alias from `MonoTools` for TOI-2076 c and d.

[2] `https://github.com/hposborn/MonoTools`

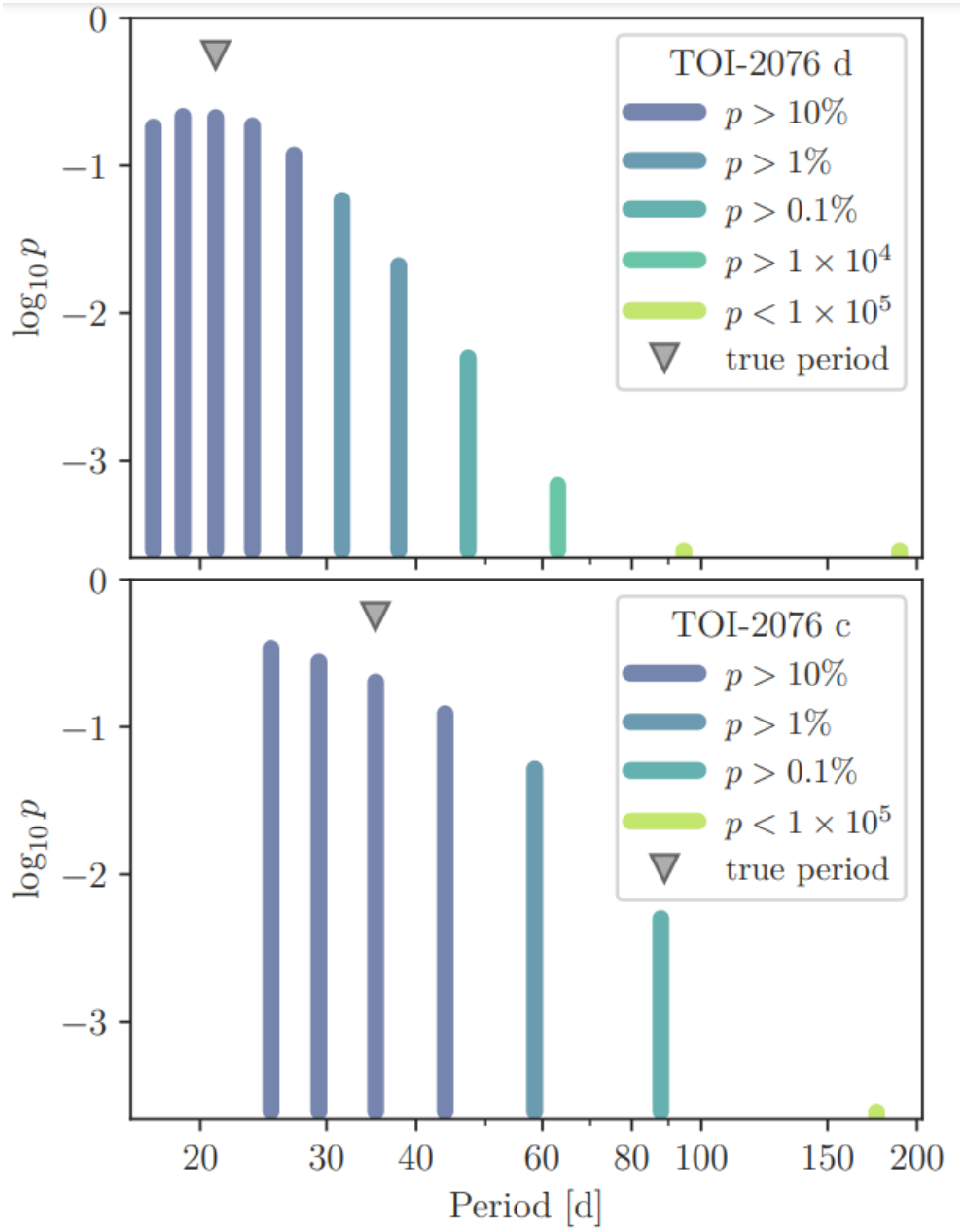

Figure 2.15: Marginalised $\log_{10}$ probabilities for TOI-2076 d (top panel) and c (bottom panel) as computed by the `MonoTools` package. Figure from Osborn et al. [2022].

2.6 Independent planet validation methods

In order for a discovery of an exoplanet to be 'confirmed', a determination of the planetary mass (or an upper mass limit) is typically required, which can be ob-

tained from spectroscopic radial velocity observations of individual targets (see Section 1.2.3). However, as missions such as *Kepler* and TESS are able to observe thousands of stars simultaneously, there are currently many hundreds of transiting exoplanet candidates that have yet to be observed and have their masses measured with ground-based spectrographs, which can only observe one object at a time. In the wake of the vast amount of data generated by the *Kepler* and K2 missions, and as many target stars are often too faint for RV observations from the ground, statistical validation tools such as `BLENDER` (Torres et al. 2011), `VESPA` (Morton 2012; Morton et al. 2016) and `PASTIS` (Díaz et al. 2014) were developed in order to provide probabilities that a transit signal was caused by a real exoplanet, and not some false-positive scenario mimicking the light curve's behaviour (see Section 2.2).
One recent validation tool that has been developed as part of analysis of TESS candidate planets is `TRICERATOPS` (Tool for Rating Interesting Candidate Exoplanets and Reliability Analysis of Transits Originating from Proximate Stars). The steps in the full `TRICERATOPS` vetting procedure are listed below, adapted from Giacalone et al. [2022]).

1. The TIC is queried for all stars within 10" of the target star, and stores their stellar properties.

2. The user selects the pixel aperture used in the extraction of the TESS data from the images for each Sector of observation.

3. The contribution of flux to the target aperture from the surrounding stars is calculated, and `TRICERATOPS` identifies any targets that would be bright enough to produce a transit signal.

4. The user provides the phase-folded or individual transit of the target, and the orbital period of the transiting object. Any available contrast curves from imaging data can be included.

5. The marginal likelihoods and prior probabilities of each scenario (see Table 2.1, adapted from Giacalone et al. 2021) are calculated over $\sim 10^6$ planetary systems to provide the overall probability of each scenario, including the False Positive Probability (FPP) and NFPP (Nearby False Positive Probability).

6. The values of FPP and NFPP are used to evaluate the transiting object as either a validated planet (FPP < 0.015, NFPP $< 10^{-3}$), likely planet (FPP < 0.5, NFPP $< 10^{-3}$), or a likely nearby false positive (NFPP $< 10^{-1}$).

Table 2.1: Descriptions of the configurations of each of the scenarios tested by `TRICERATOPS` from Giacalone et al. [2021]. NTP, NEB and NEB × 2P are only tested if the transit depth value t_{depth} is > 0 for any nearby star except for the target.

Scenario	**Description**
TP	No unresolved companion; transiting planet with P_{orb} around target star.
EB	No unresolved companion; eclipsing binary with P_{orb} around target star.
EB × 2P	No unresolved companion; eclipsing binary with $2 \times P_{orb}$ around target star.
PTP	Unresolved bound companion; transiting planet with P_{orb} around primary star.
PEB	Unresolved bound companion; eclipsing binary with P_{orb} around primary star.
PEB × 2P	Unresolved bound companion; eclipsing binary with $2 \times P_{orb}$ around primary star.
STP	Unresolved bound companion; transiting planet with P_{orb} around secondary star.
SEB	Unresolved bound companion; eclipsing binary with P_{orb} around secondary star.
SEB × 2P	Unresolved bound companion; eclipsing binary with $2 \times P_{orb}$ around secondary star.
DTP	Unresolved background star; transiting planet with P_{orb} around target star.
DEB	Unresolved background star; eclipsing binary with P_{orb} around target star.
DEB × 2P	Unresolved background star; eclipsing binary with $2 \times P_{orb}$ around target star.
BTP	Unresolved background star; transiting planet with P_{orb} around background star.
BEB	Unresolved background star; eclipsing binary with P_{orb} around background star.
BEB × 2P	Unresolved background star; eclipsing binary with $2 \times P_{orb}$ around background star.
NTP	No unresolved companion; transiting planet with P_{orb} around nearby star.
NEB	No unresolved companion; eclipsing binary with P_{orb} around nearby star.
NEB × 2P	No unresolved companion; eclipsing binary with $2 \times P_{orb}$ around nearby star.

Figure 2.16 shows the application of `TRICERATOPS` to the TESS phase-folded light curve of TIC-70561926 from Sectors 8 and 35, where the overplotted models are the fit results for each of the scenarios tested by `TRICERATOPS`. Table 2.2 shows the data output from `TRICERATOPS` for each scenario, including the stellar parameters for the target, the fitted parameters for the orbiting object, whether a transiting planet or eclipsing binary; and the probability of each scenario used in calculating the values of FPP (0.2867 ± 0.2429) and NFPP (0.0 ± 0.0).

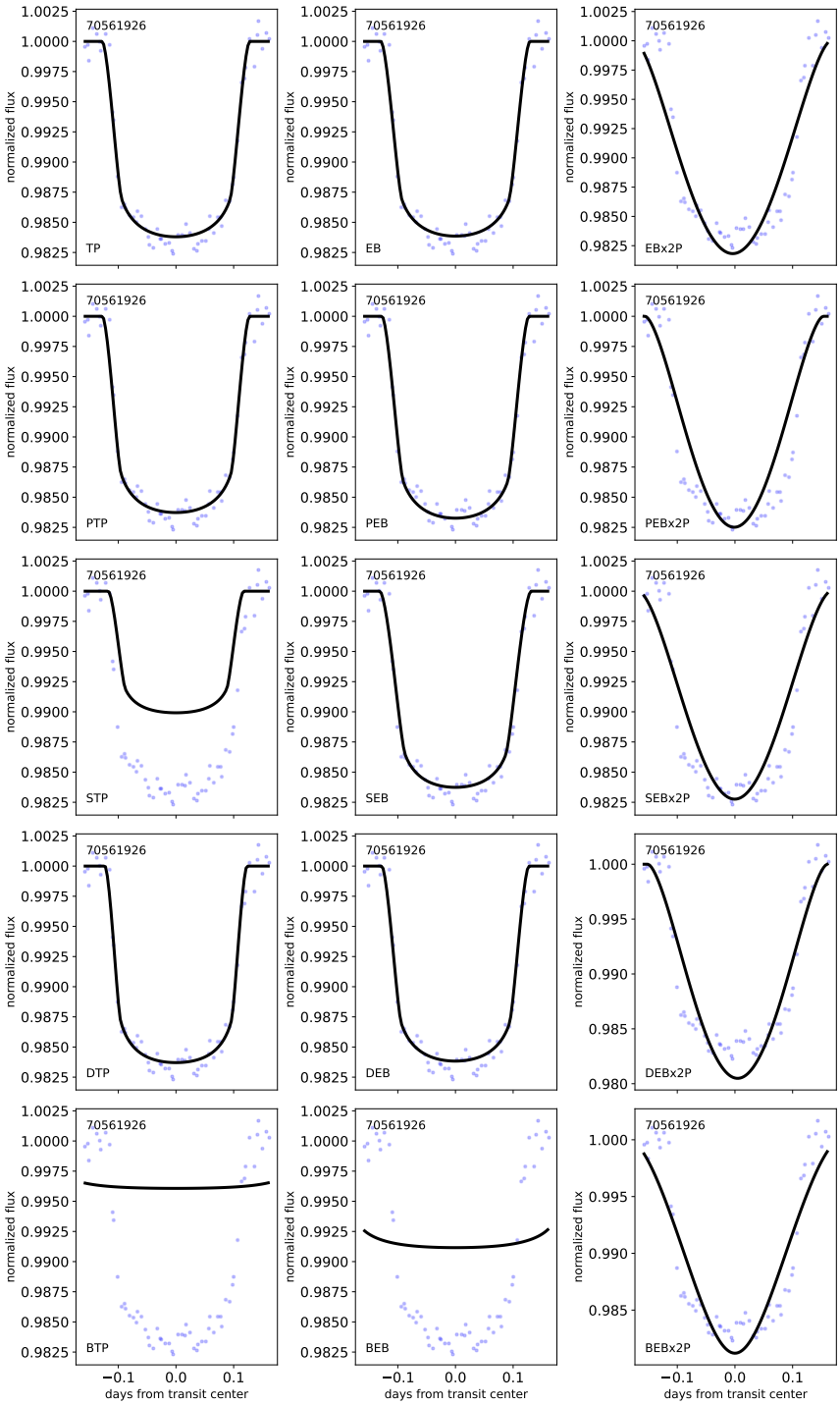

Figure 2.16: An example of output model results from evaluation of TIC-70561926 using `TRICERATOPS`. The phase-folded TESS data from Sectors 8 and 35 are shown as blue circles (also presented in Figure 2.14), with the resulting fitted models for each tested scenario overplotted in black and labelled on each subplot (Giacalone et al. 2022).

Table 2.2: An example of output results for the planetary parameters and scenario probabilities from evaluation of TIC-70561926 using `TRICERATOPS` (Giacalone et al. 2022).

ID	**scenario**	M_s	R_s	P_{orb}	**inc**	**b**	**ecc**	**w**	R_p	M_{EB}	R_{EB}	**prob**
70561926	TP	1.27700	1.35467	21.49419	88.99486	0.42128	0.09764	49.78697	17.82338	0.00000	0.00000	0.13628
70561926	EB	1.27700	1.35467	21.49419	88.96406	0.47917	0.01681	107.28680	0.00000	0.13410	0.16396	0.00175
70561926	EBx2P	1.27700	1.35467	42.98837	88.44966	0.87543	0.46272	145.73362	0.00000	1.24631	1.35467	0.00000
70561926	PTP	1.27700	1.35467	21.49419	89.11364	0.37620	0.10633	33.86277	17.81869	0.00000	0.00000	0.02923
70561926	PEB	1.27700	1.35467	21.49419	88.94760	0.49723	0.01295	339.75534	0.00000	0.13714	0.16745	0.00365
70561926	PEBx2P	1.27700	1.35467	42.98837	88.41265	1.19735	0.27503	155.76591	0.00000	1.26697	1.35467	0.00000
70561926	STP	1.26989	1.35467	21.49419	89.50223	0.24229	0.25413	329.82159	19.81809	0.00000	0.00000	0.00000
70561926	SEB	1.19034	1.33060	21.49419	89.48681	0.23380	0.11214	19.35733	0.00000	0.21993	0.24802	0.00000
70561926	SEBx2P	0.94619	1.00093	42.98837	88.88460	1.06754	0.24021	158.59967	0.00000	0.90053	0.93804	0.00000
70561926	DTP	1.27700	1.35467	21.49419	89.99332	0.00341	0.22746	316.75611	17.65654	0.00000	0.00000	0.81055
70561926	DEB	1.27700	1.35467	21.49419	89.03763	0.36194	0.20024	85.97329	0.00000	0.13370	0.16350	0.01854
70561926	DEBx2P	1.27700	1.35467	42.98837	88.27586	1.85348	0.46938	227.26388	0.00000	1.22767	1.35467	0.00000
70561926	BTP	1.62400	1.83581	21.49419	89.36908	0.24595	0.28843	210.18058	18.52445	0.00000	0.00000	0.00000
70561926	BEB	1.54600	2.05655	21.49419	89.62226	0.17298	0.42972	250.08677	0.00000	0.23602	0.26235	0.00000
70561926	BEBx2P	0.97900	0.91606	42.98837	89.44243	0.68040	0.00659	58.97505	0.00000	0.96162	0.91606	0.00000

TRICERATOPS has been used successfully to statistically analyse transit photometry data for a selection of TOIs, including the sub-Saturn exoplanet TOI-181 b (Mistry et al. 2023c), eleven TESS planets orbiting K-dwarfs (Mistry et al. 2023b), and eight super-Earths from TESS (Mistry et al. 2023a) as part of the VaTEST publication series; the sub-Neptune TOI-1221 b (Mann et al. 2023); and an interior companion to WASP-132 b (Hord et al. 2022).
TRICERATOPS is used in Chapter 6 in order to statistically examine a set of selected duotransit candidates that have had their orbital periods solved with follow-up photometric observations from NGTS.

Chapter 3

TOI-836: A super-Earth and mini-Neptune transiting a nearby K-dwarf

"Planets meeting face to face / One to the other cry, 'how sweet!' / If endlessly we might embrace / A perfect union deep in space."

'Echoes (Live at Crystal Palace)', Pink Floyd, 1971, Gilmour/Waters/Wright/Mason

Note

This chapter is a reproduction of the publication 'TOI-836: A super-Earth and mini-Neptune transiting a nearby K-dwarf' (Hawthorn et al. 2023a), originally published in Monthly Notices of the Royal Astronomical Society (MNRAS) in April 2023 with very minor edits. The majority of the writing and analysis of the paper was performed by the author, with contributions to observational data and sections of analysis made by external collaborators.

Abstract

We present the discovery of two exoplanets transiting TOI-836 (TIC 440887364) using data from TESS Sector 11 and Sector 38. TOI-836 is a bright (T = 8.5 mag),

high proper motion ($\sim 200\,\mathrm{mas\,yr^{-1}}$), low metallicity ([Fe/H]≈ -0.28) K-dwarf with a mass of $0.68 \pm 0.05\,\mathrm{M_\odot}$ and a radius of $0.67 \pm 0.01\,\mathrm{R_\odot}$. We obtain photometric follow-up observations with a variety of facilities, and we use these data-sets to determine that the inner planet, TOI-836 b, is a $1.70 \pm 0.07\,\mathrm{R_\oplus}$ super-Earth in a 3.82 day orbit, placing it directly within the so-called 'radius valley'. The outer planet, TOI-836 c, is a $2.59 \pm 0.09\,\mathrm{R_\oplus}$ mini-Neptune in an 8.60 day orbit. Radial velocity measurements reveal that TOI-836 b has a mass of $4.5 \pm 0.9\,\mathrm{M_\oplus}$, while TOI-836 c has a mass of $9.6 \pm 2.6\,\mathrm{M_\oplus}$. Photometric observations show Transit Timing Variations (TTVs) on the order of 20 minutes for TOI-836 c, although there are no detectable TTVs for TOI-836 b. The TTVs of planet TOI-836 c may be caused by an undetected exterior planet.

3.1 Introduction

Since the groundbreaking discovery of 51 Pegasi b [Mayor & Queloz, 1995], the field of exoplanet research has grown to now include an impressive 4935 [1] discoveries using a variety of detection methods. Transit photometry and radial velocity spectroscopy continue to be the most fruitful methods of exoplanet discovery, and combined they also allow us to determine the fundamental properties of exoplanets, including their mass, radius, bulk density, and possible composition. Ground-based transit photometry surveys such as HATNet [Bakos et al., 2004], WASP [Pollacco et al., 2006], KELT [Pepper et al., 2007], HAT-South [Bakos et al., 2013], and NGTS [Wheatley et al., 2018] among others have greatly added to the population of known transiting exoplanets.

The advent of space-based transit surveys such as CoRoT [Auvergne et al., 2009], *Kepler* [Borucki et al., 2010], *K2* [Howell et al., 2014], and TESS [Ricker et al., 2015] has allowed us to extend the range of detectable exoplanets down to the regimes of Neptune and super-Earth radii. In this paper we present the discovery of two such exoplanets found from TESS photometry to be transiting the bright star TOI-836. This system was included in the Magellan PFS survey paper Teske et al. [2021].

The general conclusion from a number of studies is that Kepler compact planetary systems are flat, with the inclination dispersion on the order of a few degrees [Lissauer et al., 2011; Tremaine & Dong, 2012; Figueira et al., 2012; Johansen et al., 2012; Fang & Margot, 2012; Fabrycky et al., 2014]. The discovery of such multi-planet systems [eg; Wilson et al., 2022] confers significant advantages over those stars where only a single exoplanet is detected. Firstly, the statistical likelihood that the

[1] `https://exoplanetarchive.ipac.caltech.edu` as of 2022 February 22, [Akeson et al., 2013]

transits are astrophysical false positives is greatly reduced [Lissauer et al., 2012]. Secondly, the dynamical interactions between the planets can result in observable transit timing variations (TTVs), which in some cases may reveal the presence of non-transiting planets [eg; Nesvorný et al., 2014]. Thirdly, the comparative properties of the planets can reveal possible formation and migration pathways.

One particularly interesting aspect of small-radius multi-planet systems is looking at how they might allow us to study the origin and characteristics of the radius valley seen at around $R_p \approx 2.0\,R_\oplus$ in the exoplanet population [Fulton et al., 2017; Owen & Wu, 2013]. In the case of the TOI-836 system, we find that TOI-836 b lies within the radius valley itself, and TOI-836 c lies close to the peak on the right hand side. The radius valley is valid for all systems, however multi-planet systems such as this may give us significant insights into formation mechanisms through comparative planetology.

This paper is structured as follows: we present our transit photometry, radial velocity and imaging observations of the TOI-836 system in Section 3.2, our global modelling methods, associated computational implementations and results in Section 3.3. Finally we present our discussion and conclusion of these results in Sections 3.4 and 3.5 respectively.

3.2 Observations

3.2.1 TESS discovery photometry

The transit signatures of TOI-836 b and TOI-836 c were originally identified by the TESS Science Processing Operations Center [Jenkins et al., 2016] using an adaptive matched filter [Jenkins, 2002; Jenkins et al., 2010, 2020] to search the Sector 11 light curve on 2019 June 5. The transit signatures were fitted with an initial limb-darkened transit model [Li et al., 2019], and passed all the diagnostic tests performed and reported in the Data Validation reports [Twicken et al., 2018]. The TESS Science Office reviewed the Data Validation reports and issued an alert for TOI-836 on 2019 June 17. Subsequent searches of the combined light curves from sectors 11 and 38 located the source of the transit events to within 3.73 ± 2.5" and 0.98 ± 1.5" of the host star for TOI-836 b and TOI-836 c, respectively. Note that the difference image centroiding results complement the high resolution imaging results presented in Section 3.2.5.

TOI-836 was first identified as a TESS Object of Interest [TOI; Guerrero et al., 2021] in TESS Sector 11, Camera 1, CCD 3 from 2019 April 22 to 2019 May 21. Stellar

Table 3.1: Catalog stellar parameters of TOI-836.

Property	**Value**	**Source**
Identifiers		
TIC ID	TIC 440887364	TICv8
HIP ID	HIP 73427	
2MASS ID	J15001942-2427147	2MASS
Gaia ID	6230733559097425152	*Gaia* EDR3
Astrometric properties		
R.A. (J2015.5)	$15^{\mathrm{h}}00^{\mathrm{m}}19.16^{\mathrm{s}}$	*Gaia* EDR3
Dec (J2015.5)	$-24^\circ\ 27'15.14''$	*Gaia* EDR3
Parallax (mas)	36.353 ± 0.016	*Gaia* EDR3
Distance (pc)	27.504 ± 0.029	
$\mu_{\mathrm{R.A.}}$ (mas yr^{-1})	-199.48 ± 0.018	*Gaia* EDR3
μ_{Dec} (mas yr^{-1})	-27.997 ± 0.017	*Gaia* EDR3
μ_{Total} (mas yr^{-1})	201.438 ± 0.025	*Gaia* EDR3
$\mathrm{RV_{sys}}$ (km s^{-1})	-26.603 ± 0.922	*Gaia* DR2
Photometric properties		
TESS (mag)	8.649 ± 0.006	TICv8
B (mag)	11.138 ± 0.028	APASS
V (mag)	9.920 ± 0.030	APASS
G (mag)	9.407 ± 0.0003	*Gaia* EDR3
J (mag)	7.580 ± 0.023	2MASS
H (mag)	6.983 ± 0.040	2MASS
K (mag)	6.804 ± 0.018	2MASS
Gaia BP (mag)	10.126 ± 0.003	*Gaia* EDR3
Gaia RP (mag)	8.587 ± 0.004	*Gaia* EDR3

Sources: TICv8 [Stassun et al., 2019], 2MASS [Skrutskie et al., 2006], *Gaia* Early Data Release 3 [Gaia Collaboration et al., 2021], APASS [Henden et al., 2016]

identifiers, astrometric properties and photometric properties for TOI-836 are listed in Table 3.1. Figure 3.1 shows the Target Pixel File (TPF) from TESS created in `tpfplotter`[2] [Aller et al., 2020], centred on TOI-836 (indicated by a white cross), with the *Gaia* DR2 catalog data for sources overplotted in red along with scaled magnitudes and the aperture mask for photometry extraction.

TOI-836 showed transit events from two exoplanet candidates, designated TOI-836.01 (TOI-836 c; SNR = 21) and TOI-836.02 (TOI-836 b; SNR = 17), identified from the TESS light-curves. In Sector 11, TOI-836 b shows five transit events and one partial (egress only) transit, while TOI-836 c shows two transit events. One transit event of TOI-836 b would have occurred in the gap during which the satellite

[2] `https://github.com/jlillo/tpfplotter`

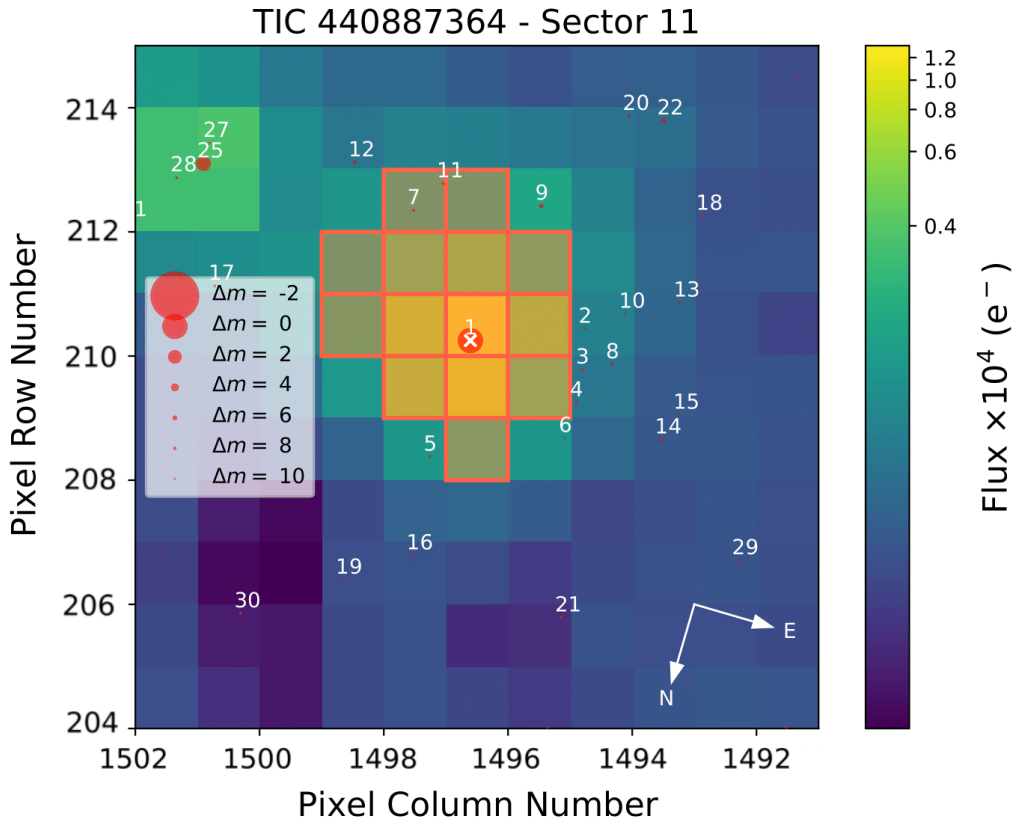

Figure 3.1: Target Pixel File (TPF) from TESS centered on TOI-836 from the *Gaia* catalog, with *Gaia* DR2 sources indicated by red circles with scaled magnitudes, where the numbers indicate ranked distance from the target represented by a white cross. The aperture mask is outlined in red.

downloads data. See Table 3.2 and the left-hand panel of Figure 3.2.

TOI-836 was observed again in the third year of TESS operations during Sector 38, Camera 1, CCD 4 from 2021 April 28 to 2021 May 26. Seven transit events were observed for TOI-836 b, and three for TOI-836 c. See Table 3.2 and right-hand panel of Figure 3.2.

The transits of TOI-836 b indicate an orbital period of 3.82 days. The transit depth was 580 ppm, implying the planet candidate is a potential hot super-Earth. For TOI-836 c the orbital period is 8.60 days, and the transit depth is 1140 ppm, implying the candidate is potentially sub-Neptune in size.

For this work we use the Presearch Data Conditioning Simple Aperture Photometry (PDC-SAP) light-curve produced by the SPOC pipeline. The PDC-SAP light-curves have non-astrophysical trends removed from the raw Simple Aperture Photometry (SAP) light-curves using the PDC algorithm [Stumpe et al., 2012, 2014; Smith et al.,

2012]. The PDC-SAP light-curves for TOI-836 were retrieved from the Mikulski Archive for Space Telescopes (MAST) portal and used in our joint model in Section 3.3.

To mitigate for the effects of stellar variability on the transit lightcurves in the Sector 11 and Sector 38 TESS data, we apply a Gaussian Process (GP) model using the `PyMC3` and `celerite` packages. We constrain this GP model for each sector using three hyperparameters as priors set up with $\log(s2)$ (a jitter term describing the excess white noise, Salvatier et al. 2016) and $\log(Sw4)$ as normal distributions with a mean equal to the variance of the flux of each sector and a standard deviation of 0.1 for Sector 11 and 0.05 for Sector 38 (this is done to prevent overfitting of the GP); and the same is applied to $\log(w0)$. $\log(Sw4)$ and $\log(w0)$ both represent terms that describe the non-periodic variability of the light-curves [Salvatier et al., 2016]. These hyperparameter setups are identical to those described for TOI-431 in Osborn et al. [2021b] and informed by the `exoplanet` and `PyMC3` documentation. These hyperparameters are then incorporated into the SHOTerm kernel within the `exoplanet` framework, representing a stochastically-driven simple harmonic oscillator [Foreman-Mackey et al., 2021a]. The GP model is then subtracted from the PDC-SAP flux to recover a flattened light curve from which transit models of TOI-836 b and TOI-836 c can be drawn. The effect of this can be seen in the first and second panels of Figure 3.2 for Sector 11 and Sector 38 of TESS respectively. We also plot the phase-folded TESS data for TOI-836 b and TOI-836 c in Figure 3.3 for both sectors.

For all follow-up photometry, we convert each time system to TBJD (TESS Barycentric Julian Date, BJD - 2457000) for consistency, and normalise each lightcurve by dividing by the median of the out-of-transit flux datapoints and subtracting the mean of the out-of-transit flux. The transits themselves are then modelled using a quadratic limb-darkened Keplerian orbit (with coefficients u_1 and u_2) according to Kipping [2013b], with parameters including stellar radius (R_*) and mass (M_*) in Solar units, planetary orbital period (P) in days, transit ephemeris (T_c) in TBJD, impact parameter (b), eccentricity (e) and argument of periastron (ω) defined for each of TOI-836 b and TOI-836 c with priors informed by our spectral analysis and catalog data (see Appendices 3.10, 3.11 and 3.12 for details of the priors used). Transit models for each set of photometry time-series data are then created using the `starry` package within `exoplanet`, along with their corresponding planetary radii (R_p), time of the data (t) and exposure times for each instrument t_{exp}.

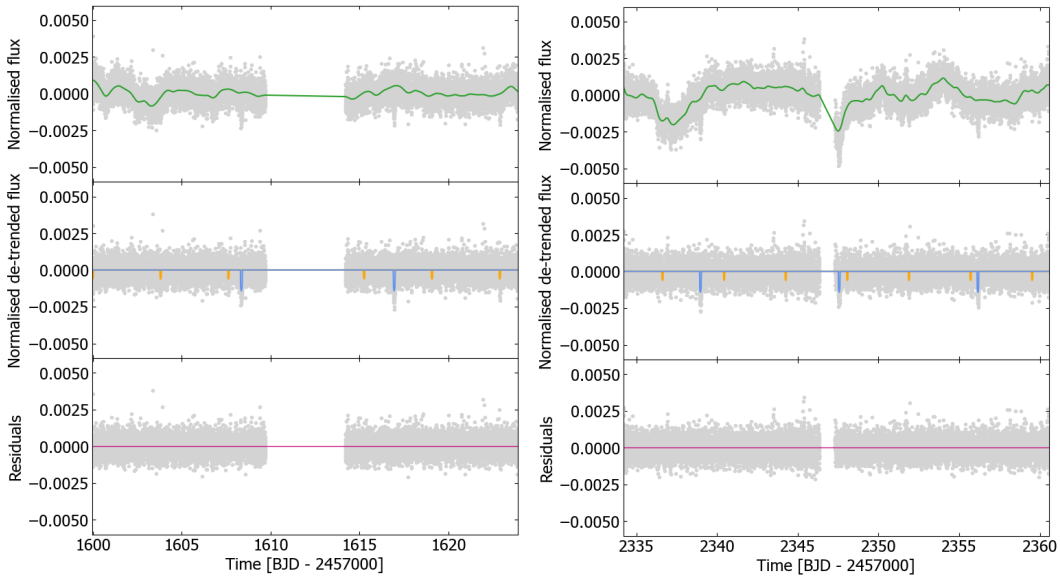

Figure 3.2: **Top left panel:** TESS PDC-SAP light curve from Sector 11 with the GP model plotted in green. **Middle left panel:** TESS PDC-SAP light curve data minus the GP model, with transits plotted for TOI-836 c (blue line) and TOI-836 b (orange line). **Bottom left panel:** Residuals between the best fit model and the TESS datapoints. **Top right panel:** TESS PDC-SAP light curve from Sector 38 with the GP model plotted in green. **Middle right panel:** TESS PDC-SAP light curve data minus the GP model, with transits plotted for TOI-836 c (blue line) and TOI-836 b (orange line). **Bottom right panel:** Residuals between the best fit model and the TESS datapoints.

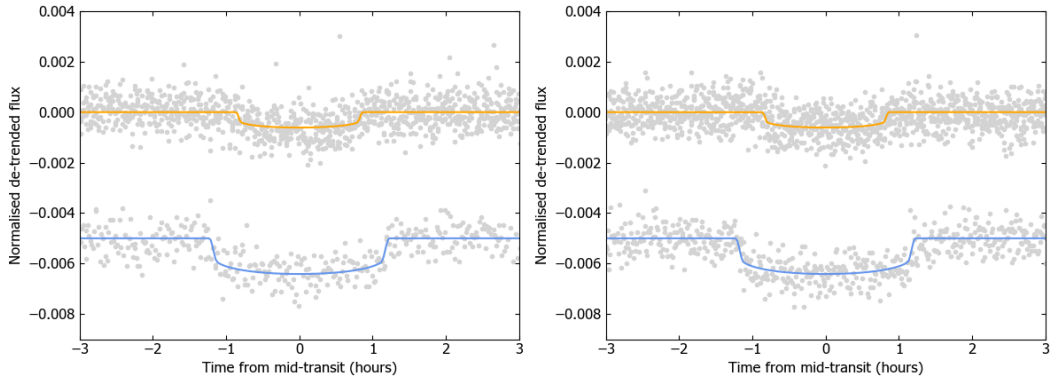

Figure 3.3: **Left panel:** TESS PDC-SAP light curve from Sector 11 minus the GP model, phase-folded to a period corresponding to that of TOI-836 b with the transit model shown in orange and phase-folded to a period corresponding to that of TOI-836 c with the transit model shown in blue. The data for TOI-836 c has been offset by -0.005 for clarity. **Right panel:** TESS PDC-SAP light curve from Sector 38 minus the GP model, phase folded and offset for each planet analogously to that of Sector 11.

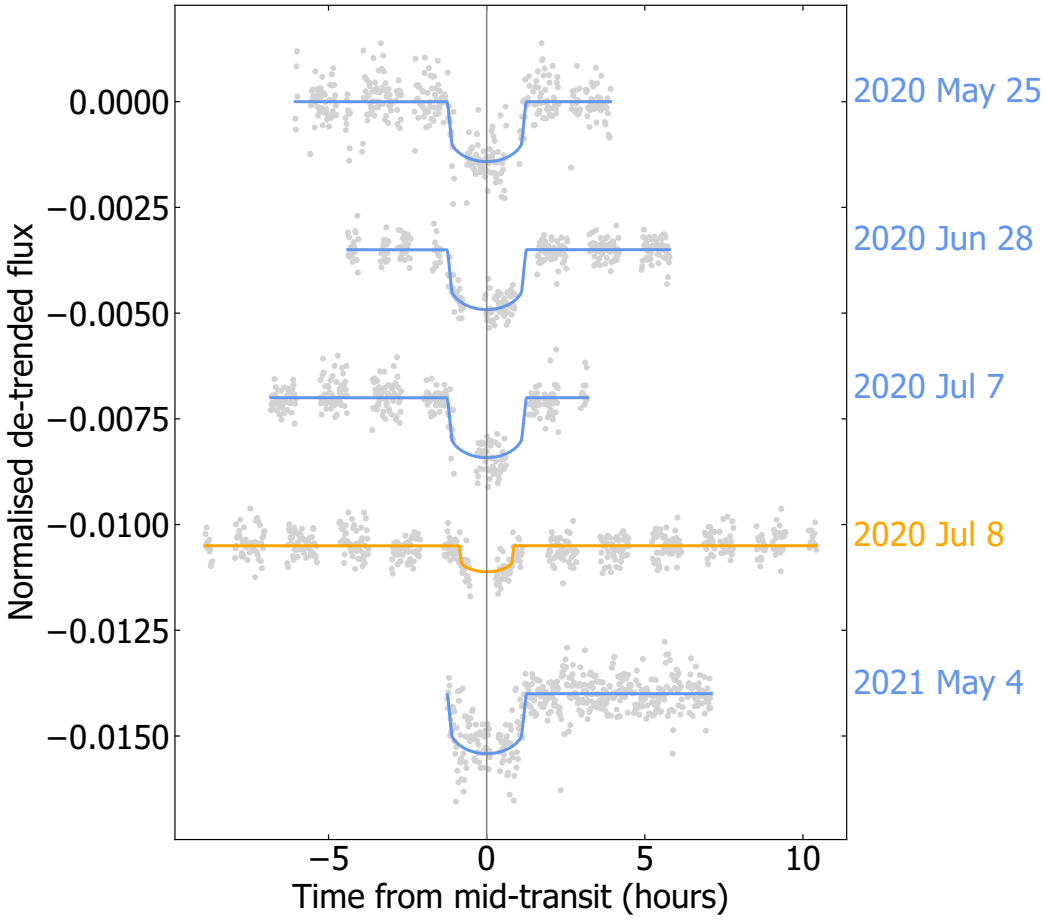

Figure 3.4: Light curves of TOI-836 b and TOI-836 c taken by the CHEOPS satellite as detailed in Table 3.2, plotted with our best fit `exoplanet` models for TOI-836 b in orange and TOI-836 c in blue, and offset for clarity.

3.2.2 CHEOPS photometry

The transit depths for TOI-836 b and TOI-836 c are 580 ppm and 1140 ppm respectively, making them challenging for photometric follow-up efforts. The CHEOPS mission is able to reach a precision of 15 ppm per 6 h for a star with V = 9 mag [Benz et al., 2021], and CHEOPS is therefore in a unique position to confirm and characterise shallow transit discoveries from TESS, as has been shown in recent publications [Bonfanti et al., 2021; Delrez et al., 2021; Leleu et al., 2021].

In order to better determine the planet radii and orbital ephemerides, and check for any TTVs, we observed TOI-836 with CHEOPS spacecraft between 2020 May 25 and 2021 May 4, as a part of the Guaranteed Time Observing programme, yielding a total of 57.81 h on target. Five observations of TOI-836 were taken by the CHEOPS satellite, resulting in the recovery of four transits of TOI-836 c, and one transit of TOI-836 b. For all visits, we use an exposure time of 60 s. See details set out in Table 3.2.

The CHEOPS spacecraft is in a low-Earth orbit and thus parts of the observations are unobtainable because the telescope passes through the South Atlantic Anomaly (SAA), and as the amount of stray-light entering the telescope becomes higher than the accepted threshold, our observations are interrupted by Earth occultations. These effects that occur on orbital timescales (∼98.77 min) result in onboard rejections of images and manifest in a decrease in observational efficiency, corresponding to 72%, 55%, 56%, 54%, & 96% per visit, as can be seen in Figure 3.4.

For all visits, the data were automatically processed using the CHEOPS data reduction pipeline (DRP v13; Hoyer et al. 2020), that conducts image calibration, such as bias, gain, non-linearity, dark current, and flat fielding corrections, and performs rectifications of environmental and instrumental effects, for example cosmic-ray hits, smearing trails, and background variations. Aperture photometry is subsequently done on the corrected images using a set of standard apertures; $R = 22.5$" (RINF), 25.0" (DEFAULT), and 30.0" (RSUP), and an additional aperture that aims to optimise the radius based on contamination level and instrumental noise (ROPT). For the CHEOPS observations of TOI-836, this radius is either 29.0 or 29.5". The DRP also computes a contamination estimate of background sources, as detailed in section 6.1 of Hoyer et al. [2020], that is subtracted from the light curves.

Due to the orbit of CHEOPS and thus the rotating field of view, CHEOPS data include short-term, non-astrophysical flux trends due to nearby contaminants, background variations, or changes in instrumental environment that vary on the timescale of the orbit of CHEOPS. Whilst previous works have used linear decorrelation with instrumental basis vectors [Bonfanti et al., 2021; Delrez et al., 2021; Leleu et al.,

2021] or Gaussian process regression [Lendl et al., 2020b], a recent study has shown that a novel PSF detrending method can also remove these roll angle trends [Wilson et al., 2022]. In brief, this method assesses PSF shape changes over a visit by conducting a principal component analysis on the autocorrelation function of the CHEOPS subarray images, as it was found that a myriad of causes of systematic variation within CHEOPS data affects the PSF shape. A leave-one-out-cross-validation [Celisse, 2008] is used to select the most prominent components that are subsequently used to decorrelate the light curve produced by aperture photometry. We apply this method to the TOI-836 CHEOPS observations with fluxes obtained with the DEFAULT aperture. The decorrelated CHEOPS data are presented in Table 3.3, along with the resulting light-curves in Figure 3.4.

3.2.3 Ground-based Follow-up Photometry

Table 3.2: Photometric observations of TOI-836.

Instrument	**Aperture**	**Filter**	**Exposure time (s)**	**No. of images**	**UT night**	**Planet**	**Epoch no.**
—	—	—		—	—	—	—
TESS	0.105 m	TESS[1]	120	19527	2019 Apr 22 - 2019 May 20	TOI-836 b TOI-836 c	Epochs 1-7 Epochs 1-2
MEarth-South	0.4 m × 7	RG715	32	3054	2019 Jul 4	TOI-836 c	Epoch 8
LCOGT-SSO	1.0 m	Y	40	232	2020 Feb 29	TOI-836 c	Epoch 36
LCOGT-CTIO[A]	1.0 m	Y	100	138	2020 Mar 8	TOI-836 b	Epoch 83
LCOGT-SSO[B]	1.0 m	Y	100	109	2020 Mar 20	TOI-836 b	Epoch 86
LCOGT-SSO	1.0 m	z_s	30	341	2020 Apr 12	TOI-836 c	Epoch 41
LCOGT-SSO	1.0 m	Y	100	260	2020 May 4	TOI-836 b	Epoch 98
LCOGT-SAAO[C]	1.0 m	z_s	30	327	2020 May 16	TOI-836 c	Epoch 45
CHEOPS	0.32 m	CHEOPS[2]	60	398	2020 May 25	TOI-836 c	Epoch 46
CHEOPS	0.32 m	CHEOPS[2]	60	319	2020 Jun 28	TOI-836 c	Epoch 50
CHEOPS	0.32 m	CHEOPS[2]	60	318	2020 Jul 7	TOI-836 c	Epoch 51
CHEOPS	0.32 m	CHEOPS[2]	60	574	2020 Jul 8	TOI-836 b	Epoch 115
LCOGT-SSO	1.0 m	z_s	30	345	2021 Apr 8	TOI-836 c	Epoch 83
ASTEP	0.4 m	R_c	25	370	2021 Apr 8	TOI-836 c (egress)	Epoch 83
NGTS	0.2 m × 3	NGTS[3]	10	5405	2021 Apr 16	TOI-836 c	Epoch 84
LCOGT-CTIO	1.0 m	z_s	30	382	2021 Apr 16	TOI-836 c	Epoch 84
TESS	0.105 m	TESS[1]	120	19226	2021 Apr 29 - 2021 May 26	TOI-836 b TOI-836 c	Epochs 194-200 Epochs 86-88
CHEOPS	0.32 m	CHEOPS[2]	60	431	2021 May 4	TOI-836 c	Epoch 86
LCOGT-CTIO	1.0 m	z_s	30	300	2021 Jun 24	TOI-836 c	Epoch 92

[1]TESS custom 600–1000 nm [2]CHEOPS custom 350–1100 nm [3]NGTS custom 520–890 nm
[A]CTIO - Cerro Tololo Inter-American Observatory [B]SSO - Siding Spring Observatory [C]SAAO - South Africa Astronomical Observatory

Table 3.3: CHEOPS photometric data for TOI-836. This table is available in its entirety online.

Time (BJD -2457000)	**Normalised flux**	**Flux uncertainty**
1994.88704	0.99981	0.00025
1994.88773	0.99955	0.00026
1994.88843	1.00105	0.00027
1994.88912	1.00140	0.00030
1994.88982	1.00033	0.00035
1994.90649	0.99897	0.00027
1994.90718	0.99896	0.00026
1994.90788	1.00011	0.00025
1994.90857	1.00045	0.00025
...	...	...

MEarth-South photometry

A transit of TOI-836 c was observed using the *MEarth-South* telescope array [Irwin et al., 2015a] at Cerro Tololo Inter-American Observatory (CTIO), Chile on 2019 July 3-4. Seven telescopes were operated defocused to a half-flux diameter of 12 pixels (10.1", given the pixel scale of 0.84"/pix), and an exposure time of 32 s, observing continuously starting from twilight until the target set below 2 airmasses. Observations were made using an RG715 filter. A meridian flip occurred during the transit and has been taken into account in the analysis by allowing for a separate magnitude zero-point on either side of the meridian to remove any residual flat fielding error.

Data were reduced following standard procedures for *MEarth-South* data (e.g. Irwin et al. 2007, 2015a) with a photometric extraction aperture of radius 17 pixels (14.3"). To account for residual colour-dependent atmospheric extinction the transit model included linear decorrelation against airmass. The edge of the photometric aperture is slightly contaminated by fainter sources, the most significant being TIC 440887361, but we estimate that this source is approximately 10.6 TESS magnitudes fainter than the target star, so the resulting dilution of the measured transit depth should be negligible. The *MEarth-South* light curve is shown in Figure 3.5 and used in the joint modeling in Section 3.3.2.

ASTEP photometry

ASTEP (Antarctic Search for Transiting ExoPlanets) is a 40 cm Newtonian telescope designed to perform high precision photometry under the extreme conditions of the Antarctic winter [Fressin et al., 2005; Daban et al., 2010; Abe et al., 2013; Guillot et al., 2015; Mékarnia et al., 2016]. It is installed at the French-Italian Concordia station at Dome C, Antarctica (75° 06' S, 123° 21' E) on a summit of the high Antarctic plateau, at an altitude of 3233 m, 1100 km inland. Dome C is an ideal location for time-series observations thanks to the 4-month continuous night during the Antarctic winter and favourable weather conditions [Crouzet et al., 2010, 2018]. ASTEP is equipped with a FLI Proline KAF 16801 E 4096×4096 pixel CCD camera observing in an R_c band-pass, the field of view is $1° \times 1°$ and the pixel size is 0.9"/pixel.

We observed TOI-836 on 2021 April 8, during 5 hours between BJD 2459313.20 and 2459313.41, and we detected the second half of the transit of TOI-836 c. We scheduled the observation using a custom scheduling tool that sends queries to the `TESS Transit Finder`. We set the exposure time to 25 s, the cadence was 50 s, and we collected 370 frames. The median Full Width Half Maximum (FWHM) was 4.06" and the airmass varied between 1.57 and 1.94. The details of the ASTEP observations are set out in Table 3.2. We performed differential aperture photometry using a custom data reduction pipeline based on the pipeline described in Mékarnia et al. [2016] and adapted to TESS follow-up. We used an aperture radius of 10 pixels (9.3") and 8 comparison stars. The light curve RMS is 1.43 ppt and decreases to 1.2 ppt after binning the light curve with a bin size of 3 points, for a predicted transit depth of 1.38 ppt. The transit appears clearly and is on target. The ASTEP light curve is shown in Figure 3.5 and used in the joint modelling in Section 3.3.2. The ASTEP telescope is now being upgraded with two new cameras that will observe simultaneously in two colors and will provide a much better throughput [Crouzet et al., 2020].

NGTS photometry

We monitored a full transit of TOI-836 c on the night of 2021 April 16 using three of the NGTS [Next Generation Transit Survey; Wheatley et al., 2018] telescopes at the ESO Paranal Observatory, Chile. The observations were performed using the NGTS multi-telescope observing method described in Bryant et al. [2020a] and Smith et al. [2020]. NGTS consists of an array of 0.2 m robotic telescopes, each with a wide field-of-view of 8 square degrees. A custom NGTS filter of 520–890 nm is used,

and images are taken using Andor iKon-L 936 cameras, which deliver a plate-scale of 5"/pix^{-1}. We use an exposure time of 10 s, and with readout time this translates to a cadence of approximately 13 s. The details of the NGTS observations are set out in Table 3.2.
The NGTS image reduction was performed using an adapted version of the standard NGTS pipeline [Wheatley et al., 2018], which has been updated to perform aperture photometry for a single star. Comparison stars which are isolated and similar to TOI-836 in brightness and CCD position were automatically identified by the pipeline using *Gaia* DR2 [Gaia Collaboration et al., 2018]. The resultant flux from each telescope was detrended independently against airmass, and the photometry from the three telescopes is combined into a single light curve file, which is publicly available from the ExoFOP-TESS website[3]. The NGTS light curve is shown in Figure 3.5 and used in the joint modeling in Section 3.3.2.

LCO photometry

We observed three full transits of TOI-836 b and six full transits of TOI-836 c from the Las Cumbres Observatory Global Telescope [LCOGT; Brown et al., 2013] 1.0 m network. The details of the LCOGT observations are set out in Table 3.2. We used the `TESS Transit Finder`, which is a customized version of the `Tapir` software package [Jensen, 2013], to schedule our transit observations. The telescopes are equipped with 4096 × 4096 SINISTRO cameras having an image scale of 0.389" per pixel, resulting in a 26'×26' field of view. The images were calibrated by the standard LCOGT `BANZAI` pipeline [McCully et al., 2018], and photometric data were extracted using `AstroImageJ` [Collins et al., 2017]. The LCOGT light curves are shown in Figure 3.6 for TOI-836 b and TOI-836 c, and used in the joint modelling in Section 3.3.2.

WASP-South photometry

The WASP-South array of 8 wide-field cameras was the Southern station of the WASP transit-search project [Pollacco et al., 2006]. WASP-South observed the field of TOI-836 repeatedly over the years 2006 to 2014, observing with a broad-band filter, and accumulating a total of 93,000 photometric data points. While the precision of these observations is not sufficient to detect the transits, the long-duration monitoring is ideal for detecting photometric activity due to star spots. We thus searched the data for a rotational modulation using the methods discussed

[3] `https://exofop.ipac.caltech.edu/tess/`

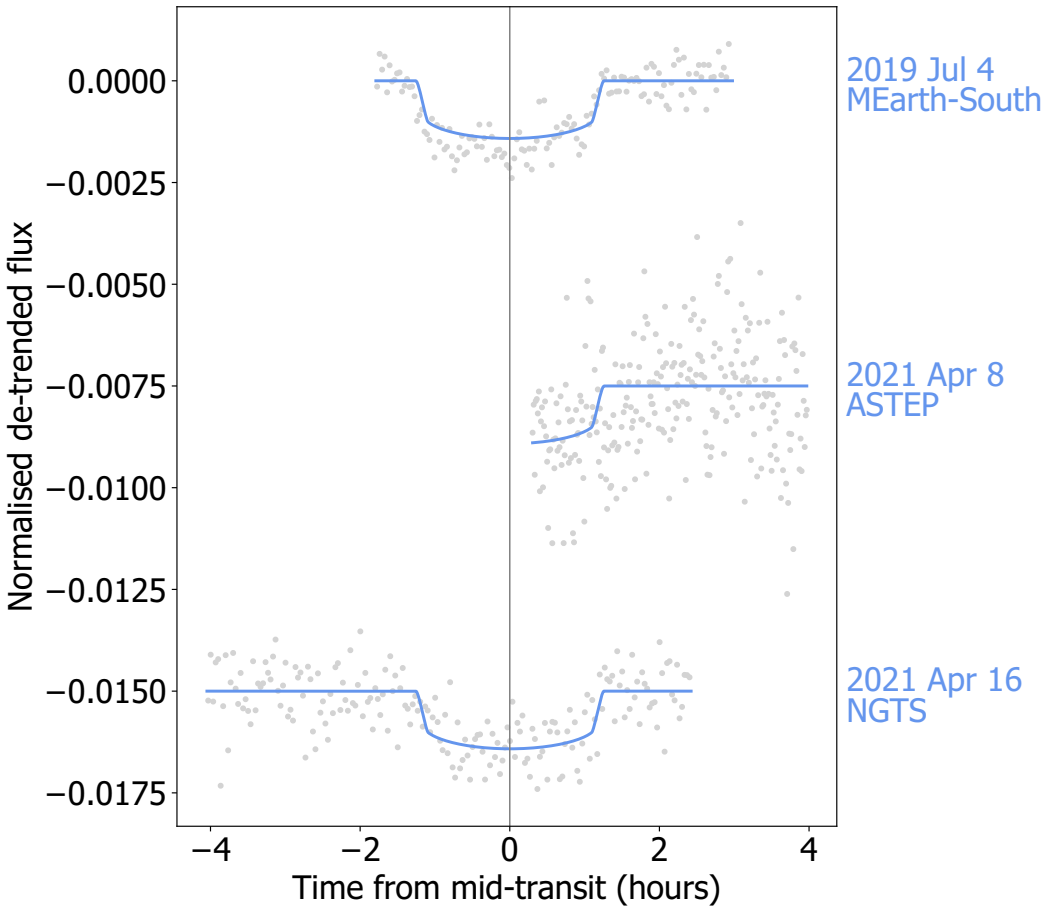

Figure 3.5: Lightcurves of TOI-836 c taken by the *MEarth-South*, NGTS and ASTEP facilities as detailed in Table 3.2, plotted with our best fit `exoplanet` models and offset for clarity.

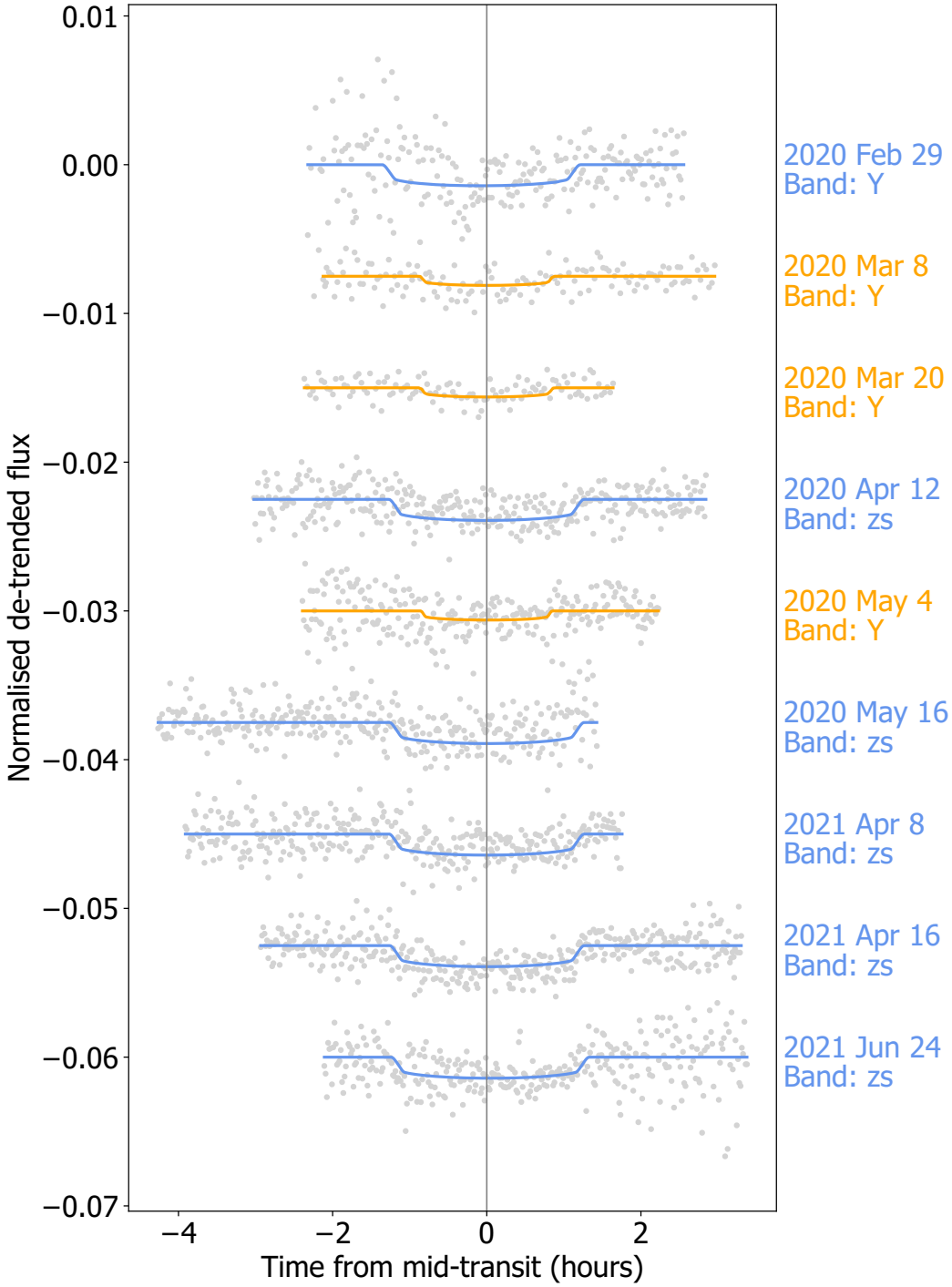

Figure 3.6: Light curves of TOI-836 b and TOI-836 c taken by the LCOGT network as detailed in Table 3.2, plotted with our best fit `exoplanet` models for TOI-836 b in orange and TOI-836 c in blue, and offset for clarity.

in Maxted et al. [2011]. We find a persistent periodicity with a period of 22.0 ± 0.1 days, where the uncertainty estimate makes allowance for phase changes caused by changing star-spot patterns. The amplitude varies from 3 to 8 mmag and the false-alarm probability in each season's dataset is typically $< 1\%$. In Figure 3.7 we show periodograms from two seasons of data, together with the resulting modulation profile from folding the data.
The 22 day period is consistent with activity seen in the TESS data, particularly in Sector 38 data (see Figure 3.2). We therefore adopt this as the likely spin period of the star and use it to inform our joint modelling in Section 3.3.2.

3.2.4 Follow-up Spectroscopy

In order to determine the stellar parameters and measure radial velocity variations, a number of spectrographs were used to observe TOI-836. Two reconnaissance spectra were taken on 2019 July 1 and 2021 May 28 with the Tillinghast Reflector Echelle Spectrograph (TRES) [Fűrész, 2008] on the 1.5 m telescope at the Fred Lawrence Whipple Observatory (FLWO). The spectra were used to derive stellar parameters using the Stellar Parameter Classification (SPC) tool [Buchhave et al., 2012; Buchhave et al., 2014]. These spectra indicated that TOI-836 is a K-dwarf with a low $v \sin i_*$ that would be amenable to high-precision radial velocity follow-up. In this section we describe these high-precision radial velocity data, which are obtained using the HARPS and PFS spectrographs. We also obtain 11 spectra from the HIRES spectrograph [Vogt & Penrod, 1988], taken from 2009 April 6 to 2013 February 3, which we use to examine long-term radial velocity trends. The iSHELL radial velocities were taken at 2.3 microns, and as we do not implement a chromatic RV analysis as in Cale et al. [2021], we exclude them from our analysis. Additional radial velocity data from MINERVA-*Australis* also exist, but the lower precision of these data mean that we omit them from our analysis.

HARPS radial velocity observations

HARPS [High Accuracy Radial velocity Planet Searcher; Pepe et al., 2002] is an Echelle spectrograph mounted on the ESO 3.6 m telescope situated at La Silla Observatory, Chile. A total of 52 spectra of TOI-836 were obtained with HARPS as part of the *NCORES* program (PI D. Armstrong, 1102.C-0249). 15 of these spectra were obtained from 2020 March 16 to 2020 March 23 (7 nights), followed by a further 37 spectra from 2021 January 22 to 2021 March 2 (39 nights). These data were obtained in HARPS High-Accuracy Mode with a 1" diameter fibre, standard

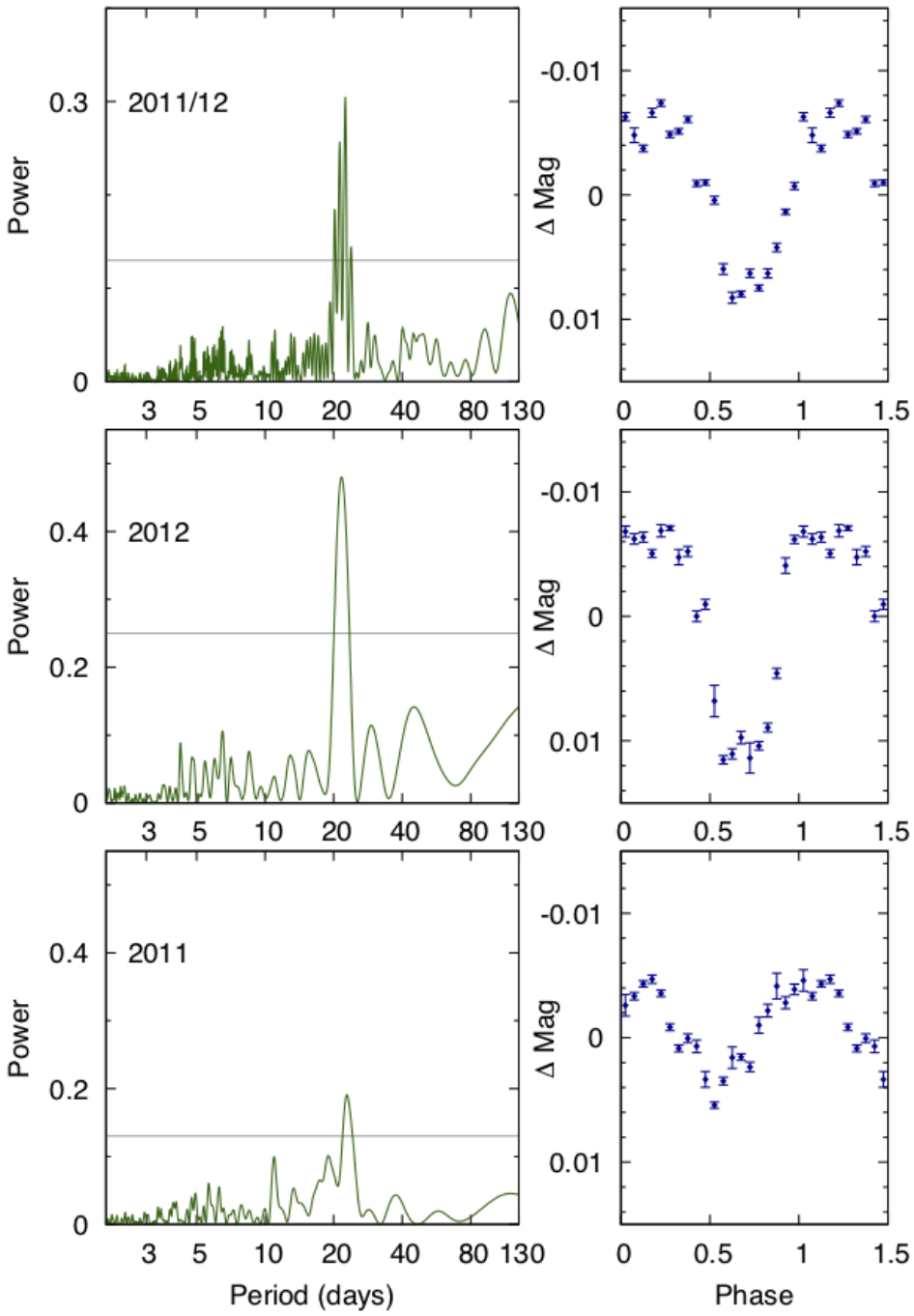

Figure 3.7: **Left panels:** Periodograms of the WASP-South lightcurves of TOI-836 from 2011 and 2012, and for 2011 & 2012 combined. The horizontal line is the estimated 1%-likelihood false-alarm level. **Right panels:** WASP-South photometry data, phase-folded to the best stellar rotation period estimate.

resolution of R∼115,000, and exposure times of approximately 1500 s. Raw data were reduced according to the standard HARPS data reduction software detailed in Lovis & Pepe [2007]. The data table for these observations can be found in Table 3.4, which we use in our joint modelling (Section 3.3.2). The HARPS data are marked with an asterisk in Table 3.5.

Table 3.4: HARPS spectroscopic data for TOI-836. This table is available in its entirety online.

Time (BJD -2457000)	**RV** ($\mathbf{m\,s^{-1}}$)	**RV error** ($\mathbf{m\,s^{-1}}$)	**FWHM** ($\mathbf{m\,s^{-1}}$)	**Bisector** ($\mathbf{m\,s^{-1}}$)	**Contrast**	**S-index$_{\mathbf{MW}}$**
1924.744232	-26270.62	1.20	6479.82	59.29	42.086199	1.118916
1924.847515	-26272.89	1.13	6477.87	58.02	42.082108	1.088405
1925.765286	-26277.15	1.33	6483.37	54.98	42.104065	1.099795
1925.897310	-26278.60	1.42	6484.65	62.33	42.063377	1.035016
1926.748165	-26279.33	1.23	6481.65	63.03	42.111069	1.073716
1926.891093	-26276.88	1.25	6474.28	65.77	42.150971	1.039492
1927.807982	-26280.90	1.66	6472.36	61.35	42.201152	1.068344
1927.885303	-26283.22	1.24	6470.19	62.19	42.177954	1.035070
1928.764641	-26288.22	1.24	6465.28	65.38	42.164275	1.058810
1928.890901	-26289.86	1.37	6466.36	65.65	42.174431	1.042093
...	...	...	...	...	...	...

Table 3.5: Radial velocity follow-up details for TOI-836. Observations used in the joint model are marked with an asterisk.

Facility	**Telescope aperture**	**No. of spectra**	**Resolution**
HARPS *	3.6 m	52	115000
HIRES	10.0 m	11	60000
PFS *	6.5 m	30	130000
iSHELL	3.0 m	10	70000
MINERVA-*Australis*	0.7 m × 6	27	75000

Sources: HARPS [Pepe et al., 2002], HIRES [Vogt & Penrod, 1988], PFS [Crane et al., 2006], iSHELL [Rayner et al., 2012], MINERVA-*Australis* [Wittenmyer et al., 2018; Addison et al., 2019, 2021]

PFS radial velocity observations

The Planet Finder Spectrograph (PFS) [Crane et al., 2006, 2008, 2010] is a high resolution optical Echelle spectrograph mounted on the 6.5 m Magellan II Telescope at Las Campanas Observatory, Chile. PFS is calibrated via an iodine-cell, and raw data are reduced to 1D spectra and relative radial velocities extracted using a custom pipeline based on Butler et al. [1996]. The spectrograph was upgraded in 2018, and now operates with a default slit width of 0.3", which delivers a resolving power of R∼130,000.

TOI-836 was observed as part of the Magellan-TESS Survey [Teske et al., 2021] between 2019 July 10 to 2020 March 17. Exposure times were approximately 900-1200 s per individual observation, and usually two observations were taken per night (separated by ∼2 hours) and binned together. In total, 38 binned radial velocities were published in Teske et al. for TOI-836, and these are set out in table 4 of Teske et al. [2021]. We use the PFS radial velocities in our joint modelling (Section 3.3.2). The PFS data are marked with an asterisk in Table 3.5.

HIRES radial velocity observations

HIRES [High Resolution Echelle Spectrometer; Vogt & Penrod, 1988] is an R∼60,000 resolving power spectrograph mounted on the 10 m Keck Telescope at Mauna Kea Observatory, Hawaii. Like PFS, HIRES also operates with an iodine-cell wavelength calibration, and data are reduced using a custom pipeline based on Butler et al. [1996].

TOI-836 was observed as part of the Lick-Carnegie Exoplanet Survey [Butler et al., 2017] between 2009 April 6 to 2013 February 3. In total, 11 observations were made over this four year time period, with a typical exposure time of approximately

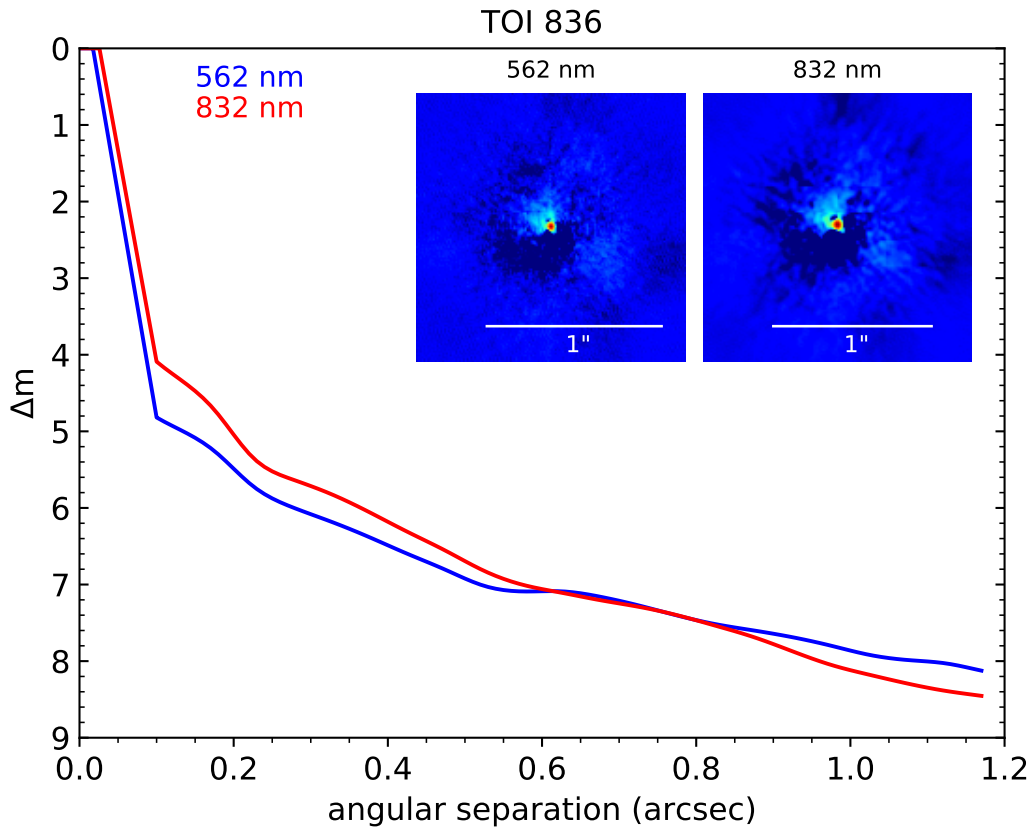

Figure 3.8: Reconstructed images and speckle sensitivity curves of TOI-836 taken on 2020 March 13 using Zorro on the *Gemini*-South 8.0 m telescope at Cerro Pachón, Chile, in each of the two bandpasses. No close companions are visible brighter than a contrast of 5 mag for separations between 0.2 and 1.2". Other direct imaging data also place similar constraints on the presence of close companions.

500 sec. These data are set out in table 1 of Butler et al. [2017]. The observations were made prior to the discovery of the transiting planets TOI-836 b and TOI-836 c. The low cadence of these observations, coupled with the stellar activity of TOI-836, means that we decided not to use them in our GP-based joint model of Section 3.3.2 - however they do enable us to study any long-term radial velocity trends for the system (see Section 3.3.2).

3.2.5 Imaging

The large size of the TESS pixels (21") necessitates a careful study of neighbouring regions in order to determine if there are stars blended in to the TESS photometric data. In such cases, planet transits can be mimicked by other stellar configurations (e.g., Lillo-Box et al. 2012; Howell et al. 2011; Lillo-Box et al. 2014; Furlan et al. 2017). *Gaia* shows TOI-836 to be a relatively isolated star, with no neighbours with $\Delta T_{mag} < 6$ in the photometric aperture to within its sensitivity limits (see Figure 3.1). To probe regions very close to TOI-836 (< 1.5"), where *Gaia* is known to be incomplete, we use direct imaging from large ground-based telescopes.
TOI-836 was imaged by multiple telescopes and instruments in order to check for close companions. This imaging includes *Gemini*-Zorro and *Gemini*-'Alopeke [Scott et al., 2021], VLT-NaCo [Rousset et al., 2003], *Keck*-2-NIRC2 [Ciardi et al., 2015] and SOAR-HRCam [Ziegler et al., 2020]. These imaging data are publicly available from the ExoFOP-TESS website[4]. The conclusion from all of these imaging data is that TOI-836 has no close companions outside a separation of 0.2".
As an example of this direct imaging data, Figure 3.8 shows the reconstructed images and speckle sensitivity curves from the observation taken using the Zorro instrument [Scott et al., 2021] on *Gemini*-South at Cerro Pachón Observatory, Chile. This imaging was taken on 2020 March 13 in two simultaneous passbands (562 nm and 832 nm), and like all the direct imaging, shows that TOI-836 is an isolated star to within the $5\,\sigma$ contrast limits.

3.3 Methods and Results

3.3.1 Stellar analysis

To determine the stellar parameters for TOI-836, we co-add the 52 HARPS spectra (Section 3.2.4) into a single combined spectrum with a signal-to-noise of ∼400 at 550 nm. We use the method described in Sousa [2014] and Santos et al. [2013] in

[4] `https://exofop.ipac.caltech.edu/tess/`

order to derive the stellar atmospheric parameters including a trigonometric surface gravity $\log g$, effective temperature T_{eff} and metallicity [Fe/H]. This method measures the equivalent widths of iron lines in the combined HARPS spectrum via the `ARES` v2 code [Sousa et al., 2015]. The abundances are then estimated using the `MOOG` code [Sneden, 1973] for radiative transfer, which includes a grid of model atmospheres from Kurucz [1993], and we find the best set of spectroscopic parameters by assuming equilibriums of ionization and excitation. Following the same methodology as described in Sousa et al. [2021], we use the *Gaia* EDR3 parallax and estimate the trigonometric surface gravity. This spectral analysis shows that TOI-836 is a K-dwarf with a $\log g = 4.743 \pm 0.105$ dex and a $T_{\mathit{eff}} = 4552 \pm 154$ K. We find a metallicity of [Fe/H] $= -0.284 \pm -0.067$ dex and a $v \sin i_* = 1.86 \pm 0.50\,\mathrm{km\,s^{-1}}$.

To obtain the radius of TOI-836, we use a Markov-Chain Monte Carlo (MCMC) modified infrared flux method (IRFM; Blackwell & Shallis 1977; Schanche et al. 2020). This is done by building spectral energy distributions (SEDs) from ATLAS Catalogue stellar atmospheric models [Castelli & Kurucz, 2003] and stellar parameters derived via our spectral analysis, and calculating synthetic fluxes by integrating the SEDs over bandpasses of interest after attenuation to account for extinction. These fluxes are compared to observed broadband photometry retrieved from the most recent data releases for the following bandpasses; *Gaia* G, G_{BP}, and G_{RP} [Gaia Collaboration et al., 2021], 2MASS J, H, and K [Skrutskie et al., 2006], and *WISE* *W1* and *W2* [Wright et al., 2010] to calculate the apparent bolometric flux, and hence the stellar angular diameter and effective temperature. By converting the angular diameter to the stellar radius using the offset-corrected *Gaia* EDR3 parallax [Lindegren et al., 2021], we obtain $R_* = 0.666 \pm 0.010\,R_\odot$.

Starting from the basic input set given by (T_{eff}, [Fe/H], R_*), we then derived the isochronal mass M_* and age t_*. To provide robust estimates, we employed two different evolutionary models, namely `PARSEC`[5] v1.2S [Marigo et al., 2017] and `CLES` [Code Liègeois d'Évolution Stellaire, Scuflaire et al., 2008]. In detail, we derived a first pair of mass and age values using the isochrone placement technique [Bonfanti et al., 2015, 2016], which we applied to pre-computed tables of `PARSEC` tracks and isochrones. Besides the basic input set, we further inputted the $v \sin i_*$ value to improve the convergence of the interpolating routine as detailed in Bonfanti et al. [2016]. A second pair of mass and age estimates was instead retrieved through the `CLES` code, which generates the best stellar evolutionary track that reproduces the basic input set following the Levenberg-Marquadt minimisation scheme [Salmon et al., 2021]. After carefully checking the mutual consistency of the two respective

[5] *PA*dova and T*R*ieste *S*tellar *E*volutionary *C*ode: `http://stev.oapd.inaf.it/cgi-bin/cmd`

pairs of values through the χ^2-based criterion outlined in Bonfanti et al. [2021], we finally merged the two output mass and age distributions and we obtained $\mathrm{M}_* = 0.678^{+0.049}_{-0.041}\,\mathrm{M}_\odot$ and $t_* = 5.4^{+6.3}_{-5.0}\,\mathrm{Gyr}$. We use these values of the stellar mass and radius as priors within our `exoplanet` modelling (described in Section 3.3.2), which are then fit for in the code to produce the final values seen in Table 3.6.
Following the formulation of Johnson & Soderblom [1987], and using the values of proper motion and parallax from *Gaia* EDR3 (see Table 3.1) and a radial velocity from *Gaia* DR2 of $-26.603 \pm 0.922\,\mathrm{km\,s^{-1}}$ [Gaia Collaboration et al., 2018], we calculate the values and uncertainties for U, V and W, the heliocentric velocity components of the Galactic space velocities, in the direction of the galactic centre, rotation, and pole respectively, in Table 3.6. We should note that we do not subtract the Solar motion and compute the U, V and W values in the right-handed system. We also use the approach of Reddy et al. [2006] in a Monte Carlo fashion with 100,000 samples to determine the probability that TOI-836 is in a given kinematic Galactic family, using a weighted average of the results obtained using the velocity dispersion standards of Bensby et al. [2003, 2014], Reddy et al. [2006], and Chen et al. [2021]. We find a Galactic thin disk membership probability for TOI-836 of 98.9%, thick disk membership probability of 1.1%, and halo membership probability of 0%. This agrees well with the Galactic eccentricity of TOI-836 of 0.08, and the high Galactic Z-component of the angular momentum of $Z \approx 1770\,\mathrm{kpc\,km\,s^{-1}}$. We compute these values using the `galpy` package after a Galactic orbit determination using the *Gaia* EDR3 position, proper motions, and parallax, and *Gaia* DR2 radial velocity integrating over 5 Gyr, as well as the typical values for [Mg/H] and [Si/H] from stellar analysis.

3.3.2 Exoplanet data analysis

We model the photometric and spectroscopic data presented in Section 3.2 using the `exoplanet` package [Foreman-Mackey et al., 2021a; Foreman-Mackey et al., 2021b], which incorporates `starry` [Luger et al., 2019], `celerite` [Foreman-Mackey et al., 2017b] and `PyMC3` [Salvatier et al., 2016] within its framework. We have selected the high-quality follow-up light curves, which includes all observations from TESS and CHEOPS as our space-based photometry, one observation from NGTS, nine observations from LCOGT, one observation from ASTEP, and one observation from *MEarth* as our ground-based photometry sample (see Table 3.2). Our radial velocity modelling of short-term trends is comprised of data from HARPS and PFS.

Transit Timing Variations

In order to account for perceived transit timing variations (TTVs) on TOI-836 c in 2020 (year 2 of observation), we introduce an offset parameter T_c. This offset parameter is calculated by fitting each detrended, normalised dataset using the `EXOFAST` modelling tool [Eastman et al., 2013, 2019]. The offset parameter represents the value of the central transit time found in `EXOFAST`, and δT_c is the difference from the expected transit ephemeris. The corresponding δT_c for each transit can be found in Table 3.7. We omit offset parameters for the transits of TOI-836 b taken by LCOGT, as these observations are not of sufficient precision to allow for suitably accurate determination of the offset parameter. We omit offset parameters for the LCOGT transit of TOI-836 c on 2020 February 29 and the ASTEP transit on 2021 April 8 for these same reasons. We also choose to omit transits of both planets in the TESS light-curves that occur very close to the start and end of sectors and close to the data download gap, as they are likely to be highly affected by systematics which may affect transit timings.

We plot the resulting offset for the central transit time T_c for each of TOI-836 b and TOI-836 c in Figure 3.9. We note that there appear to be no significant TTVs in the observed transits of TOI-836 b, however in TOI-836 c we detect an offset within the T_c values ranging from approximately 20 to 30 minutes. The presence of these TTVs is supported by observations from both the space-based CHEOPS satellite and multiple ground-based facilities. These TTV measurements alone are not enough to be able to put meaningful constraints on the mass of TOI-836 c, but with further TTV monitoring it may be possible.

Radial velocity (RV)

We model the radial velocity of TOI-836 using the HARPS and PFS data simultaneously, seen in Figure 3.10. We analysed these radial velocity data with various models, including linear and quadratic drift and a third planet. None of these were able to account for the large scatter in the radial velocity measurements, and therefore we find it necessary to apply a GP model for both of our chosen datasets in order to account for stellar variability. We apply a quasi-periodic kernel (commonly used in works with similar goals, such as Osborn et al. 2021b), as implemented in `celerite`. We assign a prior probability distribution for the rotation period as a normal distribution centered around 22 days, with a standard deviation of 0.1 days, based on the results from the WASP-South periodogram.

We note that 0.1 days is likely to be an underestimation of the true uncertainty

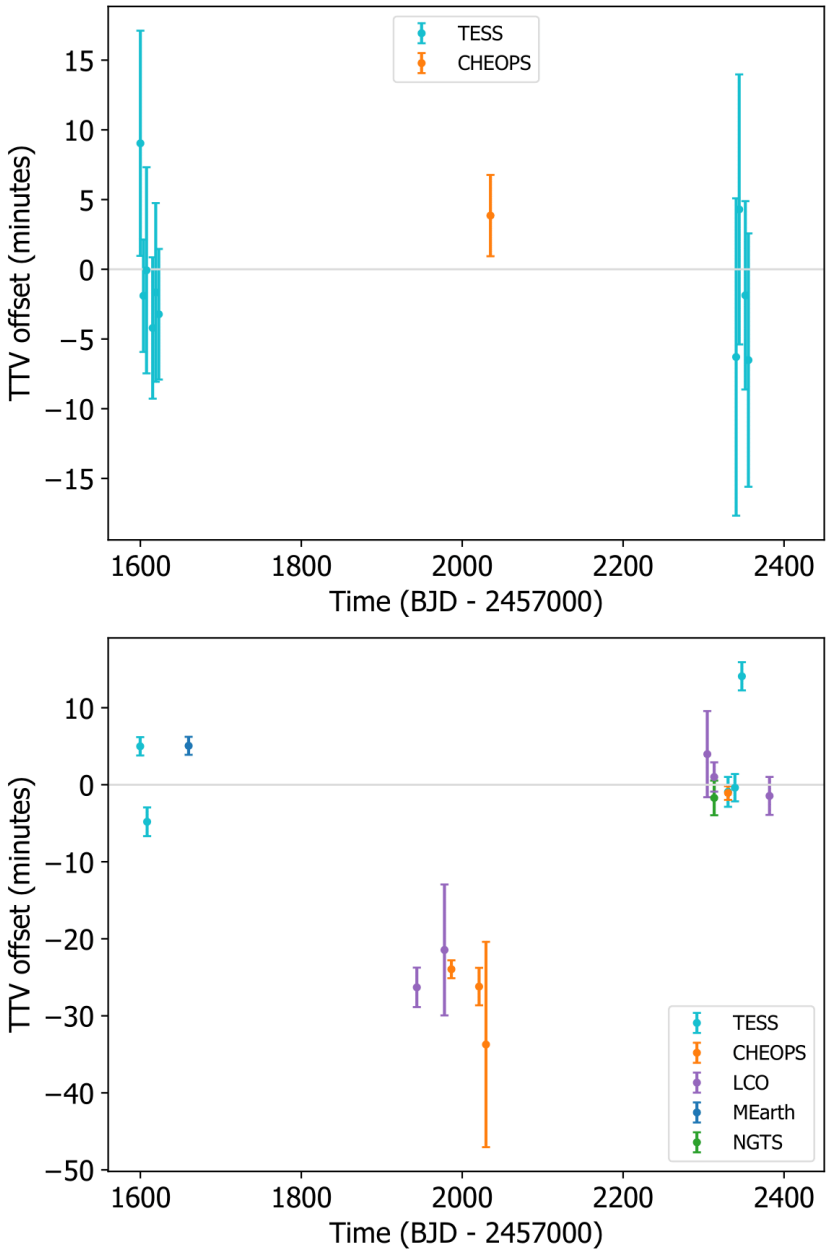

Figure 3.9: **Top panel:** Transit Timing Variations (TTVs) for each transit of TOI-836 b from the following photometry sources: TESS in turquoise and CHEOPS in yellow. **Bottom panel:** Transit Timing Variations (TTVs) for each transit of TOI-836 c from the following photometry sources: TESS in turquoise, CHEOPS in yellow, LCOGT in purple, *MEarth-South* in blue and NGTS in green.

of the stellar rotation period. It is more likely that the uncertainty for a rotation period of a relatively old, slowly-rotating host star such as this would in fact be on the order of 5-10 per cent, or approximately 1-2 days.

In completion, our kernel is a combination of two available kernels in the `PyMC3` package[6] [Salvatier et al., 2016] - the `Periodic` and `ExpQuad` kernels are multiplied to create the final quasi-periodic kernel. As part of this analysis, we define a set of GP hyperparameters which are fit concurrently for both sets of radial velocity data: η representing the GP amplitude, the stellar rotation period P, the smoothing parameter l_P and the timescale of active region evolution l_E. This has been shown to successfully model stellar activity in eg. Grunblatt et al. [2015], Santerne et al. [2018] and Osborn et al. [2021b]. The covariance function is shown in Equation 3.1:

$$k(x, x') = \eta^2 \exp\left(-\frac{\sin^2(\pi|x - x'|\frac{1}{P_{\rm rot}})}{2l_P^2} - \frac{(x - x')^2}{2l_E^2}\right). \tag{3.1}$$

When modelling the HARPS and PFS data, we utilise `exoplanet` to find values for the radial velocity semi-amplitude K with priors from 0 to 10 $\mathrm{m\,s^{-1}}$. We also fit for values for the offsets as a normal distribution centered around the mean of the radial velocity of each dataset. We also fit for jitter terms centered around the minimum radial velocity error multiplied by 2, which represent other variability not accounted for in the HARPS and PFS formal uncertainties, and the application of the GP model to the data.

Modelled planetary reflex motions are subtracted from the radial velocities at each timestamp before being passed to the GP kernel, and we use the same time system for both the HARPS and PFS data sets (BJD - 2457000). The prior distributions for each of the parameters used in the code can be found in Appendices 3.10, 3.11 and 3.12 for the host star TOI-836, and the planets TOI-836 b and TOI-836 c respectively.

Joint fitting

To bring the two observational methods together, we utilise the `exoplanet` package to fit for our initial values from the maximum log probability, which are then passed into the `PyMC3` sampler as a starting point in a No U-Turn Sampler (NUTS) variant of the Hamilton Monte Carlo (HMC) algorithm [Hoffman & Gelman, 2011]. We set our run to have a burn-in of 4000 samples, 4000 steps and 10 chains, giving our modelling significant opportunity to explore the parameter spaces.

[6] `https://docs.pymc.io/api/gp/cov.html`

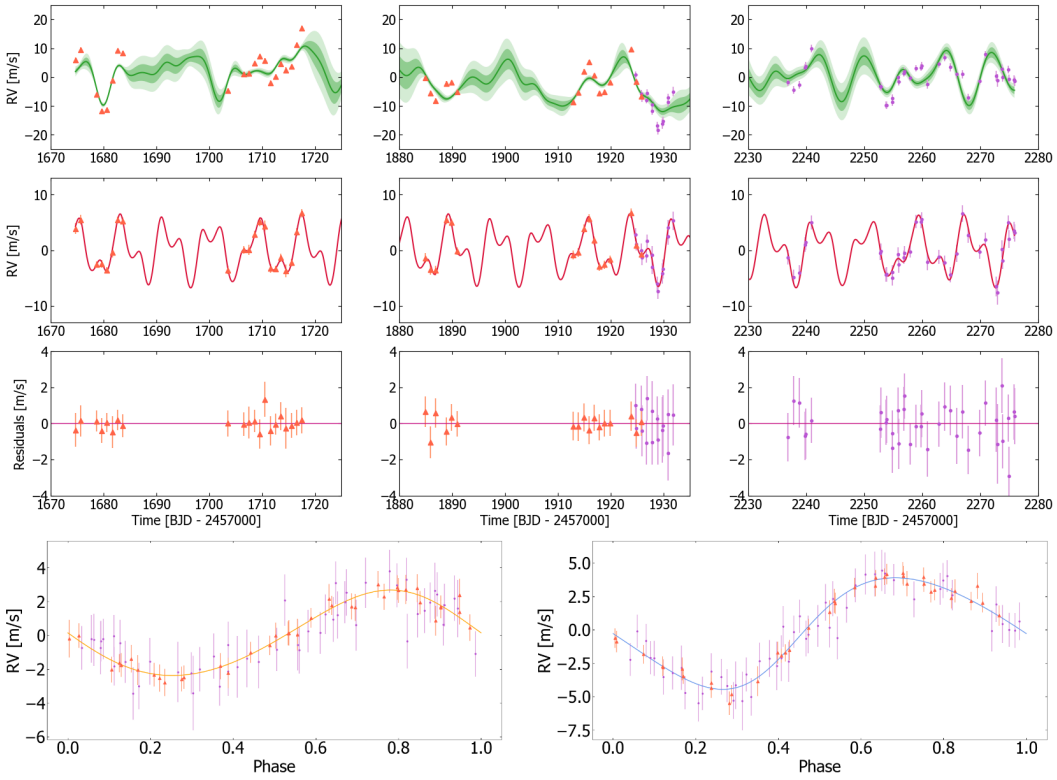

Figure 3.10: **Top panels:** HARPS (purple circles) and PFS (orange triangles) RV data with formal uncertainties with the GP model plotted as a solid green line, with 1 and 2 standard deviations in lighter shades. **Second panels:** Combined RV models of the two planets, with the GP subtracted, with HARPS and PFS RV datapoints. **Third panels:** Residuals for HARPS and PFS datapoints relative to a baseline RV of 0 $\mathrm{m\,s^{-1}}$. **Fourth panels (left):** HARPS (purple circles) and PFS (orange triangles) RV data, phase-folded to a period corresponding to that of TOI-836 b with the RV model shown in orange. **Fourth panels (right):** HARPS and PFS data, phase-folded to a period corresponding to that of TOI-836 c with the RV model shown in blue.

Table 3.6: Stellar parameters of TOI-836.

Property (unit)	**Value**	**Source**
Mass ($M_\odot$)	$0.678^{+0.049}_{-0.041}$	`exoplanet`
Radius ($R_\odot$)	0.665 ± 0.010	`exoplanet`
Density (g cm^{-3})	$3.294^{+0.079}_{-0.092}$	`exoplanet`
P_{rot} (days)	21.987 ± 0.097	`exoplanet`
LD coefficient u_1	0.039 ± 0.235	`exoplanet`
LD coefficient u_2	0.023 ± 0.335	`exoplanet`
$\log g$	4.743 ± 0.105	`ARES` + `MOOG` + *Gaia*
T_{eff} (K)	4552 ± 154	`ARES` + `MOOG`
$v \sin i_*$ (km s^{-1})	1.86 ± 0.50	`ARES` + `MOOG`
Age (Gyr)	$5.4^{+6.3}_{-5.0}$	Isochrones
Stellar abundances		
[Fe/H] (dex)	-0.284 ± -0.067	`ARES` + `MOOG`
[Mg/H] (dex)	-0.23 ± 0.17	`ARES` + `MOOG`
[Si/H] (dex)	-0.29 ± 0.20	`ARES` + `MOOG`
Galactic space velocity components		
U (km s^{-1})	-35.6 ± 0.7	*Gaia* EDR3
V (km s^{-1})	-10.7 ± 0.3	*Gaia* EDR3
W (km s^{-1})	-3.50 ± 0.5	*Gaia* EDR3

Sources: `exoplanet` [Foreman-Mackey et al., 2021a; Foreman-Mackey et al., 2021b], `ARES` [Sousa et al., 2015], `MOOG` [Sneden, 1973; Kurucz, 1993], *Gaia* [Gaia Collaboration et al., 2021]

As a result of our joint fitting of transit and radial velocity data, we find that TOI-836 b is a super-Earth planet with a radius of $1.70 \pm 0.07\,R_\oplus$ and mass of $4.5 \pm 0.9\,M_\oplus$, on a period of 3.82 days, and TOI-836 c is a sub-Neptune planet with a radius of $2.59 \pm 0.09\,R_\oplus$ and mass of $9.6 \pm 2.6\,M_\oplus$ on a period of 8.60 days. From this we can infer a bulk density of $5.02^{+0.36}_{-0.44}$ g cm^{-3} for TOI-836 b, and $3.06^{+0.47}_{-0.54}$ g cm^{-3} for TOI-836 c. A full set of parameters for TOI-836 can be found in Table 3.6, and parameters for each planet can be found in Table 3.8.

Long-term trends

In addition to our short-term radial velocity analysis with data from HARPS and PFS, we also make use of HIRES data to constrain longer-term trends. We fit the data for a linear drift, and find a drift value of $-7.95 \pm 2.14\,m\,s^{-1}\,yr^{-1}$. The fit

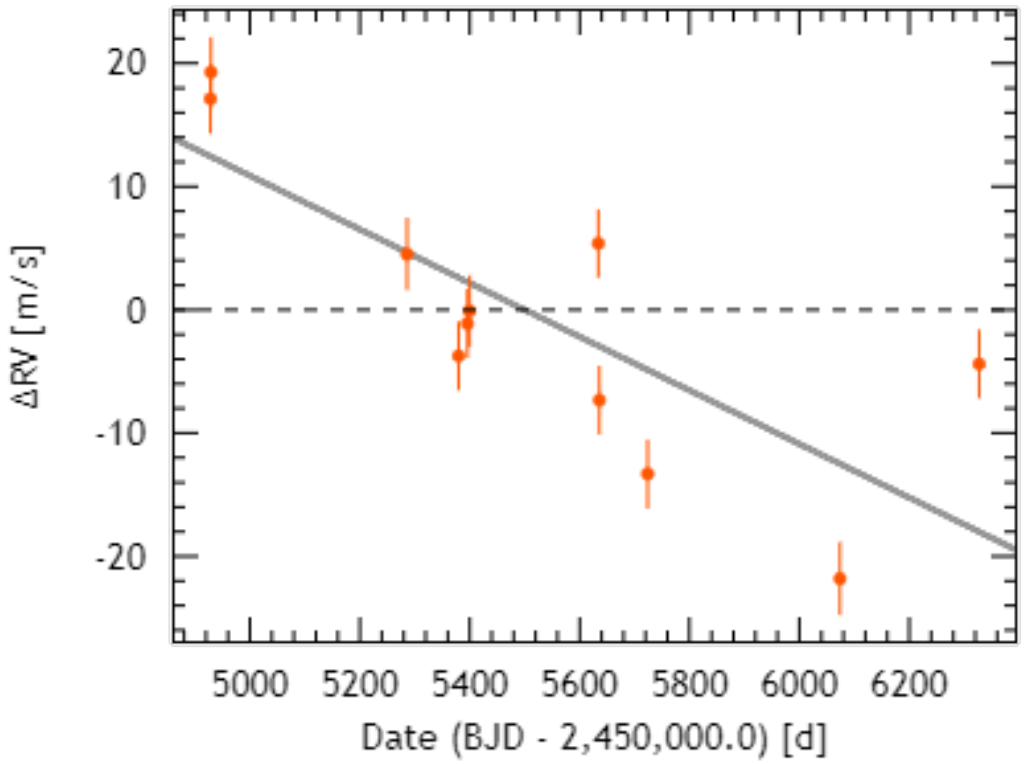

Figure 3.11: Radial velocity data of TOI-836 from the HIRES instrument on the *Keck* telescope from 2009 April 6 to 2013 February 3, and fit with a linear trend represented by the solid grey line.

is shown in Figure 3.11. The HIRES data is sparsely sampled over a duration of approximately four years. Therefore it is not possible to remove the stellar activity signal in the manner we did for the HARPS and PFS data, and so the marginally detected linear trend may not be real, and we do not use this trend when fitting the radial velocities in Section 3.3.2. However the HIRES data is able to rule out any radial velocity drift above the level of the stellar activity signal ($\sim 10\,\mathrm{m\,s^{-1}}$) over a four year time period.

3.4 Discussion

In addition to the results from our joint modelling, we find that TOI-836 has a relatively low metallicity of $[\mathrm{Fe/H}] = -0.284 \pm -0.067$ dex. As was found in Adibekyan et al. [2021], there is a strong trend between host stellar metallicity and the iron component for low-mass exoplanets. This can be interpreted as systems that formed from metal-rich proto-stellar/planetary disks have stars with metal-rich photospheres and planets with large metallic cores. This is supported by the recent study of Wilson et al. [2022] that found a correlation between sub-Neptune planet densities and stellar metallicities across all stellar types that implies that sub-Neptunes around metal-rich stars have larger metallic cores that can retain a larger atmosphere and hence appear less dense. This effect has also been observed in radius valley trends with metallicity [Chen et al., 2022]. As TOI-836 has a low-metallicity we reproduce Fig. 15 of Wilson et al. [2022] and plot the bulk densities of the two planets against the stellar metallicity in Figure 3.12, alongside a sample of planets orbiting K-dwarfs with a radius of $<4\,\mathrm{R_\oplus}$ and a density of $<15\,\mathrm{g\,cm^{-3}}$ from the NASA Exoplanet Archive. This sample of all well-characterised super-Earths and sub-Neptunes around K-dwarfs supports previous findings and strengthens the evidence that stellar composition affects planetary internal structure.

3.4.1 Positions of the planets on the mass-radius (M-R) diagram

We plot TOI-836 b and TOI-836 c on the mass-radius (M-R) diagram in Figure 3.13, using `fancy-massradius-plot`[7], alongside a sample of exoplanets from the *TEPCAT* catalog [Southworth, 2011]. It can be seen that TOI-836 b sits directly between the $MgSiO_3$ and 50% Fe–50% $MgSiO_3$ planetary composition models from Zeng et al. [2016], and TOI-836 c sits on the H_2O track. The masses and radii of TOI-836 b and TOI-836 c, along with their bulk densities, are consistent with the previously-determined populations of super-Earths and mini-Neptunes.

[7] `https://github.com/oscaribv/fancy-massradius-plot`

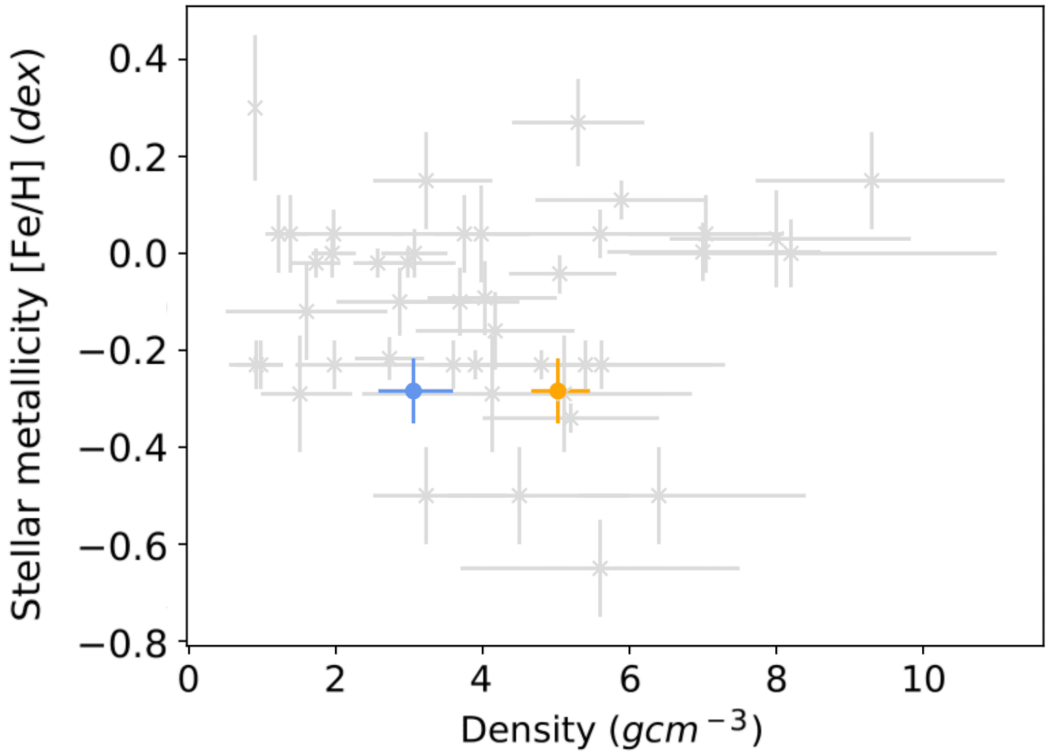

Figure 3.12: Bulk densities of TOI-836 b (orange) and TOI-836 c (blue) plotted against the stellar metallicity of TOI-836, along with a sample of planets orbiting K-dwarfs with R<4 $R_\oplus$ and ρ <15 g cm^{-3}.

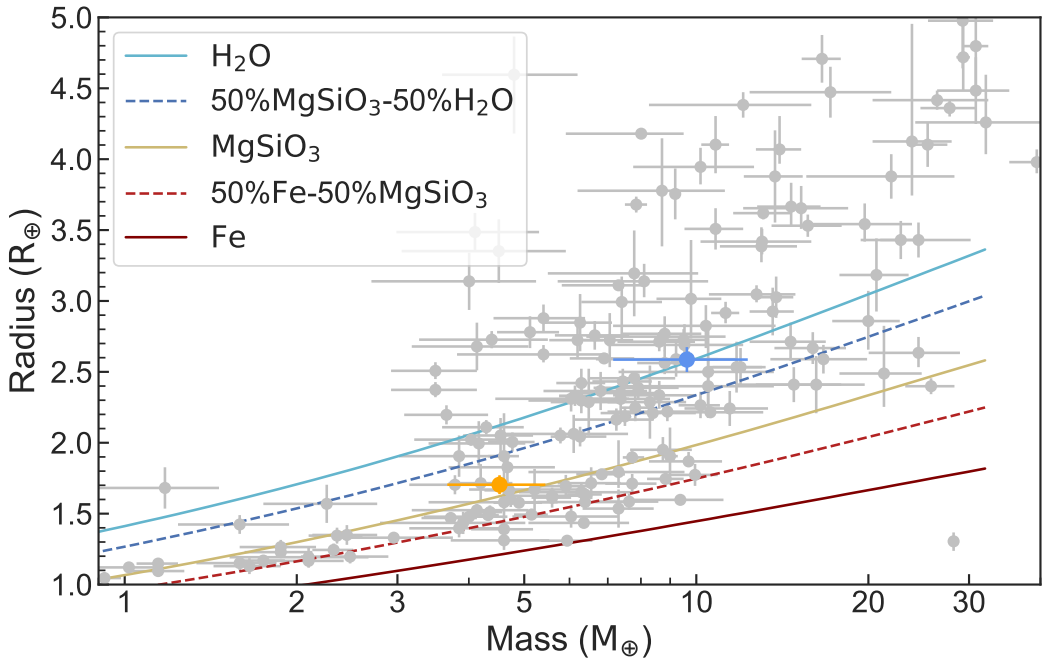

Figure 3.13: Mass-radius diagram plotted for TOI-836 b in orange and TOI-836 c with exoplanets from the *TEPCAT* catalog [Southworth, 2011] in grey and composition models from Zeng et al. [2016].

3.4.2 Internal structure modelling

Using the planetary and stellar parameters derived above, we used a Bayesian analysis to infer the internal structure of both planets. The method we use is presented in detail in Leleu et al. [2021]; we just recall here the main elements. The Bayesian analysis relies on two parts. The first one is the forward models which allows computing the planetary radius as a function of internal structure parameters, here the mass of the solid Fe/Si core, the fraction of Fe in the core, the mass of the silicate mantle and its composition (Si, Mg and Fe molar ratios), the mass of the water layer, the mass of the gas envelope (composed in this model of pure H/He), the equilibrium temperature of the planet, and its age. The second part is the Bayesian inference itself.

The details of the forward model are given in Leleu et al. [2021], we just emphasize the fact that the gaseous (H/He) part of the planet does not influence, in our model, the 'non-gas' part of the planet (core, mantle and water layer). The radius of the non-gas part is not influenced by the potential compression and thermal isolation effect from the gas envelope. The molar ratio of Fe, Si and Mg in the refractory parts of the two planets (core and mantle) are assumed to be identical and similar to the

one of the star. Note, however, that Adibekyan et al. [2021] recently showed that the stellar and planetary abundances may not be always correlated in a one-to-one relation. The water and gas mass ratio, on the other hand, are not required to be similar between the two planets. In terms of priors, we assume that the core, mantle and water mass fraction (relative to the non-gas part) are uniform (subject to the constraint that they add up to one), whereas the mass fraction of the H/He layer is assumed to be uniform in log. We point out the fact that considering, instead, a uniform prior for the H/He gas layer would translate to more gas-rich planets, and consequently less water-rich planets.

The resulting internal structure of both planets presented are summarized in Table 3.9. TOI-836 b is likely to contain a very small fraction of gas, and could have a non-negligible mass of water (although the solution with no water is also compatible with the data). TOI-836 c, on the other hand, has a much smaller density and is likely to contain more gas and/or water. We finally recall that the derived internal structure results from a Bayesian analysis, and that the distributions are of statistical nature and depend somewhat on the assumed priors.

The structure of TOI-836 b is somewhat analogous to that of TOI-1235 b [Cloutier et al., 2020], despite the difference in the host star's spectral type, and the rocky composition of the planet may support a thermally-driven or core-powered mass loss scenario rather than a gas-poor formation scenario. TOI-836 c on the other hand is a little more ambiguous, but given its insolation flux of $26.707 \pm 0.003\,S_\odot$ and radius of $2.59 \pm 0.09\,R_\oplus$, we expect a non-negligible fraction of its mass to be in gaseous form.

These two planets may also support the concept of intra-system uniformity reported by Millholland et al. [2017] and Millholland & Winn [2021], as the two planets lie close together within the mass-radius space than if two planets were to be drawn at random from the entire distribution of exoplanets according to their radii.

3.4.3 Positions of the planets compared to the radius valley

The radius valley is a bimodal distribution of planetary radii that separates super-Earths and sub-Neptunes either side of $R_p \approx 2\,R_\oplus$ [Van Eylen et al., 2018; Fulton et al., 2017], from $\approx 1.3\,R_\oplus$ and $\approx 2.6\,R_\oplus$, respectively. The radius valley is important to examine on the basis of its implications for the formation and evolution of terrestrial planets [Giacalone et al., 2022]. Some commonalities can be found within the population of super-Earths on the left side of the valley, consisting of

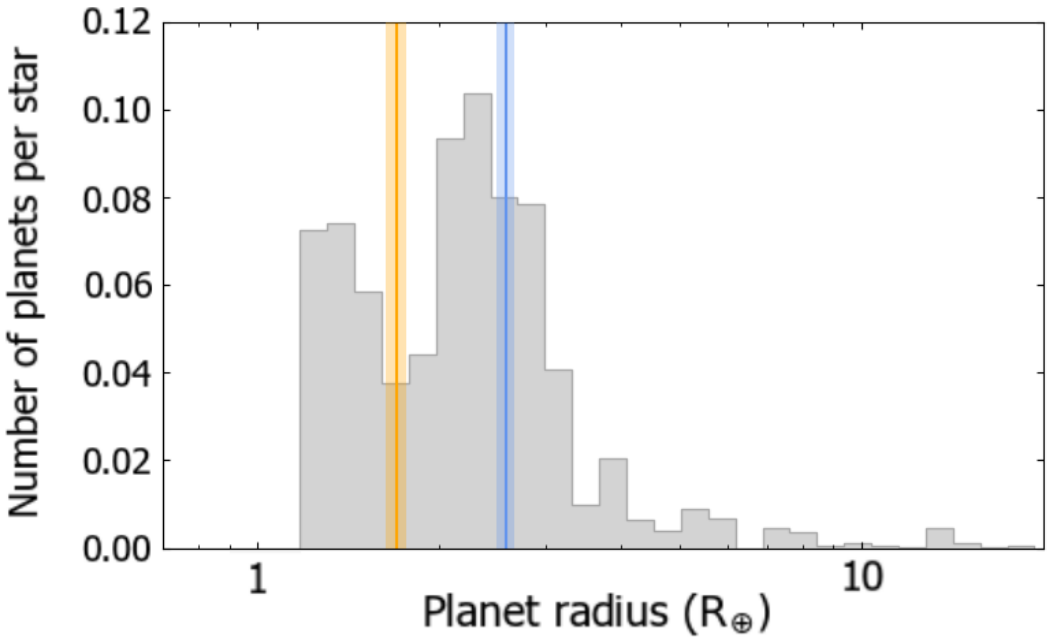

Figure 3.14: Histogram of confirmed planets with periods less than 100 days, using data from Fulton & Petigura [2018] represented in grey, overplotted with the radii of TOI-836 b in orange and TOI-836 c in blue, including 1σ standard deviations according to Table 3.8.

atmosphere-stripped rocky cores, and the population of mini-Neptunes on the right hand side, consisting of rocky cores that have retained their atmospheres [Van Eylen et al., 2021]. Many possibilities for the origin of the radius valley have been speculated, including the theory that terrestrial planets lose their atmospheres through photoevaporation [Owen & Wu, 2013; Jin & Mordasini, 2017; Van Eylen et al., 2021], mass loss due to core temperatures [Ginzburg et al., 2016], and the impacts of planetesimals [Schlichting et al., 2015].

In Figure 3.14 we plot a histogram of planets with orbital periods less than 100 days based on data from Fulton & Petigura [2018], along with the positions of TOI-836 b and TOI-836 c using the modelled values from `exoplanet` in Table 3.8. We also plot a diagram of planetary radius against the insolation fluxes in Figure 3.15, alongside a sample of the exoplanet population and the position of the radius valley as estimated by Martinez et al. [2019]. TOI-836 b can be seen to sit directly within this valley, and TOI-836 c can be seen close to the peak on the higher radius side of the valley. TOI-836 b is set at a particularly interesting location, and there may be scope for further investigation of the extent and composition of its atmosphere, especially as the host star is suspected to not be young in age (see Section 3.3.1).

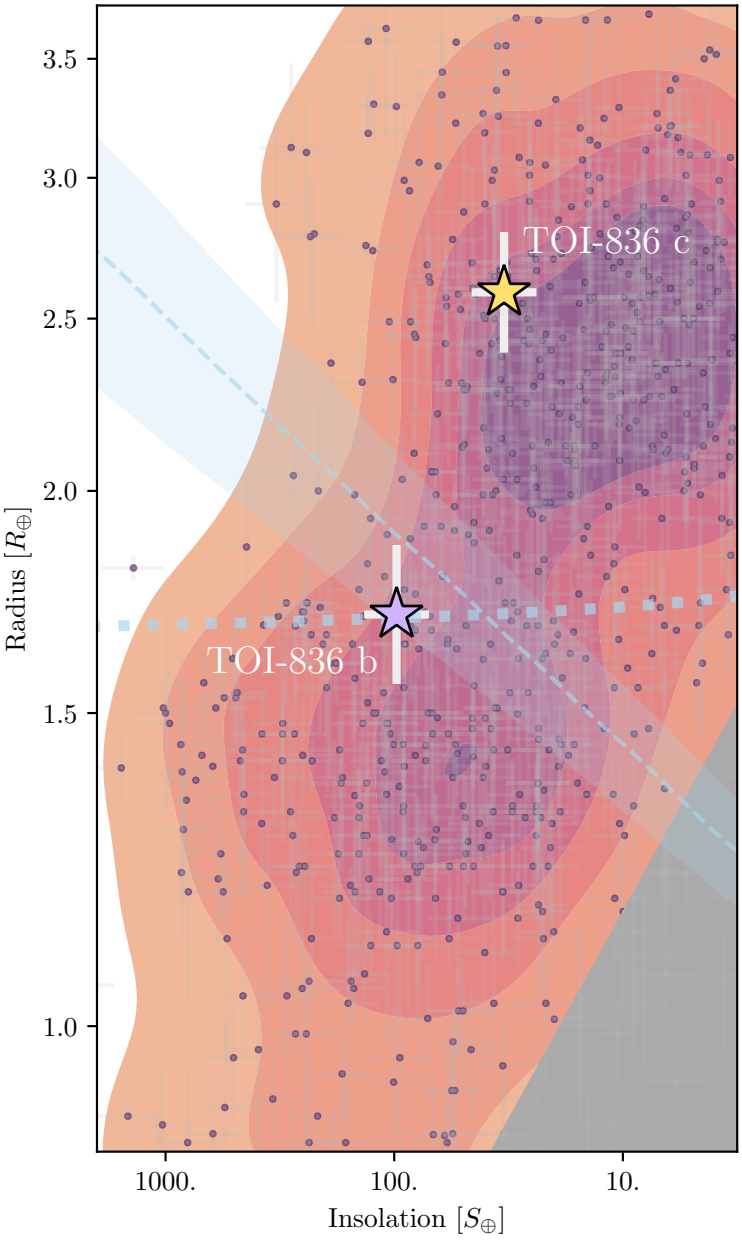

Figure 3.15: TOI-836 b and TOI-836 c (filled stars) as a function of planetary radius and insolation, compared with the population of exoplanets. Colours represent a kernel density estimation (KDE) applied to small ($R_p < 4\,R_\oplus$), transiting planets retrieved from the NASA Exoplanet Archive [Akeson et al., 2013]. The dashed line (and associated 1-σ error band) shows the estimate for the position of the evaporation valley from Martinez et al. [2019], while the dotted line shows a boundary due to gas-depleted formation derived from cool stars in *Kepler* and K2, converted to insolation using stellar parameters for TOI-836 [Cloutier & Menou, 2020].

In order to evaluate TOI-836 as a potential target for transmission spectroscopy follow-up in the era of JWST [James Webb Space Telescope; Gardner et al., 2006], we calculate a Transmission Spectroscopy Metric (TSM) for each of the planets based upon equation 1 in Kempton et al. [2018]. This value is an estimate of the observed SNR of each planet as would be achieved by the *NIRSPEC* instrument on JWST. We find a TSM for TOI-836 b of 65.7, and a TSM for TOI-836 c of 82.4 (see Table 3.8). We also note that the system has been allocated time on JWST as can be seen in Batalha et al. [2021], with the intention of further examining the atmospheric characteristics of TOI-836 b and TOI-836 c through molecular abundances. The precise masses provided in this paper will greatly help in the characterisation of the atmospheres of these planets.

3.5 Conclusion

In this paper, we have presented the TOI-836 system and the discovery of its two planets, TOI-836 b and TOI-836 c. We base our discovery upon data from two sectors of TESS data (11 and 38 from year 1 and year 3 respectively) at 2-minute cadence, and a further five space-based observations ranging from 2020 to 2021 from CHEOPS, which are complemented by ground-based photometry from the NGTS, *MEarth*, LCOGT and ASTEP facilities, with supporting evidence for a stellar rotation period of 21.99 ± 0.097 days supported by data from WASP-South. We model this photometry data jointly with radial velocity data from HARPS and PFS using the `exoplanet` package to constrain short-term trends, and HIRES data for long-term trends. We are also able to rule out the presence of blended stellar companions that may affect our photometry from an examination of the imaging from *Gemini*-Zorro. The planets orbit a K-type dwarf star with a mass of 0.68 ± 0.05 $M_\odot$ and a radius of 0.67 ± 0.01 $R_\odot$.

TOI-836 b is a super-Earth planet with a mass of $4.5 \pm 0.9\,M_\oplus$ and a radius of $1.70 \pm 0.07\,R_\oplus$, on an orbit of 3.82 days. Our internal structure modelling indicates that this planet possesses a relatively small fraction of its mass in the form of gas.

TOI-836 c is a sub-Neptune with a mass of $9.6 \pm 2.6\,M_\oplus$and a radius of $2.59 \pm 0.09\,R_\oplus$, on an orbit of 8.60 days. Our structure modelling indicates that it contains a higher proportion of gas and/or water than TOI-836 b. We also find significant Transit Timing Variations within our observations of this planet, which may indicate the presence of a third non-transiting planet in the system - however we find no transits of a third planet within our current set of photometry data, or any indication of an additional periodic signal in our current radial velocity data.

TOI-836 b appears in the centre of the radius valley, and TOI-836 c appears to sit close to the peak on the right hand side of the valley, which is an area of interest in terms of the formation and structure of terrestrial planets and the dynamics of atmospheric loss and retention. The planets also contribute to the TESS Level 1 Mission requirement, and are particularly amenable to follow-up observations in the era of JWST.

3.6 Appendix: Priors

Table 3.7: Timing offsets for observations of TOI-836 b and TOI-836 c.

Facility	**UT night**	δ**T$_c$ (days)**	δ**T$_c$ error (days)**
TOI-836 b			
TESS S11	—	0.009757	0.005609
TESS S11	—	0.002165	0.002800
TESS S11	—	0.003431	0.005132
TESS S11	—	0.000558	0.003520
TESS S11	—	0.002330	0.004450
TESS S11	—	0.001242	0.003252
LCOGT-CTIO	2020 Mar 8	—	—
LCOGT-SSO	2020 Mar 20	—	—
LCOGT-SSO	2020 May 4	—	—
CHEOPS	2020 Jul 8	0.0061575	0.002024
TESS S38	—	—	—
TESS S38	—	-0.000887	0.007903
TESS S38	—	0.006464	0.006724
TESS S38	—	—	—
TESS S38	—	0.0021850	0.004691
TESS S38	—	-0.001041	0.006310
TESS S38	—	—	—
TOI-836 c			
TESS S11	—	0.0034651	0.000826
TESS S11	—	0.0033399	0.001295
MEarth-South	2019 Jul 4	0.0035104	0.000811
LCOGT-SSO	2020 Feb 29	—	—
LCOGT-SSO	2020 Apr 12	0.0182677	0.001780
LCOGT-SAAO	2020 May 16	-0.0148950	0.005903
CHEOPS	2020 May 25	-0.0166364	0.000806
CHEOPS	2020 Jun 28	-0.0181972	0.001690
CHEOPS	2020 Jul 7	-0.0234211	0.000923
LCOGT-SSO	2021 Apr 8	0.0027583	0.003884
ASTEP	2021 Apr 8	—	—
NGTS	2021 Apr 16	-0.0011893	0.001562
LCOGT-CTIO	2021 Apr 16	0.0007001	0.001320
LCOGT-CTIO	2021 Jun 24	-0.0010068	0.001712
CHEOPS	2021 May 4	0.0007432	0.000622
TESS S38	—	-0.0006412	0.001347
TESS S38	—	-0.0002651	0.001231
TESS S38	—	0.0097779	0.001272

Sources: LCOGT [Brown et al., 2013], CHEOPS [Benz et al., 2021], ASTEP [Daban et al., 2010], NGTS [Wheatley et al., 2018], *MEarth-South* [Irwin et al., 2015b], TESS [Ricker et al., 2015]

Table 3.8: Parameters of TOI-836 b and TOI-836 c.

Property	**Value**	
	TOI-836 b	**TOI-836 c**
Identifier	TOI-836.02	TOI-836.01
Period (days)	3.81673 ± 0.00001	8.59545 ± 0.00001
Mass ($M_\oplus$)	$4.53^{+0.92}_{-0.86}$	$9.6^{+2.7}_{-2.5}$
Radius ($R_\oplus$)	1.704 ± 0.067	2.587 ± 0.088
Density (gccc)	$5.02^{+0.36}_{-0.44}$	$3.06^{+0.48}_{-0.54}$
R_p/R_*	0.0235 ± 0.0013	0.0357 ± 0.0018
T_c (TBJD)	1599.9953 ± 0.0019	1599.7623 ± 0.0008
T1-T4 duration (hours)	$1.805^{+0.222}_{-0.007}$	$2.486^{+0.161}_{-0.192}$
T2-T3 duration (hours)	$1.6823^{+0.0012}_{-0.3292}$	$2.256^{+0.144}_{-0.432}$
Impact parameter	0.58 ± 0.11	0.53 ± 0.13
K ($m\,s^{-1}$)	2.38 ± 0.35	3.86 ± 0.85
Inclination (°)	87.57 ± 0.44	88.7 ± 1.5
Semi-major axis (AU)	0.04220 ± 0.00093	0.0750 ± 0.0016
Temperature T_{eq} (K) *	871 ± 36	665 ± 27
Insolation flux ($S_\odot$)	78.838 ± 0.015	26.707 ± 0.003
Eccentricity	0.053 ± 0.042	0.078 ± 0.056
Argument of periastron (°)	9 ± 92	-28 ± 113
TSM	65.7 ± 5.8	82.4 ± 5.8

Table 3.9: Interior structure properties of TOI-836 b and TOI-836 c.

Property (unit)	**Values**	
	TOI-836 b	**TOI-836 c**
M_{core}/M_{total}	$0.12^{+0.16}_{-0.11}$	$0.10^{+0.15}_{-0.09}$
M_{water}/M_{total}	$0.18^{+0.25}_{-0.16}$	$0.33^{+0.15}_{-0.28}$
$\log(M_{gas})$	$-8.33^{+3.95}_{-3.30}$	$-1.99^{+0.93}_{-6.77}$
Fe_{core}	$0.90^{+0.09}_{-0.08}$	$0.90^{+0.09}_{-0.08}$
Si_{mantle}	$0.41^{+0.08}_{-0.07}$	$0.41^{+0.08}_{-0.07}$
Mg_{mantle}	$0.45^{+0.15}_{-0.17}$	$0.44^{+0.15}_{-0.17}$

Table 3.10: Global fit parameter prior function type and prior limits for TOI-836.

Parameter	**Prior**	**Value**
Baseline flux	$\mathcal{N}(0, 1)$	
M_* ($M_\odot$)	$\mathcal{N}(0.678, 0.049, 0.65)$	Table 3.6
R_* ($R_\odot$)	$\mathcal{N}(0.666, 0.010, 0.56)$	Table 3.6
Period (days)	$\mathcal{N}(22, 0.1)$	Table 3.6
LD coefficient u_1	Kipping [2013b]	Table 3.6
LD coefficient u_2	Kipping [2013b]	Table 3.6
TESS GP		
Sector 11		
Mean	$\mathcal{N}(0, 1)$	0.00006 ± 0.00021
log($s2$)	$\mathcal{N}$(-14.704*, 0.1)	-14.98064 ± 0.01205
log($w0$)	$\mathcal{N}(0, 0.1)$	0.10400 ± 0.09697
log($Sw4$)	$\mathcal{N}$(-14.704*, 0.1)	-14.12245 ± 0.09004
Sector 38		
Mean	$\mathcal{N}(0, 1)$	0.00008 ± 0.00031
log($s2$)	$\mathcal{N}$(-13.903*, 0.1)	-14.86420 ± 0.01063
log($w0$)	$\mathcal{N}(0, 0.05)$	0.00736 ± 0.04815
log($Sw4$)	$\mathcal{N}$(-13.903*, 0.1)	-13.47408 ± 0.04995
RV GP		
Amplitude	$\mathcal{C}(5)$	7.13782 ± 1.05463
l_E	$\mathcal{T}(22, 20, 20)$	31.59616 ± 5.63098
l_P	$\mathcal{T}(0.1, 10, 0, 1)$	0.21018 ± 0.02573
HARPS offset	$\mathcal{N}$(-26274.131†,10)	-26144.6 ± 2622.4
$\log(\text{Jitter})_{\text{HARPS}}$	$\mathcal{N}$(0.247‡,5)	-3.01818 ± 3.12178
PFS offset	$\mathcal{N}$(0.403†,10)	-0.75678 ± 1.72435
$\log(\text{Jitter})_{\text{PFS}}$	$\mathcal{N}$(-1.270‡,5)	-1.51981 ± 3.07024

Prior distributions:
(lower limit x, upper limit y) for uniform distribution $\mathcal{U}(x,y)$
(mean μ, standard deviation σ, test value α) for normal distribution $\mathcal{N}(\mu,\sigma,\alpha)$
(mean μ, standard deviation σ, lower limit x, upper limit y) for truncated normal distribution $\mathcal{T}(\mu,\sigma,x,y)$
(scale parameter β) for half-Cauchy distribution $\mathcal{C}(\beta)$
Prior values:
* Equivalent to the log of the variance of the TESS flux from the corresponding sector
† Equivalent to the mean of the radial velocity from the corresponding spectrographs
‡ Equivalent to 2 times the log of the minimum radial velocity error from the corresponding spectrographs

Table 3.11: Global fit parameter prior function type and prior limits for TOI-836 b.

Parameter	Prior
TOI-836 b	
Period (days)	$\mathcal{U}$(3.7, 3.9)
Transit ephemeris (TBJD)	$\mathcal{U}$(2458599.98, 2458600.03)
K_{RV} ($\mathrm{m\,s^{-1}}$)	$\mathcal{U}$(0, 10)
log(R_p)	$\mathcal{N}$(-4.062§, 1)
b	$\mathcal{U}$(0, 1)
e	Kipping [2013a], $\mathcal{B}$(e, 0.867, 3.03)
ω (rad)	$\mathcal{U}(-\pi, \pi)$

Numbers in brackets represent:
(lower limit x, upper limit y) for uniform distribution $\mathcal{U}(x,y)$
(mean μ, standard deviation σ, test value α) for normal distribution $\mathcal{N}(\mu,\sigma,\alpha)$
Distributions for eccentricity e are built into the `exoplanet` package and based on Kipping [2013a] which includes the Beta distribution $\mathcal{B}$(e,a,b) (exponential e, shape parameter a, shape parameter b)
§ Equivalent to $0.5\times\log(\delta)+\log(\mathrm{R}_*)$, δ represents transit depth (based on ExoFOP catalog values)

Table 3.12: Global fit parameter prior function type and prior limits for TOI-836 c.

Parameter	Prior
TOI-836 c	
Period (days)	$\mathcal{U}$(8.5, 8.7)
Transit ephemeris (TBJD)	$\mathcal{U}$(2458599.74, 2458599.79)
K_{RV} ($\mathrm{m\,s^{-1}}$)	$\mathcal{U}$(0, 10)
log(R_p)	$\mathcal{N}$(-3.701§, 1)
b	$\mathcal{U}$(0, 1)
e	Kipping [2013a], $\mathcal{B}$(e, 0.867, 3.03)
ω (rad)	$\mathcal{U}(-\pi, \pi)$

Numbers in brackets represent:
(lower limit x, upper limit y) for uniform distribution $\mathcal{U}(x,y)$
(mean μ, standard deviation σ, test value α) for normal distribution $\mathcal{N}(\mu,\sigma,\alpha)$
Distributions for eccentricity e are built into the `exoplanet` package and based on Kipping [2013a] which includes the Beta distribution $\mathcal{B}$(e,a,b) (exponential e, shape parameter a, shape parameter b)
§ Equivalent to $0.5\times\log(\delta)+\log(\mathrm{R}_*)$, δ represents transit depth (based on ExoFOP catalog values)

Chapter 4

TOI-908: a planet at the edge of the Neptune desert transiting a G-type star

"Across your face / I see what you are / You want to kill the Sun / To blot out the stars."

'The Blue', Acid Bath, 1994, Riggs/Sanchez/Duet/Pitre/Kyle

Note

This chapter is a reproduction of the publication 'TOI-908: a planet at the edge of the Neptune desert transiting a G-type star' (Hawthorn et al. 2023b), originally published in Monthly Notices of the Royal Astronomical Society (MNRAS) in September 2023 with very minor edits. The majority of the writing and analysis of the paper was performed by the author, with contributions to observational data and sections of analysis made by external collaborators.

Abstract

We present the discovery of an exoplanet transiting TOI-908 (TIC-350153977) using data from TESS sectors 1, 12, 13, 27, 28 and 39. TOI-908 is a $T = 10.7$ mag G-dwarf ($T_{eff} = 5626 \pm 61$ K) solar-like star with a mass of $0.950 \pm 0.010\,M_{\odot}$ and a

radius of $1.028 \pm 0.030\,R_\odot$. The planet, TOI-908 b, is a $3.18 \pm 0.16\,R_\oplus$ planet in a 3.18 day orbit. Radial velocity measurements from HARPS reveal TOI-908 b has a mass of approximately $16.1 \pm 4.1\,M_\oplus$, resulting in a bulk planetary density of $2.7^{+0.2}_{-0.4}\,g\,cm^{-3}$. TOI-908 b lies in a sparsely-populated region of parameter space known as the Neptune desert. The planet likely began its life as a sub-Saturn planet before it experienced significant photoevaporation due to X-rays and extreme ultraviolet radiation from its host star, and is likely to continue evaporating, losing a significant fraction of its residual envelope mass.

4.1 Introduction

In the years since *Kepler* [Borucki et al., 2010] and during the lifetime of the TESS mission [Ricker et al., 2015], a distinct dearth of exoplanets between $3 < R_\oplus < 4$ with orbital periods less than ~ 5 days has been discovered, the so-called 'Neptune desert', 'evaporation desert' or 'sub-Jovian desert' [Szabó & Kiss, 2011; Owen & Lai, 2018; Mazeh et al., 2016]. Several theories have been made to explain this sparse parameter space - including that these relatively low-mass planets have had their gaseous H/He envelopes stripped away by high levels of irradiation from their host stars [Owen & Wu, 2017], leaving behind a dense core (eg. TOI-849 b; Armstrong et al. 2020), whilst some are still undergoing this process (eg. LTT 9779 b, Jenkins et al. 2020; NGTS-4 b, West et al. 2019; TOI-969 b, Lillo-Box et al. 2022).
Many of these planets are readily observable with missions such as TESS and JWST, and also with ground-based spectroscopic instruments such as HARPS [Pepe et al., 2002] and *ESPRESSO* [Pepe et al., 2021] due to their close orbits and short periods. The HARPS-NOMADS program (PI Armstrong, 1108.C-0697) aims to significantly increase the number of planet confirmations in the Neptune desert with precise masses and radii. In this paper we present one such detection of TOI-908 b, a sub-Neptune transiting a G-type star. Precise measurements of these parameters is highly important in allowing us to constrain the density and internal structure of these planets, assisting in our understanding of the formation and evolution mechanisms that place these planets in the desert.
This paper is structured as follows: we present our observations of TOI-908 from TESS and LCOGT photometry, HARPS spectroscopy and SOAR-HRCam imaging in Section 4.2, our stellar analysis and global joint modelling of the data in Section 4.3, and our results and discussion of our findings in Section 4.4, including the position of the planet in the Neptune desert and the evolution of its envelope. We finally present our conclusions in Section 4.5.

4.2 Observations

4.2.1 TESS photometry

TESS is a space-based NASA telescope that is currently performing a survey search for transiting exoplanets around bright host stars. It is equipped with four cameras for a total combined FOV (Field-Of-View) of 24 × 96°. It splits the sky into 13 sectors per hemisphere, each of which is observed for approximately 27 days, making TESS a key mission in detecting short-period transiting exoplanets. TESS observed the bright star TOI-908 (TIC-350153977) in sectors 1, 12 and 13 during Cycle 1 of operation (2018-07-25 to 2019-07-17) at a cadence of 30 minutes, and sectors 27, 28 and 39 during Cycle 3 (2020-07-05 to 2021-06-24) at a cadence of 10 minutes. The target location at a declination of approximately -81° means it lies close to the TESS Continuous Viewing Zone (CVZ), and therefore also close to the CVZ of JWST. TOI-908 is a $T = 10.7$ mag G-dwarf with an effective temperature of 5626 ± 61 K (see Section 4.3.1). Details of TOI-908 including identifiers, astrometric and photometric properties are presented in Table 4.1, and a full list of the TESS sector details are set out in Table 4.2. We present the Target Pixel File (TPF; created with TPFPLOTTER[1] from Aller et al. 2020) in Figure 4.1 with TOI-908 as the central object with *Gaia* DR2 sources, scaled magnitudes for each object ranked by distance from TOI-908 and the aperture mask used for photometry extraction with a TIC contamination ratio of 0.040531.

The candidate was alerted as a TOI (TESS Object of Interest, Guerrero et al. 2021) and designated TOI-908.01 (hereafter TOI-908 b), based on the identification of a 3.18 day transit signal from the SPOC pipeline [Jenkins, 2002; Jenkins et al., 2010, 2020]. This pipeline uses the PDCSAP [Presearch Data Conditioning Simple Aperture Photometry; Stumpe et al., 2012, 2014; Smith et al., 2012] light-curves from the TESS HLSP (High Level Science Products), which removes instrumental and some stellar trends from the SAP (Simple Aperture Photometry) data, but retains local features such as transits. The transits of TOI-908 b passed the diagnostic tests after fitting with a limb-darkened transit model [Li et al., 2019] and were reported in the Data Validation Report [Twicken et al., 2018]. The PDCSAP light-curves are used in the joint model described in Section 4.3.2. We present the normalised light curves from each Sector of TESS along with the generated best-fitting transit models for TOI-908 b in Figure 4.2.

[1] `https://github.com/jlillo/tpfplotter`

Table 4.1: Stellar parameters of TOI-908.

Property	**Value**	**Source**
Identifiers		
TIC ID	TIC-350153977	TICv8
2MASS ID	J03323821-81150267	2MASS
Gaia ID	4619238087059206784 2	*Gaia* DR3
Astrometric properties		
R.A. (J2015.5)	$03^{\mathrm{h}}32^{\mathrm{m}}38.26^{\mathrm{s}}$	*Gaia* DR3
Dec (J2015.5)	$-81^{\circ}\ 15'02.68''$	*Gaia* DR3
Parallax (mas)	5.686 ± 0.010	*Gaia* DR3
Distance (pc)	$175.70^{+4.22}_{-0.59}$	
$\mu_{\mathrm{R.A.}}$ (mas yr^{-1})	5.898 ± 0.013	*Gaia* DR3
μ_{Dec} (mas yr^{-1})	-0.353 ± 0.015	*Gaia* DR3
μ_{Total} (mas yr^{-1})	5.909 ± 0.012	*Gaia* DR3
$\mathrm{RV_{sys}}$ (km s^{-1})	9.071 ± 0.347	*Gaia* DR3
Gaia non-single star flag	0*	*Gaia* DR3
Photometric properties		
TESS (mag)	10.651 ± 0.006	TICv8
B (mag)	12.005 ± 0.169	APASS
V (mag)	11.316 ± 0.012	APASS
G (mag)	11.1061 ± 0.0004	*Gaia* DR3
J (mag)	10.04 ± 0.02	TICv8
H (mag)	9.734 ± 0.026	TICv8
K (mag)	9.637 ± 0.021	TICv8
Gaia BP (mag)	11.4711 ± 0.0009	*Gaia* DR2
Gaia RP (mag)	10.6024 ± 0.8146	*Gaia* DR2

Sources: TICv8 [Stassun et al., 2019], 2MASS [Skrutskie et al., 2006], *Gaia* Data Release 3 [Brown et al., 2018], APASS [Henden et al., 2016], *Gaia* Data Release 2 [Gaia Collaboration et al., 2018]

* Indicates that the star does not belong to an astrometric, spectroscopic or eclipsing binary.

Table 4.2: Photometric observations of TOI-908.

Instrument	Aperture	Filter	Exposure time (s)	No. of images	UT night	Detrending	TTV (mins)
TESS S01	0.105 m	TESS[1]	1800	1337	2018 Jul 25 - 2018 Aug 22	GP model	$-0.2^{+2.4}_{-2.2}$*
TESS S12	0.105 m	TESS	1800	1340	2019 May 21 - 2019 Jun 18	GP model	$5.2^{+2.8}_{-4.3}$
TESS S13	0.105 m	TESS	1800	1365	2019 Jun 19 - 2019 Jul 17	GP model	$-0.2^{+2.2}_{-2.6}$
LCOGT-CTIO[A]	1.0 m	z_s[2]	35	302	2019 Sep 08	Time, losses	$-12.3^{+4.2}_{-3.8}$
LCOGT-SAAO[B]	1.0 m	z_s	35	252	2019 Dec 31	Time, losses	$-8.2^{+8.8}_{-6.7}$
TESS S27	0.105 m	TESS	600	3508	2020 Jul 05 - 2020 Jul 30	GP model	$-7.3^{+2.7}_{-3.2}$
TESS S28	0.105 m	TESS	600	3636	2020 Jul 31 - 2020 Aug 25	GP model	$4.7^{+4.3}_{-1.3}$
LCOGT-SAAO	1.0 m	z_s	35	227	2020 Sep 17	Airmass	$-17.3^{+9.5}_{-4.5}$
LCOGT-CTIO	1.0 m	z_s	35	176	2020 Nov 30	x-centroid	$-7.5^{+14.2}_{-7.8}$
LCOGT-CTIO	1.0 m	i_p[3]	20	308	2020 Dec 16	x-centroid, losses	$-5.1^{+8.8}_{-10.9}$
TESS S39	0.105 m	TESS	120	4024	2021 May 27	GP model	$0.9^{+1.3}_{-3.1}$

[1]TESS custom, 600–1000 nm [2]PanSTARRS z-short, $\lambda_{\rm mid} = 8700$ nm, $\delta\lambda = 1040$ nm [3]SDSS i', $\lambda_{\rm mid} = 7545$ nm, $\delta\lambda = 1290$ nm

[A]CTIO - Cerro Tololo Inter-American Observatory [B]SAAO - South Africa Astronomical Observatory

* Average TTV per TESS sector, calculated using $T_c = 2384.292 \pm 0.002$ TBJD and $P = 3.183792 \pm 0.000007$ days

See Table 4.13 for full table of TESS TTVs.

4.2.2 LCOGT follow-up photometry

The LCOGT [Las Cumbres Observatory Global Telescope network; Brown et al., 2013] was used to take a total of five time-series transit photometry observations of TOI-908, each of which is detailed in Table 4.2. We used the TESS Transit Finder, which is a customized version of the Tapir software package [Jensen, 2013], to schedule our transit observations. Each of the telescopes has a $26'' \times 26''$ FOV from 4096×4096 SINISTRO cameras with an image scale of 0.389"pix^{-1}, and observations were taken in the SDSS *i'* and PanSTARRS *z*-short bands. The LCOGT image data were processed using the standard BANZAI data reduction pipeline presented in McCully et al. [2018], and photometric data were extracted with the AstroImageJ analysis software detailed in Collins et al. [2017] using circular photometric apertures with radii 7.0" or smaller, which exclude flux from the nearest known Gaia DR3 star 13.5" northwest of TOI-908. Parametric detrending vectors were selected by jointly fitting a transit model and linear combinations of zero, one, or two detrending parameters from the available detrending vectors airmass, time, sky-background, FWHM, x-centroid, y-centroid, and total comparison star counts (a proxy for atmospheric losses). The best zero, one, or two detrend vectors were retained if they improved the Bayesian information criterion (BIC) for the fit by at least a factor of two per detrend parameter. The detrending vectors selected for each light curve are shown in Table 4.2. The LCOGT light-curves are used in the joint model in Section 4.3.2. A ∼900 ppm transit-like event was detected in the follow-up light curves (see Section 4.4), confirming that the TESS-detected signal occurs on TOI-908 relative to known *Gaia* DR3 stars. The LCOGT data is publicly available on the ExoFOP-*TESS* website[2]. We present the light curves and best-fitting transit models from LCOGT in Figure 4.3.

4.2.3 HARPS radial velocity observations

We obtained 42 spectra with the High Accuracy Radial velocity Planet Searcher [HARPS; Pepe et al., 2002]. HARPS is an echelle spectrograph mounted on the 3.6 m ESO telescope at La Silla Observatory, Chile, capable of stabilised high-resolution measurements (R∼115,000) at $\sim 1\,\mathrm{m\,s^{-1}}$ precision [Pepe et al., 2002]. These spectra were obtained through the HARPS-NOMADS program (PI Armstrong, 1108.C-0697) from 2021-10-15 to 2022-01-26 in High Accuracy Mode (HAM) with a fibre diameter of 1" and an exposure time of 1800 s, leading to a typical signal-to-noise of 40–50 per pixel at a wavelength of 550 nm. The raw HARPS data are processed

[2] `https://exofop.ipac.caltech.edu/tess/`

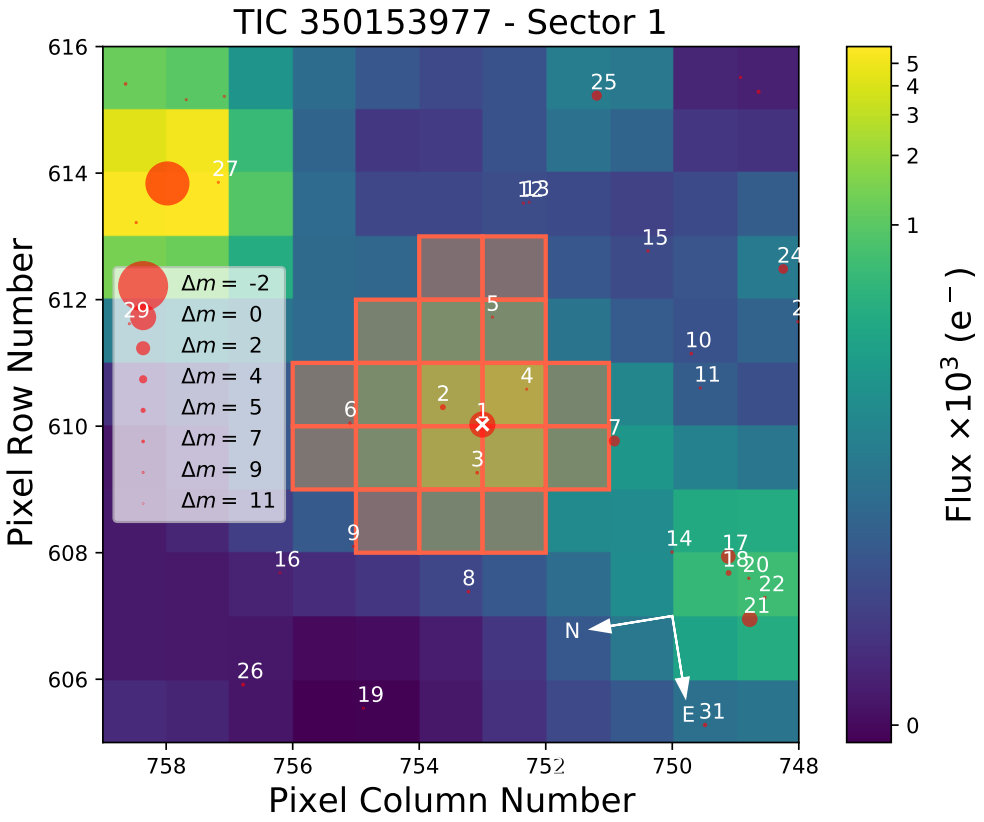

Figure 4.1: Target Pixel File (TPF) from TESS sector 1 with TOI-908 marked with a white cross. Other sources from *Gaia* DR2 are marked with red circles sized by scaled magnitudes relative to the target, ranked by distance. The aperture mask is indicated by the red outline.

using the standard data reduction pipeline presented in Lovis & Pepe [2007] using the G2 spectral mask, which also includes measurements of the Full Width Half Maximum (FWHM), the line bisector span, the contrast of the Cross-Correlation Function (CCF) and the standard activity indicators of S-index, Hα-index, Na-index and Ca-index.

Table 4.3: HARPS spectroscopic data for TOI-908. This table is available in its entirety online.

Time (BJD -2457000)	**RV ($m\,s^{-1}$)**	**RV error ($m\,s^{-1}$)**	**FWHM ($m\,s^{-1}$)**	**FWHM error ($m\,s^{-1}$)**	**Bisector ($m\,s^{-1}$)**	**Bisector error ($m\,s^{-1}$)**	**Contrast**	**Contrast error**	**S-index$_{MW}$**	**S-index$_{MW}$ error**
2502.6901	9091.80	3.25	7074.23	10.00	-21.19	4.60	49.379401	0.000001	0.15	0.01
2503.7151	9106.48	2.92	7080.40	10.01	-19.09	4.12	49.346258	0.000001	0.15	0.01
2504.7080	9109.55	2.43	7067.72	10.00	-20.01	3.43	49.306873	0.000001	0.16	0.01
2505.6817	9096.90	2.92	7063.40	9.989	-30.19	4.13	49.292743	0.000001	0.14	0.01
2505.7989	9095.50	2.50	7067.65	10.00	-31.01	3.53	49.280238	0.000001	0.16	0.01
...	...	...	...	...	...	...	...	...	...	...

It should also be noted that these data were obtained at relatively higher airmasses (∼1.66) due to the on-sky position and the low declination of the target. These data are used in the RV (Radial Velocity) component of our joint model (Section 4.3.2), and the data are presented in Table 4.3. Our radial velocity data from HARPS is shown in its entirety in Figure 4.4 along with the fitted GP model and residuals, and the same data phase folded to the period of TOI-908 b is displayed in Figure 4.5. We present the Lomb-Scargle periodograms of the data presented in Table 4.3 in Figure 4.6 and compare each to the orbital period and period aliases of TOI-908 b. The periodograms of the additional activity indicators mentioned previously and their values are presented in Figure 4.16 and Table 4.12 respectively. We find additional periodicities above the 1% False Alarm Probability (FAP) line in the CCF contrast, S-index, Na-index and Ca-index, however due to the large uncertainty in the fitted stellar rotational period we cannot attribute these periodicities to this feature, and we encourage further monitoring of the spectroscopic radial velocity of the system.

4.2.4 SOAR-HRCam speckle imaging

To check for stellar companions to TOI-836 that may be blended into the photometric data due to the comparatively large TESS pixel scale of 21", SOAR [SOuthern Astrophysical Research telescope; Tokovinin, 2018] speckle imaging observations of the target were taken on 2019-10-16 in the Cousins-I filter at a resolution of 36 mas [Ziegler et al., 2020]. We show the 5-σ sensitivity limit and Auto-Correlation Functions (ACF) for the observations in Figure 4.7, and detect no contaminating sources within 3" of the target.

4.3 Analysis

4.3.1 Stellar analysis

To derive the stellar spectroscopic parameters (T_{eff}, $\log g$, microturbulence, [Fe/H]) we used ARES+MOOG following the same methodology described in Sousa et al. [2021]; Sousa [2014]; Santos et al. [2013]. The latest version of ARES[3] [Sousa et al., 2007, 2015] was used to measure the equivalent widths (EW) of iron lines on the combined spectrum of TOI-908. We then use a minimization process to find ionization and excitation equilibrium and converge to the best set of spectroscopic parameters. This process makes use of a grid of Kurucz model atmospheres [Kurucz & Bell, 1995] and the radiative transfer code MOOG [Sneden, 1973]. We also derived

[3]The latest version, ARES v2, can be downloaded at `https://github.com/sousasag/ARES`.

a more accurate trigonometric surface gravity using recent *Gaia* data following the same procedure as described in Sousa et al. [2021].
Stellar abundances of the elements were derived using the classical curve-of-growth analysis method assuming local thermodynamic equilibrium and with the same codes and models that were used for the stellar parameters determinations. For the derivation of chemical abundances of refractory elements we closely followed the methods described in [e.g. Adibekyan et al., 2012, 2015; Delgado Mena et al., 2017]. Abundances of the volatile elements, C and O, were derived following the method of Delgado Mena et al. [2021]; Bertran de Lis et al. [2015]. All the abundance ratios [X/H] are obtained by doing a differential analysis with respect to a high S/N solar (Vesta) spectrum from HARPS. The final abundances, shown in Table 4.4, are typical of a galactic thin-disk star. Moreover, we used the chemical abundances of some elements to derive ages through the so-called chemical clocks (i.e. certain chemical abundance ratios which have a strong correlation for age). We applied the 3D formulas described in table 10 of Delgado Mena et al. [2019], which also consider the variation in age produced by the effective temperature and iron abundance. The chemical clocks [Y/Mg], [Y/Zn], [Y/Ti], [Y/Si], [Y/Al], [Sr/Ti], [Sr/Mg] and [Sr/Si] were used from which we obtain a weighted average age of 4.6 ± 1.5 Gyr.

4.3.2 Joint modelling

We use the EXOPLANET [Foreman-Mackey et al., 2021a; Foreman-Mackey et al., 2021b] code framework to jointly model the photometric and spectroscopic data for TOI-908 detailed in Section 4.2. EXOPLANET incorporates the packages STARRY [Luger et al., 2019], PyMC3 [Salvatier et al., 2016] and CELERITE [Foreman-Mackey et al., 2017b]. Our photometry data subset contains all observations presented in Table 4.2, and our RV data subset consists of the HARPS observations presented in Section 4.2.3, all of which have been converted to the TBJD time system (TESS Barycentric Julian Date; BJD - 2457000) for uniformity. To create a complete model which incorporates all observations and the GP (Gaussian Process) models for each, outlined further in Sections 4.3.2 and 4.3.2 below, we obtain our initial fit values from the maximum log probability of the PyMC3 model, and then use these values as the starting point to draw samples from the posterior distribution using a NUTS (No U-Turn Sampler) variant of the HMC [Hamilton Monte Carlo; Hoffman & Gelman, 2011] algorithm. We use a burn-in of 4000 samples which are discarded, 4000 steps and 10 chains, which gives our model good convergence without excessive computation time. The prior distributions implemented and their resulting fit values can be found in Table 4.8 for TOI-908, and Table 4.9 for TOI-908 b. The priors and

resulting fit values for the TESS GP parameters can be found in Table 4.10.

Light curve detrending

To remove residual effects of stellar variability on the TESS light curves that were not fully removed by the PDCSAP algorithm, we use a GP (Gaussian Process) model on each of the six Sectors of data using the CELERITE and PyMC3 packages. This GP model is defined by three hyper-parameters for each TESS Sector, with $\log(s2)$ describing the excess white noise in the data, and $\log(\omega 0)$ and $\log(S\omega 4)$ representing the non-periodic components of stellar variability in the light-curves [Salvatier et al., 2016]. These parameters are passed into the SHOTerm kernel in the EXOPLANET framework, which represents a stochastically-driven simple harmonic oscillator [Foreman-Mackey et al., 2021a]. The effect of these GP models can be seen in Figure 4.17, and the corresponding equation is presented in Equation 4.1, where $S_0\omega_0^4$ represents the $S\omega 4$ term as described above and $Q = \frac{1}{\sqrt{2}}$,

$$S(\omega) = \sqrt{\frac{2}{\pi}} \frac{S_0\omega_0^4}{(\omega^2 - \omega_0^2)^2 + \omega_0^2\omega^2/Q}. \tag{4.1}$$

We normalise each of our follow-up photometry observations from LCOGT by dividing each light-curve by the median of the out-of-transit flux and subtracting the mean of the out-of-transit flux. We find no need to apply a GP model to these light-curves due to the shorter baselines of the observations over the course of a single transit.

Each of the transits from the photometry data are modelled within the EXOPLANET code as a Keplerian orbit following the formalisation of Kipping [2013b], defined by the stellar parameters of radius (R_*) and mass (M_*) in Solar units, and the planetary parameters of orbital period (P) in days, central transit ephemeris (T_c) in TBJD (BJD-2457000), impact parameter (b), eccentricity (e) and argument of periastron (ω) in radians, including the limb-darkening coefficients u_1 and u_2. A set of transit models for each data set is generated using the STARRY package contained in EXOPLANET, which also incorporates the planetary radius (R_p) and exposure times for each instrument (see Table 4.2).

Radial velocity (RV) detrending

We first examine the HARPS radial velocity data (mean error $2.79\,\mathrm{m\,s^{-1}}$) using the DACE[4] platform, in which we find two significant periodic signals above the level of

[4]DACE is accessible at: `https://dace.unige.ch/`.

the 1% analytical FAP (False Alarm Probability) that are not aliases of each other (Figure 4.10). We find the planetary signal of TOI-908 b on a period of 3.182 days with a predicted radial velocity semi-amplitude K of $7.72\,\mathrm{m\,s^{-1}}$, and a secondary periodic signal at 19.29 days with a semi-amplitude of $7.25\,\mathrm{m\,s^{-1}}$ after removal of the planetary signal in DACE. We also calculate a rotational period of $20.53^{+6.77}_{-4.06}$ days based on a measured $v \sin i_*$ of $2.56 \pm 0.64\,\mathrm{km\,s^{-1}}$(Table 4.4, Section 4.3.1), and as the peak periodic signal from DACE falls within this tolerance, we attribute it to stellar rotational modulation (P_{rot}).

As with the photometric TESS data, we also apply a GP model to the HARPS data to account firstly for the stellar rotational period, and secondly for any residual instrumental or noise effects that are not accounted for in the data reduction. The prior for P_{rot} is set up as a normal distribution around the predicted value of 20.53 days with a standard deviation of 7 days (Table 4.8), based on the analysis from DACE. Our quasi-periodic GP kernel used is identical to that of Hawthorn et al. [2023a] and Osborn et al. [2021b], which is a combination of the Periodic and ExpQuad (squared exponential) kernels available from the PyMC3 package [Salvatier et al., 2016], multiplied to create our final kernel in Equation 4.2. This final kernel is parameterised by the GP amplitude η, the stellar rotation period P_{rot}, the timescale of active region evolution l_E and the smoothing parameter l_P:

$$k(x, x') = \eta^2 \exp\left(-\frac{\sin^2(\pi|x - x'|\frac{1}{P_{\mathrm{rot}}})}{2l_P^2} - \frac{(x - x')^2}{2l_E^2}\right). \tag{4.2}$$

We first find predicted values for the radial velocity of TOI-908 b at each timestamp in the HARPS data, which uses a uniform prior between 0 and 10 $\mathrm{m\,s^{-1}}$ for the semi-amplitude K of the planet signal. We also fit for the instrumental offset of HARPS to account for the differences in RV zero points between instruments, and any other residual effects not incorporated into the HARPS formal uncertainties or the GP model. Our noise model adds jitter noise in quadrature with the nominal RV uncertainties in Equation 4.3,

$$\sigma^2 = {\sigma_0}^2 + {\sigma_i}^2, \tag{4.3}$$

where σ_0 is the RMS of the jitter noise and σ_i is the nominal uncertainty of the i-th radial velocity measurement. The priors and resulting fit values for the HARPS radial velocity GP can be found in Table 4.11.

Table 4.4: Stellar parameters of TOI-908.

Property (unit)	**Value**	**Source**
Mass ($M_\odot$)	0.950 ± 0.010	EXOPLANET
Radius ($R_\odot$)	1.028 ± 0.030	EXOPLANET
Density ($g\,cm^{-3}$)	$1.235^{+0.091}_{-0.102}$	EXOPLANET
$P_{\rm rot}$ (days)	21.932 ± 6.167	EXOPLANET
LD coefficient u_1	0.296 ± 0.242	EXOPLANET
LD coefficient u_2	0.164 ± 0.291	EXOPLANET
$\log g$	4.45 ± 0.03	ARES + MOOG + *Gaia*
T_{eff} (K)	5626 ± 61	ARES + MOOG
$v \sin i_*$ ($km\,s^{-1}$)	2.560 ± 0.636	ARES + MOOG
$v_{\rm turb}$ ($km\,s^{-1}$)	0.913 ± 0.022	ARES + MOOG
Age (Gyr)	4.6 ± 1.5	Chemical clocks
Stellar abundances		
[Fe/H] (dex)	0.08 ± 0.04	ARES + MOOG
[C/H] (dex)	0.00 ± 0.03	ARES + MOOG
[O/H] (dex)	0.06 ± 0.13	ARES + MOOG
[Na/H] (dex)	0.10 ± 0.03	ARES + MOOG
[Mg/H] (dex)	0.10 ± 0.03	ARES + MOOG
[Al/H] (dex)	0.08 ± 0.04	ARES + MOOG
[Si/H] (dex)	0.07 ± 0.02	ARES + MOOG
[Ti/H] (dex)	0.09 ± 0.03	ARES + MOOG
[Ni/H] (dex)	0.07 ± 0.02	ARES + MOOG
[Cu/H] (dex)	0.08 ± 0.03	ARES + MOOG
[Zn/H] (dex)	0.05 ± 0.02	ARES + MOOG
[Sr/H] (dex)	0.16 ± 0.08	ARES + MOOG
[Y/H] (dex)	0.13 ± 0.07	ARES + MOOG
[Zr/H] (dex)	0.12 ± 0.03	ARES + MOOG
[Ba/H] (dex)	0.07 ± 0.04	ARES + MOOG
[Ce/H] (dex)	0.08 ± 0.02	ARES + MOOG
[Nd/H] (dex)	0.12 ± 0.03	ARES + MOOG

Sources: EXOPLANET [Foreman-Mackey et al., 2021a; Foreman-Mackey et al., 2021b], ARES [Sousa et al., 2015], MOOG [Sneden, 1973; Kurucz, 1993], *Gaia* [Brown et al., 2018]

4.4 Results and Discussion

The results of our joint modelling show that TOI-908 b is a sub-Neptune with a mass of $16.1 \pm 4.1\,M_\oplus$ and a radius of $3.18 \pm 0.16\,R_\oplus$ orbiting a G-dwarf star in a close-in 3.18 day orbit. Our final set of parameters for TOI-908 b can be found in Table 4.5.

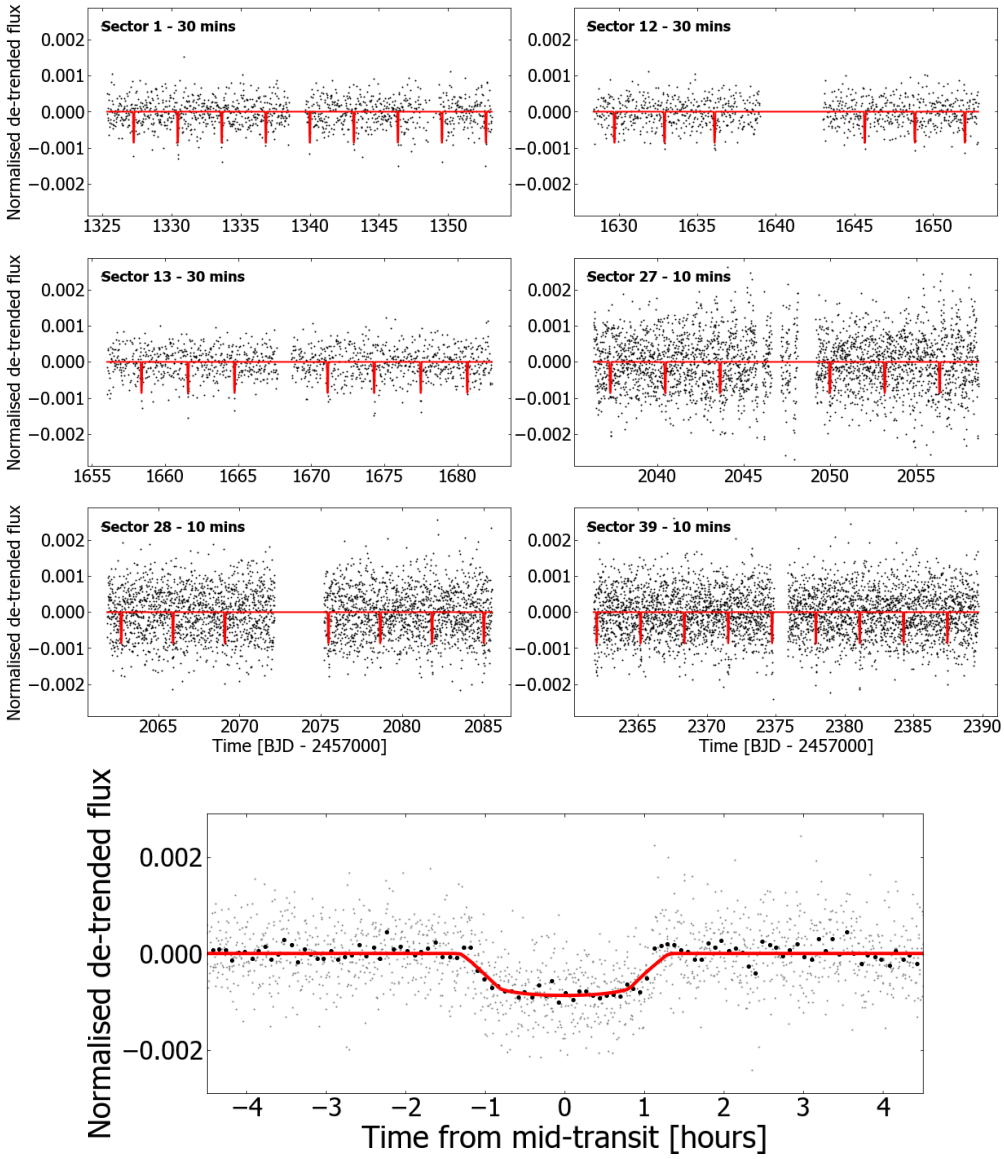

Figure 4.2: **Top panels:** TESS PDCSAP lightcurves from labelled sectors at labelled cadences with the GP model removed, overplotted with the best-fitting transit models for TOI-908 b in red. **Bottom panel:** TESS PDCSAP lightcurves from all sectors (grey points), phase folded to a period corresponding to that of TOI-908 b overplotted with the best-fitting transit model in red and binned to 10 minute intervals (black points).

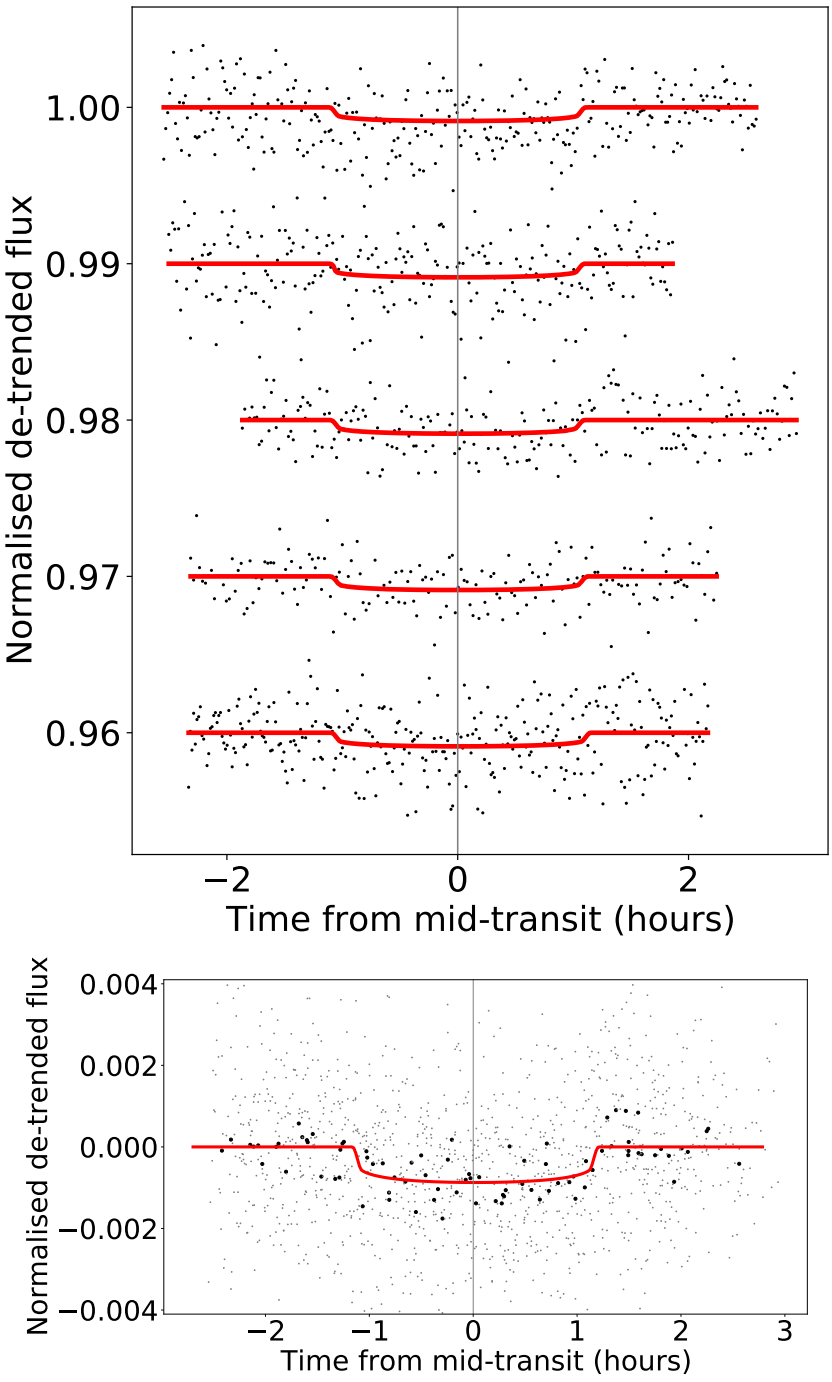

Figure 4.3: **Top panel:** Photometric observations of TOI-908 taken by the LCOGT facilities as detailed in Table 4.2 in order of observation date from top to bottom, overplotted with the best-fitting transit models in red, and offset vertically for clarity. **Bottom panel:** All LCOGT lightcurves (grey points), phase folded to a period corresponding to that of TOI-908 b, overplotted with the best-fitting transit model in red and binned to 10 minute intervals (black points).

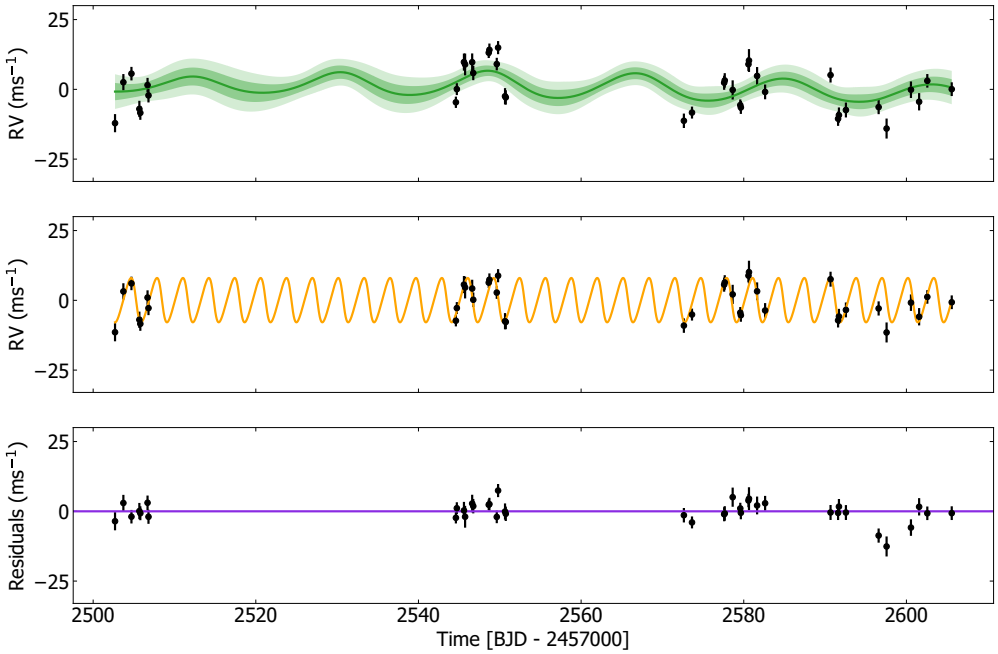

Figure 4.4: **Top panel:** HARPS radial velocity data for TOI-908 (black circles) with formal uncertainties, and the GP model plotted in green with 1 and 2 standard deviations from the model either side. **Middle panel:** Radial velocity model of TOI-908 b (orange) with the GP model subtracted, overplotted with the HARPS datapoints. **Bottom panel:** Residuals for the HARPS data.

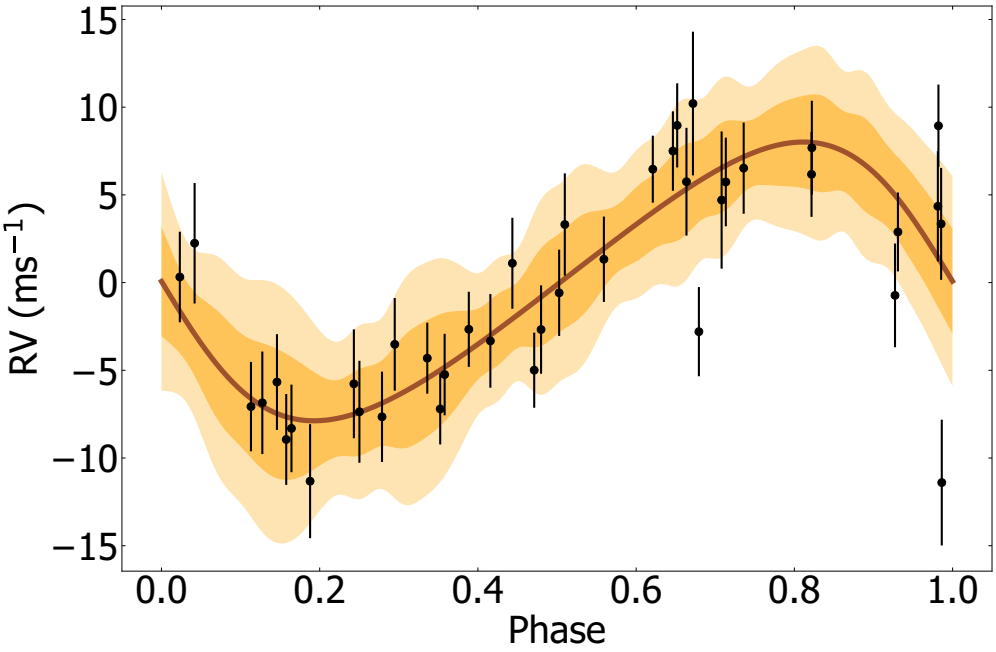

Figure 4.5: HARPS radial velocity data for TOI-908, phase folded to a period corresponding to that of TOI-908 b and overplotted with the model in orange with 1 and 2 standard deviations from the model either side.

Table 4.5: Parameters of TOI-908 b.

Property (unit)	**Value**
Catalog identifier	TOI-908.01
Period (days)	3.183792 ± 0.000007
Mass ($M_\oplus$)	$16.137^{+4.112}_{-4.039}$
Radius ($R_\oplus$)	3.186 ± 0.155
Density (g cm^{-3})	$2.742^{+0.241}_{-0.353}$
R_p/R_*	0.028 ± 0.002
T_c (TBJD)	2384.292 ± 0.002
T1-T4 duration (hours)	$2.457^{+0.120}_{-0.102}$
T2-T3 duration (hours)	$2.268^{+2.225}_{-1.437}$
Impact parameter	0.536 ± 0.191
K (m s^{-1})	7.244 ± 1.768
Inclination (°)	$86.475^{+1.258}_{-1.260}$
Semi-major axis (AU)	0.041657 ± 0.000002
Temperature $T_{\rm eq}$ (K) *	1317 ± 38
Insolation flux ($S_\odot$)	80.884 ± 0.006
Eccentricity	0.132 ± 0.091
Argument of periastron (°)	35.856 ± 94.972

* Assuming Albedo = 0 and uniform surface temperature

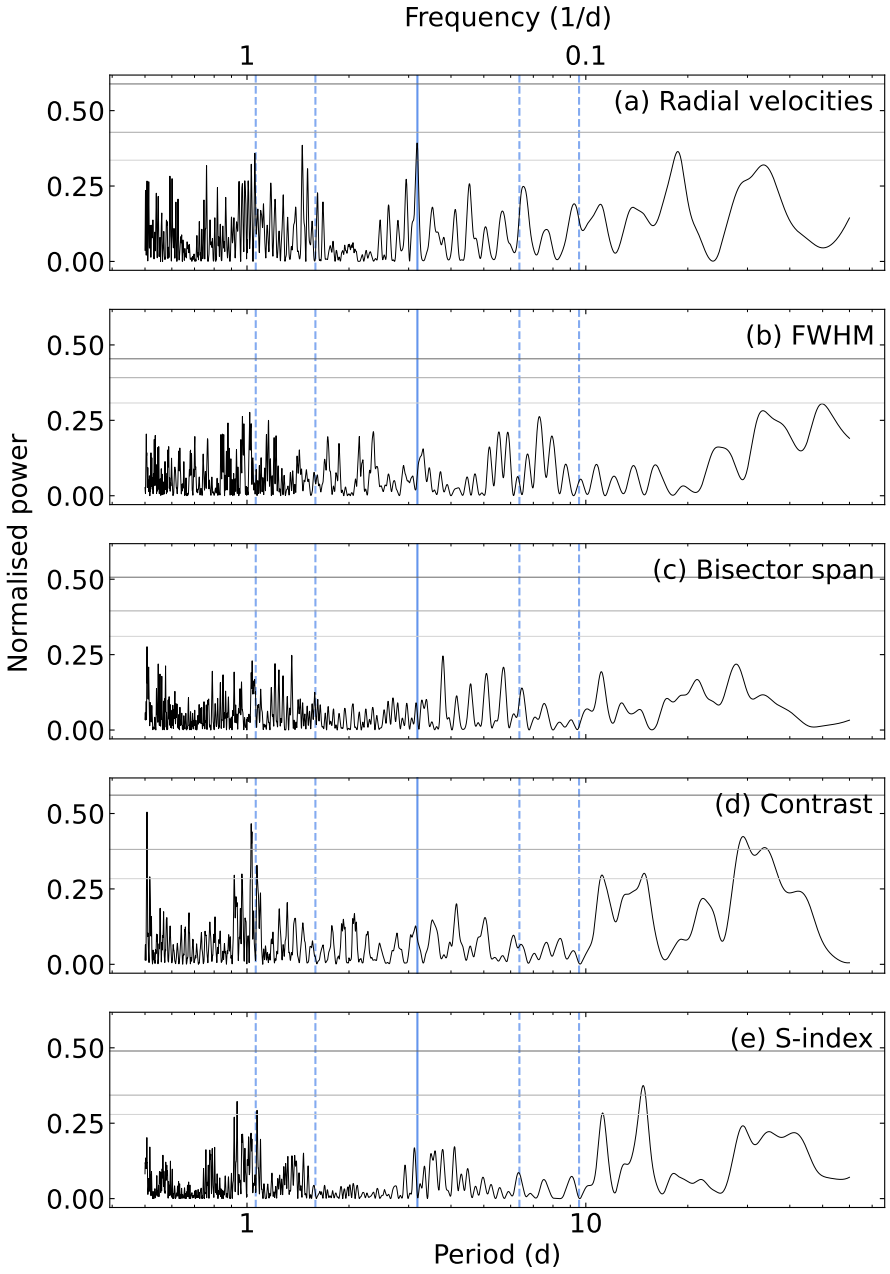

Figure 4.6: Periodograms for the HARPS radial velocity data of the values presented in Table 4.3. The orbital period of TOI-908 b is marked with a solid vertical blue line, alongside two period aliases either side of this value marked as dashed vertical blue lines. The False Alarm Probabilities (FAP) are marked as the horizontal grey lines at 0.1, 1 and 10% from top to bottom. **Panel 1**: Periodogram for the raw radial velocity data, with a peak at the orbital period value of TOI-908 b above the 0.1% FAP line. **Panels 2-5**: Periodograms for the Full-Width Half Maximum (FWHM), bisector span, contrast and S-index$_{\mathrm{MW}}$.

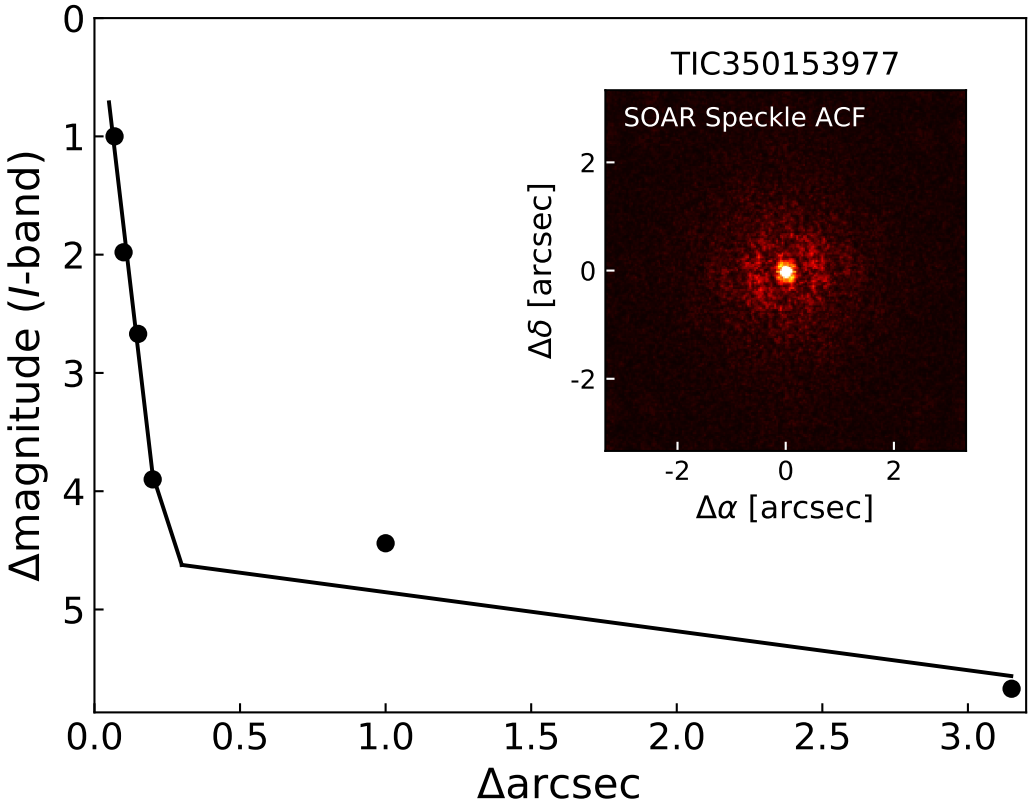

Figure 4.7: SOAR speckle imaging observations (insert), 5-σ sensitivity limit and Auto-Correlation Functions (ACF) of TOI-908, showing no detection of close companions within 3" of the target.

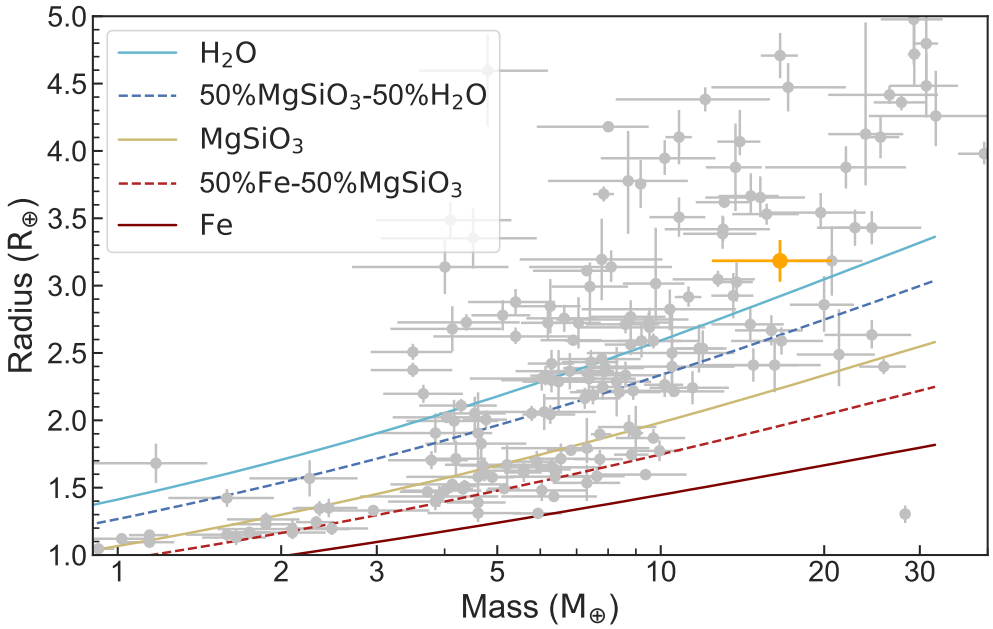

Figure 4.8: Mass-radius diagram showing the position of TOI-908 b (orange) amongst the population of exoplanets from the *TEPCAT* catalog [Southworth, 2011] (grey points), overplotted with composition models from Zeng et al. [2016].

4.4.1 Density

In Figure 4.8 we plot the position of TOI-908 b relative to the sample of planets from the *TEPCAT* catalog [Southworth, 2011], and relative to composition models obtained from [Zeng et al., 2016] using the open-source code FANCY-MASSRADIUS-PLOT[5]. TOI-908 b sits above the 100% water planetary composition model amongst a more sparse population. The mass, radius and resulting bulk density of TOI-908 b (Table 4.5) is similar to that of other known hot Neptune planets.

4.4.2 Position of the planet in the Neptune desert

In Figure 4.9 we plot the position of TOI-908 b relative to the sample of planets with measured periods, radii and masses from the NASA Exoplanet Archive, and relative to the Neptune desert boundary of Mazeh et al. [2016]. It can be seen that TOI-908 b lies just within the desert boundary.

[5] `https://github.com/oscaribv/fancy-massradius-plot`

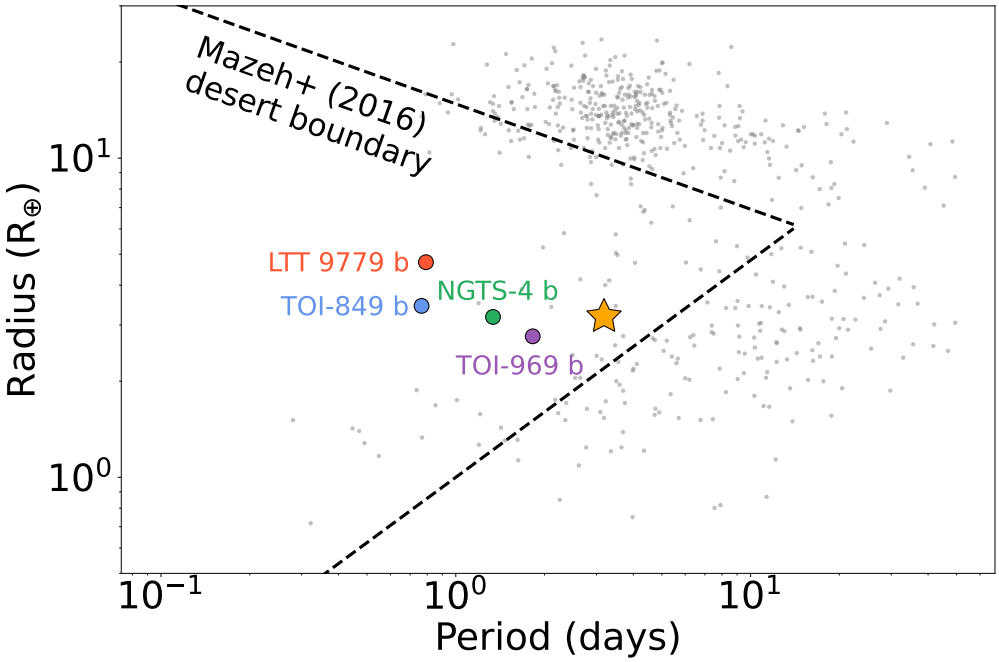

Figure 4.9: Plot showing the position of TOI-908 b (orange star) relative to the Neptune desert boundary of Mazeh et al. [2016], represented against the population of planets with measured periods and radii from the NASA Exoplanet Archive, and four confirmed planets in this parameter space: LTT 9779 b [Jenkins et al., 2020] (red circle), TOI-849 b [Armstrong et al., 2019] (blue circle), NGTS-4 b [West et al., 2019] (green circle) and TOI-969 b [Lillo-Box et al., 2022] (purple circle).

Table 4.6: Internal structure of TOI-908 b from Rogers & Owen [2021] models.

Property (unit)		Value
Core radius	$R_{\rm core}$ ($R_\oplus$)	2.31 ± 0.17
Core mass	$M_{\rm core}$ ($M_\oplus$)	16.0 ± 4.0
Envelope radius	$R_{\rm env}$ ($R_\oplus$)	0.87 ± 0.23
Envelope mass fraction	$M_{\rm env}/M_{\rm p}$	0.022 ± 0.010

4.4.3 Additional planets and TTVs

To evaluate the possible presence of additional planets in the system, both transiting and non-transiting, we implement additional searches of the TESS photometric data and the HARPS spectroscopic radial velocity data. We perform a BLS [Box Least Squares; Kovács et al., 2002] search on the TESS light curve data with the transit model for TOI-908 b subtracted, and find no evidence of additional significant signals above a False Alarm Probability (FAP) of 0.1 besides the predicted rotation period of 20.53 days. We search the HARPS data using the DACE platform, which is capable of performing a periodogram search for additional periodic signals after the removal of the TOI-908 b radial velocity signal from the periodogram and the stellar rotation signal, and again we find no evidence for additional planets in the system. We also examine the individual transits from TESS and LCOGT with the EXOFAST[6] platform to model the measured central transit times $T_{\rm cm}$ and compare them with the calculated $T_{\rm cc}$, and find that the measured transit times vary from the expected time by up to 29 minutes, consistent with our errors. We plot the TTVs for TOI-908 b in Figure 4.11.

4.4.4 Internal structure modelling

We first estimate the internal structure of the planet assuming that it is comprised of a rocky core (Earth-like bulk density) surrounded by a H/He-rich envelope, following Rogers & Owen [2021]. The internal structure can thus be described by four parameters: the core radius $R_{\rm core}$ and mass $M_{\rm core}$, the envelope radius $R_{\rm env}$, and the envelope mass fraction $f_{\rm env}$, which is defined in Equation 4.4:

$$f_{\rm env} = \frac{M_{\rm env}}{M_{\rm p}} = \frac{M_{\rm p} - M_{\rm core}}{M_{\rm p}}, \tag{4.4}$$

where $M_{\rm env}$ and $M_{\rm p}$ are the planet's envelope mass and total mass, respectively. We make use of the empirical mass–radius relations for rocky planets by Otegi et al.

[6] `https://exoplanetarchive.ipac.caltech.edu/cgi-bin/ExoFAST/nph-exofast`

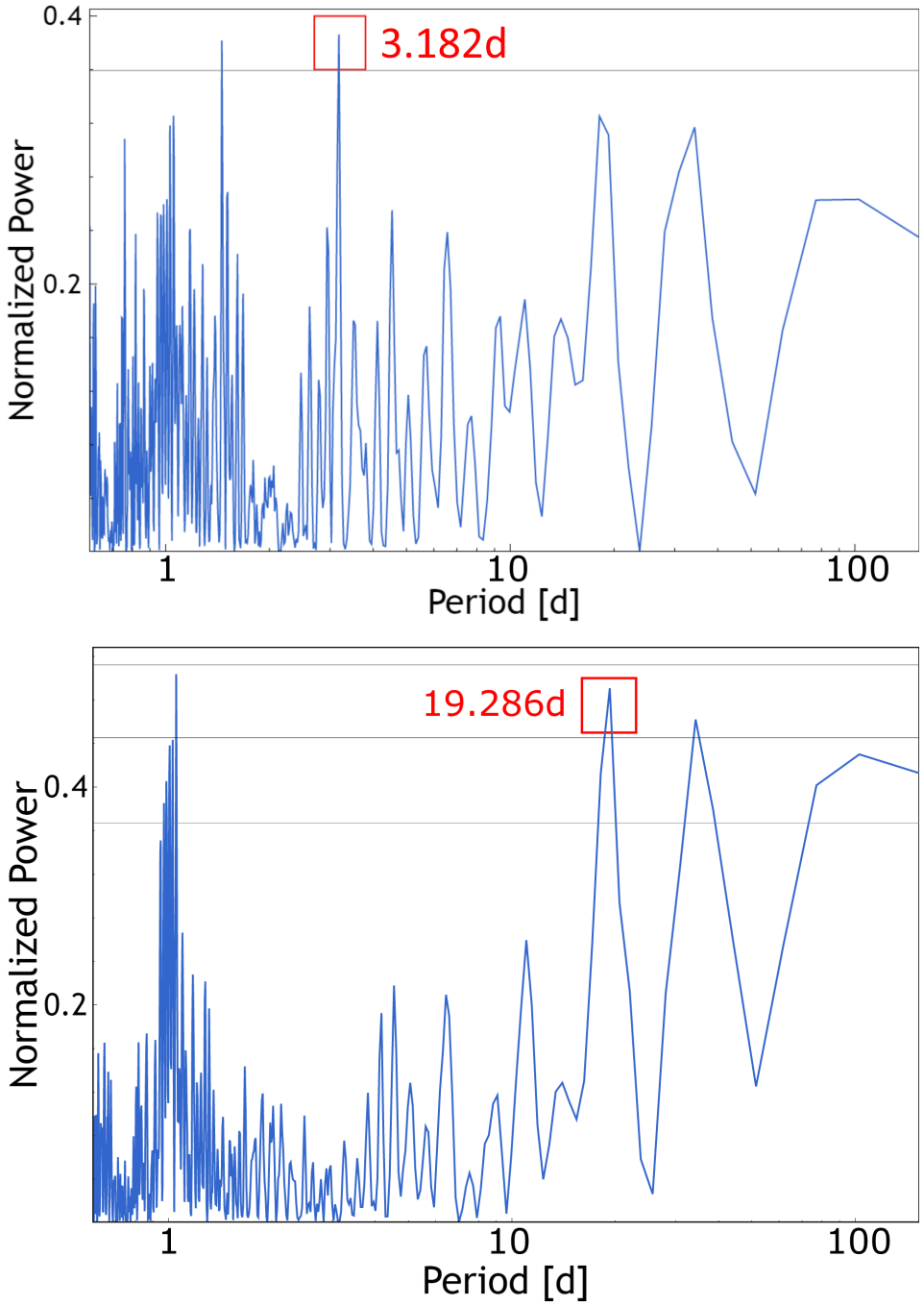

Figure 4.10: **Top panel:** Periodogram of the HARPS radial velocity data for TOI-908 showing the signal of TOI-908 b, marked with a red box. The horizontal line represents the 1% FAP level. **Bottom panel:** Periodogram of the HARPS radial velocity data for TOI-908 with the signal of TOI-908 b removed, showing the remaining stellar rotational signal. The horizontal lines represent the 0.1%, 1% and 10% FAP levels.

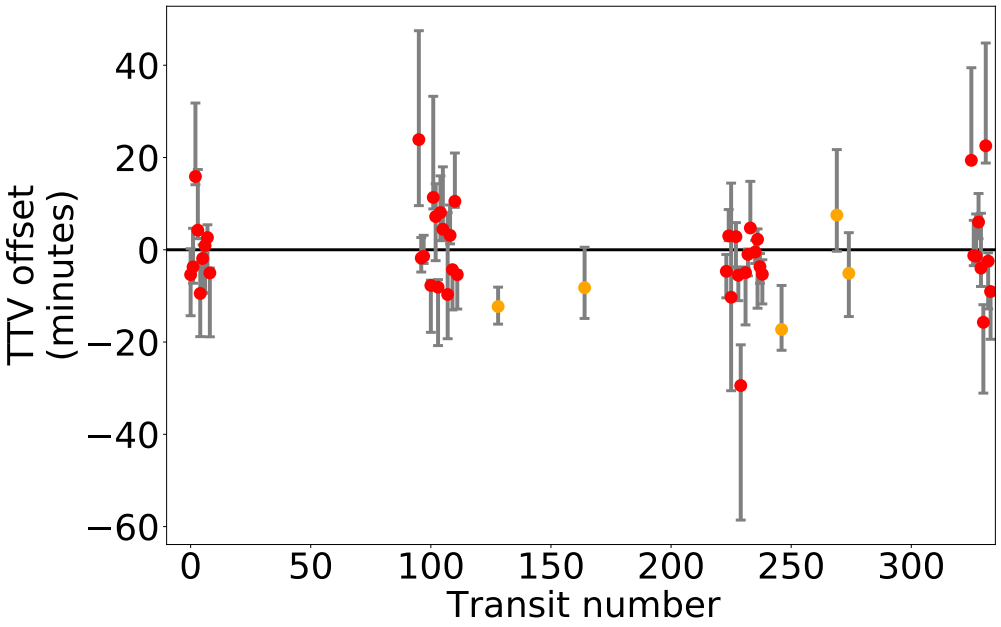

Figure 4.11: Transit Timing Varations (TTVs) for each transit of TOI-908 b from LCOGT (orange points), and each transit from TESS (red points), starting from transit number 0 taken as the first TESS transit in sector 1.

[2020] to estimate the properties of the rocky core and relate core mass to core radius. For the H/He envelope, we adopt the envelope structure model by Chen & Rogers [2016], who provide a polynomial fit to their MESA simulations of the atmospheres of sub-Neptunes, in order to link envelope mass fraction and envelope radius. These formulations together reduce the number of unknowns to two: the envelope mass fraction and the core mass, which can be related to each other with the definition of envelope mass fraction above.

The resulting internal structure, shown in Table 4.6, indicates an envelope mass fraction of $f_{\rm env} = 2.2 \pm 1.0\%$, typical of sub-Neptunes above the radius valley [Rogers & Owen, 2021].

We perform an additional study of the internal structure of the planet with a Bayesian analysis, using the derived stellar and planetary properties. This method is described in details in Leleu et al. [2021] and has been applied on several systems such as L98-59 [Demangeon et al., 2021], TOI-178 [Leleu et al., 2021] or Nu2 Lupi [Delrez et al., 2021]. In the model of planetary interior, four layers are assumed: a inner core made of iron and sulfur, a mantle of silicate (Si, Mg and Fe), a water layer and a gaseous envelope of pure H-He. The core, mantle and water layers form the 'solid' part of the planet and the thickness of the gaseous envelope depends on

Table 4.7: Internal structure of TOI-908 b from Leleu et al. [2021] models.

Property (unit)		Water	No water
Total radius	$R_{\rm tot}$ ($R_\oplus$)	2.9 ± 0.47	3.04 ± 0.46
Total mass	$M_{\rm tot}$ ($M_\oplus$)	16.5 ± 4.45	16.05 ± 4.79
Envelope radius	$R_{\rm env}$ ($R_\oplus$)	0.54 ± 0.6	1.02 ± 0.52
Envelope mass fraction	$M_{\rm env}/M_{\rm p}$	0.002 ± 0.010	0.010 ± 0.010

its mass and radius as well as the stellar age and irradiation [Lopez & Fortney, 2014]. The resulting planetary parameters are the mass fraction of each layer, the iron molar fraction in the core, the silicon and magnesium molar fraction in the mantle, the equilibrium temperature, and the age of the planet (equal to the age of the star). Uniform priors are used for these parameters, except for the mass of the gas layer which is assumed to follow a uniform-in-log prior, with the water mass fraction having an upper boundary of 0.5 [Thiabaud et al., 2014; Marboeuf et al., 2014]. For more details related to the connection between observed data and derived parameters, we refer to Leleu et al. [2021]. Two scenarios have been investigated for TOI-908 b: the case with water (water mass fraction up to 0.5) and the case without water. The figures 4.12 and 4.13 refer to these two cases respectively. Both cases give results consistent with the planetary observables. The case with water leads to an atmosphere representing 18% of the total radius, whereas the case without water produces a thicker gaseous envelope of almost 35% of the total radius.

4.4.5 Evaporation history of the planet

The Neptune desert and the radius valley are consistent with being the result of the evaporation of the atmospheres of sub-Neptunes [Lopez & Fortney, 2013, 2014; Owen & Wu, 2013; Jin et al., 2014]. The underlying cause of evaporation is still under debate, though, and several mechanisms have been proposed. One such mechanism is photoevaporation, in which X-ray and extreme ultraviolet radiation (together, XUV), originating from the host star, provides the energy for evaporation [Watson et al., 1981; Erkaev et al., 2007]. Photoevaporation has been shown to reproduce both the radius valley [Rogers & Owen, 2021] as well as the lower boundary of the Neptune desert [Owen & Lai, 2018]. Ginzburg et al. [2016] proposed an alternative mechanism for evaporation, core-powered mass loss, where the energy for atmospheric escape is provided by the internal thermal energy of the planet, and Gupta & Schlichting [2019] showed that it can also reproduce the radius-period valley. The existence of the radius valley has also been attributed to formation mechanisms [Zeng et al., 2019] and impacts by planetesimals [Wyatt et al., 2020].

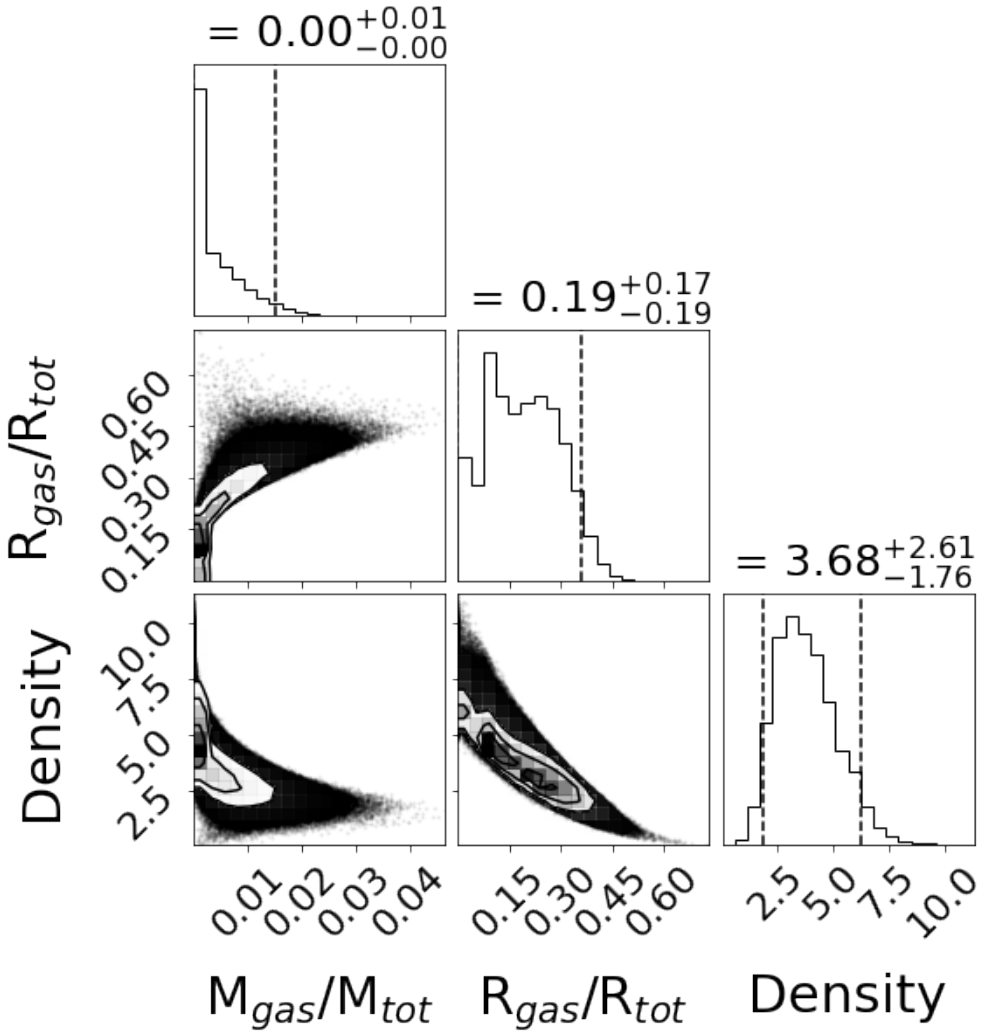

Figure 4.12: Corner plot of the derived internal structure parameters of TOI-908 b for the scenario with a water mass fraction of up to 0.5.

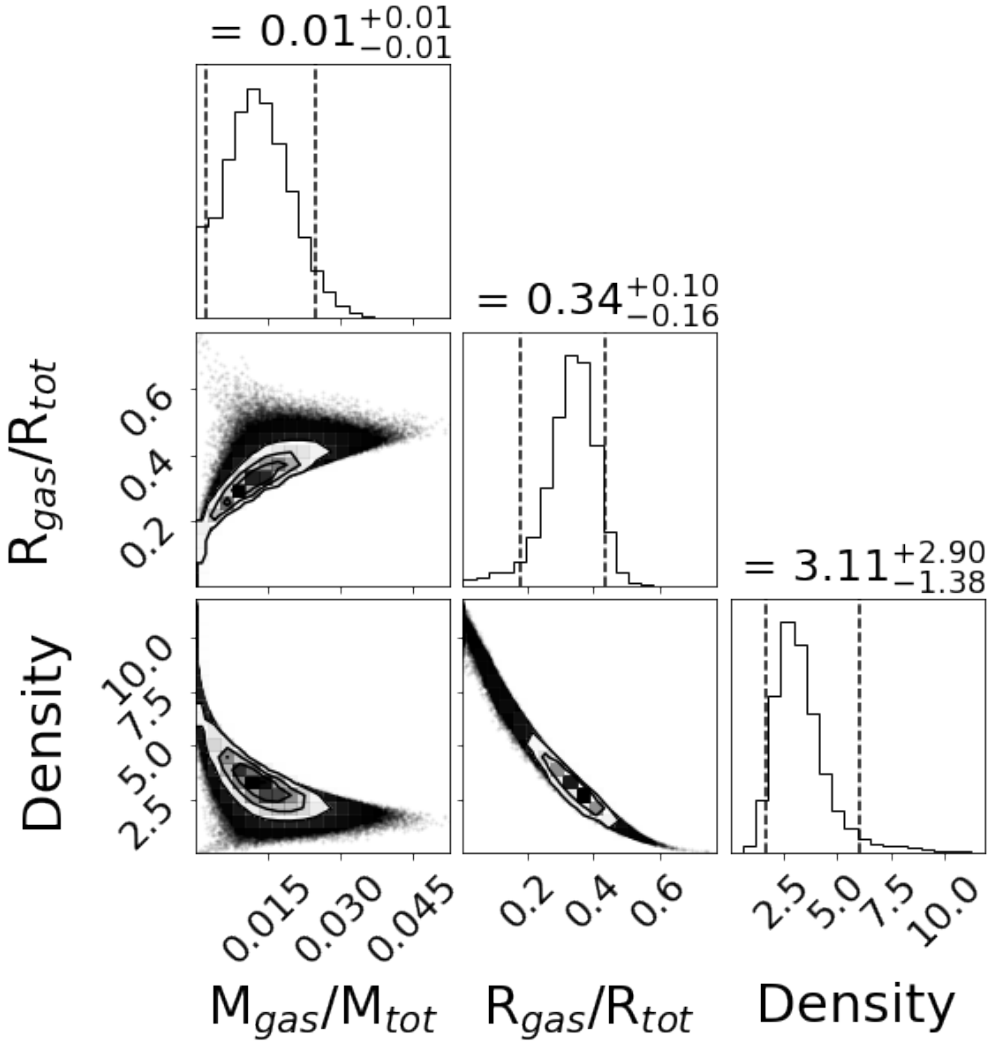

Figure 4.13: Corner plot of the derived internal structure parameters of TOI-908 b for the scenario with no water.

To study the evaporation history of the planet under this hypothesis, three ingredients are necessary: (1) a description of the XUV history of the star, (2) an envelope structure model [here we adopt Chen & Rogers, 2016], and (3) a mass loss model that relates the incident X-ray flux on the planet to the amount of mass lost.

The XUV history of a star can be estimated from its rotational history, as the two quantities are linked via the rotation–activity relation, where faster rotators produce higher X-ray fluxes [Wright et al., 2011, 2018]. The X-ray luminosity of a star also declines with age, as stars spin down due to angular momentum loss through stellar winds [Jackson et al., 2012; Tu et al., 2015; Johnstone et al., 2021]. We adopt the rotational evolution models by Johnstone et al. [2021], who model the rotational spread and evolution of FGKM stars as a function of age and stellar mass. Figure 4.14 shows the population mean and 2σ rotation tracks of a star of the mass of TOI-908, and their corresponding XUV tracks. Furthermore, we adopt the mass loss formulation by Kubyshkina & Fossati [2021], based on hydrodynamic simulations of planetary atmospheres in the context of photoevaporation.

The model by Johnstone et al. [2021] predicts that a 0.95 $M_\odot$ star has an expected rotation period of 29 days, with a 2σ spread between 27 and 30 days, at an age of 4–5 Gyr. As shown in Figure 4.14 (left hand panel), TOI-908,with an age of 4.6 ± 1.5 Gyr, has a rotation period of 21.932 ± 6.167 days, which is a factor of ~ 1.5 times faster than predicted by the model, making the star an unusually fast rotator for its age. The 1σ uncertainties in the age and spin period, however, allow for younger and slower scenarios consistent with the spin evolution models. To model the XUV history of the star, we estimate the current X-ray luminosity using the rotation-activity relation, and use it to scale the model's 2σ upper limit X-ray track to fit our estimate, as shown in Figure 4.14 (right hand panel). Furthermore, we estimate the extreme ultra-violet (EUV) luminosity of the star using the empirical relations by King et al. [2018].

We simulate the evaporation history of TOI-908 b using the PHOTOEVOLVER code[7] [Fernández Fernández et al., 2023], which evolves the planet's envelope by following these steps iteratively: first the current XUV flux on the planet is drawn from the stellar evolution tracks (see Fig. 4.14), then the mass loss rate is obtained using the model by Kubyshkina & Fossati [2021], which is then subtracted from the envelope mass, and finally the envelope size is recalculated using the Chen & Rogers [2016] model and the simulation jumps to the next timestep. We run the simulation back to the age of 10 Myr and forward to 10 Gyr from the current age of 4.6 ± 1.5 Gyr under the XUV irradiation history motivated by the star's measured spin period.

[7] `https://github.com/jorgefz/photoevolver`

We simulated the evaporation past of the planet using the two internal structures we derived in Section 4.4.4: a rocky core surrounded by a gaseous envelope consisting of $2.2 \pm 1.0\%$ of its mass, which we designated the *dry planet* scenario (shown in Table 4.6) , and the Bayesian model by Leleu et al. [2021] which accounts for the presence of water, and we designated the *water planet* scenario (shown in Table 4.7, left column). The results, shown in Figure 4.15, indicate that in the dry planet scenario, TOI-908 b could have started out as a super-Neptune of radius 5–7 $R_\oplus$ and envelope mass fraction 10–20 %. On the other hand, we find that the evaporation past of the water scenario is fairly unconstrained, with initial states ranging from a $6.5\,R_\oplus$ planet akin to the initial state of the dry planet, to a puffy Jupiter-sized planet at $12\,R_\oplus$ with a significant envelope of mass fraction 50%. Furthermore, we also find that the planet's envelope could be completely stripped by the age of 5–10 Gyr in the case of the dry planet, whereas the tenuous gas layer on the water planet is removed in tens to a hundred Myr.

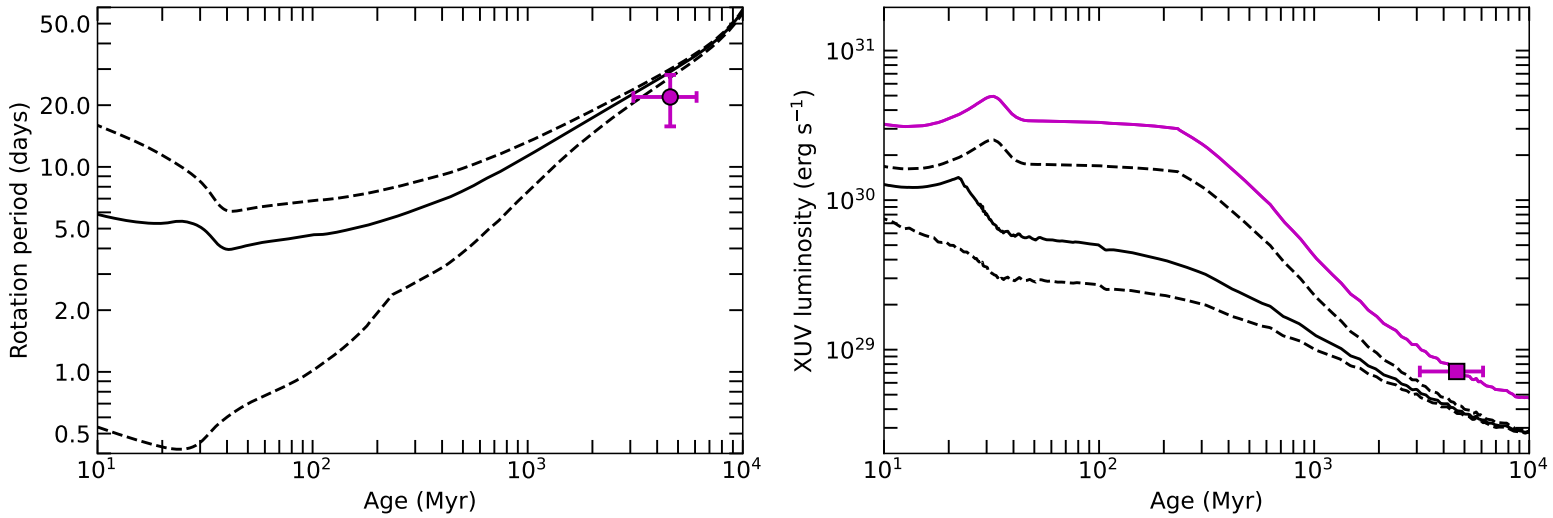

Figure 4.14: **Left panel:** Plot showing the evolution of the rotation period of a $0.95\,M_\odot$ star using the initial rotation periods of the population mean (solid line) and the 2σ spread (dashed lines), following the model by Johnstone et al. [2021]. TOI-908, with a rotation period faster than expected for its age, is plotted as a purple circle. **Right panel:** XUV evolution tracks of TOI-908 based on the rotational histories shown on the left panel. together with the expected XUV luminosity of TOI-908, based on its rotation period (purple square), and the fitted XUV track to that value (purple line).

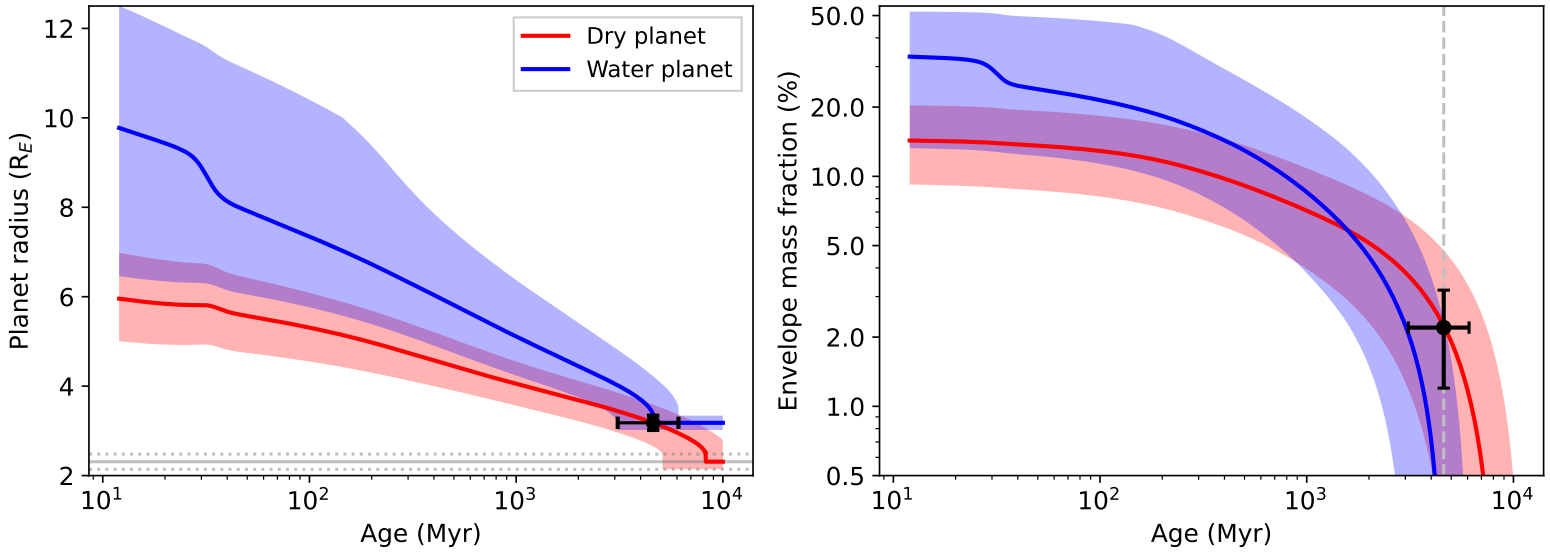

Figure 4.15: **Left panel**: plot showing the evolution of the radius of TOI-908 b using two models for the internal structure, one with a rocky core surrounded by gaseous atmosphere (red), and another with water instead of gas (blue). The shaded regions represent the spread in evaporation histories allowed by the 1σ uncertainties on the planet's mass, radius, and age. The present-day age and radius are shown with a black marker, and the rocky core radius (for the dry planet scenario) is shown as a horizontal grey line. **Right panel**: plot showing the evolution of the envelope mass fraction of TOI-908 b, akin to the left panel. The present-day envelope mass fraction for the dry planet scenario is shown as a black circle, and the current age of the planet is plotted as a grey vertical line.

4.5 Conclusion

We have presented the discovery of TOI-908 b, a hot sub-Neptune orbiting the G-type star TOI-908. We use a combination of transit photometry data from 6 sectors of TESS mission data at both 30 minute and 10 minute cadence, further follow-up observations from the LCOGT telescope network, radial velocity data from HARPS, and SOAR speckle imaging to rule out the presence of blended companions. We jointly model our transit photometry and radial velocity data, and find that the planet orbits a G-type star with a radius of $0.95 \pm 0.01\,\mathrm{M}_{\odot}$ and a radius of $1.03 \pm 0.03\,\mathrm{R}_{\odot}$.

TOI-908 b has a radius of $3.18 \pm 0.16\,\mathrm{R}_{\oplus}$ and a mass of $16.1 \pm 4.1\,\mathrm{M}_{\oplus}$, with an orbital period of 3.18 days. It lies within the parameter space of the period-radius diagram known as the 'Neptune desert', an area of parameter space where a dearth of planets is seen in current demographics. The mean density $2.7^{+0.2}_{-0.4}\,\mathrm{g\,cm^{-3}}$ of TOI-908 b indicates an internal structure consisting of a core of radius $\sim$2.3 $\mathrm{R}_{\oplus}$ and mass of 16.0 $\mathrm{M}_{\oplus}$, surrounded by an envelope of radius 0.87 $\mathrm{R}_{\oplus}$ with a mass fraction of 2.2%. Our analysis of the evaporation history of the planet indicates that its host star is rotating faster than expected, and predict that the planet was previously a super-Neptune of radius 5–7 $\mathrm{R}_{\oplus}$ with an original envelope mass fraction of 10–20%. Our models show the envelope will continue to evaporate in the future, and may be lost completely within the lifetime of the system. This planet is amenable to further follow-up with JWST, as despite its relatively low Transmission Spectroscopy Metric [TSM; Kempton et al., 2018] of 76 ± 6.7 it is a fairly bright ($T = 10.7$ mag) target undergoing atmospheric evaporation that lies close to the Continuous Viewing Zone of both TESS and JWST for ease of observation scheduling. This target should also be considered for further spectroscopic evaporation measurements via the metastable He-line [Oklopčić & Hirata, 2018] with ground-based instruments, such as *CARMENES* or *NIRSPEC*.

4.6 Appendix

Priors and GP models

Table 4.8: Global fit parameter prior function type and prior limits for TOI-908.

Parameter	**Prior**	**Value**
Baseline flux	$\mathcal{N}(0, 1)$	
M_* ($M_\odot$)	$\mathcal{N}(0.95, 0.01, 0.95)$	Table 4.4
R_* ($R_\odot$)	$\mathcal{N}(1.03, 0.03, 1.03)$	Table 4.4
$P_{\rm rot}$ (days)	$\mathcal{N}(20.53, 7.00)$	Table 4.4
LD coefficient u_1	Kipping [2013b]	Table 4.4
LD coefficient u_2	Kipping [2013b]	Table 4.4

Numbers in brackets represent:
(mean μ, standard deviation σ, test value α) for normal distribution $\mathcal{N}(\mu,\sigma,\alpha)$
Distributions for limb darkening coefficients u_1 and u_2 are built into the `exoplanet` package and based on Kipping [2013b]

Table 4.9: Global fit parameter prior function type and prior limits for TOI-908 b.

Parameter	**Prior**	**Value**
TOI-908 b		
Period (days)	$\mathcal{N}(3.1837961, 0.0000112)$	Table 4.5
Transit ephemeris (TBJD)	$\mathcal{U}(2384.25, 2384.33)$	Table 4.5
$\log(R_p)$	$\mathcal{N}$(-3.549§, 1)	Table 4.5 (R_p)
Impact parameter	$\mathcal{U}(0, 1)$	Table 4.5
Eccentricity	Kipping [2013a], $\mathcal{B}(e, 0.867, 3.03)$	Table 4.5
Argument of periastron (rad)	$\mathcal{U}(-\pi, \pi)$	Table 4.5 (°)

Numbers in brackets represent:
(mean μ, standard deviation σ) for normal distribution $\mathcal{N}(\mu,\sigma)$
(lower limit x, upper limit y) for uniform distribution $\mathcal{U}(x,y)$
§ Equivalent to $0.5\times\log(\delta)+\log(R_*)$, δ represents transit depth (based on ExoFOP catalog values)
Distributions for eccentricity e are built into the `exoplanet` package and based on Kipping [2013a] which includes the Beta distribution $\mathcal{B}(e, a, b)$ (exponential e, shape parameter a, shape parameter b)

Table 4.10: Global fit parameter prior function type and prior limits for TESS photometric data.

Parameter	**Prior**	**Value**
Sector 1		
Mean	$\mathcal{N}(0, 1)$	-0.00001 ± 0.00009
log($s2$)	$\mathcal{N}$(-15.536* , 0)	-15.781 ± 0.039
log($w0$)	$\mathcal{N}(0, 0.1)$	0.104 ± 0.095
log($Sw4$)	$\mathcal{N}$(-15.536* , 0)	-15.574 ± 0.096
Sector 12		
Mean	$\mathcal{N}(0, 1)$	-0.00001 ± 0.00008
log($s2$)	$\mathcal{N}$(-15.702* , 0.1)	-15.822 ± 0.043
log($w0$)	$\mathcal{N}(0, 0.1)$	0.132 ± 0.100
log($Sw4$)	$\mathcal{N}$(-15.702* , 0.1)	-15.757 ± 0.100
Sector 13		
Mean	$\mathcal{N}(0, 1)$	0.00004 ± 0.00014
log($s2$)	$\mathcal{N}$(-15.183* , 0.1)	-15.609 ± 0.040
log($w0$)	$\mathcal{N}(0, 0.1)$	0.019 ± 0.088
log($Sw4$)	$\mathcal{N}$(15.183* , 0.1)	-15.162 ± 0.095
Sector 27		
Mean	$\mathcal{N}(0, 1)$	0.00007 ± 0.00033
log($s2$)	$\mathcal{N}$(-13.932* , 0.1)	-14.357 ± 0.027
log($w0$)	$\mathcal{N}(0, 0.1)$	0.056 ± 0.094
log($Sw4$)	$\mathcal{N}$(-13.932* , 0.1)	-13.411 ± 0.109
Sector 28		
Mean	$\mathcal{N}(0, 1)$	0.00007 ± 0.00015
log($s2$)	$\mathcal{N}$(-14.578* , 0.1)	-14.646 ± 0.025
log($w0$)	$\mathcal{N}(0, 0.1)$	0.139 ± 0.103
log($Sw4$)	$\mathcal{N}$(-14.578* , 0.1)	-14.646 ± 0.098
Sector 39		
Mean	$\mathcal{N}(0, 1)$	0.00002 ± 0.00012
log($s2$)	$\mathcal{N}$(-14.656* , 0.1)	-14.743 ± 0.022
log($w0$)	$\mathcal{N}(0, 0.1)$	0.185 ± 0.104
log($Sw4$)	$\mathcal{N}$(-14.656* , 0.1)	-14.761 ± 0.099

Numbers in brackets represent:
(mean μ, standard deviation σ) for normal distribution $\mathcal{N}(\mu,\sigma)$
Prior values:
* Equivalent to the log of the variance of the TESS flux from the corresponding sector

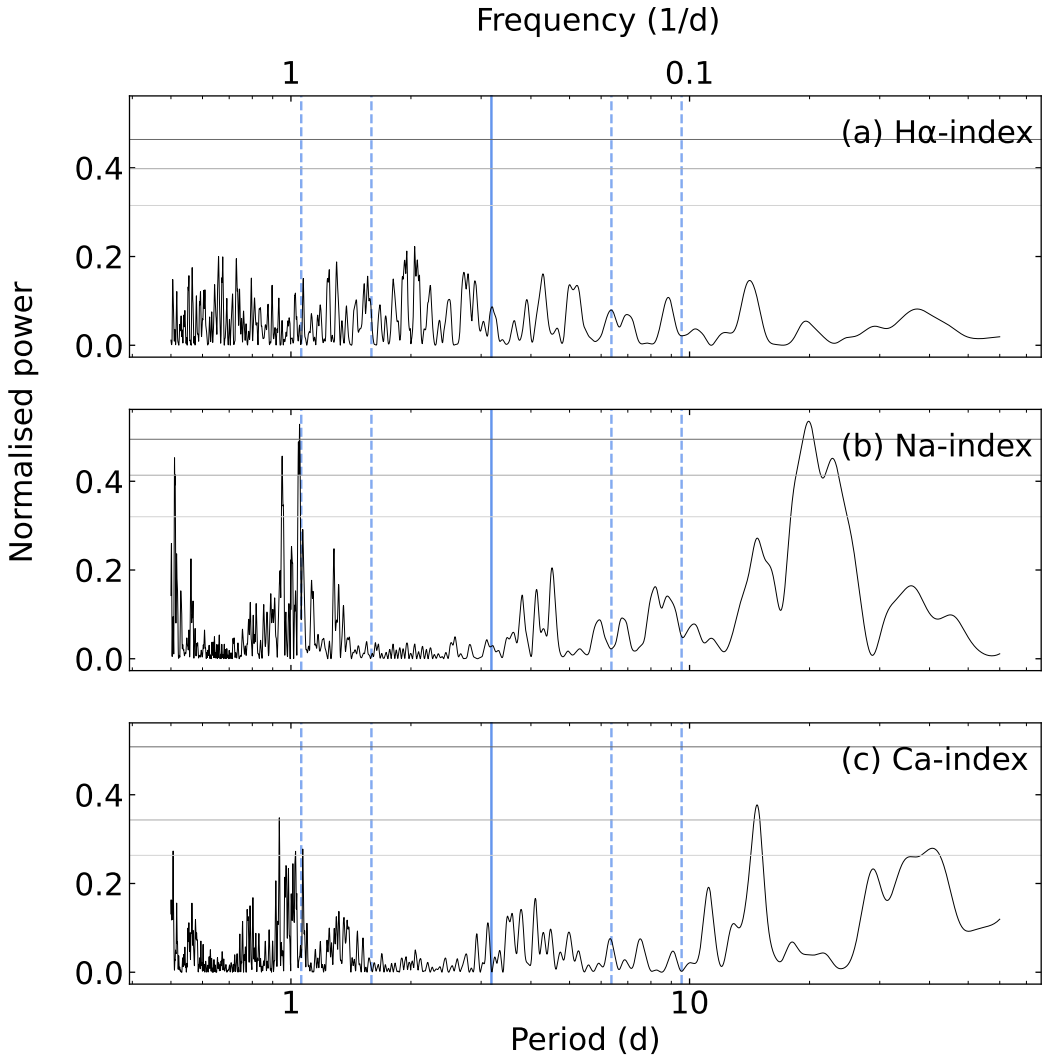

Figure 4.16: Periodograms for the HARPS radial velocity data of the values presented in Table 4.12. The orbital period of TOI-908 b is marked with a solid vertical blue line, alongside two period aliases either side of this value marked as dashed vertical blue lines. The False Alarm Probabilities (FAP) are marked as the horizontal grey lines at 0.1, 1 and 10% from top to bottom. **Panels 1-3**: Periodograms for the Hα-index, Na-index and Ca-index.

Table 4.11: Global fit parameter prior function type and prior limits for HARPS radial velocity data.

Parameter	**Prior**	**Value**
K ($\mathrm{m\,s^{-1}}$)	$\mathcal{U}(0, 10)$	Table 4.5
Amplitude	$\mathcal{C}(5)$	6.321 ± 2.657
l_E	$\mathcal{T}(20.53, 20, 20)$	34.982 ± 11.285
l_P	$\mathcal{T}(0.1, 10, 0, 1)$	0.640 ± 0.209
HARPS offset	$\mathcal{N}(9102.921^{\dagger}, 10)$	9103.035 ± 3.808
$\log(\mathrm{Jitter_{HARPS}})$	$\mathcal{N}(1.293^{\ddagger}, 5)$	-4.528 ± 2.708

Numbers in brackets represent:
(lower limit x, upper limit y) for uniform distribution $\mathcal{U}(x,y)$
(scale parameter β) for half-Cauchy distribution $\mathcal{C}(\beta)$
(mean μ, standard deviation σ, lower limit x, upper limit y) for truncated normal distribution $\mathcal{T}(\mu,\sigma,x,y)$
(mean μ, standard deviation σ) for normal distribution $\mathcal{N}(\mu,\sigma)$
Prior values:
† Equivalent to the mean of the HARPS radial velocity
‡ Equivalent to 2 times the log of the minimum HARPS radial velocity error

Table 4.12: Additional HARPS activity indicator data for TOI-908. This table is available in its entirety online.

Hα-index	**Hα-index error**	**Na-index**	**Na-index error**	**Ca-index**	**Ca-index error**
0.003024	0.000001	0.264718	0.001861	0.121843	0.004656
0.002718	0.000001	0.260553	0.001679	0.132003	0.004192
0.002366	0.000001	0.263481	0.001440	0.132657	0.003269
0.002739	0.000001	0.260150	0.001688	0.121485	0.004012
0.002411	0.000001	0.261340	0.001464	0.139120	0.003539
...	...	...	...	...	...

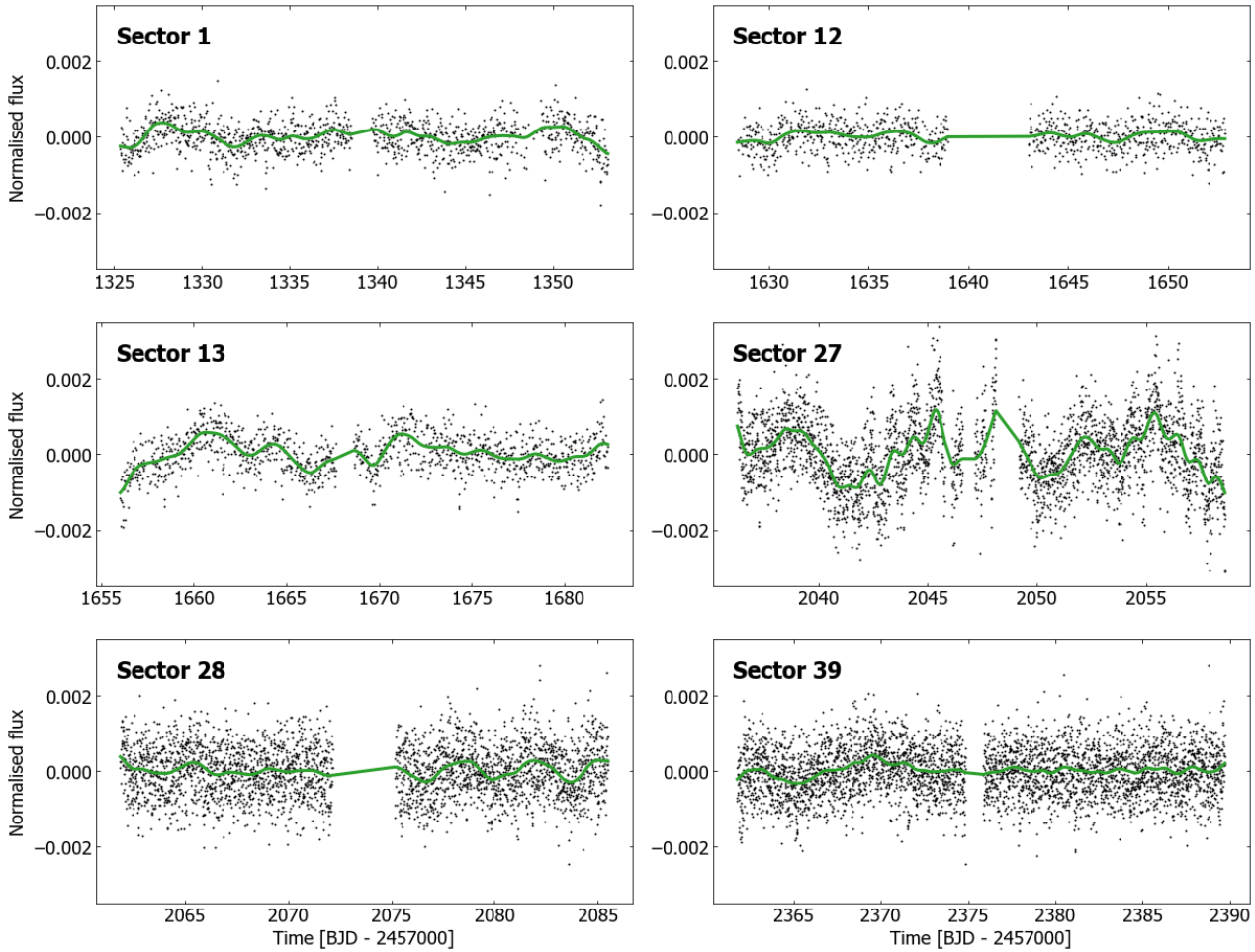

Figure 4.17: TESS PDCSAP lightcurves from labelled sectors, overplotted with the GP models in green.

Table 4.13: All TTVs from TESS.

Transit no.	**TTV (mins)**	**Transit no.**	**TTV (mins)**
0	$-5.4^{+8.9}_{-5.6}$	223	$-4.7^{+5.7}_{-3.6}$
1	$-3.7^{+3.5}_{-8.4}$	224	$3.0^{+1.0}_{-5.7}$
2	$15.9^{+1.8}_{-15.9}$	225	$-10.3^{+20.3}_{-24.7}$
3	$4.2^{+1.8}_{-13.2}$	227	$2.9^{+6.6}_{-3.0}$
4	$-9.5^{+9.4}_{6.86.8}$	228	$-5.5^{+5.5}_{-1.3}$
5	$-1.9^{+7.6}_{-3.0}$	229	$-29.4^{+29.2}_{-8.8}$
6	$0.9^{+10.2}_{-1.5}$	231	$-5.0^{+11.3}_{-1.2}$
7	$2.6^{+8.1}_{-2.8}$	232	$-1.0^{+4.7}_{-1.2}$
8	$-5.0^{+13.9}_{-1.1}$	233	$4.7^{+0.3}_{-10.1}$
95	$23.9^{+14.3}_{-23.6}$	235	$-0.5^{+2.5}_{-2.5}$
96	$-1.8^{+3.0}_{-4.4}$	236	$2.3^{+14.9}_{-2.3}$
97	$-1.4^{+1.6}_{-4.6}$	237	$-3.7^{+3.6}_{-2.8}$
100	$-7.7^{+10.2}_{-1.1}$	238	$-5.3^{+6.4}_{-6.4}$
101	$11.4^{+2.5}_{-21.9}$	325	$19.4^{+0.1}_{-20.1}$
102	$7.2^{+9.6}_{-7.1}$	326	$-1.2^{+2.2}_{-7.6}$
103	$-8.1^{+12.7}_{-1.6}$	327	$-1.4^{+1.4}_{-9.2}$
104	$8.1^{+6.1}_{-7.9}$	328	$6.0^{+3.6}_{-6.2}$
105	$4.5^{+2.4}_{-13.5}$	329	$-4.0^{+4.0}_{-11.9}$
107	$-9.7^{+9.6}_{-17.7}$	330	$-15.7^{+15.4}_{-3.8}$
108	$3.1^{+1.8}_{-6.6}$	331	$22.5^{+3.7}_{-22.3}$
109	$-4.3^{+8.7}_{-0.2}$	332	$-2.5^{+10.4}_{-1.8}$
110	$10.5^{+1.3}_{-10.5}$	333	$-9.0^{+10.4}_{-0.4}$

Chapter 5

TESS Duotransit Candidates from the Southern Ecliptic Hemisphere

"Skyway, permanent Saturday / Oh, by the way, Saturn is my rotary / Hop in, it'll be eternity / 'Til we make it to M83."

'Spacegrass', Clutch, 1995, Fallon/Sult/Maines/Gaster

Note

This chapter is a reproduction of the publication 'TESS Duotransit Candidates from the Southern Ecliptic Hemisphere' (Hawthorn et al. 2024), originally published in Monthly Notices of the Royal Astronomical Society (MNRAS) in January 2024. The majority of the writing and analysis of the paper was performed by the author, with contributions to observational data and sections of analysis made by external collaborators.

Abstract

Discovering transiting exoplanets with long orbital periods allows us to study warm and cool planetary systems with temperatures similar to the planets in our own

Solar system. The TESS mission has photometrically surveyed the entire Southern Ecliptic Hemisphere in Cycle 1 (August 2018 - July 2019), Cycle 3 (July 2020 - June 2021) and Cycle 5 (September 2022 - September 2023). We use the observations from Cycle 1 and Cycle 3 to search for exoplanet systems that show a single transit event in each year - which we call *duotransits*. The periods of these planet candidates are typically in excess of 20 days, with the lower limit determined by the duration of individual TESS observations. We find 85 duotransit candidates, which span a range of host star brightnesses between $8 < \mathrm{T_{mag}} < 14$, transit depths between 0.1 per cent and 1.8 per cent, and transit durations between 2 and 10 hours with the upper limit determined by our normalisation function. Of these candidates, 25 are already known, and 60 are new. We present these candidates along with the status of photometric and spectroscopic follow-up.

5.1 Introduction

Longer period transiting exoplanets allow us to measure the densities of warm and cool planets, assisting with studies of atmospheric composition from transit spectroscopy [e.g. Albrecht et al., 2012; Wang et al., 2021a]. Planetary obliquity is an indicator of planetary migration mechanisms [e.g. Albrecht et al., 2012], and long period planets are amenable to studies of the Rossiter-McLaughlin effect [e.g. Ulmer-Moll et al., 2023] to enable determination of the spin-orbit alignment of the system. When compared to short period hot Jupiter planets, the few well-studied long period planets discovered to date appear to be more aligned [Rice et al., 2022], indicating possible migration mechanisms operating within the protoplanetary disk [e.g. Madhusudhan et al., 2017]. Since the launch of TESS [Transiting Exoplanet Survey Satellite; Ricker et al., 2015], a total of 392[1] exoplanets have been confirmed using TESS data [NASA Exoplanet Archive; Akeson et al., 2013]. Of these systems, only 56 have orbital periods longer than the typical TESS Sector time span of 27 days.

The *Kepler* mission [Borucki et al., 2010] monitored a single 105 square degree field for approximately four years, and was therefore able to discover long period transiting exoplanets. However, most of the host stars are fainter than the capabilities of modern spectrographs to measure planetary masses and the planets cannot be confirmed and fully characterised. Hsu et al. [2019] placed a limit on the occurrence rate of $\lesssim$0.247 planets per FGK star on orbital periods from 237-500 days. The *Kepler* exoplanet sample includes 42 planets with determined periods longer than

[1] `https://exoplanetarchive.ipac.caltech.edu` (2023 Oct 09)

20 days with a robust mass determination from radial velocity confirmation.
The TESS spacecraft has completed surveys of the Southern Ecliptic Hemisphere on two occasions – in Cycle 1 (July 2018 to July 2019) and in Cycle 3 (July 2020 to July 2021). TESS has also re-observed the Southern Ecliptic Hemisphere in Cycle 5 (September 2022 to September 2023), but many of these observations are unavailable at the time of writing and thus are not included in this work. During these surveys a number of stars have shown a single transit (a *monotransit*), whereby one transit like feature is found in the lightcurve but is not seen to repeat. With only one transit we are not able to determine the orbital period of the planet, although with prior knowledge of the star we can calculate the probability distribution for the orbital period, e.g. Osborn et al. [2022]. A small number of these TESS monotransit candidates have been confirmed, e.g. Gill et al. [2020a,c] and Lendl et al. [2020a].
In addition to the TESS monotransit candidates, there exist candidates that transit exactly once in Cycle 1 and once in Cycle 3. These candidates are *biennial duotransits*, as opposed to candidates that may have two transits in a single TESS cycle. For the remainder of this paper we use the term *duotransit* to refer only to such biennial duotransits. These duotransits confer two main advantages over monotransit candidates. Firstly, the true period of a duotransit candidate is limited to a discrete set of possible periods, P_n, given by

$$P_n \in \left(\frac{\Delta T}{n}\right), n = 1, ..., n_{max}, \tag{5.1}$$

where ΔT is the time difference between the Cycle 1 and the Cycle 3 transit event and n is a whole number ranging from n=1 for the longest possible period to n_{max} for the shortest possible period. Since the duration of a TESS sector is ≈27 days, we find $P_{n_{max}}$ is typically in the region of 20 days unless there is more than one Sector of data in the TESS Cycle 1 or Cycle 3 observations. The limited set of possible periods means it is possible to check specific orbital periods via photometric monitoring of the duotransit candidate at specific times. This is much more efficient than the continuous monitoring required to find the periods of monotransit candidates.
Secondly, duotransits are more robust against false positive signals. We can check that the two transit signals for a duotransit candidate match in depth, total duration, ingress and egress duration, limb darkening parameters, and impact parameter. By contrast, we are far less certain that a single monotransit event is not caused by some systematic or non-planetary astrophysical event.
Cooke et al. [2018] predicted that hundreds of long-period planets would be detectable as monotransit events in the TESS sample, with similar results found by

Villanueva et al. [2019]. Furthermore, Cooke et al. [2021] found that many of these will have a second detectable transit in Cycle 3 of TESS data, making the true orbital period one of an average of 38 period aliases.

Both mono- and duotransits require extensive follow-up with both photometric and radial velocity observations in order to confirm the transit signal, orbital period, radius and mass. Constraining the period of a candidate can greatly reduce the number of radial velocity measurements needed to confirm the exoplanet and measure its mass [e.g. Gill et al., 2020c].

In this paper we set out our search for duotransits from the Cycle 1 and Cycle 3 TESS FFI (Full-Frame Image) lightcurves. In Section 5.2 we describe the TESS data that we use to search for duotransit candidates. In Section 5.3 we outline our search algorithm and vetting procedure. In Section 5.4 we set out the results of our search, including the details of the 85 duotransit candidates. Finally in Section 5.5 we discuss the prospects for confirming these duotransit candidates via follow-up photometric and spectroscopic programmes.

5.2 TESS Observations

TESS is a space-based NASA mission focusing on the discovery of transiting exoplanets around bright stars [Ricker et al., 2015]. TESS has four cameras, each equipped with a grid of four CCDs for a total combined field-of-view of TESS of $24^\circ \times 96^\circ$. In Cycle 1 (2018 Jul 25 - 2019 Jul 17), TESS observed almost the entire Southern Ecliptic Hemisphere in 13 Sectors, each observed for a period of approximately 27 days. Each TESS sector has a gap of approximately 2.4 days, during which time the satellite downlinks data. There is a similar gap in between Sectors. Other gaps in the data can be due to technical problems with the spacecraft or scattered light (mostly from the Earth) making some image frames unusable [e.g. Dalba et al., 2020]. Select stars were observed with 2 minute cadence, while the full frame images (FFIs) were observed with a cadence of 30 minutes.

TESS reobserved the Southern Ecliptic Hemisphere in Cycle 3 (2020 Jul 5 - 2021 Jun 24), with the FFIs collected with a shorter cadence of 10 minutes. During Cycle 3, TESS slightly shifted its survey fields in order to cover spatial gaps in between the Cycle 1 Sectors.

For our search for duotransit candidates, we use the TESS full-frame image (FFI) light curves produced by the Science Processing Operations Center pipeline [SPOC; Jenkins et al., 2016], which are publicly available from the Mikulski Archive for

Space Telescopes (MAST)[2]. The SPOC pipeline produces FFI light curves for approximately 160,000 stars per sector, based on selection criteria set out in Caldwell et al. [2020].

We focus solely on the Southern Ecliptic Hemisphere, as at the time of writing TESS had completed its campaign of the Southern Ecliptic in two cycles. We use Sector 1-13 data from Cycle 1, and Sector 27-38 data from Cycle 3. In total, this results in a sample of 1,422,473 stars. We search light curves from the Presearch Data Conditioning Simple Aperture Photometry [PDCSAP; Stumpe et al., 2012, 2014; Smith et al., 2012] lightcurves, which have instrumental systematic trends removed from the Simple Aperture Photometry (SAP) flux, but should retain stellar variability including any transit events.

In addition to using flux measurements from the FFI PDCSAP lightcurves, we also make use of the sky background and momentum centroiding measurements provided in the PDCSAP lightcurve files via the keywords SAPBKG and MOMCENTR1/MOMCENTR2 respectively. These data allow us to rule out a large number of false candidates as described in Section 5.3.2.

5.3 Duotransit Search

Our search for TESS duotransit candidates arises out of a more general search for TESS monotransits. We therefore begin by searching the entire set of 1,422,473 SPOC PDCSAP FFI light-curves for monotransit events, and then we match up events to detect duotransit candidates.

5.3.1 Searching for Monotransit Events

We begin by downloading the SAP and PDCSAP SPOC FFI light-curve products from MAST. To remove bad data points from the light-curves we discarded data points with QUALITY bit values above 0. We read the meta information for each light-curve, including the TIC ID, effective temperature, stellar radius, and metallicity if available. We assume a solar metallicity of 0 dex for stars with no metallicity value available. We split each lightcurve into segments defined by gaps in excess of 2.4 hours and normalise each separately. This accounts for gaps in individual orbits due to spacecraft data download times and regions of data flagged by the SPOC algorithm. For each segment, we smooth the lightcurve using an iterative Savitzky–Golay filter (5 iterations using a threshold of 3-σ) with a window size 48 hours [e.g. Hattori et al., 2022]. This window size strikes a balance of removing

[2]Accessible at `https://mast.stsci.edu/`

stellar activity but ultimately sets an upper limit on the width of transit events our algorithm can detect. Our tests show that transit widths below ~ 2.3 days are easily detectable using this filter width. For events wider than this, we find that the Savitzky–Golay filter begins to confuse transit signals with stellar activity and thus the event is not recovered. In addition, our tests showed that the change in cadence between Cycle 1 (30 minutes) and Cycle 3 (10 minutes) had a negligible effect on the filter. For a warm Jupiter in a circular orbit around a Solar type star, we estimate an upper limit to the possible recovered orbital periods of in excess of 1000 days.

Once the lightcurves are normalised and flattened, we pass them to `monofind`, our custom monotransit detection algorithm. `monofind` searches for monotransit events in the lightcurve where three consecutive 30-minute data points are 3 median absolute deviations below the normalised median of the lightcurve. An example of this method is shown in Figure 5.1, as applied to TOI-2447 (Gill et al., submitted). For the Cycle 1 light-curves we use the native 30 minute data points, while for the Cycle 3 lightcurves we bin the native 10-minute cadence by three to a 30-minute cadence to achieve a consistent detection threshold for transit events.

5.3.2 Selecting Duotransit Candidates

After searching all the TESS Cycle 1 and Cycle 3 SPOC FFI lightcurves for monotransit events, we cross match detections to search for stars which show exactly one monotransit event in Cycle 1 and one monotransit event in Cycle 3. This yielded a list of 9718 duotransit candidates.

We then performed a visual inspection of these 9718 lightcurves to check which of these showed two events that could possibly be transit events. This allowed us to remove obvious false positives that had triggered the `monofind` algorithm but did not have two transit-shaped events in the lightcurve. In most instances these were some kind of variable star. This quick visual inspection took us down to a total of 736 reasonable duotransit candidates. The majority of candidates that did not pass this vetting step were caused by asteroids passing through the target and/or background pixel apertures, systematics noise events due to the spacecraft, or changes in the amplitude of variable stars (see examples presented in Figure 5.2).

We examined each of these duotransit candidates in order to ascertain which appeared to be good transiting exoplanet candidates, and which were false-positives. Examples of false-positive scenarios included those causing transit-like events such as eclipsing binary stars, TESS spacecraft systematics (in particular momentum dumps), stellar variability, and Solar System asteroids passing through the back-

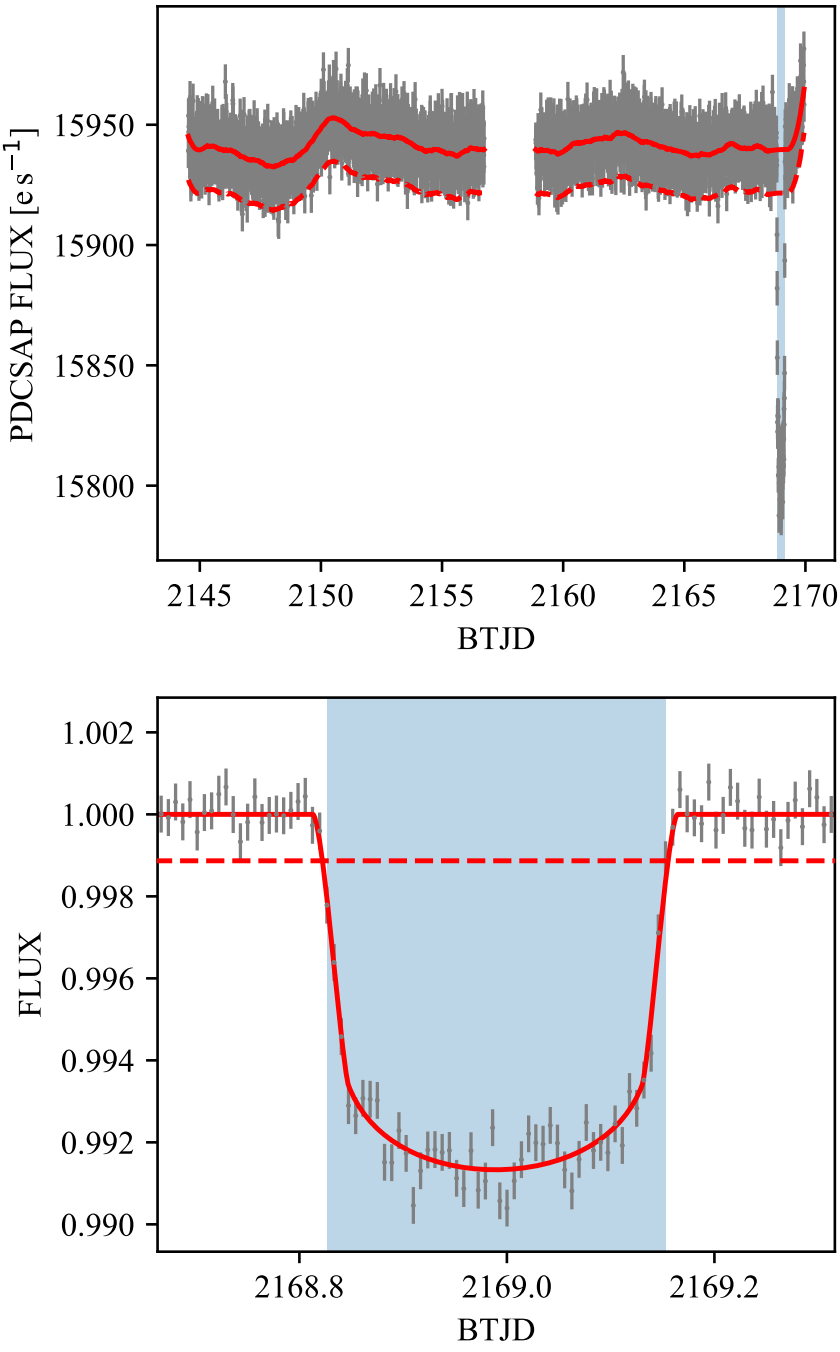

Figure 5.1: **Upper panel:** The TESS Sector 32 lightcurve of TOI-2447 (black) with detrending model (red solid line) and the 3-MAD detection threshold (red dashed line). A single event was detected highlighted in blue. **Lower panel:** An inspection of the transit event with best fitting transit model (red solid line).

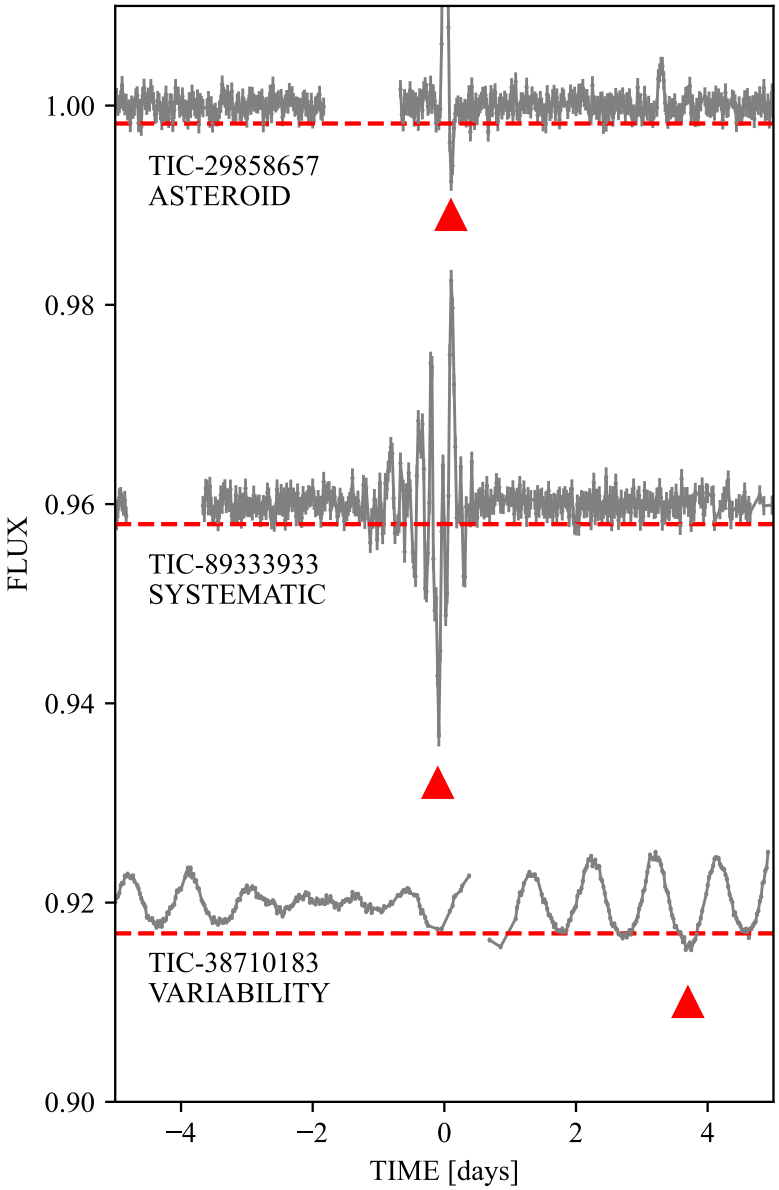

Figure 5.2: Three example duotransit candidates ruled out during the visual inspection of the transit events in the TESS light curves, with an arbitrary flux offset for clarity. The dotted red line indicates the 3 median absolute deviations detection threshold used in `monofind`. The red triangles indicate the event that triggered the detection by `monofind`. From top to bottom, these example events are caused by an asteroid passing through the target and background aperture, systematic noise caused by the spacecraft, and changes in amplitude of a variable stars.

ground and target photometric aperture.

We are able to identify events caused by asteroids crossing the photometric aperture by checking for variations in the sky background (SAPBKG) that correlate with the monotransit event. We also noticed that such events were typically very asymmetrical in shape, and therefore unlike a bona-fide monotransit event. In total, we identified 170 of our initial duotransit candidates as being due to asteroids crossing the photometric aperture in Cycle 1 or Cycle 3.

We identified monotransit events that were likely caused by eclipsing binaries by examining the results from the transit/eclipse fit from `monofind`. We designated any event with a modeled companion radius $> 2\,\mathrm{R}_J$ ($\sim 22\,\mathrm{R}_\oplus$) to be an eclipsing binary, and removed it from our duotransit candidate list. Such well-separated planets are not expected to be inflated like hot Jupiters [e.g. see figure 2 from Lopez & Fortney, 2016] and thus this limit is justified. We also designated a candidate as an eclipsing binary if there was evidence of a secondary eclipse in the lightcurve. Furthermore, we excluded events which had significant depth differences between Cycles 1 and 3. In total we identified 384 eclipsing binaries from our our initial duotransit candidate list.

We searched for blended eclipsing binaries by inspecting the lightcurves of nearby stars, by checking for centroiding offsets during the monotransit events, and by examining the Target Pixel File (TPF) using our custom `spoctpf` tool. `spoctpf` allows us to make a lightcurve for any pixel or set of pixel in the TPF, and helps determine if the monotransit event is on the star of interest, or is on a nearby star. In total we identified 58 blended eclipsing binaries from our our initial duotransit candidate list.

We also examined the pre-normalised and pre-flattened PDCSAP lightcurves, as well as the SAP lightcurves. This was to ensure that neither the PDCSAP algorithm nor our own normalisation and flattening had significantly altered the shape of the detected monotransit events. We also inspected by-eye the full unflagged SPOC lightcurve for additonal transit events that may have been excluded from the PDCSAP data.

Finally we checked if any of the duotransit candidates had an associated Data Validation Report [DVR, Twicken et al., 2019]. DVRs are created for potential TESS planets candidates processed with the SPOC pipeline and contain initial findings about the system including a detailed model fit and analysis of nearby stars to exclude blend scenarios. If a DVR determined a candidate to be a false-positive, we investigated the target further to assess if it warranted exclusion from our list.

Some candidates displayed depth differences between the Cycle 1 and Cycle 3 events.

SPOC lightcurves use unique masks for each individual Sector which may lead to different amounts of dilution from neighboring stars depending on telescope pointing and orientation for each sector [Bryant et al., 2023]. This should be accounted for in the detrended SPOC data (PDCSAP) but might not be perfect, and thus small sector-dependent depth differences are expected ($\lessapprox$2 ppt), particularly in crowded fields. Some candidates had larger depth and width differences, which could be multi-planet systems or blended eclipsing binaries. However, since they do not meet our criteria for selection as duotransit candidates, they were excluded from our list. We also found 39 duotransit candidates that we associate with spacecraft systematics (stray light, momentum dumps etc.[3]). This number also includes a few events resulting from stellar variability that was poorly matched by our detrending model.

A flowchart illustrating the candidate search and vetting process, and the associated numbers of candidates categorised at each stage, is shown in Figure 5.3.

In summary, out of the 1,422,473 unique TIC IDs, 9718 duotransit candidates were identified by the `monofind` algorithm, and after visual inspection this was reduced to 736 candidates pre-vetting. As a result of the vetting process, 58 objects were classified as blended eclipsing binaries ('blends'), 170 as Solar System asteroids, 384 as eclipsing binaries, and 39 as events caused by either spacecraft systematics or poorly-detrended stellar variability. We list a sample of these events along with their designation in Table 5.4. The vetting process left us with a final number of 85 duotransit candidates that we present as likely planetary in nature in this paper.

5.3.3 Modelling Candidate Duotransit Events

In order to derive planetary parameters for the candidates, as well as the most likely period aliases, we must fit the available transits. However, most transit model fitting requires a priori knowledge of the orbital periods, and is certainly not optimised to sample the extremely narrow but widely-separated period regions found for duotransits. We used the `MonoTools` package [Osborn, 2022] which fits transits in a way agnostic of orbital period and then computes the posterior density function of the planet candidate from the orbital velocity implied from the transit impact parameter, radius ratio and duration. This has previously been used to model other duotransiting planet candidates that were subsequently confirmed [e.g. Osborn et al., 2021a, 2022].

`MonoTools` fits transits using the `exoplanet` python library [Foreman-Mackey et al., 2021a]. Stellar parameters from the TESS Input Catalogue [TICv8; Stassun et al.,

[3]TESS Instrument Handbook; `https://archive.stsci.edu/tess/tess_drn.html`

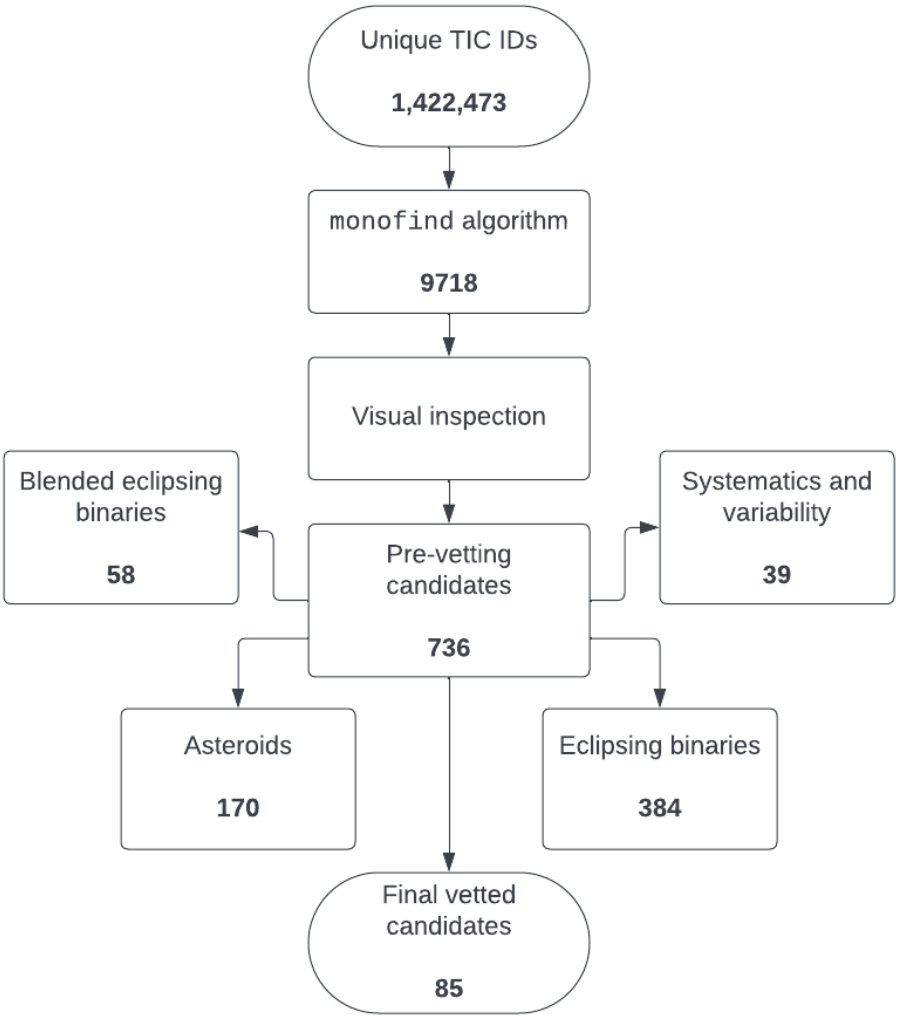

Figure 5.3: Flowchart of the `monofind` algorithm candidates and the vetting process that followed, with the number of candidates categorised at each stage as blended eclipsing binaries ('blends'), asteroids, eclipsing binaries, and other systematics and stellar variability features.

2019] were used as priors for each of the fits; as was the Kipping [2013a] eccentricity prior, the Espinoza & Jordán [2016] impact parameter prior, and quadratic limb-darkening parameters constrained using theoretical predictions for the TESS bandpass of Claret [2017]. In the majority of cases, a cubic spline was fit to the transit-masked TESS PDCSAP flux in order to pre-flatten the lightcurve and a window of 5.5 transit durations was cut around the transit. However, after modelling some of these fits appeared to poorly model the out-of-transit variability. In these cases we turned to a simple harmonic oscillator (SHOTerm) `celerite` Gaussian process [Foreman-Mackey et al., 2017a], which we constrained by first sampling out-of-transit data and then using the inferred hyperparameter distributions as priors for a combined model fit. A log scatter parameter was used to encapsulate additional noise for each transit. The transit model was then sampled using the Hamiltonian Monte Carlo of Salvatier et al. [2016] using a burn-in phase of 800 steps and 1500 samples on each of four independent chains, resulting in typical effective sample sizes of 2500-3000 for each parameter for each candidate. The derived parameters are summarised in Table 5.3. The probabilistic planetary period distributions are shown in Table 5.3 and in Figure 5.4 ordered from shortest to longest.

5.4 Results

5.4.1 85 Duotransit Planet Candidates

Following the methods described in Section 5.3, we have found a total of 85 duotransit planet candidates from our `monofind` search and vetting of the SPOC FFI lightcurves for the Southern Ecliptic TESS fields (Sectors 1-13, 27-34). The stellar properties of our candidates are set out in Table 5.1, where N_{sec} denotes the total number of TESS sectors in which the target was observed. The transit event parameters are set out in Tables 5.2 & 5.3, including the central transit times T_{c1} and T_{c2} of the Cycle 1 and Cycle 3 events respectively, and the separation between the two events in days ΔT_c. We also include the *Gaia* flags of NSS (Non-Single Star), where 0 denotes a good single-star solution, 1 denotes an astrometric binary, 2 denotes a spectroscopic binary and 3 denotes an eclipsing binary; and the *Gaia* robust radial velocity (RV) amplitude in $\mathrm{km\,s^{-1}}$, calculated using the standard deviations of individual RV measurements as set out in *Gaia* Data Release 3 [DR3, Gaia Collaboration, 2022]. We do not remove candidates from our target list based on these values, however, since an NSS designation is often consistent with the presence of a planet and it is not clear how robust the *Gaia* DR3 RV amplitudes are [e.g. Seabroke et al., 2021]. In Table 5.3, we also show the most probable value of P_n (P_{marg}) and

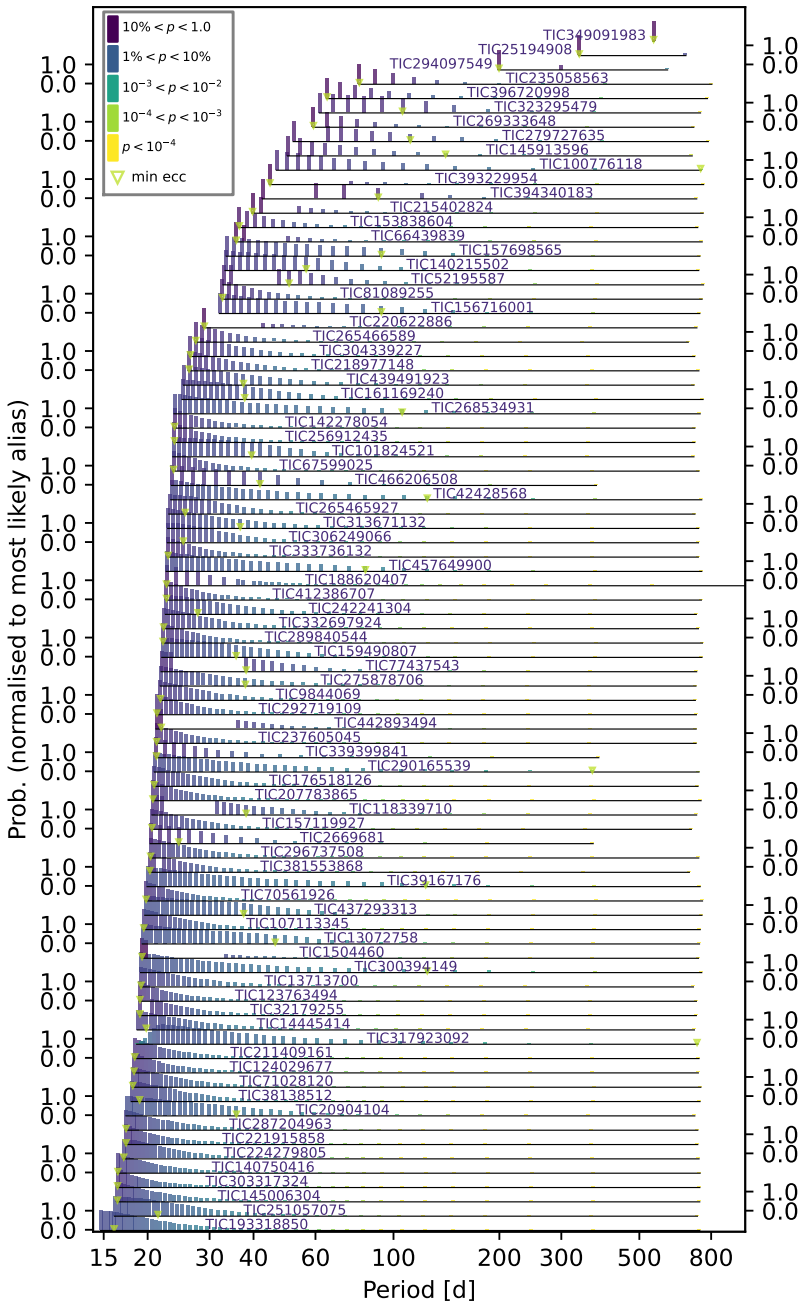

Figure 5.4: Probability distribution of possible periods for each duotransit candidate as computed by `MonoTools`, normalised to the most likely period alias. The vertical colourbars refer to six steps in the log probability of each alias, and the green triangles represent the minimum eccentricity aliases.

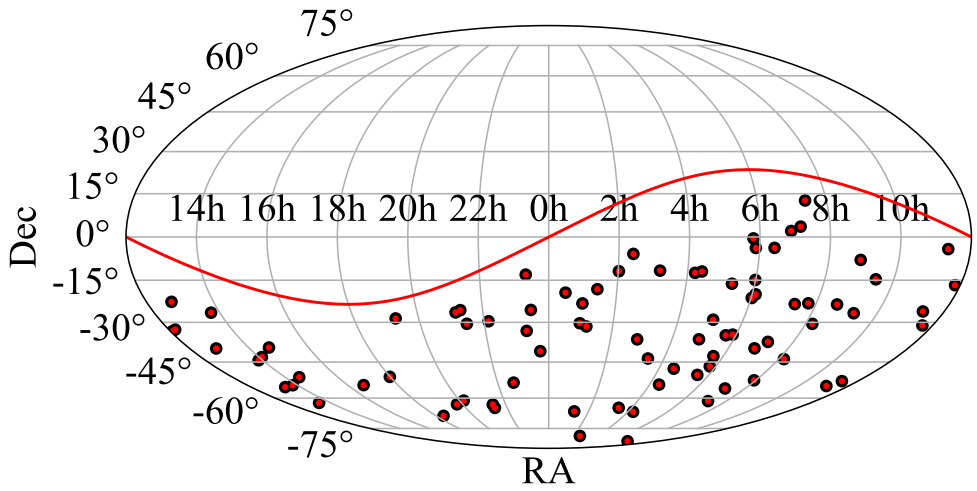

Figure 5.5: The ecliptic plane (solid red line) with the positions of the 85 duotransit candidates marked with red-inset black points.

the corresponding value of n ($N_{\rm alias}$).

The transit events for all 85 duotransit candidates are plotted in Figures 5.14-5.18. We plot the best fit transit models for each event from the `monofind` algorithm (see Section 5.3.1). We also plot the sky distribution of the candidates in Figure 5.5.

Figure 5.6 shows where our duotransit candidate host stars lie on the HR diagram, with most on the main-sequence spanning spectral types A-K, some on the main-sequence turn off, and one in the hot sub-dwarf regime (see Section 5.4.2). Our candidates span a range of brightness between $8 < \mathrm{T_{mag}} < 14$, with most candidates lying between $10 < \mathrm{T_{mag}} < 13$; see Figure 5.11. This magnitude range is largely governed by the magnitude distribution of the SPOC FFI lightcurves that cuts off at around $\mathrm{T_{mag}} = 13.5$ due to the number of lightcurves per sector being restricted to approximately 160,000 [Jenkins et al., 2016].

We calculated the total SNRs (Signal-to-Noise Ratios) for each of our candidates as a function of the SNRs of each individual transit event. The SNR of each transit event was estimated using the double box approximation model described by Kipping [2023]. Using this square well transit model, the SNR for each transit event with a depth δ in ppm, a duration $T_{\rm dur}$ in hours, light curve noise σ in ppm, and a contamination ratio C was calculated using Equation 5.2:

$$\mathrm{SNR} = \frac{1}{C} \times \frac{\delta}{\sigma} \sqrt{T_{\rm dur}}. \tag{5.2}$$

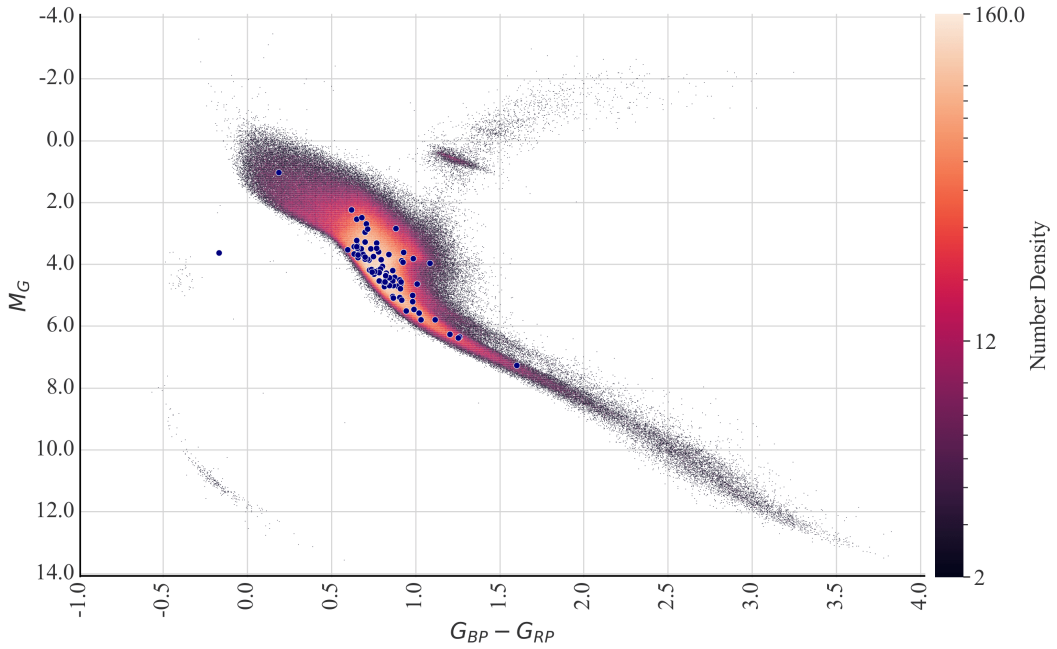

Figure 5.6: *Gaia* DR3 [Gaia Collaboration, 2022] colour-magnitude diagram (corrected for extinction and reddening) showing all stars with TESS full frame image SPOC lightcurves from Cycle 1 and Cycle 3 that have measured *Gaia* DR3 distances. Blue circles indicate the positions of our 85 duotransit candidates. The colourbar shows the relative number density of stars at each location in the diagram. For six of the duotransit candidates there was no *Gaia* DR3 distance measurement so we estimate the distance from the parallax and do not correct for reddening or extinction.

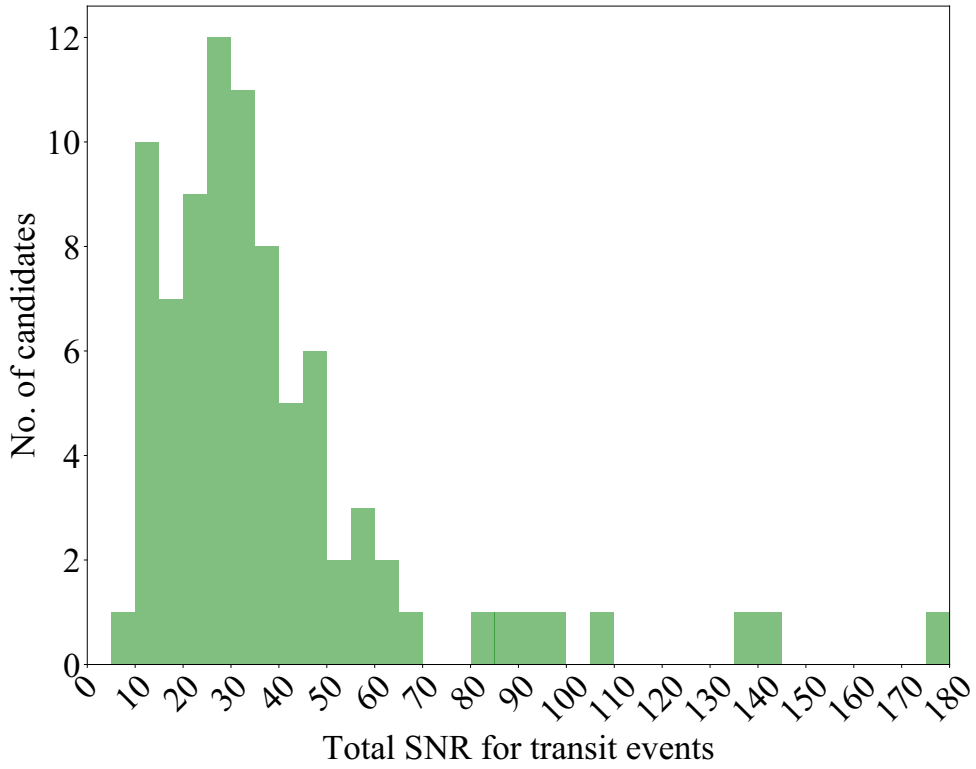

Figure 5.7: The distribution of total transit event SNR values (see Section 5.4.1) for our 85 duotransit candidates.

The contamination ratio and noise value were both extracted directly from the headers of the SPOC lightcurves. In some cases these values were missing from the headers of the Cycle 3 lightcurves, in such instances we used the same noise as the Cycle 1 lightcurve. To combine the SNR across both transit events we add the individual SNR for each event in quadrature.
We plot the distribution of the total SNR values for our 85 candidates in Figure 5.7, and find that most candidates have a SNR between 10-70, with the distribution peaking at SNR values of 25-30. There is one candidate with a total SNR value below 10 and four candidates with a SNR value above 100.

5.4.2 Candidates of Special Interest

Based on our *Gaia* H-R diagram in Figure 5.6, we identify three candidates that are distinct from the rest.

A1V type host star, TIC-221915858

TIC-221915858 (candidate 45) is the most luminous star in our sample and resides in the region of the colour-magnitude diagram where the main-sequence approaches the sub-giant branch (Figure 5.6). This is complemented by *Gaia* DR3 stellar parameters suggesting that TIC-221915858 is a hot (T_{eff} = 9000 K) A1 star with a RUWE of 0.814 indicative of a good astrometric solution. The fitted spectral energy distribution in TIC V8, which uses *Gaia* DR2 along with 2MASS colours, suggests TIC-221915858 is a main sequence A1 (T_{eff} = 9475 ± 187 K) star with mass and radius of $2.41 \pm 0.33\,M_\odot$ and $2.47 \pm 0.09\,R_\odot$ respectively. In addition to being the most luminous host star in our sample, TIC-221915858 is also the hottest on the main sequence and represents a under-sampled population of exoplanets around hot stars. If a planet is confirmed around TIC-221915858, it would be the hottest planet host star discovered by the TESS mission[4]. The 5.74 ppt transit depth is detectable with ground-based photometric facilities and so it is possible to recover the orbital period with ground-based instruments. However, recovering the spectroscopic orbit will be challenging, in-part due to the typical rotation and lack of absorption lines in A-type stars making it difficult to measure a precise CCF (Cross-Correlation Function) centre. Doppler tomography [e.g. Watson et al., 2019] has been used successfully to determine the radial-velocity semi-amplitude of fast-rotating stars with broad CCFs [Temple et al., 2018, 2019] and could be applicable to TIC-221915858 once the orbital period is known. We provide the light curves and transit models for this candidate in Figure 5.15.

Late K-dwarf host, TOI-4310/TIC-303317324

While the majority of our duotransit candidates orbit F, G and early K type dwarf stars, the candidate TOI-4310 (TIC-303317324, candidate 65) is a late K-dwarf star with T_{eff} = 4159 K. This is an outlier amongst our candidates on the *Gaia* colour-magnitude diagram (Fig 5.6), positioned much further down the main sequence than any of our other candidates. The estimated radius of TOI-4130 is $0.72\,R_\odot$, and the transit model indicates the transiting planet would have a radius of $2.67\,R_\oplus$, making it one of the smallest of our duotransit planet candidates. We provide the light curves and transit models for this candidate in Appendix Figure 5.14.

[4]exoplanetarchive.ipac.caltech.edu (as of 2023 Oct 10)

Hot subdwarf host, TOI-709/TIC-396720998

TOI-709 (TIC-396720998, candidate 78) has two ~ 6 ppt deep transits with durations of $\sim$4.3 hours. It is the only candidate in our list categorised as a hot subdwarf host star [LB 1721; Culpan et al., 2022], residing on the $G_{BP} - G_{RP} < 0$ region of the colour-magnitude diagram in Figure 5.6 outside of the main population of exoplanet hosts from our candidates. Hot subdwarfs are evolved compact stars, mainly resulting from enhanced mass-loss at the tip of the red giant branch, which likely occurred due to binary interaction [Han et al., 2002, 2003; Maxted et al., 2001; Pelisoli et al., 2020]. This makes them targets of interest for probing the survivability of planets to both stellar evolution and binary environments. Most hot subdwarf companions fall into two populations containing either close white dwarf or M-dwarf/brown dwarf companions or wide FGK-type companions [e.g. Schaffenroth et al., 2022], with no planetary companions confirmed to date [e.g. Van Grootel et al., 2021; Thuillier et al., 2022].

Parameters from TICv8 poorly constrain the mass and a radius of the host to $0.5 \pm 0.3\,\mathrm{M}_\odot$ and $0.15 \pm 0.11\,\mathrm{R}_\odot$ ($\log\ g = 5.8 \pm 0.9$), which are consistent with a hot subdwarf and make it the smallest candidate host star in our list. Jeffery et al. [2021] obtained for this star a T_{eff} of $45,600 \pm 1000$ K and a consistent $\log g$ of 6.08 ± 0.04 and classified it as helium-rich sdO (He-sdO). They reported no radius or mass estimate. To derive a radius consistent with the precise T_{eff} and $\log g$ of Jeffery et al. [2021], we performed a spectral energy distribution (SED) fit using `speedyfit`[5]. We employed spectral models from the Tübingen NLTE Model-Atmosphere Package [TMAP, Werner & Dreizler, 1999; Werner et al., 2003; Rauch & Deetjen, 2003]. Initial attempts revealed the existence of excess flux towards the red/near-infrared compared to the hot subdwarf model. We therefore included a second component in the fit, modelled with ATLAS9 spectra [Castelli & Kurucz, 2003]. The $\log g$ was kept fixed at the spectroscopic value for the hot subdwarf (as it is poorly constrained by a SED fit), and a Gaussian prior was applied on the temperature. The temperature of the companion star was allowed to vary freely within 3500 and 6000 K [restricted by the lack of contribution to the spectrum in Jeffery et al., 2021, : higher temperatures would lead to visible lines in the spectrum; for lower temperatures, the hot subwarf would completely dominate and a companion would have no effect] and the $\log g$ was left to vary in the range of 4 to 5. A prior on the *Gaia* parallax was also applied, which enables the determination of precise radii. The MCMC fit converged to radii of $0.18^{+0.06}_{-0.03}\,\mathrm{R}_\odot$ and $0.88^{+0.30}_{-0.15}\,\mathrm{R}_\odot$ for

[5] https://speedyfit.readthedocs.io/

the hot subdwarf and the companion, respectively. The companion T_{eff} was found to be 5100±120 K, consistent with a K-type main sequence star. FGK-type companions are found with 30 per cent of hot subdwarfs [Stark & Wade, 2003], and their periods are in the range of 100-1000 days [e.g. Vos et al., 2019], which could be consistent with the orbital period of the duotransit signal. We note that there is also another much deeper (5.8%) transit/eclipse signal with a 32 day period that is reported in TFOP, and was the reason this candidate was flagged as a TOI. However that signal is distinct from the duotransit signal that we report in this paper. We provide the light curves and transit models for this candidate in Appendix Figure 5.17.

5.4.3 Other notable candidates

Continuous Viewing Zone candidates

Three of our candidates lie inside or close to the TESS Continuous Viewing Zone (CVZ), where targets are observed in every Sector. TIC-25194908 (candidate 8) was observed in Sectors 1-13 during Cycle 1, and Sectors 27-38 in Cycle 3, for a total of 24 Sectors, with only two transits detected. TIC-294097549 (candidate 62) was observed in multiple Sectors across Cycle 1 and Cycle 3 for a total of 13 Sectors, also with only two transits detected. This additional TESS coverage rules out most alias periods, and only 2 and 3 periods are possible respectively for these candidates. These are likely to be among the longest periods from our sample, with the remaining allowed periods in the range 337–675 d and 299–599 d respectively (see Table 5.3).

TIC-349091983 (candidate 74) was observed in all Sectors in Cycle 1 with the exception of Sector 5, and again in Cycle 3 in all Sectors with the exception of Sector 35, for a total of 24 Sectors. There is only one possible period for this candidate of approximately ~ 549 days, and thus the true orbital period is solved from TESS alone.

TOI and CTOI candidates

TESS Objects of Interest (TOIs) are planet candidates that have been vetted by the TESS Science Office (TSO), the TESS Follow-up Observing Program (TFOP) and designated as promising candidates for follow-up and publication. 11 of our total 85 candidates have previously been flagged as TESS Objects of Interest (TOI), and these are labelled in Table 5.1.

Another 14 of our 85 candidates have previously been flagged as Community TESS Objects of Interest (CTOIs), and these are also labelled in Table 5.1. CTOIs are

typically planet candidates submitted by additional community projects outside of the official TOI planet search pipelines, and CTOIs are reviewed by the TESS TOI team before being promoted to TOI status and assigned a number.
The majority of CTOIs have been identified by the *WINE* (Warm gIaNts with tEss) collaboration [e.g. Schlecker et al., 2020; Jordán et al., 2020; Hobson et al., 2021], the *PHT* (Planet Hunters TESS) project [Eisner et al., 2021], and the *STF* (Single-Transit Finder) project.

Confirmed and published candidates

Two of our duotransit planet candidates have already been confirmed and published. TOI-5153 (candidate 25; TIC-124029677) has been published by Ulmer-Moll et al. [2022]. The planet is a large warm Jupiter ($\mathrm{M} = 3.26^{+0.18}_{-0.17}\,\mathrm{M}_J$, $\mathrm{R} = 1.06^{+0.04}_{-0.04}\,\mathrm{R}_J$) orbiting an F8-type star on a period of 20.33 days. We find that our fitted planetary radius from Table 5.3 is in agreement with this published value. TIC-466206508 (candidate 85; TOI-5542) has also been published by Grieves et al. [2022]. The planet is an old warm Jupiter orbiting a relatively metal-poor G-dwarf host star on a period of 75.12 days, with a mass of $\mathrm{M} = 1.32^{+0.10}_{-0.10}\,\mathrm{M}_J$ and a radius of $\mathrm{R} = 1.01^{+0.04}_{-0.04}\,\mathrm{R}_J$. Other publications for these solved systems are forthcoming, e.g. TIC-77437543 (Henderson et al. 2023, in preparation), TIC-333736132 (Kendall et al. 2023, in preparation), and TIC-224279805.

5.4.4 Previous TOIs and CTOIs identified as false positives

Some of the candidates that were detected in our transit search but rejected as false positives have previously been announced as TOIs or CTOIs. In all cases, we found these to be examples of passing asteroids that caused peaks in the SAP background time series and hence false dips in the target light curve (see Section 5.3.2). These false positives are TOI-4312 (TIC-251086776) and the CTOIs TIC-152070435 and TIC-275180352.

5.5 Discussion

From our initial set of 1,422,473 unique TIC IDs, 9718 were identified as duotransit candidates from our `monofind` algorithm in the first instance, and after a quick visual inspection to reject obvious variable stars this was reduced to 736 candidates pre-vetting (see Section 5.3.2. From these candidates, 651 were determined to be caused by false-positive scenarios including blended sources, asteroid crossing events,

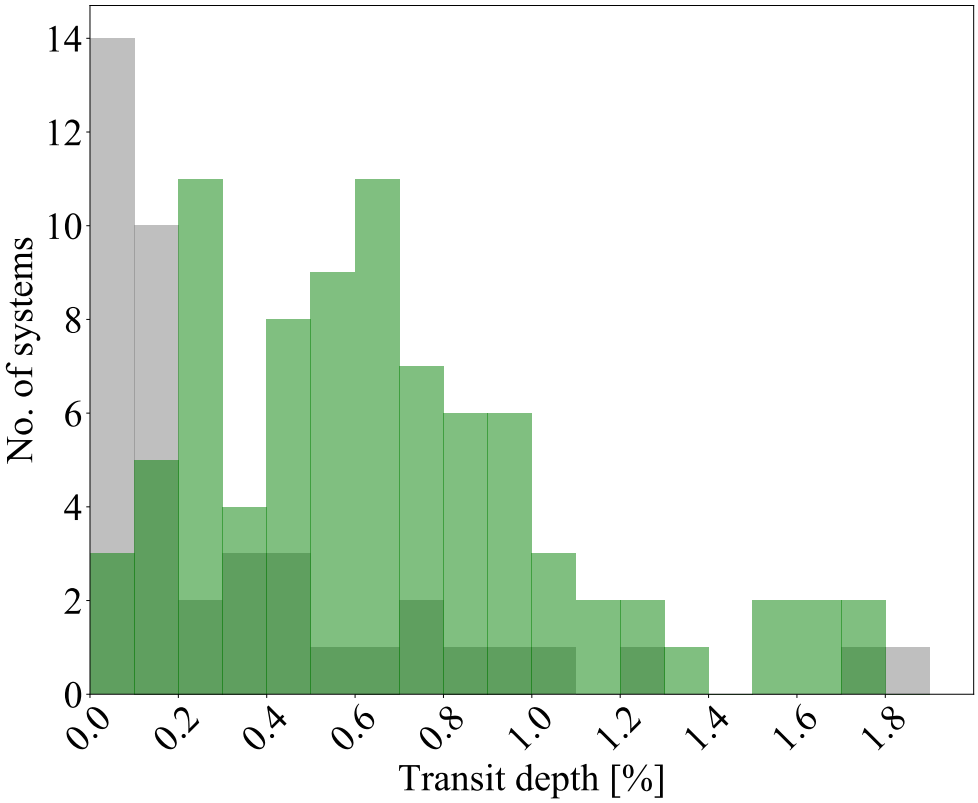

Figure 5.8: The distribution of transit depths for our duotransit candidates (green) and the confirmed TESS discovered exoplanets from the Southern Ecliptic Hemisphere (grey).

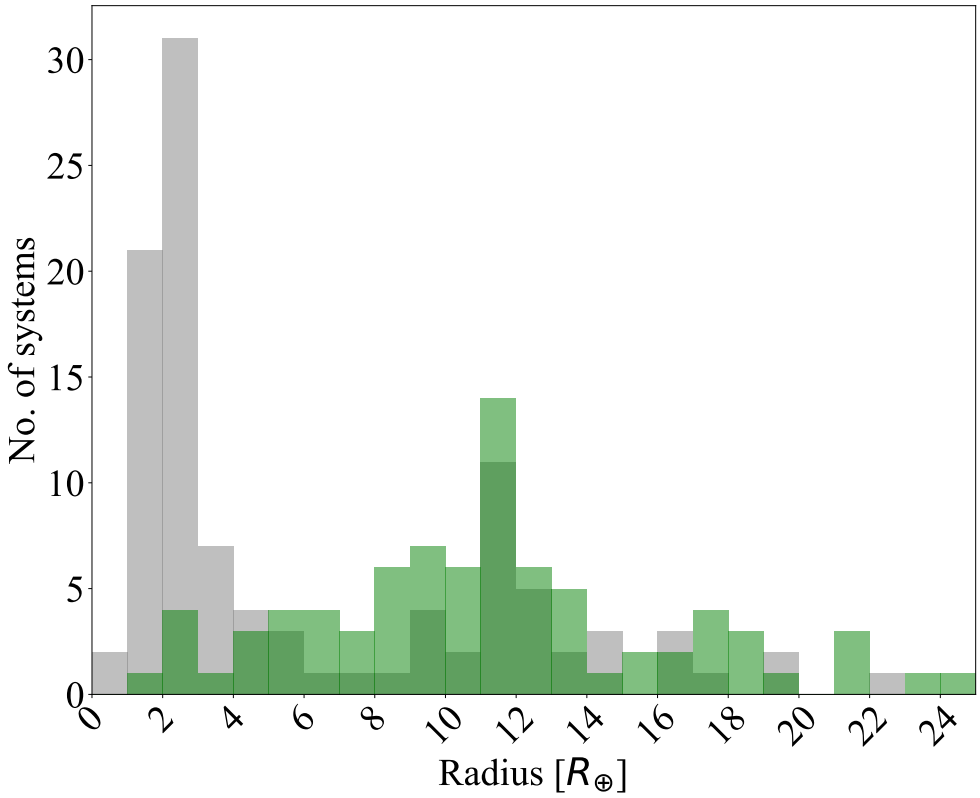

Figure 5.9: The distribution of planet radii for our duotransit candidates (green) and the confirmed TESS discovered exoplanets from the Southern Ecliptic Hemisphere (grey).

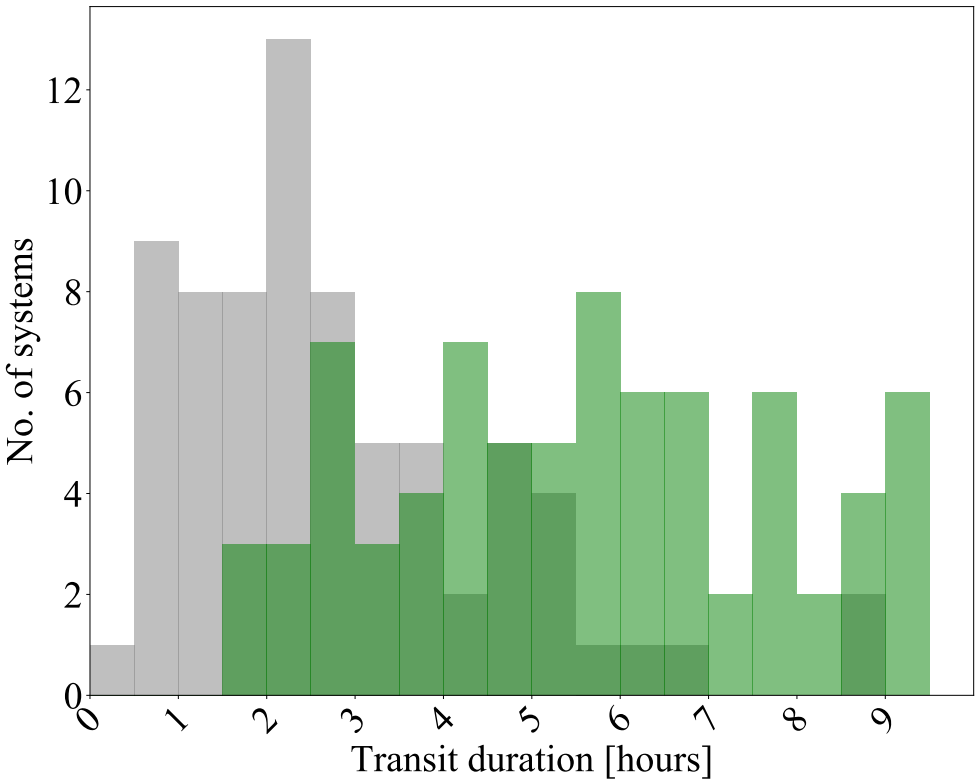

Figure 5.10: The distribution of transit durations for our duotransit candidates (green) and the confirmed TESS discovered exoplanets from the Southern Ecliptic Hemisphere (grey).

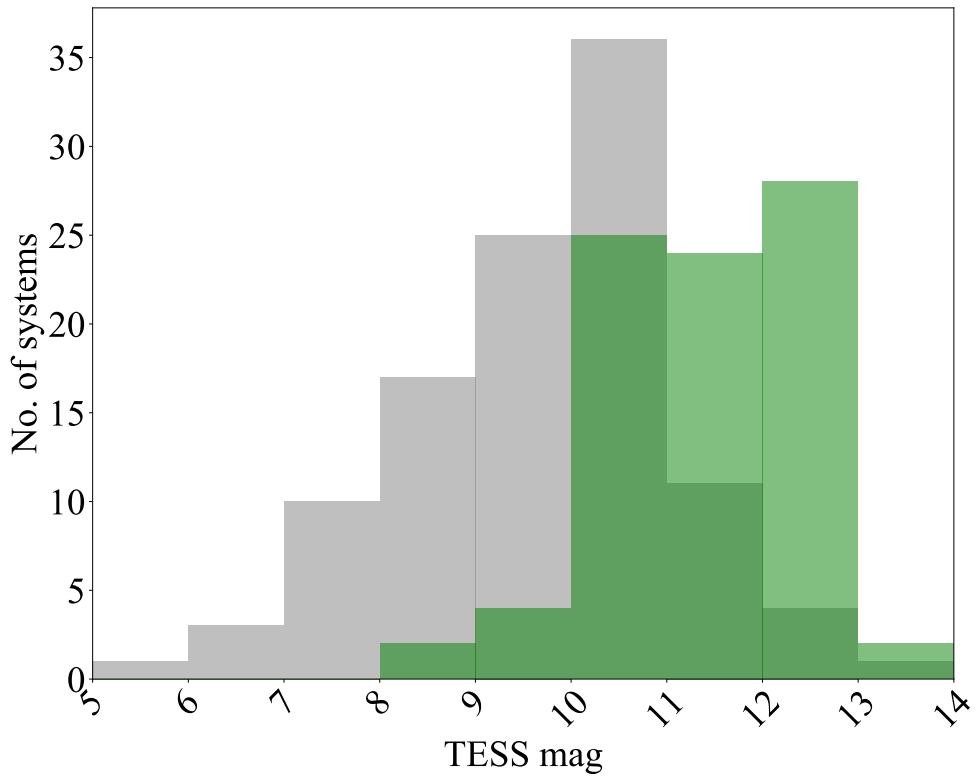

Figure 5.11: The distribution of TESS magnitudes for our duotransit candidate host stars (green) and the confirmed TESS discovered exoplanet host stars from the Southern Ecliptic Hemisphere (grey).

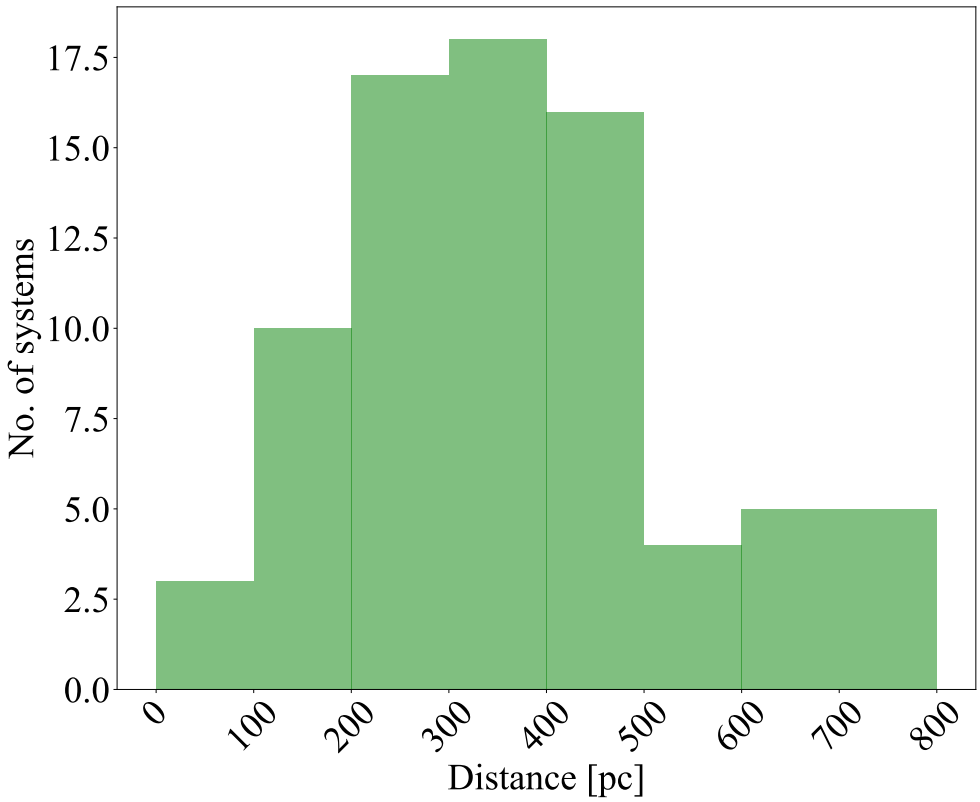

Figure 5.12: The distribution of *Gaia* DR3 distances (in parsecs) for our duotransit candidate host stars.

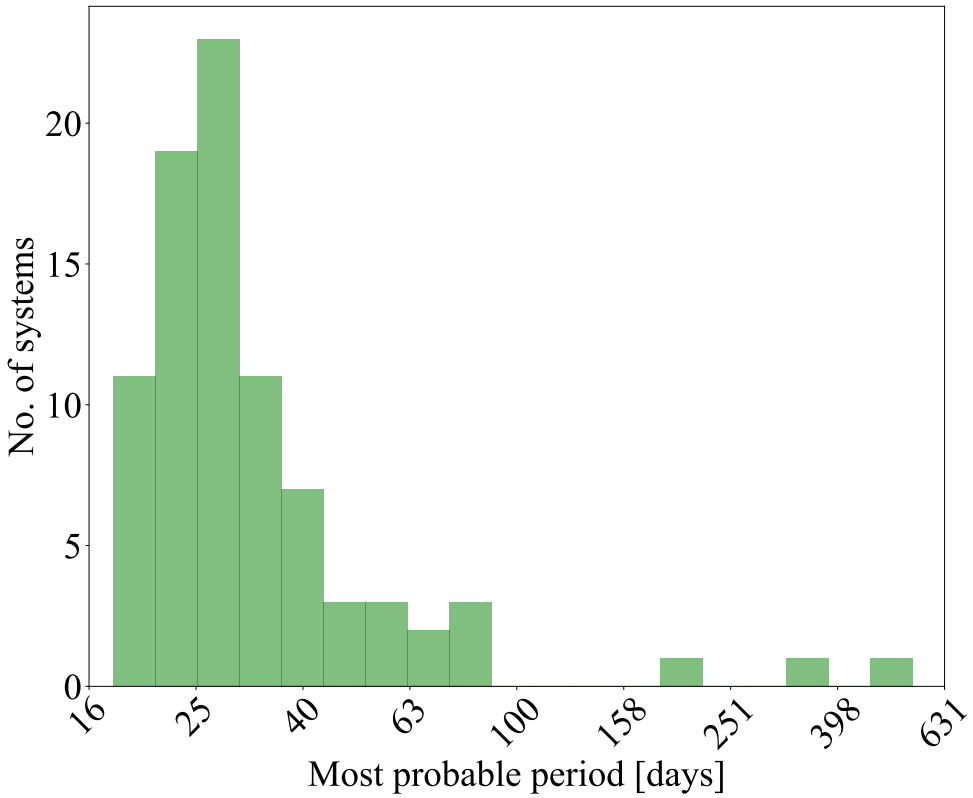

Figure 5.13: The distribution of most probable periods from modelling with `MonoTools` for our duotransit candidates.

eclipsing binaries, systematics and stellar variability. This leads to a final list of 85 duotransit candidates presented in this work (see Section 5.4 and Tables 5.1-5.3). We have submitted all of our non-TOI/CTOI duotransit planet candidates to the TESS follow-up program (TFOP) (60 candidates). We hope that this will allow the community to follow-up these interesting systems further with the aim of determining their true orbital periods and providing confirmation and full characterisations of new long-period planets.

5.5.1 Duotransit candidate properties

We plot the transit depths of our 85 duotransit candidates in Figure 5.8, and for comparison we overlay the TESS planets that have been confirmed in the Southern Ecliptic Hemisphere[6]. The transit depths of our duotransit candidates range from approximately 0.1 percent to 1.8 percent, peaking around 0.7 percent. This is significantly deeper than is typical for the confirmed TESS exoplanets, the majority of which are less than 0.2 percent. This depth difference is to be expected given that the `monofind` algorithm is designed to detect individual high-SNR transits, which will naturally be deeper than the general TOI population.

In Figure 5.9 we plot the best-fitting radii of our duotransit planet candidates, again in comparison with the TESS confirmed planet sample. We find that our sample peaks at around the radius of Jupiter (11 $R_\oplus$), which is also to be expected for a sample of individual high-SNR transits. Our sample extends to radii exceeding 16 $R_\oplus$, and while the sample of confirmed TESS planets also extends to similar radii, these are hot Jupiters with radii inflated by irradiation, which we would not expect for long-period planets [Gu et al., 2003]. Nevertheless, rather than applying an arbitrary upper radius cut, we keep these candidates in our sample for completeness and will rely on follow-up observations to determine the upper radius limit of long-period planets.

Figure 5.10 shows that most of our candidates have significantly longer transit durations than many of the confirmed TESS planets. This is expected as we are probing planets with orbital periods in excess of ~ 17 days, which is significantly longer than the median orbital period of TESS planets (~ 5.8 days).

In Figure 5.11 we plot the TESS magnitudes of the host stars of our candidates, again comparing with the sample of confirmed TESS planets. Here it can be seen that our long-period planet candidates tend to orbit stars that are significantly fainter than the confirmed planet sample (typically T_{mag} of 10–13). This is for three

[6]NASA Exoplanet Archive; `https://exoplanetarchive.ipac.caltech.edu/`, accessed 2023 Jul 15

reasons. First, the confirmed TESS sample is biased towards bright stars, partly because brighter stars make it easier to detect shallow transits, and partly because follow-up efforts tend to be focused on bright host stars. Second, the much smaller transit probabilities of wide-separation planets means that long-period transiting candidates are rare, and so the brightest detected examples will be around fainter stars, which are more numerous (the absence of brighter examples is not a selection effect because such systems would readily detected). Third, gas giant planets are inherently rarer than the sub-Neptune sized planets that make up the bulk of the confirmed TESS sample. The steep cut-off in our detected candidates at T_{mag}=13 simply reflects the selection criteria for the SPOC FFI lightcurves [Caldwell et al., 2020].

In Figure 5.12 we plot the distances of our duotransit candidate host stars from the *Gaia* DR3 catalog. We find that most candidate host stars are at distances from 200-500 pc, with the furthest object being TIC-218977148 at a distance of $\sim$ 826 pc, and the closest being TIC-303317324/TOI-4310 at a distance of $\sim$ 40 pc.

As described in Section 5.3.3, we use the shape and width of our detected transit events to determine the most probable orbital period for each candidate [e.g. Osborn et al., 2022]. The probability of each allowed alias is indicated on Figure 5.13 and the most probable period for each candidate is listed in Table 5.3. We plot a histogram of these most probable period in Figure 5.4. We find that our distribution peaks at periods around 20-30 days. While these values are the most probable periods according to the information and data available, they are not necessarily the correct values, and the true orbital periods must be determined through follow-up observations. We also note the three candidates in our sample with the longest periods: TIC-294097549 with a value of $P_{\rm marg}$ of 200 days, TIC-25194908 with a value of $P_{\rm marg}$ of 338 days, and TIC-349091983 with a value of $P_{\rm marg}$ of 549 days (see Table 5.3).

5.5.2 Follow-up programme

Photometric period determination

The limited number of discrete period alias for duotransit candidates means that precise orbital periods can be determined efficiently with photometric follow-up targeted at predicted transit times for each alias.

Our own team is actively following up the duotransit candidates presented here using the Next Generation Transit Survey [NGTS; Wheatley et al., 2018]. NGTS is a ground-based facility located at the ESO Paranal Observatory in Chile that deploys

an array of twelve telescopes optimised for photometric detection of exoplanet transits [e.g. Bryant et al., 2020b]. Our monotransit programme with NGTS confirmed the first planet that was initially identified as a single-transit event with TESS [Gill et al., 2020c], and has since confirmed several other long-period planets [e.g. Ulmer-Moll et al., 2022; Grieves et al., 2022, Gill et al., submitted]. We have also confirmed three long-period, low-mass eclipsing binary systems [Gill et al., 2020a; Lendl et al., 2020a; Gill et al., 2020b].
We are also searching TESS Cycle 5 data as it is released for third transits of our duotransit candidates. In some cases this will significantly reduce the number of period aliases to search, although with a similar two-year gap between Cycles 1, 3 and 5 a third transit usually still leaves multiple aliases to be searched.

Radial velocity detections

Our team has also begun a spectroscopic campaign using the *CORALIE* spectrograph [Queloz et al., 1999] on the Swiss 1.2 m Leonhard Euler Telescope at La Silla Observatory (program ID 500) to help confirm our candidates. With a first *CORALIE* spectrum, we are able to identify and remove double-line spectroscopic binary (SB2) systems, and detect rapidly rotating stars from the broadening of the cross-correlation function. With a second *CORALIE* spectrum, taken about one week later, we are able to exclude systems for which the change of measured radial velocity is too large to be consistent with a planetary companion ($>1\ \mathrm{km\,s^{-1}}$). Bright targets hosting relatively massive planetary companions exhibit radial velocity variations detectable with *CORALIE* [$\sim 6\mathrm{m\,s^{-1}}$ for bright stars; e.g. Marmier et al., 2013] and for other targets we use HARPS. Previous efforts to confirm these mono- and duotransiting planets using spectroscopic observations have been successful [e.g. Ulmer-Moll et al., 2022; Grieves et al., 2022; Ulmer-Moll et al., 2023].

5.6 Conclusion

We have presented the discovery of 85 duotransit candidates from the TESS-SPOC FFI light curves from the Southern Ecliptic Hemisphere. The candidates were found using our custom-built `monofind` algorithm through which all SPOC pipeline data products were passed. We also employed a vetting procedure to rule out false-positive scenarios such as eclipsing binaries and asteroids in the sample. A total of 25 of our candidates have previously been flagged as either TOIs or CTOIs, and we found during our vetting process 3 TOI/CTOI objects outside of our duotransits falsely flagged as such that are asteroids. A dedicated program on the NGTS facility

is now being used to determine the true orbital periods of these systems, and we welcome other community efforts in this difficult task. We also have programs on instruments such as *CORALIE* and HARPS to acquire radial velocity measurements to confirm the planetary nature of these systems and to determine the mass of the exoplanets. Once confirmed, these planets will form the basis for characterisation studies into their atmospheric compositions and orbital obliquities, and hence into the formation, evolution and migration of warm and cool gas giant exoplanets.

5.7 Appendix

Candidates and Light Curves

Table 5.1: Properties of the host stars of our duotransit candidates.

ID	TIC ID	TOI/CTOI	RA (deg)	Dec (deg)	T_{mag}	R_* ($R_\odot$)	T_{eff} (K)	N_{sec}
1	1504460	–	131.9658	-23.9895	11.63	1.5	6218	2
2	2669681	–	289.368	-28.5803	11.47	1.88	5160	2
3	9844069	–	48.03923	-11.6808	12.96	1.61	5665	2
4	13072758	CTOI	76.08837	-29.0342	12.22	1.43	6313	2
5	13713700	–	133.6396	-7.94134	12.29	0.97	5864	2
6	14445414	–	110.8209	12.66321	11.02	1.31	6425	2
7	20904104	–	7.41368	-19.3663	9.76	0.88	5628	2
8	25194908	–	63.90318	-66.3519	12.46	1.32	6309	24
9	32179255	–	332.0396	-29.6093	10.52	1.75	5989	2
10	38138512	–	170.4183	-4.19721	12.94	1.34	6300	2
11	39167176	–	88.32738	-3.79767	12.01	1.56	8416	2
12	42428568	–	96.29347	-3.76657	10.83	2.16	6686	2
13	52195587	–	19.24834	-66.1636	12.25	1.2	5736	4
14	66439839	–	14.47851	-30.3231	11.97	1.03	5882	3
15	67599025	CTOI	17.69268	-31.5055	11.96	0.78	4816	2
16	70561926	–	139.2559	-26.7007	11	1.35	6386	2
17	71028120	–	66.12741	-11.9835	10.44	1.37	5596	2
18	77437543	TOI-2490	73.12441	-36.2572	11.28	1.17	5459	3
19	81089255	CTOI	122.6942	-43.8535	11.84	1.43	7459	4
20	100776118	CTOI	88.31784	-34.5185	11.51	1.25	6439	4
21	101824521	–	206.004	-26.4978	12.61	1.23	5553	2

Table 5.1: Properties of the host stars of our duotransit candidates.

ID	**TIC ID**	**TOI/CTOI**	**RA (deg)**	**Dec (deg)**	$\mathbf{T_{mag}}$	$\mathbf{R_*}$ ($\mathbf{R_\odot}$)	$\mathbf{T_{\mathit{eff}}}$ **(K)**	$\mathbf{N_{sec}}$
22	107113345	–	183.0341	-32.6628	10.34	1.31	6696	2
23	118339710	CTOI	129.572	-23.5502	10.35	1.56	6119	3
24	123763494	–	90.30269	-21.2359	11.73	1.22	5568	2
25	124029677	TOI-5153	91.54028	-19.9533	11.21	1.38	6408	2
26	140215502	CTOI	85.15071	-34.7664	11.23	0.93	5528	4
27	140750416	–	116.4382	-23.143	11.81	0.87	5331	2
28	142278054	–	180.7626	-33.343	10.28	2.39	6400	2
29	145006304	–	193.3345	-39.7347	11.3	1.12	6340	2
30	145913596	–	123.1298	-30.5555	10.17	1.45	6467	4
31	153838604	–	68.07396	-47.6088	12.48	0.91	5649	4
32	156716001	–	103.1063	-39.6876	10.9	1.08	6129	4
33	157119927	–	175.2155	-31.1374	11.64	1.04	5765	2
34	157698565	TOI-2589	107.4883	-37.231	10.72	1.07	5938	3
35	159490807	–	220.2349	-39.3757	10.57	1.69	6556	2
36	161169240	CTOI	339.3573	-53.3188	12.12	1.19	5952	2
37	176518126	–	87.1832	-0.49503	10.48	1.36	7927	2
38	188620407	CTOI	350.0511	-13.0494	11.57	1.31	6169	3
39	193318850	–	177.7302	-16.7417	12.76	0.79	5560	2
40	207783865	–	207.0609	-54.4206	10.54	1.04	5936	2
41	211409161	–	321.7768	-30.5273	10.44	0.78	4660	2
42	215402824	–	43.0624	-36.2887	12.97	1.33	6180	4

Table 5.1: Properties of the host stars of our duotransit candidates.

ID	**TIC ID**	**TOI/CTOI**	**RA (deg)**	**Dec (deg)**	$\mathbf{T_{mag}}$	$\mathbf{R_*}$ ($\mathbf{R_\odot}$)	$\mathbf{T_{\mathit{eff}}}$ **(K)**	$\mathbf{N_{sec}}$
43	218977148	–	349.5331	-33.1369	12.58	1.61	6214	2
44	220622886	–	84.89306	-42.6811	12	2.56	5671	3
45	221915858	–	249.513	-54.3579	10.07	2.47	9475	2
46	224279805	CTOI	355.7386	-40.7722	12.15	1.2	5591	2
47	235058563	–	83.51699	-50.1216	12.43	1.47	6438	6
48	237605045	–	103.2896	2.05465	10.29	2.92	6577	2
49	242241304	CTOI	211.5851	-43.0447	11.81	1.14	5781	2
50	251057075	–	36.17507	-5.85401	11.05	0.84	5225	2
51	256912435	–	200.5462	-55.2184	11.8	1.19	5650	2
52	265465927	CTOI	320.9166	-62.9238	12.08	1.16	6099	2
53	265466589	–	321.0794	-64.4743	12.61	1.03	5834	2
54	268534931	CTOI	15.12618	-23.1795	12.22	0.78	5179	2
55	269333648	TOI-2529	118.9944	-52.3549	10.67	1.75	5822	6
56	275878706	–	207.9018	-44.3144	12.17	0.93	5038	2
57	279727635	–	50.59176	-64.4444	12.5	1.05	5851	6
58	287204963	–	30.28722	-11.8835	13.25	1.04	5344	2
59	289840544	–	317.5455	-26.3999	10.64	1.75	5989	2
60	290165539	–	319.8521	-25.5971	11.99	1.33	5895	2
61	292719109	–	107.416	3.56756	10.1	2.08	6216	2
62	294097549	–	107.67	-55.7967	10.47	1.15	5872	13
63	296737508	CTOI	142.1793	-14.6864	9.2	1.27	5700	2

Table 5.1: Properties of the host stars of our duotransit candidates.

ID	TIC ID	TOI/CTOI	RA (deg)	Dec (deg)	T_{mag}	R_* ($R_\odot$)	T_{eff} (K)	N_{sec}
64	300394149	–	170.747	-52.6986	10.13	1.42	5997	2
65	303317324	TOI-4310	351.9037	-25.5081	9.5	0.72	4159	2
66	304339227	TOI-4629	275.9439	-68.3449	8.66	1.13	6012	2
67	306249066	–	166.7285	-54.7388	10.54	1.14	6139	2
68	313671132	–	202.1582	-62.1699	10.08	1.22	5878	2
69	317923092	–	89.85183	-14.9061	12.26	1.34	7604	2
70	323295479	TOI-1861	130.7987	-83.061	9.95	1.06	5684	5
71	332697924	–	63.26121	-12.4593	11	1.32	6266	2
72	333736132	CTOI	170.2765	-26.0666	12.07	0.76	4722	2
73	339399841	–	296.0705	-62.8136	12.35	1.55	5686	2
74	349091983	–	107.7051	-61.3524	12.29	1.5	6083	24
75	381553868	–	269.7743	-50.9212	11.85	1.59	6355	2
76	393229954	–	86.74486	-46.7119	11.77	0.9	5571	5
77	394340183	–	39.32208	-79.4583	10.95	1.04	6325	2
78	396720998	TOI-709	65.65532	-54.1472	13.99	0.15	50000	6
79	404518509	TOI-4320	51.64036	-43.6136	8.6	1.04	5871	4
80	412386707	–	110.4871	-23.414	10.92	1.96	6304	2
81	437293313	–	191.2234	-22.6177	12.97	0.94	5536	2
82	439491923	–	21.38365	-18.1471	12.87	1.26	5944	2
83	442893494	–	80.00938	-16.2193	12.41	1.39	6322	3
84	457649900	TOI-4958	217.9991	-51.0744	10.75	2.11	6713	2

Table 5.1: Properties of the host stars of our duotransit candidates.

ID	**TIC ID**	**TOI/CTOI**	**RA (deg)**	**Dec (deg)**	$\mathbf{T_{mag}}$	$\mathbf{R_*}$ ($\mathbf{R_\odot}$)	$\mathbf{T_{\mathit{eff}}}$ **(K)**	$\mathbf{N_{sec}}$
85	466206508	TOI-5542	302.7985	-61.1355	11.85	1.27	5393	2

Table 5.2: The transit event properties of our duotransit candidates.

ID	**TIC ID**	**T_{c1}**	**T_{c2}**	**Depth**	**Duration**
—	—	**(TBJD, [Sector])**	**(TBJD, [Sector])**	**(ppt)**	**(hours)**
1	1504460	1528.39739 [08]	2261.11990 [35]	3.367 [08], 3.415 [35]	3.78
2	2669681	1676.73302 [13]	2044.45589 [27]	7.879 [13], 7.037 [27]	9.69
3	9844069	1431.16511 [04]	2148.92146 [31]	13.452 [04], 12.224 [31]	7.20
4	13072758	1455.59404 [05]	2193.21295 [32]	7.023 [05], 6.755 [32]	9.25
5	13713700	1536.98226 [08]	2245.82903 [34]	7.234 [08], 4.700 [34]	3.26
6	14445414	1497.55590 [07]	2210.97620 [33]	2.317 [07], 2.179 [33]	2.86
7	20904104	1390.11189 [03]	2105.36177 [29]	0.738 [03], 1.065 [29]	4.61
8	25194908	1402.29491 [03]	2077.28343 [28]	6.590 [03], 6.266 [28]	9.16
9	32179255	1345.87922 [01]	2068.45418 [28]	3.619 [01], 4.682 [28]	3.71
10	38138512	1559.95080 [09]	2300.02560 [36]	17.907 [09], 18.148 [36]	6.73
11	39167176	1470.62312 [06]	2211.42630 [33]	7.282 [06], 8.112 [33]	6.25
12	42428568	1475.69109 [06]	2224.32460 [33]	5.380 [06], 4.939 [33]	10.20
13	52195587	1350.27811 [01]	2107.61083 [29]	5.775 [01], 6.138 [29]	9.07
14	66439839	1386.34406 [03]	2137.03203 [30]	6.227 [03], 5.420 [30]	2.16
15	67599025	1404.02101 [03]	2138.82557 [30]	6.684 [03], 7.345 [30]	3.27
16	70561926	1523.06353 [08]	2275.36040 [35]	16.290 [08], 16.053 [35]	5.91
17	71028120	1445.81123 [05]	2189.95412 [32]	1.238 [05], 1.025 [32]	6.11
18	77437543	1456.70241 [05]	2180.69226 [32]	9.825 [05], 9.326 [32]	7.93
19	81089255	1509.94498 [07]	2260.20690 [35]	7.318 [07], 6.372 [35]	5.14
20	100776118	1472.81029 [06]	2219.67770 [33]	13.264 [06], 13.070 [33]	22.34

Table 5.2: The transit event properties of our duotransit candidates.

ID	**TIC ID**	**T_{c1}**	**T_{c2}**	**Depth**	**Duration**
—	—	**(TBJD, [Sector])**	**(TBJD, [Sector])**	**(ppt)**	**(hours)**
21	101824521	1620.35423 [11]	2331.52820 [37]	9.396 [11], 9.103 [37]	8.52
22	107113345	1576.32832 [10]	2317.29675 [37]	1.771 [10], 2.035 [37]	1.77
23	118339710	1525.64667 [08]	2249.54641 [34]	4.329 [08], 3.977 [34]	8.68
24	123763494	1486.92891 [06]	2209.76758 [33]	10.645 [06], 11.728 [33]	2.47
25	124029677	1486.12090 [06]	2218.00409 [33]	6.368 [06], 6.105 [33]	4.58
26	140215502	1460.54584 [05]	2194.44033 [32]	2.959 [05], 4.468 [32]	7.14
27	140750416	1504.80151 [07]	2245.39501 [34]	8.912 [07], 9.197 [34]	3.85
28	142278054	1595.02504 [10]	2310.35369 [37]	2.177 [10], 2.022 [37]	4.82
29	145006304	1579.50384 [10]	2318.24443 [37]	2.048 [10], 2.772 [37]	5.19
30	145913596	1539.51696 [08]	2242.69675 [34]	1.728 [08], 2.163 [34]	8.50
31	153838604	1447.10227 [05]	2176.13853 [32]	15.209 [05], 16.237 [32]	2.61
32	156716001	1485.40631 [06]	2224.51833 [33]	2.652 [06], 3.037 [33]	9.11
33	157119927	1591.62175 [10]	2291.00613 [36]	5.445 [10], 6.897 [36]	2.57
34	157698565	1494.57973 [07]	2234.11360 [34]	9.825 [07], 9.338 [34]	6.38
35	159490807	1606.22551 [11]	2355.93796 [38]	5.155 [11], 5.184 [38]	5.38
36	161169240	1328.25945 [01]	2083.31754 [28]	9.707 [01], 10.134 [28]	7.82
37	176518126	1489.05533 [06]	2219.53761 [33]	3.565 [06], 3.244 [33]	5.61
38	188620407	1375.48660 [02]	2461.70715 [42]	5.467 [02], 4.512 [42]	6.08
39	193318850	1553.77031 [09]	2292.51011 [36]	6.916 [09], 7.143 [36]	3.89
40	207783865	1608.93692 [11]	2354.11345 [38]	17.211 [11], 17.729 [38]	1.99

Table 5.2: The transit event properties of our duotransit candidates.

ID	**TIC ID**	**T_{c1}**	**T_{c2}**	**Depth**	**Duration**
—	—	**(TBJD, [Sector])**	**(TBJD, [Sector])**	**(ppt)**	**(hours)**
41	211409161	1335.10057 [01]	2070.36583 [28]	13.629 [01], 12.232 [28]	2.14
42	215402824	1413.62655 [04]	2169.04205 [31]	5.589 [04], 9.955 [31]	1.87
43	218977148	1355.47069 [02]	2090.09772 [29]	5.597 [02], 4.944 [29]	8.13
44	220622886	1479.52544 [06]	2204.58502 [33]	4.324 [06], 3.501 [33]	4.43
45	221915858	1643.35799 [12]	2372.55118 [39]	5.737 [12], 5.526 [39]	3.05
46	224279805	1369.72941 [02]	2105.21571 [29]	6.392 [02], 6.618 [29]	5.93
47	235058563	1416.61066 [04]	2216.44259 [33]	6.164 [04], 5.630 [33]	10.17
48	237605045	1489.04268 [06]	2210.29724 [33]	6.212 [06], 7.014 [33]	4.42
49	242241304	1623.07095 [11]	2345.37403 [38]	6.158 [11], 6.186 [38]	4.72
50	251057075	1426.31846 [04]	2154.02335 [31]	1.986 [04], 2.348 [31]	4.42
51	256912435	1623.43775 [11]	2338.70979 [38]	20.396 [11], 21.562 [38]	2.72
52	265465927	1342.64749 [01]	2058.60913 [27]	8.678 [01], 8.720 [27]	6.05
53	265466589	1352.52439 [01]	2037.86660 [27]	6.818 [01], 6.664 [27]	4.14
54	268534931	1398.29475 [03]	2139.09941 [30]	5.829 [03], 6.133 [30]	7.82
55	269333648	1538.52419 [08]	2249.05416 [34]	4.162 [08], 4.032 [34]	9.46
56	275878706	1621.08010 [11]	2341.78257 [38]	6.544 [11], 5.320 [38]	4.38
57	279727635	1343.22676 [01]	2124.62930 [30]	7.181 [01], 6.789 [30]	5.71
58	287204963	1402.93640 [03]	2132.33438 [30]	11.498 [03], 10.182 [30]	4.73
59	289840544	1331.28977 [01]	2083.28790 [28]	2.702 [01], 1.997 [28]	2.99
60	290165539	1332.75615 [01]	2067.97094 [28]	13.627 [01], 15.056 [28]	11.50

Table 5.2: The transit event properties of our duotransit candidates.

ID	**TIC ID**	**T_{c1}**	**T_{c2}**	**Depth**	**Duration**
—	—	**(TBJD, [Sector])**	**(TBJD, [Sector])**	**(ppt)**	**(hours)**
61	292719109	1499.70159 [07]	2222.31933 [33]	2.859 [07], 2.677 [33]	9.08
62	294097549	1657.74149 [13]	2256.34250 [35]	1.977 [13], 1.426 [35]	7.96
63	296737508	1538.00622 [08]	2271.99796 [35]	2.021 [08], 1.854 [35]	5.65
64	300394149	1576.88642 [10]	2325.42588 [37]	2.051 [10], 2.195 [37]	13.40
65	303317324	1365.17582 [02]	2104.34337 [29]	1.360 [02], 1.323 [29]	5.74
66	304339227	1673.33918 [13]	2388.01911 [39]	0.522 [13], 0.464 [39]	5.79
67	306249066	1593.97611 [10]	2326.51397 [37]	7.873 [10], 7.061 [37]	4.03
68	313671132	1604.35452 [11]	2337.72693 [38]	3.408 [11], 3.506 [38]	5.70
69	317923092	1479.81772 [06]	2209.42617 [33]	4.358 [06], 6.715 [33]	12.96
70	323295479	1622.92483 [11]	2365.44036 [39]	8.727 [11], 8.609 [39]	6.51
71	332697924	1445.74977 [05]	2178.22194 [32]	1.042 [05], 1.423 [32]	6.63
72	333736132	1551.55292 [09]	2283.54681 [36]	15.856 [09], 16.440 [36]	2.96
73	339399841	1662.10984 [13]	2043.59486 [27]	4.773 [13], 6.471 [27]	6.66
74	349091983	1603.10253 [11]	2152.16754 [31]	8.301 [11], 8.133 [31]	9.52
75	381553868	1677.32594 [13]	2367.57869 [39]	5.653 [13], 6.030 [39]	6.49
76	393229954	1446.79953 [05]	2204.55168 [33]	8.172 [05], 6.652 [33]	2.67
77	394340183	1664.84261 [13]	2389.11243 [39]	11.255 [13], 10.820 [39]	8.65
78	396720998	1399.21966 [03]	2176.27178 [30]	6.360 [03], 6.082 [30]	4.33
79	404518509	1431.26615 [04]	2134.88294 [30]	0.842 [04], 0.598 [30]	5.02
80	412386707	1493.95365 [07]	2240.57066 [34]	3.442 [07], 3.587 [34]	5.23

Table 5.2: The transit event properties of our duotransit candidates.

ID	**TIC ID**	**T_{c1}**	**T_{c2}**	**Depth**	**Duration**
—	—	**(TBJD, [Sector])**	**(TBJD, [Sector])**	**(ppt)**	**(hours)**
81	437293313	1578.44737 [10]	2328.08914 [37]	9.891 [10], 8.462 [37]	6.58
82	439491923	1405.41115 [03]	2116.79038 [30]	11.608 [03], 11.766 [30]	6.70
83	442893494	1472.65885 [06]	2194.38454 [32]	5.776 [06], 6.458 [32]	7.70
84	457649900	1606.96984 [11]	2355.79522 [38]	2.857 [11], 2.945 [38]	7.61
85	466206508	1679.34576 [13]	2054.97133 [27]	11.214 [13], 9.274 [27]	8.03

Table 5.3: Properties of our duotransit candidates. $N_{\rm alias}$ is the alias number corresponding to the most probable orbital period $P_{\rm marg}$.

ID —	**TIC ID** —	R_p ($R_\oplus$)	$\mathbf{P_{min}}$, $\mathbf{P_{max}}$ **(days)**	$N_{\rm alias}$ —	$P_{\rm marg}$ **(days)**	b —	*Gaia* **NSS**	*Gaia* **RV amp** ($\mathbf{km\,s^{-1}}$)	**Total SNR** —
1	1504460	9.6 ± 1.0	19.80333, 732.72251	24	$20.0^{+19.0}_{-1.0}$	$0.78^{+0.12}_{-0.37}$	0	13.84	14.82
2	2669681	17.0 ± 1.2	21.63067, 367.72287	18	$24.5^{+8.9}_{-2.9}$	$0.66^{+0.09}_{-0.24}$	0	36.15	41.8
3	9844069	18.9 ± 1.4	22.42991, 717.75635	33	$25.6^{+7.0}_{-3.2}$	$0.62^{+0.12}_{-0.3}$	0	–	46.12
4	13072758	$11.78^{+0.67}_{-0.65}$	19.93567, 737.61891	38	26.0 ± 10.0	0.31 ± 0.22	0	20.36	35.92
5	13713700	8.3 ± 1.0	19.69018, 708.84677	37	$22.9^{+8.0}_{-3.2}$	$0.79^{+0.11}_{-0.28}$	0	–	19.73
6	14445414	$7.5^{+3.9}_{-1.2}$	19.28163, 713.42031	38	$22.3^{+7.4}_{-3.0}$	$0.93^{+0.06}_{-0.18}$	0	4.78	12.08
7	20904104	2.6 ± 0.19	17.88103, 715.24989	41	$23.0^{+11.0}_{-4.0}$	$0.27^{+0.25}_{-0.19}$	0	2.9	11.84
8	25194908	11.18 ± 0.68	337.49490, 674.98980	2	337.49490	$0.7^{+0.1}_{-0.28}$	0	–	31.43
9	32179255	21.0 ± 8.0	20.64500, 722.57496	36	$22.6^{+6.3}_{-1.9}$	$0.999^{+0.07}_{-0.045}$	2	49.01	36.77
10	38138512	17.8 ± 1.0	18.50185, 740.07480	41	$21.1^{+6.3}_{-2.2}$	0.32 ± 0.2	0	–	49.35
11	39167176	$18.8^{+8.9}_{-2.9}$	20.57787, 740.80317	37	$26.0^{+20.0}_{-5.0}$	$0.947^{+0.081}_{-0.044}$	0	81.59	40.79
12	42428568	$24.0^{+11.0}_{-5.0}$	24.14954, 748.63351	32	$31.0^{+22.0}_{-6.0}$	$0.981^{+0.066}_{-0.038}$	0	16.42	56.65
13	52195587	9.28 ± 0.52	34.42428, 757.33272	18	50.0 ± 17.0	0.29 ± 0.22	0	–	35.19
14	66439839	$9.1^{+2.8}_{-1.0}$	37.53440, 750.68798	17	$38.0^{+20.0}_{-2.0}$	$0.87^{+0.09}_{-0.29}$	0	30.94	19.55
15	67599025	6.86 ± 0.57	24.49349, 734.80456	31	$27.2^{+7.8}_{-2.7}$	$0.62^{+0.13}_{-0.35}$	0	9.86	29.54
16	70561926	17.51 ± 0.82	20.33234, 752.29687	38	$22.1^{+5.7}_{-1.8}$	0.15 ± 0.12	2	18.35	144.8
17	71028120	4.74 ± 0.31	18.60345, 744.14289	41	$21.3^{+6.3}_{-2.7}$	$0.38^{+0.22}_{-0.25}$	0	2.53	14.28
18	77437543	$10.98^{+0.66}_{-0.63}$	22.62465, 723.98986	22	$38.0^{+14.0}_{-15.0}$	0.31 ± 0.22	2	14.02	83.13
19	81089255	12.19 ± 0.69	34.10282, 750.26191	23	$37.5^{+9.4}_{-4.9}$	$0.76^{+0.07}_{-0.26}$	0	24.24	25.14
20	100776118	16.19 ± 0.74	49.79069, 746.86040	16	$62.0^{+31.0}_{-12.0}$	0.842 ± 0.01	3	30.51	177.47
21	101824521	12.17 ± 0.72	24.52324, 711.17397	30	31.0 ± 10.0	$0.18^{+0.18}_{-0.13}$	0	–	34.34

Table 5.3: Properties of our duotransit candidates. $N_{\rm alias}$ is the alias number corresponding to the most probable orbital period $P_{\rm marg}$.

ID	**TIC ID**	R_p	$\mathbf{P_{min}}$, $\mathbf{P_{max}}$	$N_{\rm alias}$	$P_{\rm marg}$	b	*Gaia*	*Gaia* **RV**	**Total SNR**
—	—	($R_\oplus$)	**(days)**	—	**(days)**	—	**NSS**	**amp** ($\mathbf{km\,s^{-1}}$)	—
22	107113345	$9.2^{+5.1}_{-2.3}$	20.02618, 740.96843	38	$22.5^{+6.0}_{-2.4}$	0.976 ± 0.048	0	19.1	12.5
23	118339710	$10.64^{+0.65}_{-0.61}$	21.29118, 723.89974	26	33.0 ± 12.0	0.48 ± 0.29	0	4.13	62.67
24	123763494	$19.8^{+7.1}_{-4.5}$	19.53618, 722.83868	38	$21.9^{+5.9}_{-2.4}$	$0.97^{+0.076}_{-0.062}$	0	15.94	37.36
25	124029677	11.35 ± 0.59	18.76624, 731.88319	40	$20.9^{+5.2}_{-2.1}$	$0.43^{+0.22}_{-0.28}$	0	11.35	46.16
26	140215502	$5.78^{+0.38}_{-0.34}$	34.94727, 733.89270	22	$43.0^{+18.0}_{-8.0}$	$0.31^{+0.3}_{-0.21}$	0	9.83	32.98
27	140750416	8.55 ± 0.54	16.83165, 740.59260	45	$19.0^{+4.9}_{-2.2}$	0.36 ± 0.22	0	11.19	30.13
28	142278054	$11.49^{+0.96}_{-0.91}$	24.66649, 715.32865	30	$27.5^{+6.6}_{-2.8}$	$0.79^{+0.11}_{-0.38}$	0	7.72	23.25
29	145006304	$5.33^{+0.47}_{-0.43}$	16.78954, 738.74000	45	$18.9^{+5.7}_{-2.2}$	$0.62^{+0.17}_{-0.35}$	0	6.03	13.84
30	145913596	$6.9^{+2.7}_{-1.1}$	54.09067, 703.17978	14	$59.0^{+29.0}_{-8.0}$	$0.91^{+0.07}_{-0.32}$	0	5.83	25.32
31	153838604	$17.1^{+4.7}_{-3.3}$	38.37032, 729.03626	20	$41.0^{+12.0}_{-4.0}$	$0.961^{+0.068}_{-0.062}$	0	–	42.87
32	156716001	5.97 ± 0.3	33.59600, 739.11201	23	$43.0^{+30.0}_{-10.0}$	0.28 ± 0.22	0	4.73	33.42
33	157119927	$13.4^{+5.9}_{-3.1}$	21.19346, 699.38439	34	$24.1^{+6.3}_{-2.9}$	$0.983^{+0.071}_{-0.048}$	2	64.82	25.01
34	157698565	11.66 ± 0.59	35.21588, 739.53387	22	$46.0^{+28.0}_{-11.0}$	$0.827^{+0.025}_{-0.041}$	0	3.49	105.68
35	159490807	$15.4^{+4.7}_{-1.6}$	22.71853, 749.71245	34	29.0 ± 8.0	$0.938^{+0.048}_{-0.025}$	0	6.08	45.05
36	161169240	$12.19^{+0.77}_{-0.73}$	26.03638, 755.05809	30	$31.0^{+13.0}_{-4.0}$	$0.47^{+0.21}_{-0.29}$	0	32.37	52.27
37	176518126	8.3 ± 1.1	21.48477, 730.48210	35	$24.3^{+7.4}_{-2.9}$	0.3 ± 0.22	0	9.38	32.89
38	188620407	$9.58^{+0.57}_{-0.54}$	24.13819, 1086.21870	35	28.0 ± 10.0	0.39 ± 0.24	0	11.56	33.51
39	193318850	7.08 ± 0.47	15.07635, 738.73979	50	$17.6^{+5.5}_{-2.2}$	0.31 ± 0.22	0	–	17.05
40	207783865	15.31 ± 0.76	21.29077, 745.17689	36	$23.3^{+6.5}_{-2.0}$	$0.802^{+0.023}_{-0.035}$	2	13.91	95.83
41	211409161	$13.1^{+4.5}_{-2.6}$	18.85295, 735.26527	40	$21.0^{+5.3}_{-2.2}$	$0.943^{+0.077}_{-0.066}$	0	38.64	38.49
42	215402824	$16.0^{+10.0}_{-3.0}$	41.96752, 755.41550	16	$42.0^{+21.0}_{-2.0}$	$0.93^{+0.11}_{-0.22}$	0	–	12.73
43	218977148	11.9 ± 0.82	27.20845, 734.62703	28	$30.6^{+8.1}_{-3.4}$	$0.4^{+0.22}_{-0.26}$	0	–	22.83

Table 5.3: Properties of our duotransit candidates. $N_{\rm alias}$ is the alias number corresponding to the most probable orbital period $P_{\rm marg}$.

ID	**TIC ID**	R_p	$\mathbf{P_{min}}$, $\mathbf{P_{max}}$	$N_{\rm alias}$	$P_{\rm marg}$	b	*Gaia*	*Gaia* **RV**	**Total SNR**
—	—	($R_\oplus$)	**(days)**	—	**(days)**	—	**NSS**	**amp** ($\mathbf{km\,s^{-1}}$)	—
44	220622886	$28.0^{+16.0}_{-8.0}$	42.65054, 725.05958	18	$29.0^{+23.0}_{-0.0}$	$0.994^{+0.071}_{-0.048}$	0	65.91	18.89
45	221915858	$21.3^{+3.7}_{-1.4}$	17.78520, 729.19319	42	$19.7^{+5.4}_{-1.9}$	$0.911^{+0.044}_{-0.025}$	0	60.96	33.79
46	224279805	10.55 ± 0.64	17.51161, 735.48631	43	$19.9^{+5.5}_{-1.9}$	0.24 ± 0.18	0	17.77	30.43
47	235058563	11.47 ± 0.61	88.87019, 799.83193	10	$89.0^{+25.0}_{-9.0}$	0.38 ± 0.23	0	–	27.17
48	237605045	$44.0^{+17.0}_{-11.0}$	21.85618, 721.25400	34	$24.0^{+6.0}_{-2.2}$	$1.01^{+0.067}_{-0.051}$	0	36.88	68.84
49	242241304	9.7 ± 1.0	23.30012, 722.30308	32	$28.0^{+10.0}_{-4.0}$	$0.855^{+0.061}_{-0.071}$	0	7.03	28.72
50	251057075	3.88 ± 0.3	16.53870, 727.70489	45	$20.2^{+7.8}_{-3.3}$	0.27 ± 0.22	0	7.82	15.54
51	256912435	$25.5^{+4.6}_{-3.8}$	24.66455, 715.27204	30	$27.5^{+6.6}_{-2.8}$	0.95 ± 0.051	0	46.85	57.7
52	265465927	11.73 ± 0.63	23.86539, 715.96164	31	$27.5^{+8.3}_{-3.7}$	0.27 ± 0.19	0	19.67	38.93
53	265466589	8.57 ± 0.59	28.55588, 685.34120	25	$31.2^{+9.2}_{-3.7}$	$0.49^{+0.21}_{-0.33}$	0	–	13.71
54	268534931	6.12 ± 0.39	24.69345, 740.80465	31	$32.0^{+25.0}_{-7.0}$	0.29 ± 0.23	0	25.23	29.74
55	269333648	11.72 ± 0.67	64.59377, 710.52997	12	$65.0^{+24.0}_{-5.0}$	$0.64^{+0.1}_{-0.25}$	0	3.2	54.46
56	275878706	$8.1^{+3.1}_{-1.3}$	22.52196, 720.70247	33	$27.0^{+11.0}_{-4.0}$	$0.88^{+0.09}_{-0.21}$	1	21.81	20.68
57	279727635	$10.5^{+4.0}_{-1.2}$	65.11699, 781.40254	13	$71.0^{+41.0}_{-19.0}$	0.905 ± 0.078	0	–	28.36
58	287204963	11.3 ± 2.2	17.79021, 729.39798	42	$20.3^{+5.8}_{-2.5}$	$0.41^{+0.25}_{-0.28}$	0	–	17.86
59	289840544	$14.0^{+9.1}_{-3.6}$	22.78782, 751.99813	34	$25.1^{+6.3}_{-2.3}$	$0.984^{+0.063}_{-0.045}$	0	6.43	17.85
60	290165539	$23.4^{+6.3}_{-3.4}$	21.62396, 735.21479	35	$27.0^{+19.0}_{-5.0}$	$0.95^{+0.066}_{-0.046}$	0	45.38	92.47
61	292719109	11.07 ± 0.59	21.89747, 722.61775	34	$24.1^{+7.3}_{-2.2}$	0.34 ± 0.23	0	2.5	45.22
62	294097549	4.79 ± 0.33	199.535169, 598.60600	3	$199.5^{+99.8}_{-0}$	$0.6^{+0.17}_{-0.37}$	0	4.14	22.63
63	296737508	5.88 ± 0.36	20.97145, 733.99174	36	$23.7^{+6.9}_{-2.7}$	$0.6^{+0.12}_{-0.26}$	0	1.12	41.08
64	300394149	6.46 ± 0.34	19.69843, 748.53947	39	$26.0^{+16.0}_{-6.0}$	0.27 ± 0.22	0	4.92	36.29
65	303317324	2.67 ± 0.26	16.79925, 739.16710	45	$18.5^{+4.6}_{-1.7}$	0.12 ± 0.11	0	1.16	22.71

Table 5.3: Properties of our duotransit candidates. $N_{\rm alias}$ is the alias number corresponding to the most probable orbital period $P_{\rm marg}$.

ID	**TIC ID**	R_p	$\mathbf{P_{min}}$, $\mathbf{P_{max}}$	$N_{\rm alias}$	$P_{\rm marg}$	b	*Gaia*	*Gaia* **RV**	**Total SNR**
—	—	($R_\oplus$)	**(days)**	—	**(days)**	—	**NSS**	**amp** ($\mathbf{km\,s^{-1}}$)	—
66	304339227	2.65 ± 0.17	27.48783, 714.68370	27	$31.1^{+8.6}_{-3.6}$	0.34 ± 0.24	0	2.19	13.81
67	306249066	11.09 ± 0.61	23.63027, 732.53786	32	$27.1^{+7.8}_{-3.5}$	0.867 ± 0.021	0	7.34	49.32
68	313671132	$7.78^{+0.67}_{-0.62}$	23.65724, 733.37241	32	$28.0^{+13.0}_{-5.0}$	$0.81^{+0.08}_{-0.22}$	0	7.02	27.41
69	317923092	$12.5^{+4.8}_{-1.4}$	19.19983, 729.59400	39	$27.0^{+19.0}_{-5.0}$	$0.928^{+0.062}_{-0.048}$	0	35.1	30.15
70	323295479	11.28 ± 0.6	67.50129, 742.51554	12	$83.0^{+41.0}_{-15.0}$	0.85 ± 0.013	0	2.43	138.65
71	332697924	4.69 ± 0.33	22.88951, 732.47218	33	$26.2^{+7.1}_{-3.3}$	0.34 ± 0.23	0	5.6	11.96
72	333736132	$10.25^{+0.87}_{-0.82}$	23.61270, 731.99390	32	$26.1^{+7.1}_{-2.5}$	$0.751^{+0.045}_{-0.091}$	0	13.92	55.96
73	339399841	$13.0^{+1.7}_{-1.1}$	22.44020, 381.48503	18	$25.4^{+9.2}_{-4.2}$	$0.73^{+0.15}_{-0.34}$	0	–	21.13
74	349091983	$21.3^{+8.8}_{-4.8}$	549.0649, 549.06501	1	549.0649	$0.975^{+0.075}_{-0.058}$	0	–	44.11
75	381553868	12.41 ± 0.84	20.91681, 690.25274	33	$23.8^{+6.2}_{-2.9}$	$0.39^{+0.22}_{-0.26}$	0	9.94	22
76	393229954	$9.3^{+4.1}_{-1.2}$	75.77521, 757.75214	11	$45.0^{+31.0}_{-0.0}$	$0.907^{+0.082}_{-0.098}$	0	12.97	33.63
77	394340183	10.87 ± 0.61	60.35608, 724.27290	10	$60.0^{+30.0}_{-18.0}$	0.29 ± 0.21	0	6.77	85.43
78	396720998	$1.45^{+0.96}_{-0.85}$	70.64108, 777.05180	12	$78.0^{+19.0}_{-13.0}$	0.46 ± 0.32	0	–	6.44
79	404518509	2.72 ± 0.17	23.45386, 703.61679	18	$23.0^{+12.0}_{-1.0}$	$0.35^{+0.28}_{-0.24}$	0	0.93	22.52
80	412386707	12.37 ± 0.81	23.33181, 746.61701	33	$25.7^{+6.7}_{-2.4}$	$0.65^{+0.15}_{-0.38}$	0	6.18	28.97
81	437293313	$8.57^{+0.56}_{-0.52}$	20.26060, 749.64177	38	27.0 ± 9.0	0.25 ± 0.2	0	–	26.34
82	439491923	13.9 ± 1.3	26.34748, 711.37923	28	$31.0^{+14.0}_{-5.0}$	$0.7^{+0.14}_{-0.3}$	0	–	36.2
83	442893494	$11.55^{+0.67}_{-0.63}$	21.87047, 721.72570	22	36.0 ± 12.0	$0.34^{+0.25}_{-0.23}$	0	–	24.76
84	457649900	$18.0^{+9.8}_{-3.9}$	23.40078, 748.82538	33	$30.0^{+20.0}_{-6.0}$	$0.986^{+0.058}_{-0.033}$	0	13.11	29.26
85	466206508	13.55 ± 0.82	25.04186, 375.62557	16	$31.0^{+16.0}_{-6.0}$	0.37 ± 0.2	0	12.81	64.68

Table 5.4: A sample of events from `monofind` that were not planetary in nature. This table is available in its entirety online.

TIC ID	**Designation**	$\mathbf{T_{c1}}$ **(TBJD, [Sector])**	$\mathbf{T_{c2}}$ **(TBJD, [Sector])**
82286	Asteroid	1606.56693 [11]	2337.34989 [38]
109979	Asteroid	1601.53746 [11]	2355.66990 [38]
2490309	Asteroid	1577.58862 [10]	2309.44366 [37]
3835932	Asteroid	1392.54454 [03]	2133.24553 [30]
5740937	Asteroid	1378.87982 [02]	2097.43075 [29]
...	...	...	...

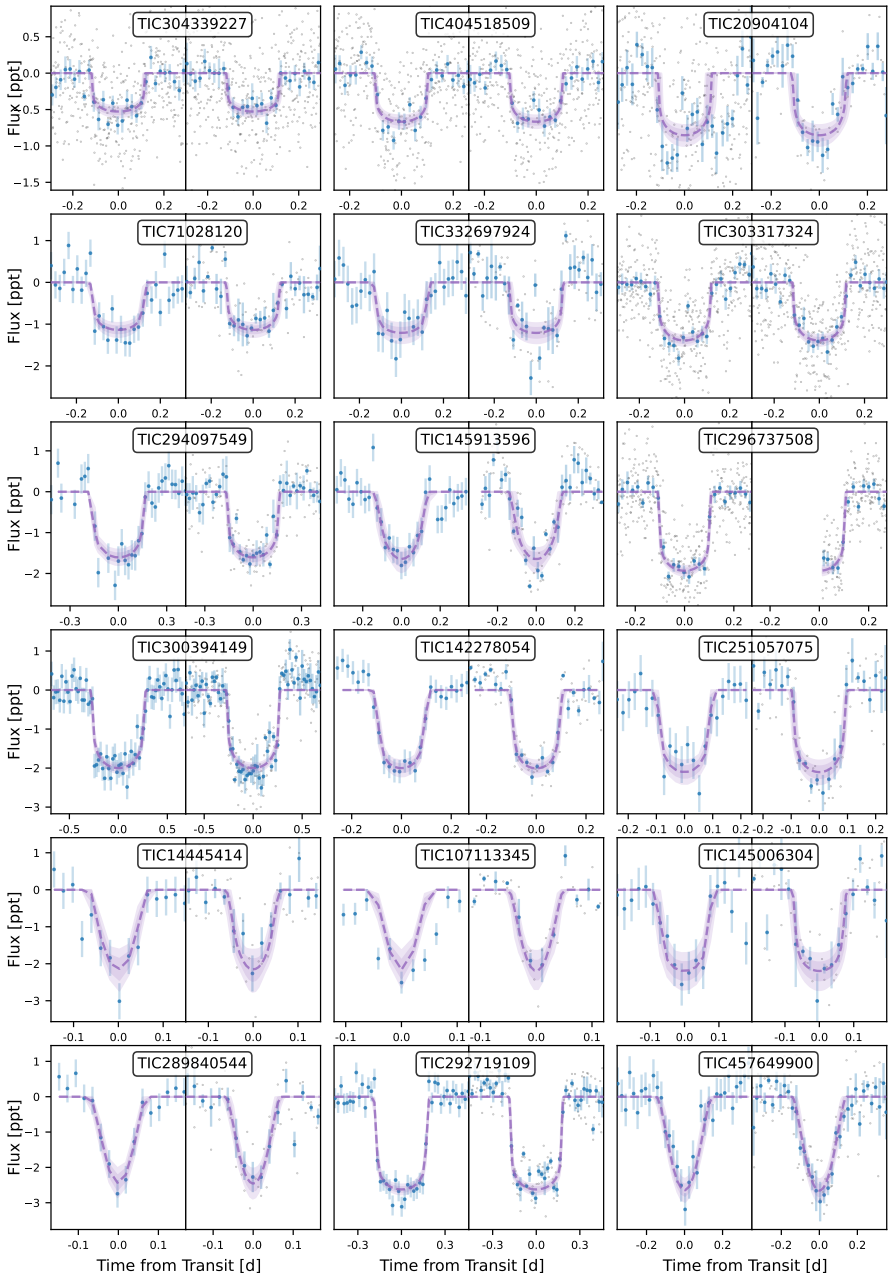

Figure 5.14: Zoomed-in transit events for duotransit candidates TIC-304339227 to TIC-156716001 ordered by transit depth. The left panel shows the Year 1 transit, and the right panel shows the Year 3 transit. The data in blue is the TESS PDC-SAP photometry (see Section 5.2). In cases with < 15 minute cadence blue points represent 30 minute bins with raw photometry shown in grey. The dashed purple lines show the best fit transit model with 1 and 2 standard deviations as shaded purple regions.

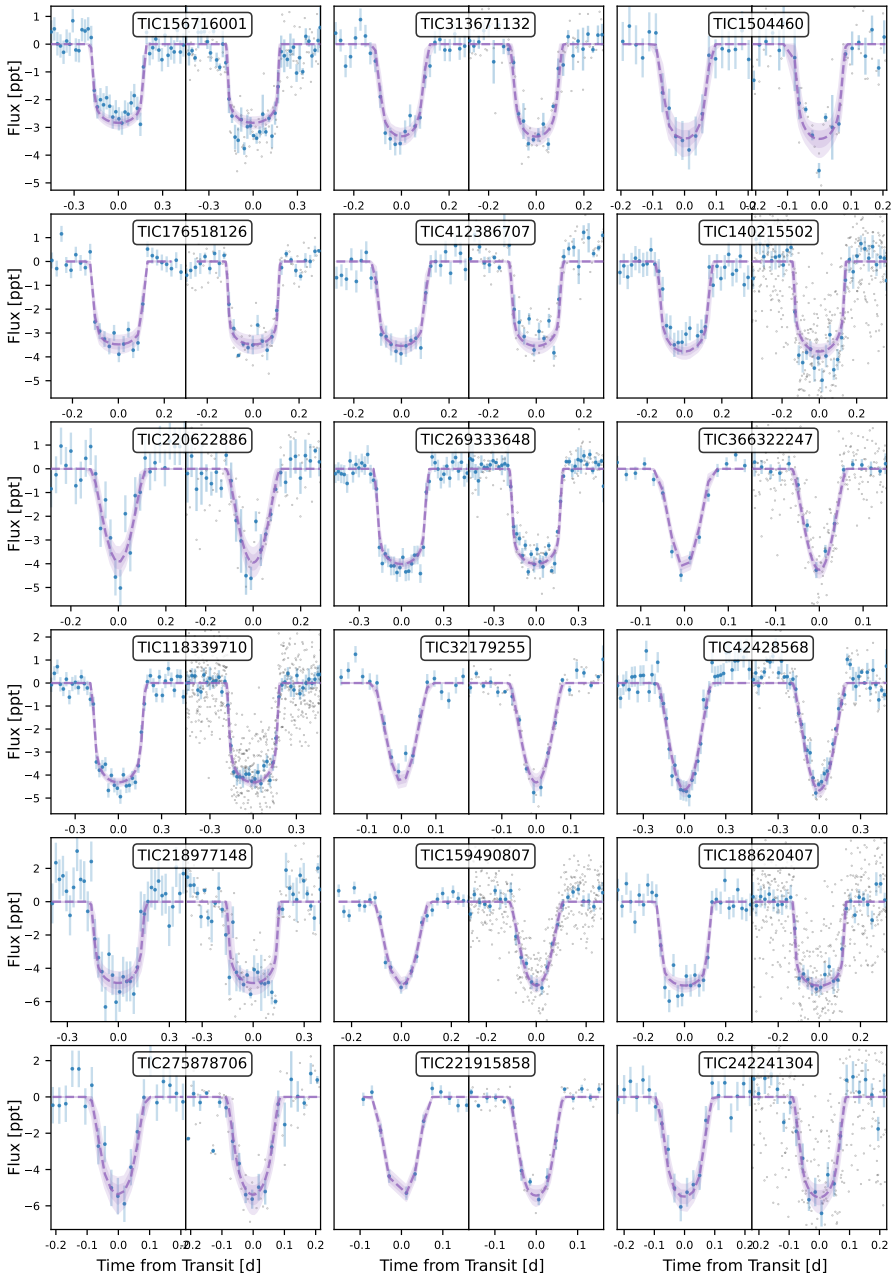

Figure 5.15: Zoomed-in transit events for duotransit candidates TIC-313671132 to TIC-381553868 ordered by transit depth. The left panel shows the Year 1 transit, and the right panel shows the Year 3 transit. The data in blue is the TESS PDC-SAP photometry (see Section 5.2). In cases with < 15 minute cadence blue points represent 30 minute bins with raw photometry shown in grey. The dashed purple lines show the best fit transit model with 1 and 2 standard deviations as shaded purple regions.

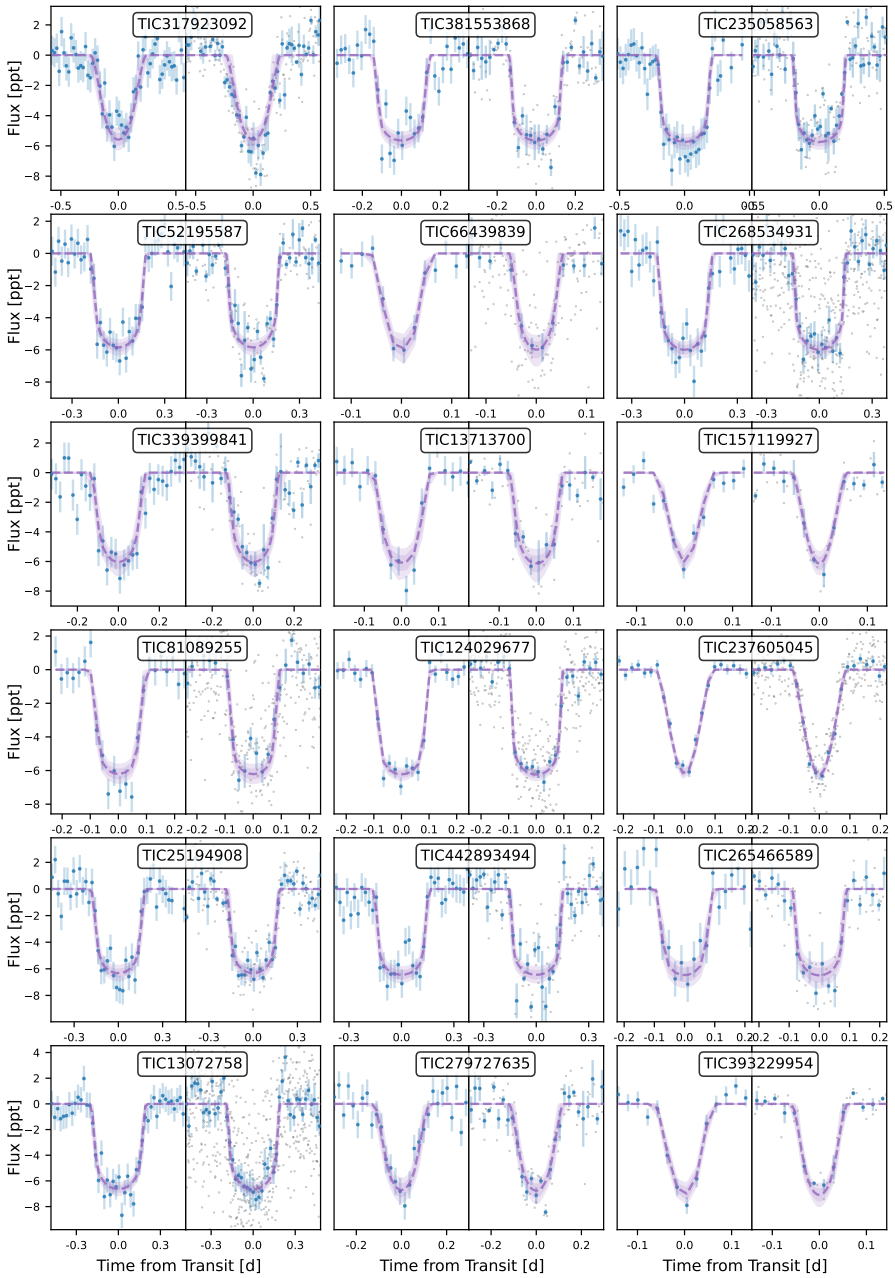

Figure 5.16: Zoomed-in transit events for duotransit candidates TIC-235058563 to TIC-306249066. The left panel shows the Year 1 transit, and the right panel shows the Year 3 transit. The data in blue is the TESS PDCSAP photometry (see Section 5.2). The dashed purple line is the best fit transit model with 1 and 2 standard deviations either side.

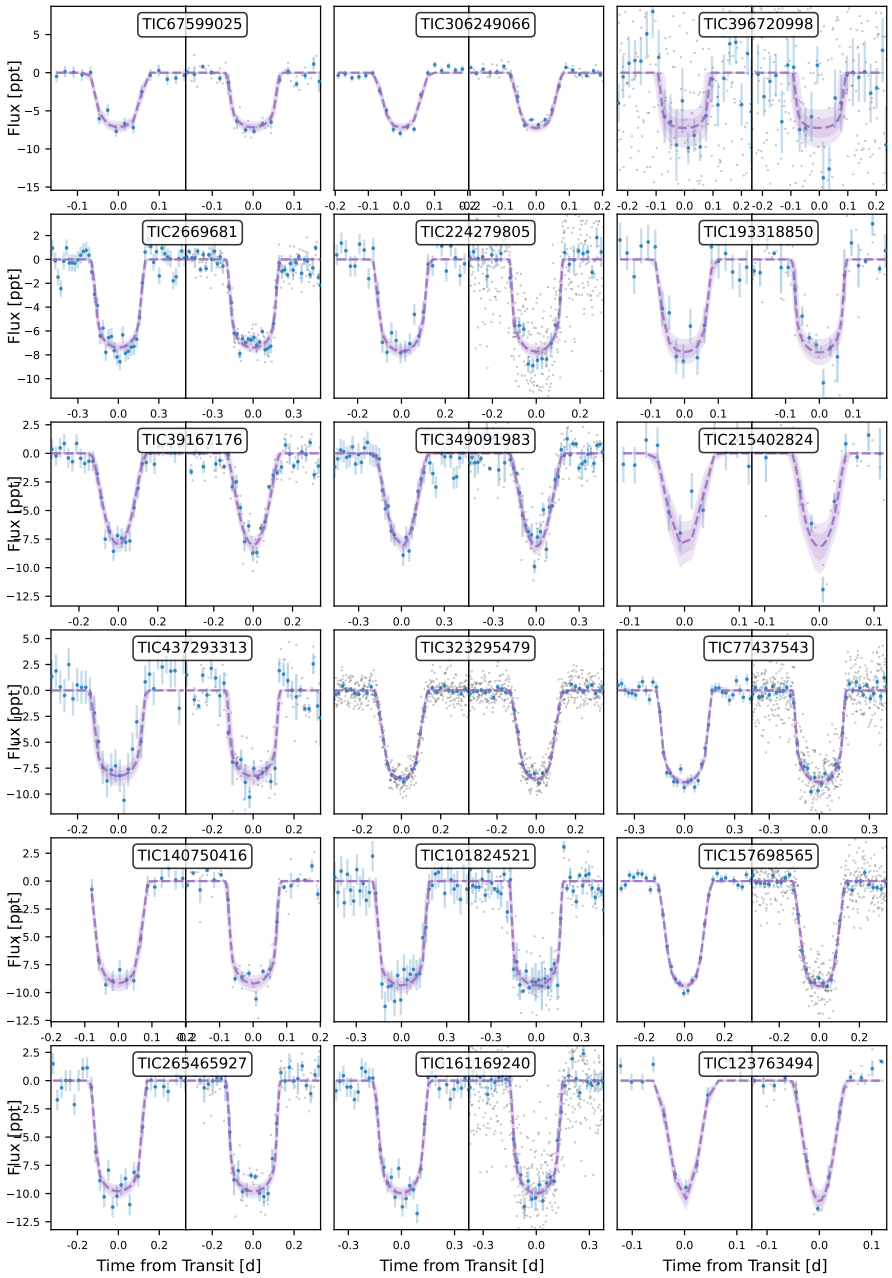

Figure 5.17: Zoomed-in transit events for duotransit candidates TIC-396720998 to TIC-439491923. The left panel shows the Year 1 transit, and the right panel shows the Year 3 transit. The data in blue is the TESS PDCSAP photometry (see Section 5.2). The dashed purple line is the best fit transit model with 1 and 2 standard deviations either side.

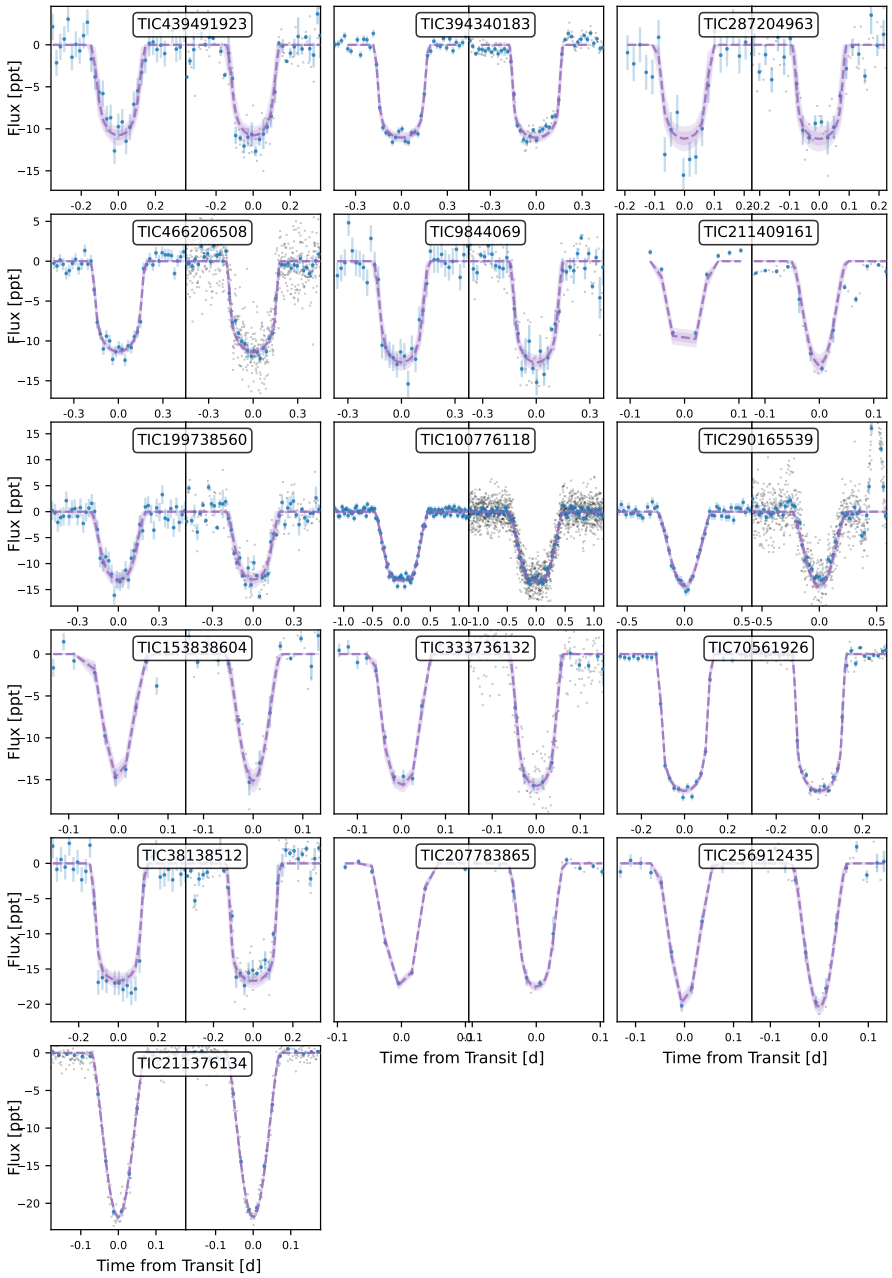

Figure 5.18: Zoomed-in transit events for duotransit candidates TIC-287204963 to TIC-256912435. The left panel shows the Year 1 transit, and the right panel shows the Year 3 transit. The data in blue is the TESS PDCSAP photometry (see Section 5.2). The dashed purple line is the best fit transit model with 1 and 2 standard deviations either side.

Chapter 6

Statistical analysis of seven *TESS* duotransit exoplanet candidates

"There's a rift out in space / And it could be the door / But you know I'm not sure."

'The Rift', Ween, 2005, Freeman/Melchiondo

Note

This chapter is a reproduction of the publication 'Statistical analysis of seven TESS duotransit exoplanet candidates' (Hawthorn et al. in preparation), currently being prepared for submission to Monthly Notices of the Royal Astronomical Society (MNRAS). The writing and analysis of the paper was performed in entirety by the author.

Abstract

Studying long-period planets allows us to understand their formation and evolution processes, and make comparisons with the relatively warm and cool planets of the Solar system. We have identified seven systems which originally showed only two transits throughout Cycle 1 (August 2018 - July 2019) and Cycle 3 (July 2020 - June 2021) of TESS observations, so-called 'duotransiting' planets, which have subsequently had their orbital periods solved fully with observations of period aliases

from NGTS follow-up efforts. We perform statistical validation on the photometric transit data of each of our seven candidates from the TESS mission using the `TRICERATOPS` program, and use it to compute the false-positive probabilities and the probabilities for a set of transiting planet and non-planetary scenarios for each candidate. We find that out of our seven candidates, five are classified as likely planets, and two are classified as likely false positives. We present these candidates and the statistical results for each, and discuss future directions for prioritising targets for radial velocity follow-up using `TRICERATOPS`.

6.1 Introduction

Over the lifetime of the field of exoplanet discovery, a total of 5602[1] planets as of 2024 Apr 01 [Exoplanet Archive; Akeson et al., 2013] have been confirmed from combinations of data from both space-borne missions and instruments operating on the ground.

In recent years a total of 432 exoplanet discoveries have originated from the Transiting Exoplanet Survey Satellite [TESS; Ricker et al., 2015] mission. TESS is a space-based photometric mission, launched by NASA in 2018, focusing primarily on the detection of planets transiting bright host stars. TESS observes the sky in 'Sectors' with a total FOV of $24 \times 96^{\circ}$ using four cameras. The duration of each Sector is approximately 27 days, meaning that most discoveries from TESS are short period exoplanets ($P < 10$ days). However longer period transiting exoplanets are detectable in the TESS data, often as monotransits or duotransit candidates - e.g. TOI-5152 b and TOI-5153 b (Ulmer-Moll et al. 2022); TOI-2447 (Gill et al., submitted).

A 'confirmation' typically entails the determination of a robust mass measurement of an exoplanet from radial velocity data, following observations of transit events in their light curves in order to determine their orbital periods and radii. In recent years, with the launch of exoplanet-focused space missions such as *Kepler* [Borucki et al., 2010], its extended mission K2 and TESS [Transiting Exoplanet Survey Satellite; Ricker et al., 2015], we have been provided with a wealth of transit photometry data for the initial detection of planet candidates due to their improved sensitivity. However, there are still many hundreds of these planet candidates that are yet to receive ground-based high-stability spectrographic observations from facilities such as HARPS [Mayor et al., 2003] and *ESPRESSO* [Pepe et al., 2021] to provide them with a radial velocity and thus mass measurement and therefore lead to a confirma-

[1] `https://exoplanetarchive.ipac.caltech.edu`

tion. In some cases these measurements can also serve to provide a determination of the true nature of a planet candidate as being an eclipsing binary or other false-positive scenario mimicking a planet transit signal. As of 2024 Apr 01, a total of 432 planets specifically from TESS have been confirmed, with a further 7125 awaiting further study and confirmation [Exoplanet Archive; Akeson et al., 2013].

Long-period planets are particularly challenging to study from the perspectives of both photometric monitoring for transits and spectroscopic radial velocities. They circle their stars on widely-separated orbits, meaning that the induced radial velocity is particularly small and a mass determination remains elusive. Their long periods also mean that continuous monitoring over many years is preferable, however with the limitations of time and scope of ground-based spectroscopy observations, only a few radial velocity points may ever be monitored. In order to mitigate for this lack of potential for a planetary mass measurement and confirmation, many tools have been developed in order to provide a statistically-motivated method for assessing the true source and nature of a transit-like signal in space mission photometry data. `BLENDER` [Torres et al., 2011], `VESPA` [Morton, 2012; Morton et al., 2016] and `PASTIS` [Díaz et al., 2014] were originally developed as statistical validation frameworks for the *Kepler* mission, with varying methodologies and computation times.

The Next Generation Transit Survey [NGTS; Wheatley et al., 2018] is currently undertaking a large program to follow-up monotransit and duotransit candidates from the TESS mission. NGTS is a ground-based photometric observatory at the Paranal site of ESO in Chile. It is comprised of an array of twelve 20 cm telescopes, each with a field-of-view of 8 square degrees, and observes in a custom filter of 520–890 nm. NGTS is specifically designed for high-precision follow-up of transiting exoplanet targets, and matches the precision of TESS for stars with $T_{mag} > 12$ with an RMS of 400 ppm in 30 mins, and stars with $T_{mag} > 9$ when multiple telescopes are used with an RMS of 100 ppm in 30 mins [Bryant et al., 2020b].

NGTS identified seven TESS duotransit candidates from Hawthorn et al. [2024] that could be photometrically monitored by the NGTS facility. NGTS detected transit events in each seven of these candidates, and these candidates form the basis of this paper.

In Section 6.2 we describe the observations for our seven candidates. In Section 6.3 we describe global model fitting for each system, and the validation method using the `TRICERATOPS` [Giacalone et al., 2021] algorithm. We discuss the individual system results and the scope of future work in Section 6.4; and summarise our findings in Section 6.5.

6.2 Observations

6.2.1 Duotransit Candidates

We study seven duotransit exoplanet candidates: TIC-13072758, TIC-39167176, TIC-142278054, TIC-224279805, TIC-333736132, TIC-339399841, TIC-439491923. These candidates were originally identified in a search of TESS data for duotransit candidates [Hawthorn et al., 2024]. The candidates were subsequently added to the NGTS observing schedule, and transit events were detected with NGTS which allow us to precisely determine the periods of the candidates. The stellar properties of the candidates are set out in Table 6.1.

Table 6.1: Properties of the host stars of each candidate.

Property	**TIC-13072758**	**TIC-39167176**	**TIC-142278054**	**TIC-224279805**
R.A. (J2000)	$05^{\mathrm{h}}04^{\mathrm{m}}21.22^{\mathrm{s}}$	$05^{\mathrm{h}}53^{\mathrm{m}}18.57^{\mathrm{s}}$	$12^{\mathrm{h}}03^{\mathrm{m}}03.01^{\mathrm{s}}$	$23^{\mathrm{h}}42^{\mathrm{m}}57.32^{\mathrm{s}}$
Dec (J2000)	$-29^{\circ}\ 02'03.03''$	$-03^{\circ}\ 47'51.60''$	$-33^{\circ}\ 20'35.07''$	$-40^{\circ}\ 46'20.02''$
TESS (mag)	12.224	12.008	10.281	12.145
V (mag)	12.696	12.731	10.880	12.616
G (mag)	12.587	12.491	10.641	12.612
R_* ($R_\odot$)	1.43 ± 0.07	1.56 ± 0.09	2.39 ± 0.12	1.20 ± 0.07
T_{eff} (K)	6313 ± 120	8415 ± 143	6400 ± 123	5591 ± 123
Distance (pc)	$601.42^{+2.95}_{-3.19}$	$486.84^{+3.95}_{-1.46}$	$418.42^{+1.64}_{-2.10}$	$422.59^{+3.22}_{-3.10}$
Gaia RUWE†	0.876	3.888	1.006	0.994
Property	**TIC-333736132**	**TIC-339399841**	**TIC-439491923**	
R.A. (J2000)	$11^{\mathrm{h}}21^{\mathrm{m}}06.32^{\mathrm{s}}$	$19^{\mathrm{h}}44^{\mathrm{m}}16.92^{\mathrm{s}}$	$01^{\mathrm{h}}25^{\mathrm{m}}32.07^{\mathrm{s}}$	
Dec (J2000)	$-26^{\circ}\ 03'59.82''$	$-62^{\circ}\ 48'49.16''$	$-18^{\circ}\ 08'49.71''$	
TESS (mag)	12.074	12.353	12.875	
V (mag)	13.059	13.059	13.453	
G (mag)	12.716	12.843	12.296	
R_* ($R_\odot$)	0.76 ± 0.06	1.55 ± 0.08	1.26 ± 0.06	
T_{eff} (K)	4722 ± 127	5686 ± 131	5944 ± 124	
Distance (pc)	$178.23^{+0.58}_{-1.38}$	$596.49^{+4.80}_{-5.11}$	$631.09^{+11.04}_{-9.75}$	
Gaia RUWE†	1.040	0.933	1.023	

Sources: TICv8 [Stassun et al., 2019], *Gaia* Data Release 3 [Brown et al., 2018]
†**RUWE** - Renormalised Unit Weight Error, targets with RUWE > 1.4 are generally considered to be non-single stars.

6.2.2 TESS photometry

The seven candidates were observed by the TESS spacecraft during Cycle 1 (2018 Jul 25 – 2019 Jul 17) and Cycle 3 (2020 Jul 05 – 2021 Jun 24). The observations are from the Full-Frame-Images (FFI), meaning the Cycle 1 data is at 30 minute cadence, while the Cycle 3 data is at 10 minute cadence.

For each candidate we downloaded the SPOC FFI lightcurve (Jenkins et al. 2016) from the MAST portal (`https://mast.stsci.edu/`). We used the Pre-Search Data Conditioning Simple Aperture Photometry (PDCSAP) lightcurve data (Jenkins et al. 2010), which removes most of the co-trended instrumental noise. The target pixel files for each candidate are displayed in Figure 6.1 with `tpfplotter`[2] [Aller et al., 2020]. Each plot shows the referenced TIC candidate as the central object with *Gaia* DR2 sources (Gaia Collaboration et al. 2018), scaled magnitudes for each object ranked by distance from the targets and the aperture masks used for photometry extraction that are input into the `TRICERATOPS` validation process. We note that most of the candidates are relatively isolated, except for TIC-339399841 which shows a close (140.0") neighbour.

Two transit events for each candidates were discovered in the work of Hawthorn et al. [2024]. A summary of the key properties of the transit events for each candidate are list in Table 6.2, and the light-curves featuring the transit events are plotted in Figures 6.4 to 6.10.

[2] `https://github.com/jlillo/tpfplotter`

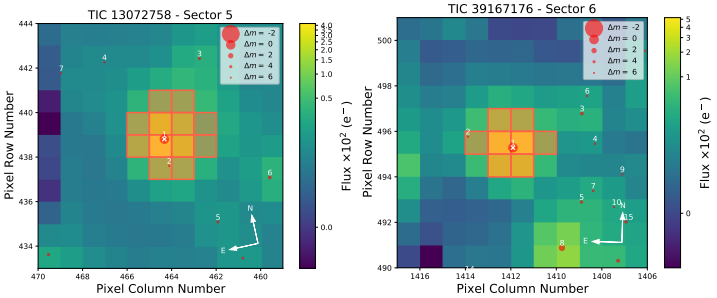

(a) TIC-13072758, Sector 5 (b) TIC-39167176, Sector 6

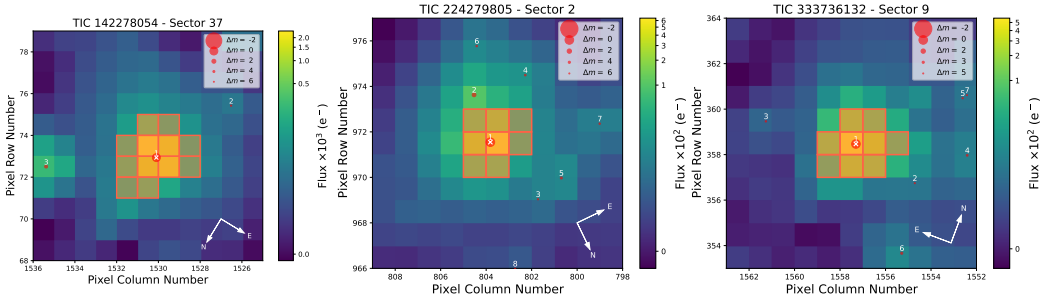

(c) TIC-142278054, Sector 37 (d) TIC-224279805, Sector 2 (e) TIC-333736132, Sector 9

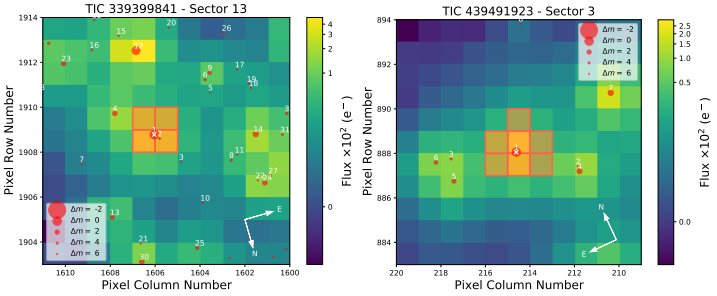

(f) TIC-339399841, Sector 13 (g) TIC-439491923, Sector 3

Figure 6.1: **Subfigures a-g:** Target Pixel Files (TPFs) from TESS with the target stars marked with a white cross. Other sources from *Gaia* DR2 are marked with red circles sized by scaled magnitudes relative to the targets, ranked by distance. The aperture masks are indicated by the red outline.

Table 6.2: TESS transit event properties for each of the duotransit planet candidates.

TIC ID	**Period (d)**	**T_{c1} (BJD)**	**T_{c2} (BJD)**	**Depth (mmag)**	**Duration (hours)**	**TESS Sector of Transits**
13072758	23.79413	2458455.59542	2459193.21321	8.3	8.50	05, 32
39167176	21.78824	2458470.62139	2459211.42524	8.5	6.75	06, 33
142278054	26.49380	2458595.02542	2459310.34700	2.1	5.50	10, 37
224279805	22.98409	2458369.72616	2459105.21576	7.9	5.75	02, 29
333736132	25.24115	2458551.55576	2459283.54739	17.5	2.25	09, 36
339399841	27.24932	2458662.11103	2459043.60913	7.0	5.25	13 ,27
439491923	27.36078	2458405.41942	2459116.79844	12.0	6.25	03, 30

6.2.3 NGTS photometry

The duotransit candidates were photometrically monitored using the NGTS facility as part of larger program on NGTS to follow-up TESS single-transit and duotransit candidates. This program has already successfully confirmed long-period transiting exoplanets and low-mass eclipsing binary systems [Gill et al., 2020c,b; Lendl et al., 2020a].

We observed the duotransit candidates using NGTS telescopes over the 2022 and 2023 seasons. We observed each candidates with between two and nine telescopes whenever a period alias existed and the target was above an elevation of 30 degrees and weather conditions suitable for observing. Imaging was carried out in the NGTS passband with 10 s exposure times. The images were reduced to light curves after each night using the NGTS real-time aperture photometry pipeline fully described in Bryant et al. [2020b]. We used the template matching algorithm described in Gill et al. [2020b] to search the NGTS light curve for transit events. We observed at least one partial transit event for each of the duotransit candidates, and summarise these detections in Table 6.3. The transit events are shown in Figures 6.4 to 6.10.

Table 6.3: NGTS observations showing transit events for each duotransit candidate.

TIC ID	Date	Transit Event Detected
13072758	2022 Dec 16	Ingress with baseline
39167176	2022 Nov 02	Ingress
142278054	2023 Mar 21	Ingress
224279805	2022 Nov 25	Ingress
224279805	2022 Dec 18	Ingress
333736132	2022 Dec 25	Ingress with baseline
333736132	2023 Mar 11	Egress with baseline
333736132	2023 Apr 05	Ingress with baseline
333736132	2023 Jun 20	Egress with baseline
339399841	2022 May 25	Ingress with baseline
339399841	2022 Sep 10	Ingress with baseline
339399841	2023 Jul 07	Egress with baseline
339399841	2023 Aug 03	Ingress with baseline
439491923	2022 Aug 09	Egress
439491923	2022 Oct 02	Egress with baseline
439491923	2022 Oct 29	Ingress with baseline

6.2.4 Gaia

Data from *Gaia* DR3 [Brown et al., 2018] provides important information that can help identify binary star systems. In particular, the NSS (Non-Single Star) flag classifies each star in the *Gaia* catalogue with a flag: 0 indicates a single star, 1 denotes an astrometric binary, 2 denotes a spectroscopic binary, and 3 denotes an eclipsing binary. Each of the seven duotransit transit candidates presented in this work have a *Gaia* NSS flag of 0, indicating there is no strong evidence from *Gaia* data that the star is part of a binary system.
The *Gaia* RUWE (Renormalised Unit Weight Error) values indicate the goodness-of-fit of a single-star solution to the astrometric observations; values > 1.4 are generally interpreted as an indication the star may be in a binary system (Stassun & Torres 2021). We list the RUWE values for each of our seven candidates in Table 6.1. We note that all RUWE values are < 1.4, with the exception of TIC-39167176 that has a very high RUWE of 3.888.

6.2.5 Gemini-Zorro imaging

Complementary to the TESS and NGTS photometric data, we obtained an imaging contrast curve for one of our targets in order to assist with ruling out close companions. This data is also fed into the `TRICERATOPS` process to further constrain the FPP. All imaging data is publicly available from the ExoFOP-TESS website[3].
Gemini-Zorro is an imaging instrument mounted on the *Gemini*-South 8.0 m telescope at Cerro Pachón, Chile. Observations of TIC-333736132 were taken on 2022 May 18 in the two simultaneous bandpasses of 562 and 832 nm, and the reconstructed images and speckle sensitivity curves are shown in Figure 6.2. No close companions are present between angular separations of 0.2" and 1.2" for the target.

6.3 Methodology

6.3.1 Fitting with `exoplanet`

We use the `exoplanet` package [Foreman-Mackey et al., 2021a] to jointly model the TESS and NGTS photometry. Initial fit values are obtained by maximising the log p probability from the `PyMC3` model [Salvatier et al., 2016], and these values are then used as a starting point to draw samples from the posterior distributions of parameters using the NUTS (No U-Turn Sampler) version of the HMC (Hamiltonian Monte Carlo; Hoffman & Gelman [2011]) algorithm. A burn-in of 4000 discarded

[3] `https://exofop.ipac.caltech.edu/tess/`

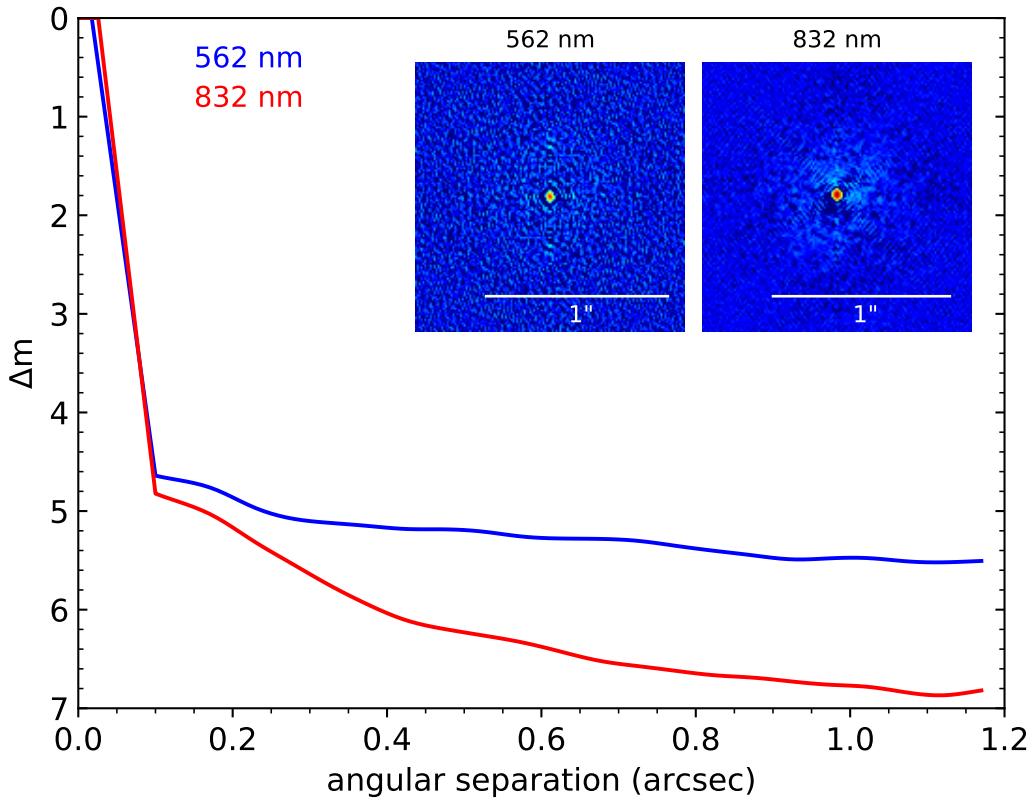

Figure 6.2: Reconstructed images and speckle sensitivity curves for the *Gemini*-Zorro speckle observation of TIC-333736132 in each of the two bandpasses (562 nm and 832 nm). No companion stars are present for angular separations between 0.2" and 1.2".

samples are used, followed by 4000 steps across 10 chains. The priors used for fitting of the stellar parameters are presented in Table 6.7, and the priors for planetary parameters in Table 6.8. Posterior derived values for the stellar and planetary parameters for each target are presented in Tables 6.4 and 6.5 respectively.
We detrend the TESS light curves using a method identical to that of Hawthorn et al. [2023b], using Gaussian Process (GP) modelling in the `celerite` [Foreman-Mackey et al., 2017b] and `PyMC3` packages with a SHOTerm kernel [Foreman-Mackey et al., 2021a] in order to remove the effects of variability from the photometry. The GP model is bounded by three hyperparameters: $log(s2)$ representing excess white noise, and $log(\omega 0)$ and $log(Sw4)$ representing non-periodic components of the stellar variability [Salvatier et al., 2016]. The full equation for the detrending is presented in Equation 6.1:

$$S(\omega) = \sqrt{\frac{2}{\pi}} \frac{S_0 \omega_0^4}{(\omega^2 - \omega_0^2)^2 + \omega_0^2 \omega^2 / Q}. \tag{6.1}$$

Priors and results for the GP components of the TESS fit are presented in Table 6.9. It should be noted that we do not detrend the NGTS light curves in this way due to the shorter out-of-transit baseline of the observations, however we do include a dilution factor D in the TESS data to account for the difference in pixel scales between the two facilities.
The TESS and NGTS light curves are fitted using a Keplerian orbital model as parameterised in Kipping [2013b]. As a prior on the stellar mass (M_*) and radius (R_*), we use the values given in TICv8 catalog [Stassun et al., 2019]. We set a loose prior on the orbital period P based on the solved period from the NGTS transit(s) analysis. A prior on the transit epoch (T_c) is taken from the first transit event in the TESS data (see columns 2 of Table 6.2). The limb-darkening parameters u_1 and u_2 and eccentricity have priors set using the parameterisation of Kipping [2013b]. The impact parameter has a uniform prior from 0 to 1. All priors used for the global fit are set out in Table 6.7 and Table 6.8. Transit models are generated by the `starry` component [Luger et al., 2019] of `exoplanet`.

6.3.2 Validation with `TRICERATOPS`

`TRICERATOPS` [Giacalone et al., 2021] is an algorithm designed to determine the likelihood that a transiting exoplanet candidate from TESS is really a transiting exoplanet as opposed to some other astrophysical system such as an eclipsing binary. Before passing the TESS PDCSAP light curves to `TRICERATOPS`, we first cut out a region of the lightcurve around the transit features, retaining some baseline ei-

ther side. We then detrend the light-curve sections to remove any variability not removed in the PDCSAP process - which may include astrophysical variability or some spacecraft systematics. To do this we mask the in-transit points and apply a third-degree polynomial model to the remaining out-of-transit points, which is then subtracted from the transit data.

Each of these cut-out and detrended TESS lightcurves are passed to `TRICERATOPS`. `TRICERATOPS` first queries the TICv8 catalog for all stars within 10" of the target for their stellar properties. `TRICERATOPS` calculates the total flux contribution to the target aperture by the surrounding stars, and identifies any targets bright enough to produce the observed transit signal. The program requires the transit depth and orbital period of each candidate as priors before computing the FPPs (False-Positive Probabilities). The target apertures in each case were identical to those employed by the SPOC pipeline of TESS (see Section 6.2.2 and Figure 6.1), and the orbital periods were obtained from our global fit (see subsection 6.3.1). The marginal likelihoods and prior probabilities of each scenario are calculated for 10^6 planetary systems to find the overall probabilities, and the values of FPP (False-Positive Probability) and NFPP (Nearby False-Positive Probability). We also fold in the imaging contrast curve data from *Gemini*-Zorro for TIC-333736162 (see Section 6.2.5) to further constrain the final FPP value output by `TRICERATOPS`. Table 1 in Giacalone et al. [2021] lists the scenarios tested by the `TRICERATOPS` algorithm and their descriptions.

The value of FPP is the summation of the probabilities of the TP, PTP and DTP scenarios. Identical to the process described in Giacalone et al. [2021], if the resultant FPP value is < 0.015 we classify it as a 'validated planet', if the FPP value is < 0.5 we classify it as a 'likely planet', and if neither condition is met we classify it as a 'likely false positive'. It should be noted that the NGTS lightcurves are not included in the validation process, as `TRICERATOPS` is built for use with TESS, *Kepler* and K2 data only.

6.4 Results and Discussion

Table 6.4: Fitted host stellar parameters of each candidate.

Property	**TIC-13072758**	**TIC-39167176**	**TIC-142278054**	**TIC-224279805**
Mass ($M_\odot$)	1.240 ± 0.010	2.041 ± 0.308	1.328 ± 0.196	1.002 ± 0.126
Radius ($R_\odot$)	1.436 ± 0.030	1.576 ± 0.090	2.361 ± 0.120	1.182 ± 0.066
Density ($\mathrm{g\,cm^{-3}}$)	0.590 ± 0.032	0.734 ± 0.096	0.142 ± 0.002	0.856 ± 0.038
LD coefficient u_1	0.652 ± 0.284	1.141 ± 0.562	0.528 ± 0.362	0.741 ± 0.277
LD coefficient u_2	0.025 ± 0.330	0.321 ± 0.474	0.093 ± 0.357	0.071 ± 0.317
Property	**TIC-333736132**	**TIC-339399841**	**TIC-439491923**	
Mass ($M_\odot$)	0.771 ± 0.061	1.012 ± 0.131	1.080 ± 0.130	
Radius ($R_\odot$)	0.761 ± 0.036	1.547 ± 0.080	1.266 ± 0.059	
Density ($\mathrm{g\,cm^{-3}}$)	2.469 ± 0.157	0.385 ± 0.012	0.751 ± 0.017	
LD coefficient u_1	0.359 ± 0.024	0.921 ± 0.503	0.998 ± 0.441	
LD coefficient u_2	0.141 ± 0.029	0.149 ± 0.444	0.201 ± 0.403	

Table 6.5: Fitted planetary parameters of each candidate.

Property	**TIC-13072758**	**TIC-39167176**	**TIC-142278054**	**TIC-224279805**
Period (days)	23.7940 ± 0.0002	21.7883 ± 0.0002	26.4937 ± 0.0002	22.9840 ± 0.0001
Radius ($R_\oplus$)	12.3782 ± 0.5761	17.5929 ± 4.4135	13.0909 ± 1.2688	10.8034 ± 0.7662
R_p/R_*	0.0790 ± 0.0054	0.1023 ± 0.0315	0.0508 ± 0.0075	0.0838 ± 0.0106
T_c (TBJD)	1455.5935 ± 0.0050	1470.6250 ± 0.0042	1595.0211 ± 0.0058	1369.7271 ± 0.0028
T1-T4 duration (hours)	7.2338 ± 0.2938	5.3986 ± 0.2347	8.7897 ± 0.4221	6.3327 ± 0.2457
T2-T3 duration (hours)	6.0766 ± 0.4594	3.5907 ± 1.5755	7.0518 ± 1.6669	5.2680 ± 0.2476
Impact parameter	0.3003 ± 0.1950	0.6936 ± 0.2765	0.7303 ± 0.2098	0.3083 ± 0.1789
Semi-major axis (AU)	0.1740 ± 0.0001	0.1938 ± 0.0001	0.1912 ± 0.0001	0.1584 ± 0.0001
$T_{\rm eq}$ (K)	874.6007 ± 25.9823	1157.4166 ± 52.7160	1084.3274 ± 48.3806	736.4638 ± 36.9246
Insolation flux ($S_\odot$)	4.6357 ± 0.0008	3.7388 ± 0.0016	3.8374 ± 0.0017	5.5958 ± 0.0017
Inclination (°)	89.3395 ± 0.4290	88.4963 ± 0.5996	87.5969 ± 0.6909	89.3870 ± 0.3557
Eccentricity	0.4065 ± 0.2043	0.3522 ± 0.2003	0.4596 ± 0.2107	0.1635 ± 0.1337
Argument of periastron (°)	-93.5779 ± 32.4639	-55.3312 ± 82.4584	79.6242 ± 62.2427	16.0802 ± 108.2435
Dilution factor (%)	15.0027 ± 0.0015	15.0025 ± 0.0014	24.0025 ± 0.0014	10.0025 ± 0.0014
Property	**TIC-333736132**	**TIC-339399841**	**TIC-43949123**	
Period (days)	25.2411 ± 0.0001	27.2487 ± 0.0006	27.3608 ± 0.0003	
Radius ($R_\oplus$)	11.3475 ± 0.6483	14.4895 ± 2.5177	14.6009 ± 1.47928	
R_p/R_*	0.1368 ± 0.0142	0.0859 ± 0.0194	0.1057 ± 0.0179	
T_c (TBJD)	1551.5536 ± 0.0012	1662.1144 ± 0.0062	1405.4127 ± 0.0053	
T1-T4 duration (hours)	4.0176 ± 0.1400	7.3962 ± 0.3183	6.8334 ± 0.2711	
T2-T3 duration (hours)	2.3390 ± 0.7821	5.5102 ± 1.4614	5.2379 ± 0.8632	
Impact parameter	0.6817 ± 0.0437	0.6381 ± 0.2359	0.4437 ± 0.2420	
Semi-major axis (AU)	0.1545 ± 0.0001	0.1780 ± 0.0001	0.1824 ± 0.0001	
$T_{\rm eq}$ (K)	505.2652 ± 25.6000	808.3039 ± 39.7854	755.0274 ± 33.2958	
Insolation flux ($S_\odot$)	5.8812 ± 0.0009	4.4286 ± 0.0035	4.2178 ± 0.0019	
Inclination (°)	89.1056 ± 0.0573	88.5223 ± 0.5465	89.1795 ± 0.4475	
Eccentricity	0.3462 ± 0.0172	0.2639 ± 0.1711	0.2098 ± 0.1678	
Argument of periastron (°)	89.7827 ± 1.4645	10.0922 ± 102.6792	-34.8325 ± 98.4322	
Dilution factor (%)	25.0026 ± 0.0002	20.0025 ± 0.0014	23.0025 ± 0.0014	

In Table 6.6, we list the individual TP (transiting planet) scenario probabilities, the combined TP which is a summation of the individual TP probabilities, and the FPP value, used to classify each of the candidates. We include the fitted planetary radius value R_p for each of our candidates for the TP scenario.

Table 6.6: False-Positive Probabilities (FPPs) and Nearby False-Positive Probabilities (NFPPs) from `TRICERATOPS` for each of the duotransit candidates, the combined probability that the event is a transiting planet ('Σ TP'), each of the transiting planet scenarios as set out in Table 1 of Giacalone et al. [2021] and the classifications of the duotransit planet candidates based on the FPP values according to Giacalone et al. [2021]. The 'Other' column encapsulates all other Eclipsing Binary ('EB') scenarios and EB with twice the orbital period ('EB×2P') scenarios tested for by `TRICERATOPS`, and represents scenarios not involving a transiting planet in any configuration. We also include the fitted planetary radius value R_p from the TP scenario results.

TIC ID	**FPP**	**NFPP**	**Σ TP**	**TP**	**PTP**	**STP**	**DTP**	**BTP**
13072758	0.0422 ± 0.0361	0.00000	0.96095	0.70165	0.14640	0.08235	0.03055	0.00000
39167176	0.9752 ± 0.0311	0.00000	0.01037	0.00482	0.00166	0.00000	0.00389	0.00000
142278054	0.4155 ± 0.0847	0.00000	0.99672	0.55024	0.14880	0.26471	0.03296	0.00000
224279805	0.0486 ± 0.0236	0.00000	0.95669	0.66395	0.15980	0.03361	0.09933	0.00000
333736132	0.0885 ± 0.1275	0.00000	0.87899	0.56161	0.25361	0.00029	0.06348	0.00000
339399841	0.6970 ± 0.0506	0.25008	0.28370	0.16011	0.07610	0.00363	0.04381	0.00005
439491923	0.2367 ± 0.0503	0.00000	0.81924	0.42657	0.20706	0.12289	0.06272	0.00000

TIC ID	**NTP 1**	**NTP 2**	**Other**	**R_p ($R_\oplus$)**	**Classifications**
13072758	—	—	0.03905	11.77529	Likely planet
39167176	—	—	0.98963	15.46155	Likely false positive
142278054	—	—	0.00328	10.98291	Likely planet
224279805	0.00000	—	0.04331	10.90225	Likely planet
333736132	—	—	0.12101	9.79974	Likely planet
339399841	0.00000	0.00000	0.71630	15.60767	Likely false positive
439491923	—	—	0.18076	14.35336	Likely planet

6.4.1 TIC-13072758

TIC-13072758 is a $1.24 \pm 0.01\,M_{\odot}$, $1.44 \pm 0.03\,R_{\odot}$, 12.70 Vmag star hosting a companion of radius $12.38 \pm 0.58\,R_{\oplus}$ on an orbital period of 23.7940 ± 0.0002 days, that originally had two transits observed in Sectors 5 and 32 of TESS, along with one observation of a transit ingress from NGTS that confirmed its period. Its overall FPP value from `TRICERATOPS` of 0.0422 ± 0.0361 is the lowest of the candidates and gives it a classification of 'likely planet'. The radius from `TRICERATOPS` of $11.77529\,R_{\oplus}$ is close to the fitted radius from our analysis with EXOPLANET, however it should be noted that the `exoplanet` fit also takes into account the NGTS data, whereas `TRICERATOPS` is only given the TESS data for its analysis (this also applies to all other candidates presented here). The NGTS transit data is consistent with the shape, duration and depth of the phase-folded TESS transits. In addition to the TESS and NGTS data used in our analysis, there also exists one spectrum from FEROS (not suitable for precise radial velocities) and two light curves from the *Observatoire Moana* telescope at El Sauce Observatory in Chile (described in Jones et al. 2024) as part of the *WINE* (Warm gIaNts with tEss) collaboration (Hobson et al. 2021), the first of which is unclear, and the second of which shows a full transit consistent with the depths and durations of the TESS transits presented here. The light curves modelled with `exoplanet` are shown in Figure 6.4.

6.4.2 TIC-39167176

TIC-39167176 is a $2.04 \pm 0.31\,M_{\odot}$, $1.58 \pm 0.09\,R_{\odot}$ 12.73 Vmag star hosting a companion of radius $17.59 \pm 4.41\,R_{\oplus}$ on an orbital period of 21.7883 ± 0.0002 days, observed in Sectors 6 and 33 of TESS and one NGTS transit ingress. It has the shortest orbital period of our sample, and possesses both the largest radius and the highest equilibrium temperature of 1157.4 ± 52.7 K. It is classified as a 'likely false positive' by `TRICERATOPS`, with an FPP value of 0.9572 ± 0.0311 and a probability of other scenarios involving an eclipsing binary configuration of 0.98963; the highest of which is the SEB scenario at a probability of 0.38086 (an unresolved bound companion; eclipsing binary with the orbital period around the secondary star). We are continuing to investigate the cause of the NGTS transit being shallower than the observed TESS phase-folded data, but this colour dependent depth may be further indication that the candidate is a blended eclipsing binary (e.g. Louie et al. 2020; Wang et al. 2021b). There is no additional data from other facilities currently available for this target. The light curves modelled with `exoplanet` are shown in Figure 6.5.

6.4.3 TIC-142278054

TIC-142278054 is a $1.33 \pm 0.20\,M_{\odot}$, $2.36 \pm 0.12\,R_{\odot}$, 10.88 Vmag star hosting a companion of radius $13.09 \pm 1.27\,R_{\oplus}$ on an orbital period of 26.4937 ± 0.0002 days. It was observed in Sectors 10 and 37 of TESS, and one NGTS observation of a transit ingress. The host star is the largest and least dense of our sample ($0.142 \pm 0.002\,g\,cm^{-3}$), meaning it may be slightly inflated. Its FPP value of 0.4155 ± 0.0847 classifies it as a 'likely planet'. We estimate that the increased scatter in the NGTS data towards the latter half of the transit could be caused by an increase in the target airmass, but are currently continuing to further investigate the NGTS data. The target has also been observed in Sector 63, camera 1 of TESS, and shows an additional transit around timestamp 3025.75 TBJD of depth ∼2.1 mmag and duration ∼5.50 hours, which provides additional data for future fitting and is consistent with the other TESS transits presented here. The light curves modelled with `exoplanet` are shown in Figure 6.6.

6.4.4 TIC-224279805

TIC-224279805 is a $1.00 \pm 0.13\,M_{\odot}$, $1.18 \pm 0.07\,R_{\odot}$, 12.62 Vmag star hosting a planet of radius $10.80 \pm 0.77\,R_{\oplus}$ on an orbital period of 22.9840 ± 0.0001 days. TESS observed the target in Sectors 2 and 29, and NGTS observed two consecutive transit ingresses of epochs 126 and 127 which confirmed the period, albeit with minimal baseline and only partial transit coverage. `TRICERATOPS` calculates an overall FPP of 0.0486 ± 0.0236, meaning this companion is classified as a 'likely planet'. It is also the smallest of the sample according to our modelling with EXOPLANET, which takes into account all available photometry from TESS and NGTS. As with TIC-142278054, the increase in both the scatter and the uncertainties in the second half of the NGTS data for epoch 126 may be caused by heightened airmass, but we are continuing to examine the data further. In addition to the TESS and NGTS data used in our analysis, there also exists one spectra from FEROS (not suitable for precise radial velocities) and one light curve from the *Observatoire Moana* as part of the *WINE* collaboration that is unclear. The light curves modelled with `exoplanet` are shown in Figure 6.7.

6.4.5 TIC-333736132

TIC-333736162 is a $0.77 \pm 0.06\,M_{\odot}$, $0.76 \pm 0.05\,R_{\odot}$, 13.06 Vmag star hosting a companion of radius $11.35 \pm 0.65\,R_{\oplus}$ on an orbital period of 25.2411 ± 0.0001 days. Transits were observed in Sectors 9 and 36 of TESS, and NGTS provided four ob-

servations of transit ingresses from Dec 2022 to Jun 2023. It is both the closest to its star (0.1545 ± 0.0001 AU) and the lowest in equilibrium temperature (510 ± 30 K) of our candidates, most likely owing to its smaller and cooler (4722 K) K-dwarf host. It has an overall FPP of 0.0885 ± 0.1275, and we therefore classify it as a 'likely planet'. It is also the only candidate to include a contrast curve from *Gemini*-Zorro (see Figure 6.2) to further constrain its FPP value. We are currently investigating the NGTS data to determine the source of some depth inconsistencies for epochs 119 and 120. The target has also been observed in Sector 63, camera 1 of TESS, and shows an additional transit around timestamp 3015.55 TBJD, which has a depth of ∼17.5 mmag and a duration of ∼2.25 hours, which is consistent with the TESS transits presented here and provides additional data for future fitting. This target has also been promoted to TOI status (TOI-6669), and is the subject of an upcoming publication (Kendall et al., in prep). The light curves modelled with `exoplanet` are shown in Figure 6.8.

6.4.6 TIC-339399841

TIC-339399841 is a $1.012 \pm 0.131\,M_{\odot}$, $1.547 \pm 0.080\,R_{\odot}$, 13.06 Vmag star hosting a companion of radius $14.49 \pm 2.52\,R_{\oplus}$ on an orbital period of 27.2487 ± 0.0006 days. TESS observed transits in Sectors 13 and 27, and NGTS observed four transits comprised of three ingresses and one egress from May 2022 to Aug 2023 that solved the orbital period of the companion. Our analysis with `TRICERATOPS` classifies it as a 'likely false positive', as it has a high FPP value of 0.6970 ± 0.0506 and an NFPP value of 0.25008. The highest probability scenario is the NEB scenario (no unresolved companion; eclipsing binary with the orbital period around a nearby star), the most likely host being TIC-339399847, with a probability of 0.17835 and an overall non-transiting-planet probability of 0.71630. As with other targets, we are investigating the NGTS data to determine the source of increased uncertainties and the precise timings of the transit epochs in the NGTS data. There is no additional data currently available for this target. The light curves modelled with `exoplanet` are shown in Figure 6.9.

6.4.7 TIC-439491923

TIC-439491923 is a $1.08 \pm 0.13\,M_{\odot}$, $1.27 \pm 0.06\,R_{\odot}$, 13.45 Vmag star hosting a companion of radius $14.60 \pm 1.48\,R_{\oplus}$ on an orbital period of 27.3608 ± 0.0003 days. It was observed by TESS in Sectors 3 and 30, and NGTS observed three transits (one ingress and two egresses) from Aug 2022 to Oct 2022. It is the longest pe-

riod candidate of our sample, but also orbits the faintest of the targets. Analysis with TRICERATOPS indicates that it is a 'likely planet' with an overall FPP value of 0.2367 ± 0.0503 and a combined transiting planet probability of 0.81924, the most probable scenario of which is a transiting planet around the target star of 0.42657. We currently have an additional NGTS observation for this target, taken on 2022 Dec 23 and not shown here, but we are still disentangling the true nature of this event. There is no additional data currently available for this target. The light curves modelled with exoplanet are shown in Figure 6.10.

6.4.8 Summary of results

We find that five of our seven candidates are classified as 'likely planets', and two are classified as 'likely false positives' based on their individual FPPs. TIC-142278054 has the highest combined TP probability over all scenarios of 0.99672, but an on-target TP probability of 0.55024. Only one target, TIC-339399841, has a small probability of orbiting an unresolved background star (BTP) of 0.00005, and no candidates are likely to be orbiting nearby stars (NTP), even if these scenarios were tested for. TIC-333736132/TOI-6669 is the subject of a future publication (Kendall et al., in prep), and is classified by TRICERATOPS as a likely planet scenario with an overall low FPP of 0.0885, and its highest probability scenario is a planet around the target star (TP) at 0.56161. It should be noted that while five of our candidates are classified as 'likely planets', none of them can be classified as 'validated planets' as none possess an FPP < 0.015.

For the two candidates classified as likely false positives, we find that the most probable scenario for TIC-39167176 is an SEB scenario, i.e. an unresolved bound companion in an eclipsing binary with an orbital period of 21.78824 days around the secondary star; with a probability of 0.38086. For TIC-339399841 the most probable scenario is an NEB scenario, i.e. an eclipsing binary with an orbital period of 27.24932 days around the TESS object TIC-339399847; with a probability of 0.17835.

In Figure 6.3 we plot the periods and radii of the confirmed TESS planets from the Exoplanet Archive with measured masses against our duotransit candidates assessed with TRICERATOPS, colour-coded by classification.

6.5 Conclusion

We have presented seven long-period duotransiting planets from TESS that have had their periods solved with NGTS observations. Each candidate was analysed

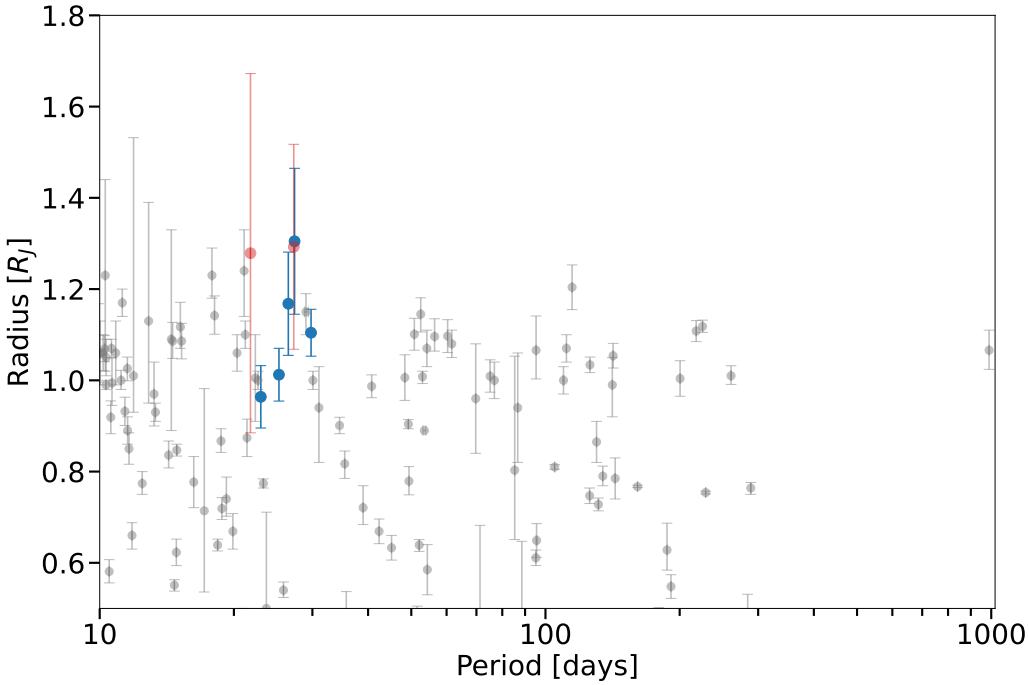

Figure 6.3: Confirmed long period (P $>$ 10 days) transiting giant exoplanets (R $>$ 0.5 R_J). Our sample of duotransit candidates are plotted in blue (likely planets) and red (likely false positives). Other discovered planets with measured masses and radii are plotted in grey.

with the `TRICERATOPS` package in order to determine the probabilities of a set of transiting planet (TP) scenarios, and their overall false positive probabilities (FPPs). We classified each candidate based on the metrics of Giacalone et al. [2021], and found that five candidates were designated as 'likely planets', and two are 'likely false positives'. NGTS is continuing to monitor a more complete set of duotransiting planets with a view to solving their orbital periods, which will be able to be passed to `TRICERATOPS` to determine the most suitable candidates for follow-up with ground-based high-resolution spectrographs such as HARPS and *ESPRESSO*. With the eventual mass determinations and confirmations of these candidates, we will be able to further examine and characterise a set of long-period warm and cool planets for the purposes of studying their formation and evolution processes.

6.6 Appendix

Priors and fits with `exoplanet`

Table 6.7: Priors for the host stellar parameters of each candidate.

Property	**Type**	**TIC-13072758**	**TIC-39167176**	**TIC-142278054**	**TIC-224279805**
Baseline flux	$\mathcal{N}$	(0,1)	(0,1)	(0,1)	(0,1)
Mass ($M_\odot$)	$\mathcal{N}$	(1.24,0.01)	(2.09,0.30)	(1.28,0.20)	(0.99,0.13)
Radius ($R_\odot$)	$\mathcal{N}$	(1.43,0.03)	(1.56,0.09)	(2.39,0.12)	(1.19,0.07)
LD coefficient u_1	Kipping [2013b]				
LD coefficient u_2	Kipping [2013b]				
Property		**TIC-333736132**	**TIC-339399841**	**TIC-43949123**	
Baseline flux	$\mathcal{N}$	(0,1)	(0,1)	(0,1)	
Mass ($M_\odot$)	$\mathcal{N}$	(0.76,0.09)	(1.01,0.13)	(1.09,0.13)	
Radius ($R_\odot$)	$\mathcal{N}$	(0.76,0.06)	(1.55,0.08)	(1.26,0.06)	
LD coefficient u_1	Kipping [2013b]				
LD coefficient u_2	Kipping [2013b]				

Numbers in brackets represent:
(mean μ, standard deviation σ) for normal distribution $\mathcal{N}(\mu,\sigma)$
Distributions for limb darkening coefficients u_1 and u_2 are built into the `exoplanet` package and based on Kipping [2013b]

Table 6.8: Priors for the planetary parameters of each candidate.

Property	**Type**	**TIC-13072758**	**TIC-39167176**	**TIC-142278054**	**TIC-224279805**
Period (days)	$\mathcal{N}$	(23.79413,1)	(21.78824,1)	(26.49380,1)	(22.98409,1)
log(R_p) §	$\mathcal{N}$	(-2.143,1)	(-1.989,1)	(-2.212,1)	(-2.291,1)
T_c (TBJD)	$\mathcal{U}$	(1455.35,1455.85)	(1470.37, 1470.87)	(1594.78, 1595.28)	(1369.48,1369.98)
Impact parameter	$\mathcal{U}$	(0,1)	(0,1)	(0,1)	(0,1)
Eccentricity	Kipping [2013b], $\mathcal{B}$	(e, 0.867, 3.03)	(e, 0.867, 3.03)	(e, 0.867, 3.03)	(e, 0.867, 3.03)
Argument of periastron (rad)	$\mathcal{U}$	(-π, π)	(-π, π)	(-π, π)	(-π, π)
Dilution factor (%)	$\mathcal{D}$	(15,15.005)	(0,0.005)	(24, 24.005)	(10,10.005)
Property		**TIC-333736132**	**TIC-339399841**	**TIC-43949123**	
Period (days)	$\mathcal{N}$	(25.24115,1)	(27.24932,1)	(27.36078,1)	
log(R_p) §	$\mathcal{N}$	(-2.559,1)	(-2.152,1)	(-1.994,1)	
T_c (TBJD)	$\mathcal{U}$	(1551.31,1551.81)	(1661.86,1662.36)	(1405.17,1405.67)	
Impact parameter	$\mathcal{U}$	(0,1)	(0,1)	(0,1)	
Eccentricity	Kipping [2013b], $\mathcal{B}$	(e, 0.867, 3.03)	(e, 0.867, 3.03)	(e, 0.867, 3.03)	
Argument of periastron (rad)	$\mathcal{U}$	(-π, π)	(-π, π)	(-π, π)	
Dilution factor (%)	$\mathcal{D}$	(25,25.005)	(20,20.005)	(23,23.005)	

Numbers in brackets represent:
(mean μ, standard deviation σ) for normal distribution $\mathcal{N}(\mu,\sigma)$
(lower limit x, upper limit y) for uniform distribution $\mathcal{U}(x,y)$
Distributions for eccentricity e are built into the `exoplanet` package and based on Kipping [2013a] which includes the Beta distribution $\mathcal{B}(e, a, b)$ (exponential e, shape parameter a, shape parameter b)
§ Equivalent to $0.5\times\log(\delta)+\log(R_*)$, δ represents transit depth (based on ExoFOP catalog values)

Table 6.9: Priors and fitted parameter values for the TESS GP models of each candidate.

Property	**Type**	**TIC-13072758**		**TIC-39167176**		**TIC-142278054**		**TIC-224279805**	
Sector 1		**Prior**	**Value**	**Prior**	**Value**	**Prior**	**Value**	**Prior**	**Value**
Mean	$\mathcal{N}$	(0,1)	$1.78e^{-5} \pm 2.24e^{-4}$	(0,1)	$-1.72e^{-5} \pm 2.32e^{-4}$	(0,1)	$2.31e^{-5} \pm 1.45e^{-4}$	(0,1)	$1.05e^{-5} \pm 1.98e^{-4}$
$log(s2)$*	$\mathcal{N}$	(-13.528,0.1)	-13.88 ± 0.04	(-13.720,0.1)	-14.10 ± 0.04	(-15.222,0.1)	-15.94 ± 0.05	(-13.732,0.1)	-14.07 ± 0.04
$log(\omega 0)$	$\mathcal{N}$	(0,0.1)	0.16 ± 0.10	(0,0.1)	0.15 ± 0.10	(0,0.1)	0.05 ± 0.09	(0,0.1)	0.16 ± 0.10
$log(Sw4)$*	$\mathcal{N}$	(-13.528,0.1)	-13.61 ± 0.10	(-13.720,0.1)	-13.79 ± 0.10	(-15.222,0.1)	-15.04 ± 0.09	(-13.732,0.1)	-13.82 ± 0.10
Sector 2									
Mean	$\mathcal{N}$	(0,1)	$5.43e^{-5} \pm 3.45e^{-4}$	(0,1)	$-3.67e^{-7} \pm 2.75e^{-4}$	(0,1)	$1.17e^{-5} \pm 1.32e^{-4}$	(0,1)	$-2.71e^{-5} \pm 3.41e^{-4}$
$log(s2)$*	$\mathcal{N}$	(-12.589,0.1)	-12.72 ± 0.02	(-12.906,0.1)	-13.03 ± 0.02	(-14.915,0.1)	-15.10 ± 0.03	(-12.826,0.1)	-13.05 ± 0.03
$log(\omega 0)$	$\mathcal{N}$	(0,0.1)	0.20 ± 0.10	(0,0.1)	0.21 ± 0.11	(0,0.1)	0.14 ± 0.10	(0,0.1)	0.16 ± 0.11
$log(Sw4)$*	$\mathcal{N}$	(-12.589,0.1)	-12.66 ± 0.10	(-12.906,0.1)	-13.04 ± 0.10	(-14.915,0.1)	-14.86 ± 0.10	(-12.826,0.1)	-12.92 ± 0.10
		TIC-333736132		**TIC-339399841**		**TIC-439491923**			
Sector 1		**Prior**	**Value**	**Prior**	**Value**	**Prior**	**Value**		
Mean	$\mathcal{N}$	(0,1)	$4.52e^{-5} \pm 3.73e^{-4}$	(0,1)	$2.60e^{-5} \pm 2.19e^{-4}$	(0,1)	$-3.04e^{-5} \pm 4.25e^{-4}$		
$log(s2)$*	$\mathcal{N}$	(-13.004,0.1)	-14.05 ± 0.05	(-13.467,0.1)	-13.65 ± 0.04	(-12.797,0.1)	-12.97 ± 0.05		
$log(\omega 0)$	$\mathcal{N}$	(0,0.1)	0.08 ± 0.09	(0,0.1)	0.18 ± 0.10	(0,0.1)	0.12 ± 0.10		
$log(Sw4)$*	$\mathcal{N}$	(-13.004,0.1)	-13.00 ± 0.08	(-13.467,0.1)	-13.56 ± 0.10	(-12.797,0.1)	-12.75 ± 0.10		
Sector 2									
Mean	$\mathcal{N}$	(0,1)	$3.94e^{-4} \pm 7.10e^{-4}$	(0,1)	$1.83e^{-5} \pm 4.26e^{-4}$	(0,1)	$-6.09e^{-5} \pm 5.48e^{-4}$		
$log(s2)$*	$\mathcal{N}$	(-11.808,0.1)	-12.94 ± 0.03	(-12.487,0.1)	-12.59 ± 0.03	(11.756,0.1)	-11.91 ± 0.02		
$log(\omega 0)$	$\mathcal{N}$	(0,0.1)	0.05 ± 0.06	(0,0.1)	0.15 ± 0.10	(0,0.1)	0.16 ± 0.11		
$log(Sw4)$*	$\mathcal{N}$	(-11.808,0.1)	-11.82 ± 0.08	(-12.487,0.1)	-12.54 ± 0.10	(11.756,0.1)	-11.89 ± 0.10		

Numbers in brackets represent:
(mean μ, standard deviation σ) for normal distribution $\mathcal{N}(\mu,\sigma)$
Prior values:
* Equivalent to the log of the variance of the TESS flux from the corresponding sector

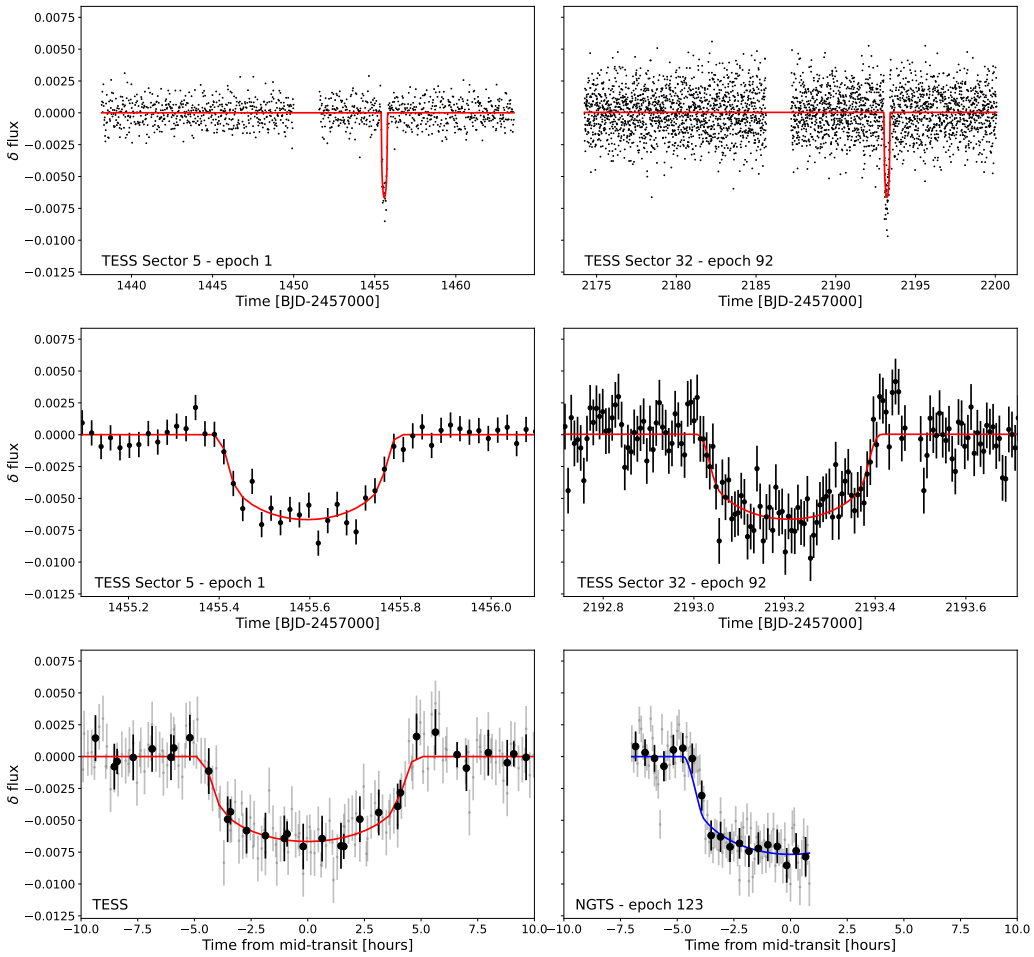

Figure 6.4: **TIC-13072758 - First row panels:** TESS data from each Sector (black points), overplotted with the transit models (red). **Second row panels:** TESS data from each Sector (black points), zoomed in to show individual transits and overplotted with the transit models (red). **Third row panels left:** TESS data (grey points), phase-folded to period and epoch values from Table 6.5, binned to 10 minutes (black points) and overplotted with the transit model (red). **Third row panels right:** NGTS data for TIC-13072758 (grey points) binned to 5 minutes (black points) overplotted with the transit model (blue).

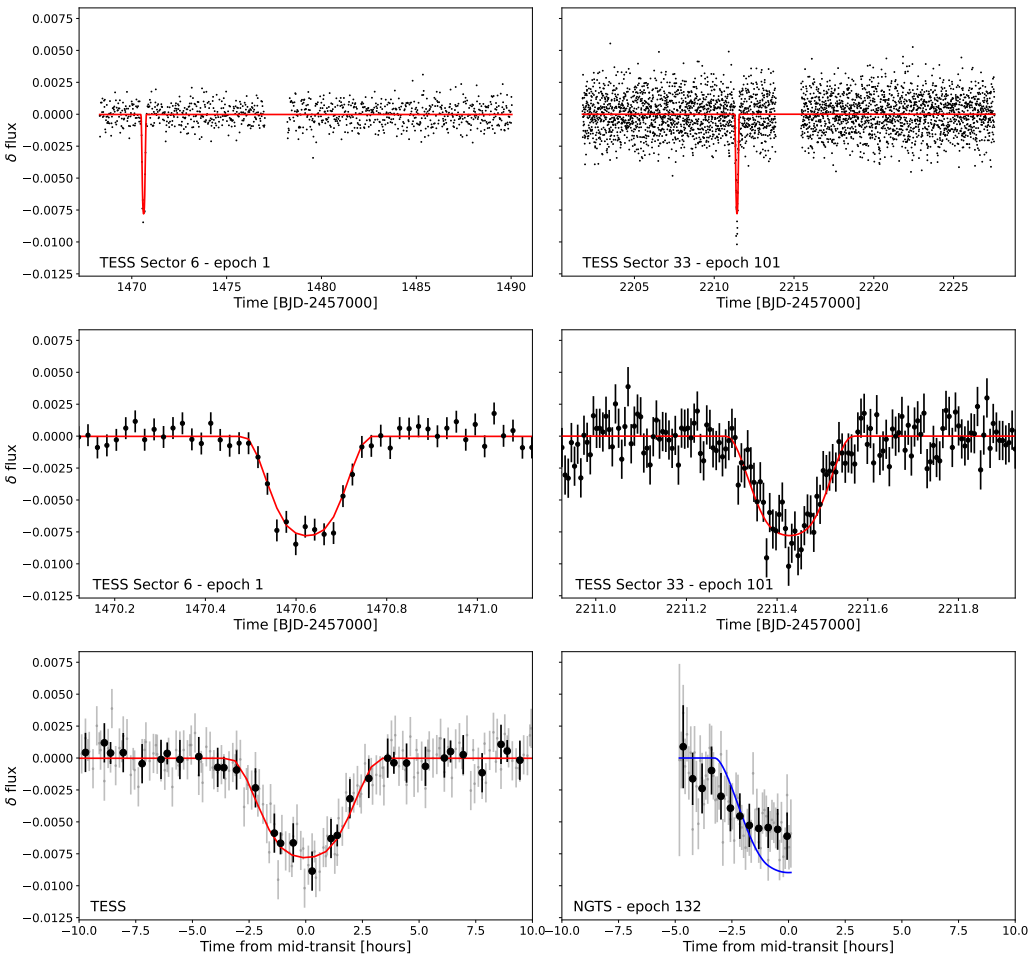

Figure 6.5: Same as for Figure 6.4, for TIC-39176176.

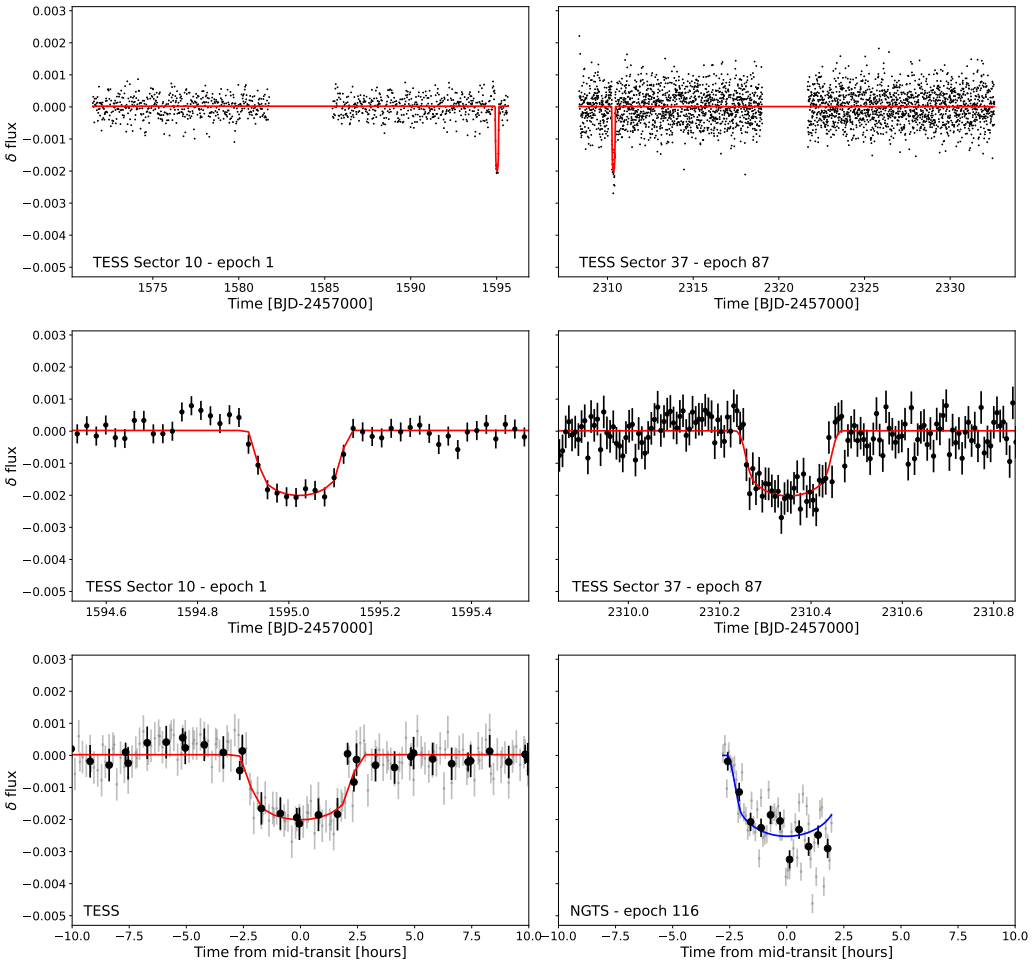

Figure 6.6: Same as for Figure 6.4, for TIC-142278054.

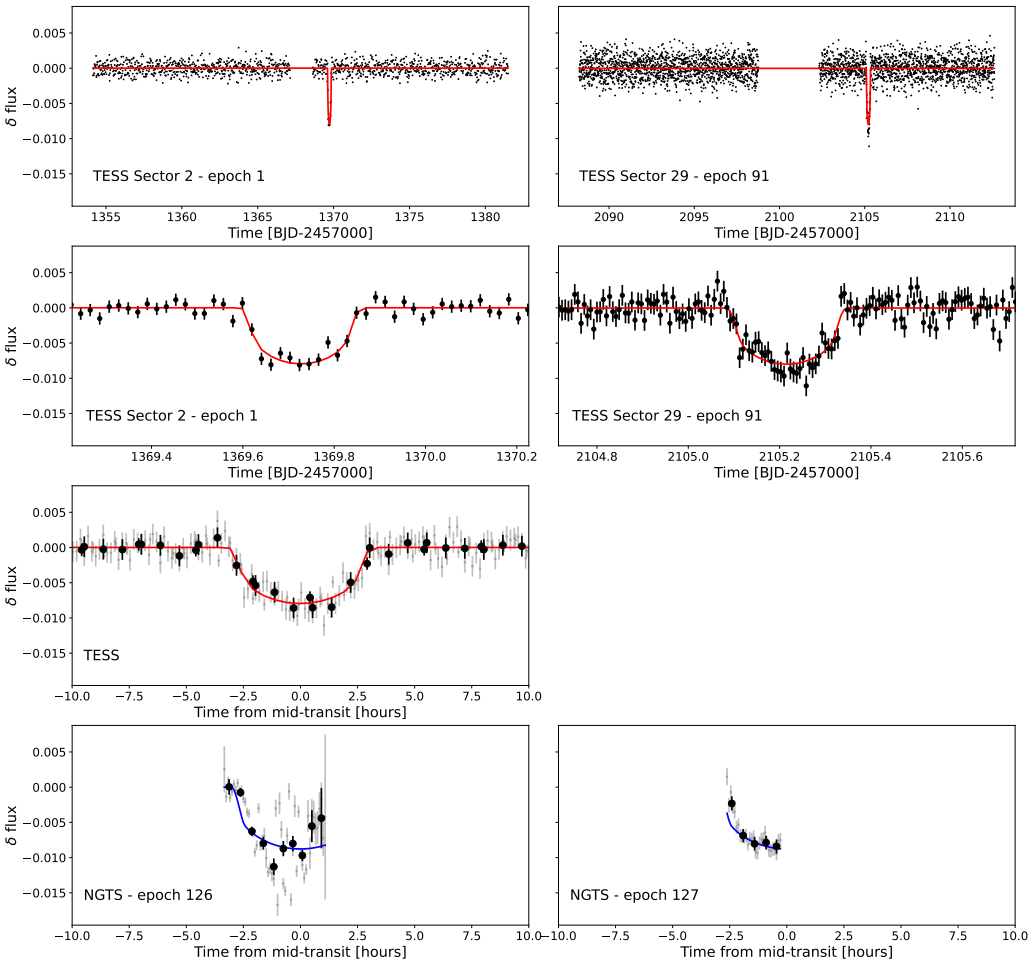

Figure 6.7: Same as for Figure 6.4, for TIC-224279805.

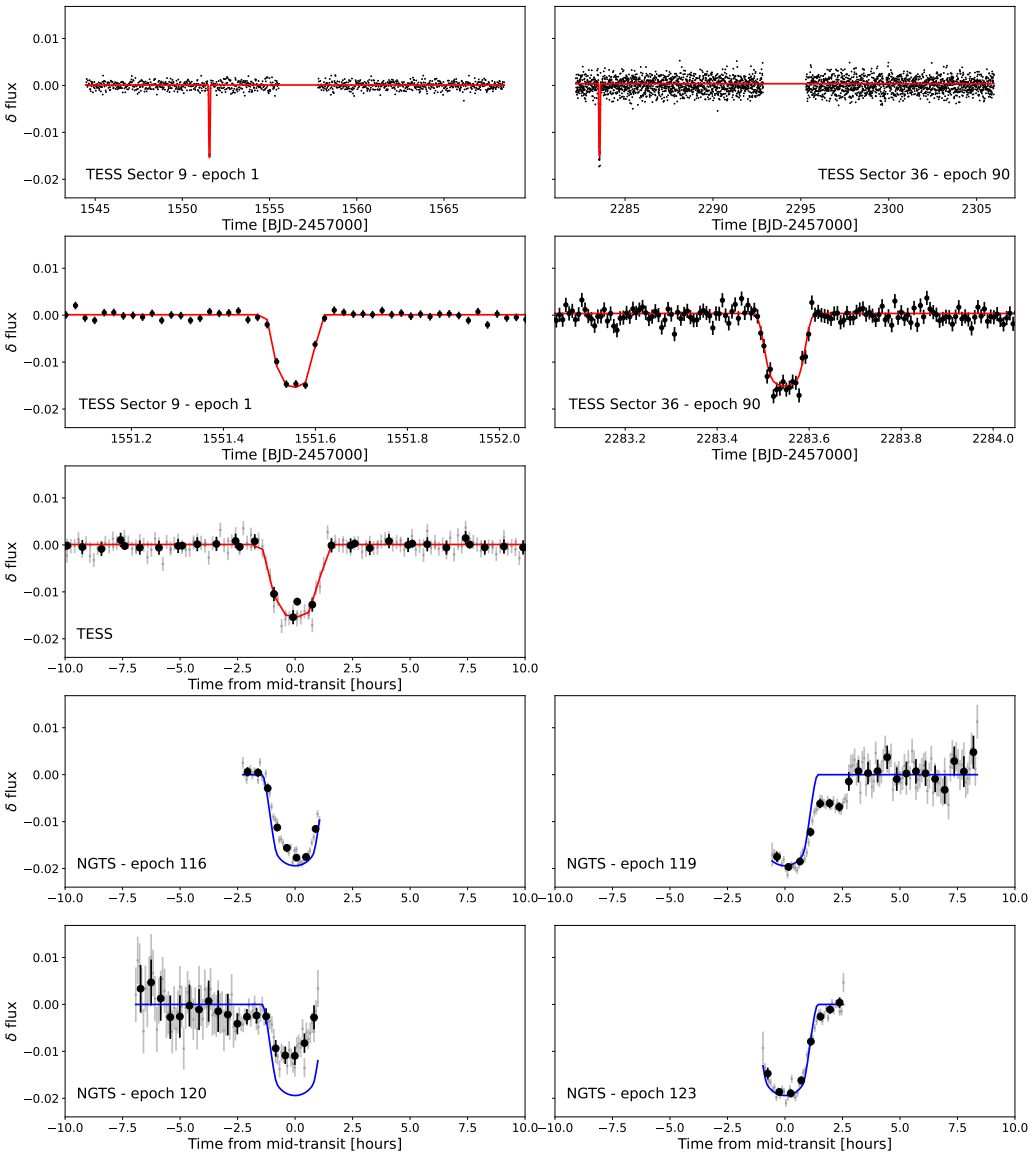

Figure 6.8: Same as for Figure 6.4, for TIC-333736132.

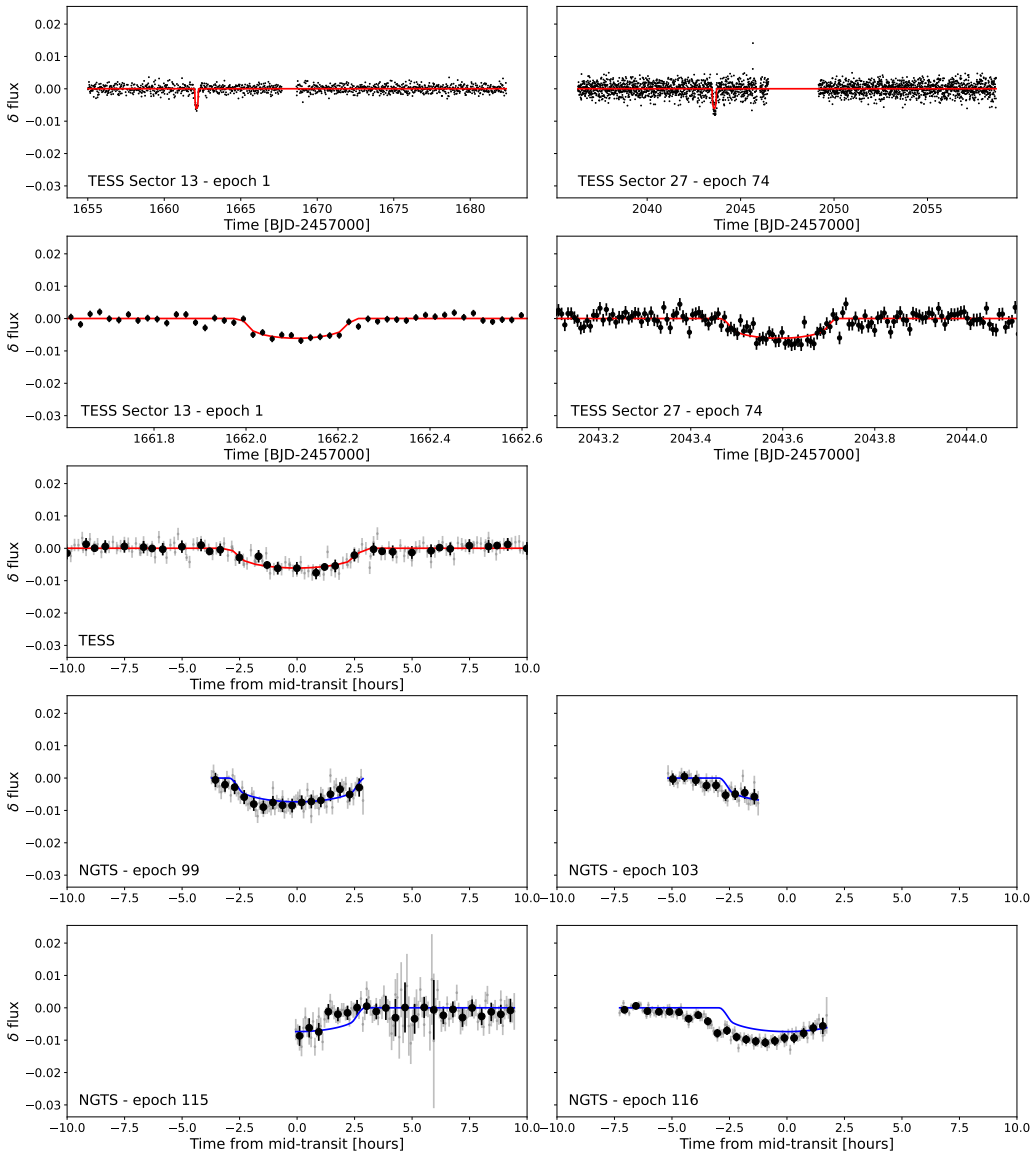

Figure 6.9: Same as for Figure 6.4, for TIC-339399841.

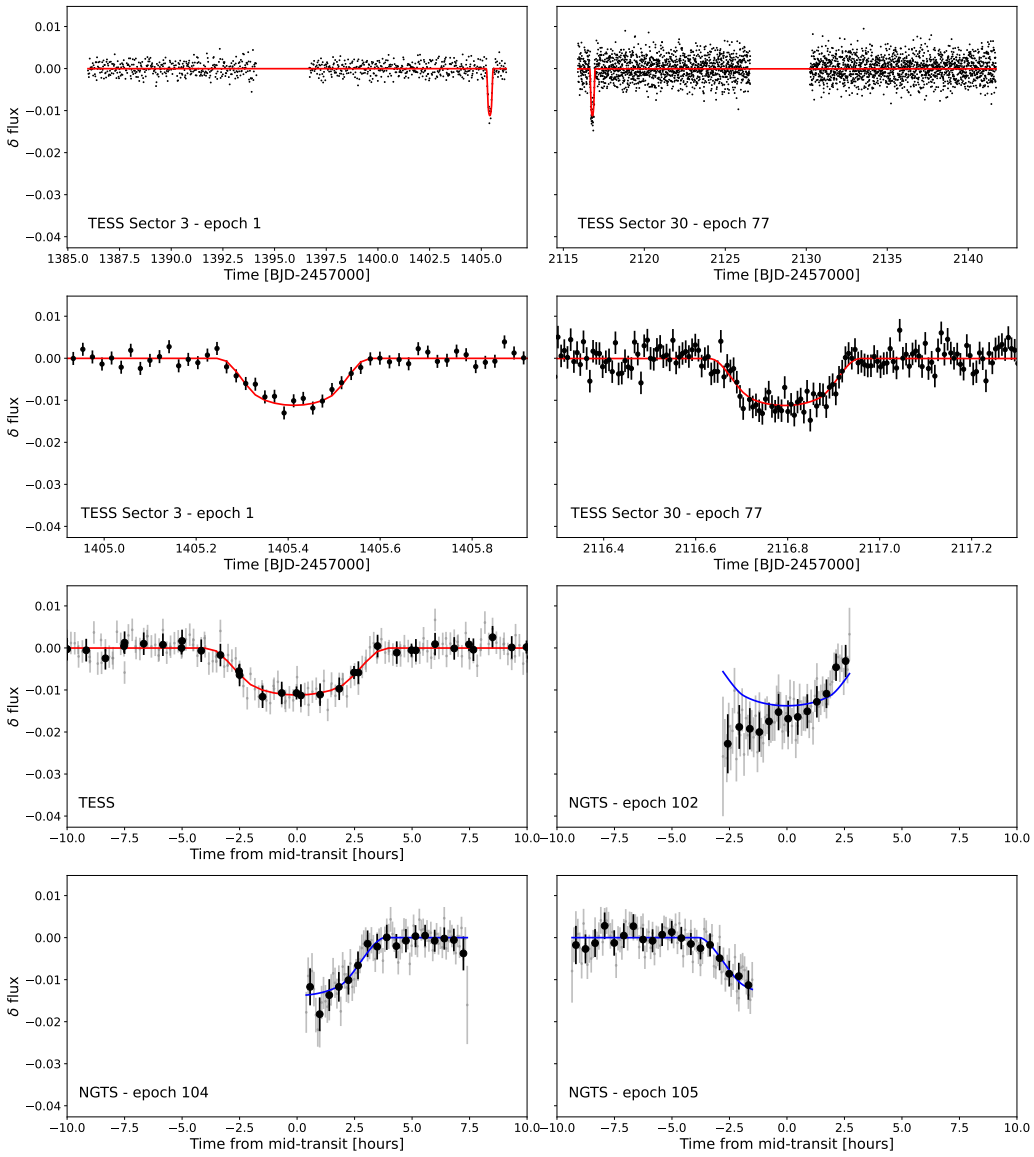

Figure 6.10: Same as for Figure 6.4, for TIC-439491923.

Chapter 7

Conclusions

"Then according to the man who showed his outstretched arm to space / He turned around and pointed, revealing all the human race."

'Close to the Edge', Yes, 1972, Anderson/Howe

This thesis has presented the detection and characterisation of two exoplanet systems, TOI-836 (Chapter 3) and TOI-908 (Chapter 4); 85 duotransiting exoplanet candidates from a search of TESS data in the Southern Ecliptic hemisphere (Chapter 5); and the statistical analysis of seven solved duotransiting planet candidates using NGTS follow-up photometry and the validation tool `TRICERATOPS` (Chapter 6). Here I will summarise the general results of each publication, and the potential future work related to each, alongside a general discussion of the future of exoplanet science.

7.1 TOI-836

Chapter 3 presented the discovery and characterisation of the two planets of the TOI-836 system. TOI-836 b is a super-Earth residing in the radius valley (see Section 1.9.1) with a radius of $1.70 \pm 0.07\,R_\oplus$ and a mass of $4.5 \pm 0.9\,M_\oplus$, and orbits the host star on an orbital period of 3.82 days. TOI-836 c is a mini-Neptune with a radius of $2.59 \pm 0.09\,R_\oplus$, a mass of $9.6 \pm 2.6\,M_\oplus$, and an orbital period of 8.60 days. Photometric transit data was obtained from TESS in Sectors 11 and 38, alongside 4 transits of TOI-836 c and 1 of TOI-836 b from CHEOPS. This was combined with single transit observations from the LCOGT, *MEarth*, ASTEP and NGTS facilities,

and long-term photometric monitoring from WASP assisted in the confirmation of a stellar rotation period of 21.99 ± 0.097 days. Radial velocity data from HARPS and PFS was used to constrain the masses of the planets, and HIRES was used to constrain a long-term RV trend of $-7.95 \pm 2.14\,\mathrm{m\,s^{-1}\,yr^{-1}}$. Imaging data was taken with *Gemini*-Zorro and *Gemini*-'Alopeke, VLT-NaCo, *Keck*-2-NIRC2 and SOAR-HRCam, none of which found any close companions to the host star.

The `exoplanet` package was used to globally model the photometric and spectroscopic data for the system and provide the planetary and stellar parameters. Gaussian Process models were used in order to mitigate for stellar activity and the derived rotation period, and stellar modelling for the fundamental parameters, estimated age and abundances was performed using the `ARES+MOOG` packages. We also examined the metallicity of the star in relation to the wider population of planets orbiting K-dwarfs. The internal structures of the two planets were modelled using Bayesian analysis methods, and it was found that TOI-836 b is likely to be comprised of a small fraction of gas with a non-negligible amount of water, whereas TOI-836 c likely has higher masses of both gas and water due to its lower bulk density.

As a result of our global modelling we found that TOI-836 b lies in the radius valley parameter space, where a dearth of planets around $\sim 2\,\mathrm{R_\oplus}$ is seen. Such planets are valuable to study in the context of planetary formation and evolution, as the distribution is split between rocky super-Earths and sub-Neptunes with larger atmospheres, and there are many existing theories as to the origin of the radius valley between them. This work has since been cited in multiple works, including in the contexts of detrending CHEOPS data (Singh et al. 2024; Heidari et al. 2024), planets in systems with host stars $0.5 \leq \mathrm{M_*/M_\odot} < 0.9$ as part of a study into the radius valley for low-mass host stars (Ho et al. 2024), TOIs that are most suitable for atmospheric characterisation with JWST (Hord et al. 2023), and the radius valley in relation to planet migration and resonant chain breaking (Izidoro et al. 2022).

Future work for TOI-836

TTVs of up to $\sim$ 20 minutes were detected in observations with CHEOPS and LCOGT in the time between the two TESS Sectors, which we attribute to a possible as-yet undetected and potentially non-transiting exterior planet. Photometric observations of the system to monitor and potentially eventually constrain the TTVs and/or the presence of a third planet are ongoing, managed by the TFOP working group. This process was successful in discovering a potential second planet in the Kepler-19 system, by studying the TTVs of the inner planet Kepler-19 b (Ballard et al. 2011). TOI-836 was also selected for observations with JWST-

NIRSpec/G395H as part of the COMPASS program described in Batalha et al. [2021], with the aim of studying the atmospheres of small exoplanets such as these. The JWST transmission spectra of TOI-836 b were the subject of Alderson et al. [2024] which concluded that the planet does not have a H2-dominated atmosphere, and observations for TOI-836 c were described in Wallack et al. [2024], which may possess a H2/He envelope.
The nearby sub-Earth GJ 314 b (Kirk et al. 2024) was recently observed with JWST-NIRCam, observations from which were consistent with either no atmosphere, an atmosphere with hazes, or an atmosphere with molecular species that are not covered by the NIRSpec bandpass.

7.2 TOI-908

Chapter 4 presented the discovery, characterisation and analysis of the TOI-908 system and its planet, TOI-908 b, a Neptune-analog residing in the Neptune desert parameter space (see Section 1.9.2). It has a radius of $3.18 \pm 0.16\,R_\oplus$ and a mass of $16.1 \pm 4.1\,M_\oplus$, giving it an overall density of $2.7^{+0.2}_{-0.4}\,g\,cm^{-3}$. It orbits its G-type host star on a period of 3.18 days, which places it on the edge of the Neptune desert. Similarly to TOI-836, we obtained transit photometry data from TESS in Sectors 1, 12, 13, 27, 28 and 39, which was combined with ground-based photometry of 5 individual transits from LCOGT. 42 RV spectra were taken with HARPS as part of the HARPS-NOMADS program, and imaging data from SOAR found no close companions within 3" of the target. The transit and RV data were globally modelled using the `exoplanet` package.
Gaussian process models were also applied to the photometric and spectroscopic data to mitigate for the stellar activity, which included an approximate rotation period of 21.9 ± 6.2 days, constrained by the residuals of the HARPS RVs after removal of the planetary signal. Stellar analysis of the primary parameters, estimated age and molecular abundances was performed with the `ARES+MOOG` framework. Internal structure modelling was performed following the implementation of methods Rogers & Owen [2021], from which we found an overall envelope mass fraction of $\sim 2.2 \pm 0.1\%$, and we implemented additional models of the internal structure of the planet for the cases with and without water using methods from Leleu et al. [2021]. We found no evidence for any additional planets in the system from analysis of the TESS residuals using BLS methods (Section 2.1.1) or from the HARPS residuals using RV periodograms (Section 2.1.2).
TOI-908 b lies in the 'Neptune desert', a subset of period-radius space in which

there is an observed dearth of approximately Neptune-sized planets on short orbital periods. It is currently thought that this phenomenon may be caused by the photo-evaporation of planetary atmospheres by extreme insolation from their host stars. By modelling the evaporation history of the planet using the `photoevolver` code and knowledge of the star's current rotation period and approximate age, we found that TOI-908 b likely began its life around the size of Saturn before its atmosphere experienced extreme XUV irradiation due to its proximity to the star.

Future work for TOI-908

We estimate that the atmosphere of TOI-908 b will continue to evaporate, and the planet may lose the entirety of its atmosphere over its total lifetime. Further observations of the atmospheric constituents with JWST will help to constrain individual molecular components, and despite its low TSM value it orbits a bright star that lies close to the TESS and JWST CVZ, making it amenable to continued monitoring and easy scheduling of observations of its high-frequency transits. Observations of the metastable He-line with ground-based spectrographs may also help to study the planetary evaporation process.

7.3 *TESS* Duotransits

Chapter 5 presented the detection of 85 planetary candidates that are 'duotransiting', meaning that they transit once in Cycle 1 of TESS, and transit a second time in Cycle 3. Duotransiting exoplanets are particularly valuable to find and study as they exhibit longer orbital periods compared to much of the current TESS exoplanet sample of at least 20 days, and up to ~ 700 days, meaning that many of them may be more similar to the gas giant planets of the Solar system. Their orbital periods are limited to a discrete set of values ('aliases') determined by the separation between the two transits, allowing for ease of scheduling of follow-up transit observations with ground and space-based instruments.

We employed a novel algorithm to search the TESS SPOC data for targets showing such duotransit events in their light curves. `monofind` searches the flattened light curves by finding three consecutive points that lie below 3 median absolute deviations from the baseline, and flagging them as potential candidates, of which it found 9718 in the first instance. After a vetting procedure to remove false-positive sources, including eclipsing binaries, Solar system asteroids and other systematics; we obtained a list of 85 final vetted planetary candidates. We modelled each candidate's TESS light curves using the `MonoTools` package in order to find the most

probable orbital periods, which will assist further with follow-up observations to determine the true periods. We also identified three candidates of note in our sample based on their positions on the H-R diagram, including an A1V-type host star, a late K-dwarf host star, and a hot subdwarf host. We additionally found that 14 of our candidates were already flagged as CTOIs, two were published at the time of writing: TOI-5153 in Ulmer-Moll et al. [2022] and TOI-5542 in Grieves et al. 2022, and three TOIs/CTOIs that had been falsely flagged as such and were actually asteroids. We also examined the properties of the candidates in the context of the wider population of confirmed exoplanets from TESS. The new candidates from our search were submitted to TFOP as CTOIs. This work has since been cited in other publications in the contexts of estimating yields of long-period planets in TESS SPOC light curves from Cycles 1 and 3 (Rodel et al. 2024), cool gaseous exoplanets with the upcoming *Twinkle* mission (Booth et al. 2024; Edwards et al. 2019; Stotesbury et al. 2022), and monotransiting planets with PLATO (Magliano et al. 2024).

Future work on duotransiting planets

Photometric follow-up of these candidates is ongoing as part of the NGTS long-period planets working group. Successful confirmations of orbital periods of planets that were originally mono- or duotransits in TESS using NGTS include NGTS-11 b (Gill et al. 2020c), TOI-5153 b (Ulmer-Moll et al. 2022) and TOI-5542 b (Grieves et al. 2022). As TESS Cycle 5 data is currently being released Sector-by-Sector by the SPOC pipeline, we are also continuing to search the Southern Ecliptic hemisphere for third transit events of our candidates. We anticipate that these additional transits will not necessarily solve the orbital periods entirely, but may help to greatly reduce the number of aliases to observe to confirm their true periods.

Radial velocity observations of these candidates using CORALIE is also ongoing, with a current program on the instrument aiming to identify potential double-line spectroscopic (SB2) binaries in our sample using an initial spectrum. A second spectrum from CORALIE will indicate whether or not the change in radial velocity is consistent with a planetary or binary scenario. Again, such efforts were successful in helping to confirm TOI-5153 b and TOI-5542 b as true planets.

We are currently performing a similar search for duotransit events in the Northern Ecliptic hemisphere, which was observed in Cycles 2 and 4 of TESS using `monofind`. We expect that the yield of duotransits may be affected by the slightly different observing strategy, as it is comprised of 16 Sectors instead of the usual 13, Sectors 42-46 point towards the ecliptic, and 52-53 are shifted Northwards to avoid scattered

light (see Figure 1.19), however we still anticipate that a significant number of new candidates will be found.

7.4 Statistical analysis with *TRICERATOPS*

Chapter 6 presented the analysis of seven duotransiting planet candidates from TESS Cycles 1 and 3 using the statistical evaluation tool `TRICERATOPS` (Giacalone et al. 2021). The seven candidates are TIC-13072758, TIC-39167176, TIC-142278054, TIC-224279805, TIC-333736132 and TIC-439491923, all of which are also presented in Hawthorn et al. [2024] (Chapter 5 of this work). Period aliases of each of the candidates were observed with NGTS in 2022 and 2023, and the obtained transit light curves were able to solve the orbital periods of the systems. We use the SPOC PDCSAP lightcurves from TESS as they have most of the instrumental noise effects removed, and only this TESS data is given to `TRICERATOPS` for analysis of the transit light curves. TIC-333736132 also has imaging contrast data from *Gemini*-Zorro observations which is folded into the `TRICERATOPS` process. We compute the False Positive Probabilities (FPPs), Nearby False Positive Probabilities (NFPPs) and individual scenario probabilities for each candidate, and classify each target based on the FPP and NFPP values as outlined in Giacalone et al. [2021]. We additionally use `exoplanet` (Foreman-Mackey et al. 2021a) to model the TESS and NGTS photometry data from each target to obtain sets of parameters for each. Overall, we find that `TRICERATOPS` classifies five of the targets as 'likely planets', and two as 'likely false positives'. We discuss each target in turn and contextualise them in the wider population of long-period giant exoplanets, and prioritisation of targets for observations with high-resolution spectrographs such as HARPS and *ESPRESSO*.

Future work with `TRICERATOPS`

Due to the limited time available for radial velocity campaigns to study long-period planets, which typically require extended time in order to fully constrain their phase curves, we anticipate that `TRICERATOPS` will be a useful tool in order to prioritise the long-period targets most likely to be planetary in nature for such campaigns. We also anticipate that further ground-based photometry data (whether from NGTS or other sources) for these and other duotransit candidates will be obtained in the months and years to come, further helping to determine accurate periods, epochs and even transit timing variations (TTVs) for future studies, and allowing us to expand upon the list of candidates that can be assessed with `TRICERATOPS`.
In addition, TESS is observing the Southern Ecliptic Hemisphere for a third time in

Cycle 5, and we expect that many of these duotransit candidates will be observed during this period. However, these observations are unlikely to solve the periods of unconstrained duotransits, meaning that NGTS is still able to serve an important purpose in confirming period aliases from the ground. We expect that more long-period TESS candidates, whether mono- or duotransits, will be obtained with the advent of Cycle 5 data; which can be followed-up with NGTS and assessed with `TRICERATOPS`. The NGTS long-period planets working group has already successfully solved and confirmed a number of planets that were formerly TESS mono- or duotransits, including e.g. NGTS-11 b (Gill et al. 2020c).

Additional possible work with `TRICERATOPS` includes analysis of duotransits from the Northern Ecliptic hemisphere (TESS Cycles 2 and 4; work for which is currently ongoing) which are anticipated to also have their orbital periods solved with ground-based photometric facilities. The potential to use `TRICERATOPS` for the entirety of the Southern and Northern duotransit samples can also be explored in future, and compared with estimates of long-period planet yields (as described in Rodel et al. 2024).

Furthermore, given that `TRICERATOPS` is currently only able to work with data from the TESS, *Kepler* and K2 missions, there may be additional merit in adding functionality for ground-based facility data such as that from NGTS in order to further constrain FPPs and the probabilities of specific transiting planet scenarios. There remain a number of NGTS Objects of Interest (NOIs) awaiting analysis which may be too faint for radial velocity observations; and compounded by the competitive environment in obtaining data from high-precision spectrographs, `TRICERATOPS` will be a useful tool for analysing these targets.

7.5 The future of exoplanet discovery and characterisation

It is currently expected that transit photometry and RV spectroscopy will continue to dominate the field of exoplanet detection and characterisation for short period exoplanets, with astrometric detections of large, long-period planets from *Gaia* appearing in future data releases (Perryman et al. 2014). The PLATO mission (see Section 1.7.3) is still set to launch in 2026, and it is anticipated that many new and smaller planets residing in the Habitable Zones of their stars will be added to the exoplanet sample, ultimately aiding in the search for an Earth analog. In addition, TESS is planned to continue its campaign of all-sky observations until at least Cycle 7 (October 2024 - September 2025, Sectors 84-96, see Figure 1.19).

JWST is currently observing many exoplanet targets with instruments such as *MIRI* and *NIRSpec* in order to constrain the chemical compositions of their atmospheres through transmission spectroscopy (e.g.WASP-39 b; Rustamkulov et al. 2023). From the ground, the *HARPS3* instrument (Thompson et al. 2016) is set to be installed on the 2.54 m Isaac Newton Telescope (*INT*, discussed in Sánchez-Blázquez et al. 2006) in La Palma, which will incorporate a 10-year RV campaign to find Earth-size exoplanets around Sun-like stars (Terra Hunting Experiment; Yahalomi et al. 2023). Furthermore, the EPRV (Extreme Precision Radial Velocity) Working Group has identified that obtaining RV precisions of less than $10\,\mathrm{cm\,s^{-1}}$ would be required in order to detect Earth-size exoplanets in the HZs of FGK-type stars, and has recommended a ground-based program plan to achieve this (detailed in Crass et al. 2021). The overall Exoplanet Science Strategy report (Charbonneau & Gaudi 2018) additionally provides guidance for prioritising large-scale efforts by the exoplanet community to further overall scientific goals.

New missions and projects such as the Nancy Grace Roman Space Telescope (*NGRST*, formerly *WFIRST*, Spergel et al. 2015) and the *Euclid* Legacy Survey (*ExELS*, Laureijs et al. 2011; Penny et al. 2013; McDonald et al. 2014) are expected to also add significant numbers of exoplanets on wider orbits to the current sample through the microlensing method (see Section 1.2.5), including a potential subset of 'rogue'/free-floating exoplanets (e.g. OGLE-2016-BLG-1928; Mróz et al. 2020).

Many exoplanet discovered to date reside on relatively short orbital periods, including TOI-836 (3.82 days) and TOI-908 (3.18 days). However, transiting exoplanets with long orbital periods are often not easily found or well-characterised - leading to a necessity to use the observing strategies of missions such as TESS in novel ways to find them, as in the duotransits (and monotransits) component of this work. Planets that reside in the radius valley and Neptune desert are of particular interest, as they directly relate to the wider population of exoplanets, and could help to further understand the mechanics of planetary systems that place exoplanets within these regions of parameter space.

The PLATO mission will operate similarly to the first phase of Kepler, staring at a single patch of the sky for an extended period of time, and focusing on the detection of Earth-size exoplanets in the Habitable Zones of their host stars. Likewise, missions such as Gaia and the Nancy Grace Roman Space Telescope (Spergel et al. [2015]) are expected to add many more discoveries of long-period planets to the population using alternative methods such as astrometry and gravitational microlensing.

In addition, the precision of existing parameters of individual planets and their systems must be increased, in order to better disentangle the various theories around

planetary formation and migration mechanisms. PLATO will assist with this effort by providing asteroseismology data, improving the host star parameters, and precision of light curves and derived planet properties.
Efforts are currently being made to characterise the atmospheres of exoplanets with missions such as JWST, however fewer planets are needed for very detailed characterisation. This work is currently focusing on planets orbiting bright stars, and robustly chaacterising terrestrial rocky exoplanets. The future may include space missions and instruments (such as the Habitable Worlds Observatory, Mamajek & Stapelfeldt [2024]) focusing on resolving planets around stars at larger orbital separations using direct imaging, and performing spectroscopic observations on such planets.
It is clear that the field of exoplanets will continue to grow into new and exciting frontiers of discovery, characterisation and understanding.

7.6 Closing statements

Since the first discovery of a planet orbiting a Sun-like star, the field of exoplanet studies has expanded enormously to currently encompass a total of 5609 confirmed planets at the time of writing, with many thousands more potentially on the horizon. Advancements in photometric and spectroscopic observations and methods have led to successful characterisations of these systems and their planets, and we are continuing to build a wider picture of the overall planetary population based on their bulk properties, leading to an ever-greater understanding of planetary formation, evolution and migration processes. Many of the planets and system architectures we see are in no way like those of the Solar system, challenging not only our perceptions of the universe we live in, but our place within it.

Bibliography

Abe L., et al., 2013, A&A, 553, A49

Addison B., et al., 2019, PASP, 131, 115003

Addison B. C., et al., 2021, MNRAS, 502, 3704

Adibekyan V. Z., Sousa S. G., Santos N. C., Delgado Mena E., González Hernández J. I., Israelian G., Mayor M., Khachatryan G., 2012, A&A, 545, A32

Adibekyan V., et al., 2015, A&A, 583, A94

Adibekyan V., et al., 2021, Science, 374, 330

Akeson R. L., et al., 2013, PASP, 125, 989

Albrecht S., et al., 2012, ApJ, 757, 18

Alderson L., et al., 2024, arXiv e-prints, p. arXiv:2404.00093

Aller A., Lillo-Box J., Jones D., Miranda L. F., Barceló Forteza S., 2020, A&A, 635, A128

Anderson D. R., et al., 2010, ApJ, 709, 159

Anderson D. R., et al., 2012, MNRAS, 422, 1988

Andrews S. M., et al., 2018, ApJ, 869, L41

Armstrong D. J., Meru F., Bayliss D., Kennedy G. M., Veras D., 2019, ApJ, 880, L1

Armstrong D. J., et al., 2020, Nature, 583, 39

Auvergne M., et al., 2009, A&A, 506, 411

Bakos G., Noyes R. W., Kovács G., Stanek K. Z., Sasselov D. D., Domsa I., 2004, PASP, 116, 266

Bakos G. Á., et al., 2010, ApJ, 710, 1724

Bakos G. Á., et al., 2013, PASP, 125, 154

Ballard S., et al., 2011, ApJ, 743, 200

Baluev R. V., 2008, MNRAS, 385, 1279

Barclay T., et al., 2013, Nature, 494, 452

Barros S. C. C., et al., 2015, MNRAS, 454, 4267

Baruteau C., et al., 2014, in Beuther H., Klessen R. S., Dullemond C. P., Henning T., eds, Protostars and Planets VI. pp 667–689 (arXiv:1312.4293), doi:10.2458/azu˙uapress˙9780816531240-ch029

Batalha N. M., 2014, Proceedings of the National Academy of Science, 111, 12647

Batalha N. M., et al., 2011, ApJ, 729, 27

Batalha N., et al., 2021, Seeing the Forest and the Trees: Unveiling Small Planet Atmospheres with a Population-Level Framework, JWST Proposal. Cycle 1

Bayliss D., et al., 2020, The Messenger, 181, 28

Becker J. C., Vanderburg A., Adams F. C., Rappaport S. A., Schwengeler H. M., 2015, ApJ, 812, L18

Bell T. J., et al., 2023, Nature, 623, 709

Bensby T., Feltzing S., Lundström I., 2003, A&A, 410, 527

Bensby T., Feltzing S., Oey M. S., 2014, A&A, 562, A71

Benz W., et al., 2020, Experimental Astronomy, 51, 109–151

Benz W., et al., 2021, Experimental Astronomy, 51, 109

Bertran de Lis S., Delgado Mena E., Adibekyan V. Z., Santos N. C., Sousa S. G., 2015, A&A, 576, A89

Birnstiel T., Klahr H., Ercolano B., 2012, A&A, 539, A148

Black D. C., Scargle J. D., 1982, ApJ, 263, 854

Blackwell D. E., Shallis M. J., 1977, MNRAS, 180, 177

Bodenheimer P., Pollack J. B., 1986, Icarus, 67, 391

Bohn A. J., et al., 2020, ApJ, 898, L16

Bond I. A., et al., 2004, ApJ, 606, L155

Bonfanti A., Ortolani S., Piotto G., Nascimbeni V., 2015, A&A, 575, A18

Bonfanti A., Ortolani S., Nascimbeni V., 2016, A&A, 585, A5

Bonfanti A., et al., 2021, A&A, 646, A157

Booth L., Sarkar S., Griffin M., Edwards B., 2024, MNRAS,

Borucki W. J., Summers A. L., 1984, ICARUS, 58, 121

Borucki W. J., et al., 2010, Science, 327, 977

Borucki W. J., et al., 2011, ApJ, 736, 19

Boss A. P., 1997, Science, 276, 1836

Bowler B. P., 2016, PASP, 128, 102001

Brahm R., et al., 2016, AJ, 151, 89

Brown T. M., et al., 2013, PASP, 125, 1031

Brown A., et al., 2018, Astronomy and Astrophysics, 616

Bruno G., Maddamma M., 2013, De l'infinito, universo e mondi. Le porte di Venexia, Venexia, `https://books.google.co.uk/books?id=VADfngEACAAJ`

Bryant E. M., et al., 2020a, MNRAS, 494, 5872

Bryant E. M., et al., 2020b, MNRAS, 499, 3139

Bryant E. M., Bayliss D., Van Eylen V., 2023, MNRAS, 521, 3663

Buchhave L. A., et al., 2012, Nature, 486, 375

Buchhave L. A., et al., 2014, Nature, 509, 593

Butler R. P., Marcy G. W., Williams E., McCarthy C., Dosanjh P., Vogt S. S., 1996, PASP, 108, 500

Butler R. P., et al., 2017, AJ, 153, 208

Cadieux C., et al., 2022, AJ, 164, 96

Caldwell D. A., et al., 2020, Research Notes of the American Astronomical Society, 4, 201

Cale B. L., et al., 2021, AJ, 162, 295

Campbell B., Walker G. A. H., Yang S., 1988, APJ, 331, 902

Castelli F., Kurucz R. L., 2003, in Piskunov N., Weiss W. W., Gray D. F., eds, IAU Symposium Vol. 210, Modelling of Stellar Atmospheres. p. A20 (arXiv:astro-ph/0405087)

Cegla H. M., Watson C. A., Shelyag S., Mathioudakis M., Moutari S., 2019, ApJ, 879, 55

Celisse A., 2008, arXiv e-prints, p. arXiv:0811.0802

Chao K.-H., deGraffenried R., Lach M., Nelson W., Truax K., Gaidos E., 2021, Chemie der Erde / Geochemistry, 81, 125735

Charbonneau D., Gaudi S., 2018, Exoplanet Science Strategy. The National Academies Press, doi:10.17226/25187

Charbonneau D., Brown T. M., Latham D. W., Mayor M., 2000, ApJ, 529, L45

Chauvin G., Lagrange A. M., Dumas C., Zuckerman B., Mouillet D., Song I., Beuzit J. L., Lowrance P., 2004, A&A, 425, L29

Chen H., Rogers L. A., 2016, ApJ, 831, 180

Chen D.-C., et al., 2021, ApJ, 909, 115

Chen D.-C., et al., 2022, AJ, 163, 249

Christiansen J., et al., 2010, in AAS/Division for Planetary Sciences Meeting Abstracts #42. p. 59.03

Ciardi D. R., Beichman C. A., Horch E. P., Howell S. B., 2015, ApJ, 805, 16

Claret A., 2017, A&A, 600, A30

Cloutier R., Menou K., 2020, AJ, 159, 211

Cloutier R., et al., 2020, AJ, 160, 22

Coffinet A., Lovis C., Dumusque X., Pepe F., 2019, A&A, 629, A27

Collins K. A., Kielkopf J. F., Stassun K. G., Hessman F. V., 2017, AJ, 153, 77

Cooke B. F., Pollacco D., West R., McCormac J., Wheatley P. J., 2018, A&A, 619, A175

Cooke B. F., et al., 2021, MNRAS, 500, 5088

Cosentino R., et al., 2012, in McLean I. S., Ramsay S. K., Takami H., eds, Society of Photo-Optical Instrumentation Engineers (SPIE) Conference Series Vol. 8446, Ground-based and Airborne Instrumentation for Astronomy IV. p. 84461V, doi:10.1117/12.925738

Costes J. C., et al., 2021, MNRAS, 505, 830

Crane J. D., Shectman S. A., Butler R. P., 2006, in McLean I. S., Iye M., eds, Society of Photo-Optical Instrumentation Engineers (SPIE) Conference Series Vol. 6269, Society of Photo-Optical Instrumentation Engineers (SPIE) Conference Series. p. 626931, doi:10.1117/12.672339

Crane J. D., Shectman S. A., Butler R. P., Thompson I. B., Burley G. S., 2008, in McLean I. S., Casali M. M., eds, Society of Photo-Optical Instrumentation Engineers (SPIE) Conference Series Vol. 7014, Ground-based and Airborne Instrumentation for Astronomy II. p. 701479, doi:10.1117/12.789637

Crane J. D., Shectman S. A., Butler R. P., Thompson I. B., Birk C., Jones P., Burley G. S., 2010, in McLean I. S., Ramsay S. K., Takami H., eds, Society of Photo-Optical Instrumentation Engineers (SPIE) Conference Series Vol. 7735, Ground-based and Airborne Instrumentation for Astronomy III. p. 773553, doi:10.1117/12.857792

Crass J., et al., 2021, arXiv e-prints, p. arXiv:2107.14291

Crouzet N., et al., 2010, A&A, 511, A36

Crouzet N., et al., 2018, A&A, 619, A116

Crouzet N., et al., 2020, in Society of Photo-Optical Instrumentation Engineers (SPIE) Conference Series. p. 114470O, doi:10.1117/12.2562550

Culpan R., Geier S., Reindl N., Pelisoli I., Gentile Fusillo N., Vorontseva A., 2022, A&A, 662, A40

Cumming A., 2004, MNRAS, 354, 1165

Curiel S., Ortiz-León G. N., Mioduszewski A. J., Sanchez-Bermudez J., 2022, AJ, 164, 93

Daban J.-B., et al., 2010, in Ground-based and Airborne Telescopes III. p. 77334T, doi:10.1117/12.854946

Dalba P. A., et al., 2020, AJ, 159, 241

Davenhall A. C., Privett G. J., Taylor M. B., 2001, Starlink Cookbook, 5

Dawson R. I., Fabrycky D. C., 2010, ApJ, 722, 937

Deeg H. J., Alonso R., 2018, in Deeg H. J., Belmonte J. A., eds, , Handbook of Exoplanets. Springer International Publishing AG, p. 117, doi:10.1007/978-3-319-55333-7˙117

Deeg H. J., Belmonte J. A., 2018, Handbook of Exoplanets. Springer, doi:10.1007/978-3-319-55333-7

Delgado Mena E., Tsantaki M., Adibekyan V. Z., Sousa S. G., Santos N. C., González Hernández J. I., Israelian G., 2017, A&A, 606, A94

Delgado Mena E., et al., 2019, A&A, 624, A78

Delgado Mena E., Adibekyan V., Santos N. C., Tsantaki M., González Hernández J. I., Sousa S. G., Bertrán de Lis S., 2021, A&A, 655, A99

Delrez L., et al., 2021, Nature Astronomy, 5, 775

Demangeon O. D. S., et al., 2021, Astronomy and Astrophysics, 653, A41

Díaz R. F., Almenara J. M., Santerne A., Moutou C., Lethuillier A., Deleuil M., 2014, MNRAS, 441, 983

Dorn C., Venturini J., Khan A., Heng K., Alibert Y., Helled R., Rivoldini A., Benz W., 2017, A&A, 597, A37

Doyon R., et al., 2023, PASP, 135, 098001

Dressing C. D., Charbonneau D., 2013, ApJ, 767, 95

Duncan D. K., et al., 1991, ApJS, 76, 383

Eastman J., Gaudi B. S., Agol E., 2013, PASP, 125, 83

Eastman J. D., et al., 2019, arXiv e-prints, p. arXiv:1907.09480

Edwards B., et al., 2019, Experimental Astronomy, 47, 29

Einstein A., 1916, Annalen der Physik, 354, 769

Eisner N. L., et al., 2021, MNRAS, 501, 4669

Encrenaz T., Tinetti G., Coustenis A., 2018, Experimental Astronomy, 46, 31

Erkaev N. V., Kulikov Y. N., Lammer H., Selsis F., Langmayr D., Jaritz G. F., Biernat H. K., 2007, A&A, 472, 329

Espinoza N., Jordán A., 2016, MNRAS, 457, 3573

Espinoza N., Kossakowski D., Brahm R., 2019, MNRAS, 490, 2262

Fűrész G., 2008, PhD thesis, University of Szeged, Hungary

Fabrycky D. C., et al., 2014, ApJ, 790, 146

Fang J., Margot J.-L., 2012, ApJ, 761, 92

Feinstein A. D., et al., 2023, Nature, 614, 670

Fernández Fernández J., Wheatley P. J., King G. W., 2023, MNRAS,

Figueira P., et al., 2012, A&A, 541, A139

Fleming S. W., Kane S. R., McCullough P. R., Chromey F. R., 2008, MNRAS, 386, 1503

Foreman-Mackey D., Agol E., Ambikasaran S., Angus R., 2017a, Astrophysics Source Code Library, pp ascl–1709

Foreman-Mackey D., Agol E., Ambikasaran S., Angus R., 2017b, celerite: Scalable 1D Gaussian Processes in C++, Python, and Julia (ascl:1709.008)

Foreman-Mackey D., et al., 2021a, exoplanet-dev/exoplanet v0.4.5, doi:10.5281/zenodo.1998447, `https://doi.org/10.5281/zenodo.1998447`

Foreman-Mackey D., et al., 2021b, The Journal of Open Source Software, 6, 3285

Fressin F., et al., 2005, in M. Giard, F. Casoli, & F. Paletou ed., EAS Publications Series Vol. 14, EAS Publications Series. pp 309–312, doi:10.1051/eas:2005049

Fressin F., et al., 2013, ApJ, 766, 81

Fulton B. J., Petigura E. A., 2018, AJ, 156, 264

Fulton B. J., et al., 2017, AJ, 154, 109

Furlan E., et al., 2017, AJ, 153, 71

Gaia Collaboration 2022, VizieR Online Data Catalog, p. I/355

Gaia Collaboration et al., 2016a, A&A, 595

Gaia Collaboration et al., 2016b, A&A, 595, A2

Gaia Collaboration et al., 2018, A&A, 616, A1

Gaia Collaboration et al., 2021, A&A, 649, A1

Gaidos E., 2013, ApJ, 770, 90

Galle J. G., 1846, MNRAS, 7, 153

Gardner J. P., et al., 2006, Space Sci. Rev., 123, 485

Gaudi B. S., Winn J. N., 2007, ApJ, 655, 550

Gaudi B. S., et al., 2017, in American Astronomical Society Meeting Abstracts #230. p. 102.06

Giacalone S., et al., 2021, AJ, 161, 24

Giacalone S., et al., 2022, AJ, 163, 99

Gilbert E. A., et al., 2023, ApJ, 944, L35

Gill S., et al., 2020a, MNRAS, 491, 1548

Gill S., et al., 2020b, MNRAS, 495, 2713

Gill S., et al., 2020c, ApJ, 898, L11

Ginzburg S., Schlichting H. E., Sari R., 2016, ApJ, 825, 29

Goldreich P., 1965, MNRAS, 130, 159

Goldreich P., Tremaine S., 1979, ApJ, 233, 857

Goldreich P., Ward W. R., 1973, ApJ, 183, 1051

Gomes da Silva J., Bensabat A., Monteiro T., Santos N. C., 2022, A&A, 668, A174

Grieves N., et al., 2022, A&A, 668, A29

Grunblatt S. K., Howard A. W., Haywood R. D., 2015, ApJ, 808, 127

Gu P.-G., Lin D. N. C., Bodenheimer P. H., 2003, ApJ, 588, 509

Guerrero N. M., et al., 2021, ApJS, 254, 39

Guillot T., et al., 2015, Astronomische Nachrichten, 336, 638

Günther M. N., Daylan T., 2019, allesfitter: Flexible star and exoplanet inference from photometry and radial velocity, Astrophysics Source Code Library, record ascl:1903.003

Günther M. N., Daylan T., 2021, ApJS, 254, 13

Gupta A., Schlichting H. E., 2019, MNRAS, 487, 24

Han Z., Podsiadlowski P., Maxted P. F. L., Marsh T. R., Ivanova N., 2002, MNRAS, 336, 449

Han Z., Podsiadlowski P., Maxted P. F. L., Marsh T. R., 2003, MNRAS, 341, 669

Hartman J. D., et al., 2015, AJ, 149, 166

Hastings W. K., 1970, Biometrika, 57, 97

Hattori S., Foreman-Mackey D., Hogg D. W., Montet B. T., Angus R., Pritchard T. A., Curtis J. L., Schölkopf B., 2022, AJ, 163, 284

Hatzes A. P., Cochran W. D., Endl M., McArthur B., Paulson D. B., Walker G. A. H., Campbell B., Yang S., 2003, APJ, 599, 1383

Hawthorn F., et al., 2023a, MNRAS, 520, 3649

Hawthorn F., et al., 2023b, MNRAS, 524, 3877

Hawthorn F., et al., 2024, Monthly Notices of the Royal Astronomical Society, 528, 1841

Hebb L., et al., 2009, ApJ, 693, 1920

Hedges C., 2021, Research Notes of the American Astronomical Society, 5, 262

Heidari N., et al., 2024, A&A, 681, A55

Hellier C., et al., 2017, MNRAS, 465, 3693

Henden A. A., Templeton M., Terrell D., Smith T. C., Levine S., Welch D., 2016, VizieR Online Data Catalog, p. II/336

Herschel W., Watson D., 1781, Philosophical Transactions of the Royal Society of London Series I, 71, 492

Hippke M., Heller R., 2019, A&A, 623, A39

Ho C. S. K., Rogers J. G., Van Eylen V., Owen J. E., Schlichting H. E., 2024, arXiv e-prints, p. arXiv:2401.12378

Hobson M. J., et al., 2021, AJ, 161, 235

Hoffman M. D., Gelman A., 2011, arXiv e-prints, p. arXiv:1111.4246

Holman M. J., et al., 2010, Science, 330, 51

Hooton M. J., et al., 2022, A&A, 658, A75

Hord B. J., et al., 2022, AJ, 164, 13

Hord B. J., et al., 2023, arXiv e-prints, p. arXiv:2308.09617

Howard A. W., et al., 2012, ApJS, 201, 15

Howell S. B., 1989, PASP, 101, 616

Howell S. B., 2000, Handbook of CCD Astronomy. Cambridge University Press

Howell S. B., Everett M. E., Sherry W., Horch E., Ciardi D. R., 2011, AJ, 142, 19

Howell S. B., et al., 2014, PASP, 126, 398

Hoyer S., Guterman P., Demangeon O., Sousa S. G., Deleuil M., Meunier J. C., Benz W., 2020, A&A, 635, A24

Hsu D. C., Ford E. B., Ragozzine D., Ashby K., 2019, AJ, 158, 109

Huang C. X., et al., 2020a, Research Notes of the American Astronomical Society, 4, 204

Huang C. X., et al., 2020b, Research Notes of the American Astronomical Society, 4, 206

Irwin J., Irwin M., Aigrain S., Hodgkin S., Hebb L., Moraux E., 2007, MNRAS, 375, 1449

Irwin J. M., Berta-Thompson Z. K., Charbonneau D., Dittmann J., Falco E. E., Newton E. R., Nutzman P., 2015a, in 18th Cambridge Workshop on Cool Stars, Stellar Systems, and the Sun. pp 767–772 (arXiv:1409.0891)

Irwin J., Berta-Thompson Z. K., Charbonneau D., Dittmann J., Newton E. R., 2015b, in American Astronomical Society Meeting Abstracts #225. p. 258.01

Izidoro A., Schlichting H. E., Isella A., Dasgupta R., Zimmermann C., Bitsch B., 2022, ApJ, 939, L19

JWST Transiting Exoplanet Community Early Release Science Team et al., 2023, Nature, 614, 649

Jackson A. P., Davis T. A., Wheatley P. J., 2012, MNRAS, 422, 2024

Jakobsen P., et al., 2022, A&A, 661, A80

Jeffery C. S., Miszalski B., Snowdon E., 2021, MNRAS, 501, 623

Jenkins J. M., 2002, ApJ, 575, 493

Jenkins J. M., et al., 2010, in Radziwill N. M., Bridger A., eds, Society of Photo-Optical Instrumentation Engineers (SPIE) Conference Series Vol. 7740, Software and Cyberinfrastructure for Astronomy. p. 77400D, doi:10.1117/12.856764

Jenkins J. M., et al., 2016, in Software and Cyberinfrastructure for Astronomy IV. p. 99133E, doi:10.1117/12.2233418

Jenkins J. M., Tenenbaum P., Seader S., Burke C. J., McCauliff S. D., Smith J. C., Twicken J. D., Chandrasekaran H., 2020, Kepler Data Processing Handbook: Transiting Planet Search, Kepler Science Document KSCI-19081-003

Jensen E., 2013, Tapir: A web interface for transit/eclipse observability, Astrophysics Source Code Library (ascl:1306.007)

Jin S., Mordasini C., 2017, The Astrophysical Journal, 853

Jin S., Mordasini C., Parmentier V., van Boekel R., Henning T., Ji J., 2014, ApJ, 795, 65

Johansen A., Davies M. B., Church R. P., Holmelin V., 2012, ApJ, 758, 39

Johnson D. R. H., Soderblom D. R., 1987, AJ, 93, 864

Johnstone C. P., Bartel M., Güdel M., 2021, A&A, 649, A96

Jones M. I., et al., 2024, A&A, 683, A192

Jordán A., et al., 2020, AJ, 159, 145

Kasting J. F., Whitmire D. P., Reynolds R. T., 1993, Icarus, 101, 108

Kempton E. M. R., et al., 2018, PASP, 130, 114401

King G. W., et al., 2018, MNRAS, 478, 1193

Kipping D. M., 2013a, MNRAS, 434, L51

Kipping D. M., 2013b, MNRAS, 435, 2152

Kipping D., 2023, MNRAS, 523, 1182

Kirk J., et al., 2024, AJ, 167, 90

Knutson H. A., Charbonneau D., Noyes R. W., Brown T. M., Gilliland R. L., 2007, ApJ, 655, 564

Knutson H. A., et al., 2014, ApJ, 785, 126

Koch D. G., et al., 2004, in Mather J. C., ed., Society of Photo-Optical Instrumentation Engineers (SPIE) Conference Series Vol. 5487, Optical, Infrared, and Millimeter Space Telescopes. pp 1491–1500, doi:10.1117/12.552346

Kopparapu R. K., et al., 2013, ApJ, 765, 131

Koshimoto N., et al., 2017, AJ, 154, 3

Kovács G., Zucker S., Mazeh T., 2002, A&A, 391, 369

Kral Q., Wyatt M. C., Triaud A. H. M. J., Marino S., Thébault P., Shorttle O., 2018, MNRAS, 479, 2649

Kubyshkina D. I., Fossati L., 2021, Research Notes of the American Astronomical Society, 5, 74

Kuntzer T., 2013, arXiv e-prints, p. arXiv:1310.7800

Kurokawa H., Nakamoto T., 2014, ApJ, 783, 54

Kurucz R. L., 1993, Physica Scripta Volume T, 47, 110

Kurucz R., Bell B., 1995, Atomic Line Data (R.L. Kurucz and B. Bell) Kurucz CD-ROM No. 23. Cambridge, 23

Lagrange A. M., Desort M., Meunier N., 2010, A&A, 512, A38

Lammer H., et al., 2009, A&A Rev., 17, 181

Laureijs R., et al., 2011, arXiv e-prints, p. arXiv:1110.3193

Lecavelier des Etangs A., Lissauer J. J., 2022, New A Rev., 94, 101641

Léger A., et al., 2004, Icarus, 169, 499

Leleu A., et al., 2021, Astronomy and Astrophysics, 649, A26

Lendl M., et al., 2020a, MNRAS, 492, 1761

Lendl M., et al., 2020b, A&A, 643, A94

Li J., Tenenbaum P., Twicken J. D., Burke C. J., Jenkins J. M., Quintana E. V., Rowe J. F., Seader S. E., 2019, PASP, 131, 024506

Libby-Roberts J. E., et al., 2023, AJ, 165, 249

Lillo-Box J., Barrado D., Bouy H., 2012, A&A, 546, A10

Lillo-Box J., Barrado D., Bouy H., 2014, A&A, 566, A103

Lillo-Box J., et al., 2022, arXiv e-prints, p. arXiv:2210.08996

Lindegren L., et al., 2021, A&A, 649, A4

Lissauer J. J., et al., 2011, ApJS, 197, 8

Lissauer J. J., et al., 2012, ApJ, 750, 112

Lomb N. R., 1976, Ap&SS, 39, 447

Lopez E. D., Fortney J. J., 2013, ApJ, 776, 2

Lopez E. D., Fortney J. J., 2014, The Astrophysical Journal, 792, 1

Lopez E. D., Fortney J. J., 2016, ApJ, 818, 4

Louie D. R., Narita N., Fukui A., Palle E., Tamura M., Kusakabe N., Parviainen H., Deming D., 2020, PASP, 132, 084403

Lovis C., Fischer D., 2010, in Seager S., ed., , Exoplanets. University of Arizona Press, pp 27–53

Lovis C., Pepe F., 2007, A&A, 468, 1115

Luger R., Agol E., Foreman-Mackey D., Fleming D. P., Lustig-Yaeger J., Deitrick R., 2019, aj, 157, 64

Macintosh B., et al., 2014, Proceedings of the National Academy of Science, 111, 12661

Mackay D. J. C., 2003, Information Theory, Inference and Learning Algorithms. 'Cambridge University Press'

Madhusudhan N., 2019, ARA&A, 57, 617

Madhusudhan N., Bitsch B., Johansen A., Eriksson L., 2017, MNRAS, 469, 4102

Magliano C., et al., 2024, MNRAS, 528, 2851

Malavolta L., et al., 2017, AJ, 153, 224

Mamajek E., Stapelfeldt K., 2024, arXiv e-prints, p. arXiv:2402.12414

Mann C., et al., 2023, AJ, 165, 217

Marboeuf U., Thiabaud A., Alibert Y., Cabral N., Benz W., 2014, Astronomy and Astrophysics, 570, A36

Marigo P., et al., 2017, ApJ, 835, 77

Marmier M., et al., 2013, A&A, 551, A90

Martinez C. F., Cunha K., Ghezzi L., Smith V. V., 2019, The Astrophysical Journal, 875, 29

Matsakos T., Königl A., 2016, ApJ, 820, L8

Maxted P. F. L., Heber U., Marsh T. R., North R. C., 2001, MNRAS, 326, 1391

Maxted P. F. L., et al., 2011, PASP, 123, 547

Mayor M., Queloz D., 1995, Nature, 378, 355

Mayor M., et al., 2003, The Messenger, 114, 20

Mayor M., et al., 2011, arXiv e-prints, p. arXiv:1109.2497

Mazeh T., Holczer T., Faigler S., 2016, A&A, 589, A75

McCormac J., et al., 2020, MNRAS, 493, 126

McCully C., Volgenau N. H., Harbeck D.-R., Lister T. A., Saunders E. S., Turner M. L., Siiverd R. J., Bowman M., 2018, in Proc. SPIE. p. 107070K (arXiv:1811.04163), doi:10.1117/12.2314340

McDonald I., et al., 2014, MNRAS, 445, 4137

McKee B. J., Montet B. T., 2023, AJ, 165, 236

McLaughlin D. B., 1924, ApJ, 60, 22

Mékarnia D., et al., 2016, MNRAS, 463, 45

Metropolis N., Rosenbluth A. W., Rosenbluth M. N., Teller A. H., Teller E., 1953, J. Chem. Phys., 21, 1087

Meunier N., Desort M., Lagrange A. M., 2010, A&A, 512, A39

Millholland S. C., Winn J. N., 2021, ApJ, 920, L34

Millholland S., Wang S., Laughlin G., 2017, ApJ, 849, L33

Mistry P., et al., 2023a, arXiv e-prints, p. arXiv:2311.00688

Mistry P., et al., 2023b, AJ, 166, 9

Mistry P., et al., 2023c, MNRAS, 521, 1066

Montalto M., et al., 2021, A&A, 653, A98

Mordasini C., Burn R., 2024, Reviews in Mineralogy and Geochemistry, 90, 55

Morton T. D., 2012, ApJ, 761, 6

Morton T. D., Bryson S. T., Coughlin J. L., Rowe J. F., Ravichandran G., Petigura E. A., Haas M. R., Batalha N. M., 2016, ApJ, 822, 86

Mróz P., et al., 2020, ApJ, 903, L11

Murray C. D., Correia A. C. M., 2010, Keplerian Orbits and Dynamics of Exoplanets. University of Arizona Press, pp 15–23

Nascimbeni V., et al., 2022, A&A, 658, A31

Neal R., 2011, in , Handbook of Markov Chain Monte Carlo. Chapman and Hall/CRC, pp 113–162, doi:10.1201/b10905

Nesvorný D., Kipping D., Terrell D., Feroz F., 2014, ApJ, 790, 31

Nikolov N., et al., 2021, AJ, 162, 88

Nutzman P., Charbonneau D., 2008, PASP, 120, 317

O'Connor C. E., Bildsten L., Cantiello M., Lai D., 2023, ApJ, 950, 128

Oklopčić A., Hirata C. M., 2018, ApJ, 855, L11

Osborn H. P., 2022, MonoTools: Planets of uncertain periods detector and modeler, Astrophysics Source Code Library, record ascl:2204.020 (ascl:2204.020)

Osborn H. P., et al., 2016, MNRAS, 457, 2273

Osborn H. P., et al., 2021a, MNRAS, 502, 4842

Osborn A., et al., 2021b, MNRAS, 507, 2782

Osborn H. P., et al., 2022, A&A, 664, A156

Otegi J. F., Bouchy F., Helled R., 2020, A&A, 634, A43

Owen J. E., Lai D., 2018, MNRAS, 479, 5012

Owen J. E., Wu Y., 2013, ApJ, 775, 105

Owen J. E., Wu Y., 2017, ApJ, 847, 29

Pál A., et al., 2008, ApJ, 680, 1450

Panahi A., et al., 2022, A&A, 663, A101

Parviainen H., Aigrain S., 2015, MNRAS, 453, 3821

Pearson K. A., 2019, AJ, 158, 243

Pelisoli I., Vos J., Geier S., Schaffenroth V., Baran A. S., 2020, A&A, 642, A180

Penny M. T., et al., 2013, MNRAS, 434, 2

Pepe F., et al., 2000, in Iye M., Moorwood A. F., eds, Society of Photo-Optical Instrumentation Engineers (SPIE) Conference Series Vol. 4008, Optical and IR Telescope Instrumentation and Detectors. pp 582–592, doi:10.1117/12.395516

Pepe F., et al., 2002, The Messenger, 110, 9

Pepe F., et al., 2021, A&A, 645, A96

Pepper J., et al., 2007, PASP, 119, 923

Perryman M., Hartman J., Bakos G. Á., Lindegren L., 2014, ApJ, 797, 14

Petigura E. A., Marcy G. W., Howard A. W., 2013, ApJ, 770, 69

Piaulet C., et al., 2023, Nature Astronomy, 7, 206

Podolak M., Weizman A., Marley M., 1995, Planet. Space Sci., 43, 1517

Pojmanski G., 2002, Acta Astron., 52, 397

Pollacco D. L., et al., 2006, PASP, 118, 1407

Pollack J. B., Hubickyj O., Bodenheimer P., Lissauer J. J., Podolak M., Greenzweig Y., 1996, Icarus, 124, 62

Queloz D., et al., 1999, arXiv e-prints, pp astro–ph/9910223

Queloz D., et al., 2009, A&A, 506, 303

Rauch T., Deetjen J. L., 2003, in Hubeny I., Mihalas D., Werner K., eds, Astronomical Society of the Pacific Conference Series Vol. 288, Stellar Atmosphere Modeling. p. 103 (arXiv:astro-ph/0403239), doi:10.48550/arXiv.astro-ph/0403239

Rauer H., et al., 2014, Experimental Astronomy, 38, 249

Rauer H., et al., 2024, arXiv e-prints, p. arXiv:2406.05447

Rayner J., Bond T., Bonnet M., Jaffe D., Muller G., Tokunaga A., 2012, in McLean I. S., Ramsay S. K., Takami H., eds, Society of Photo-Optical Instrumentation Engineers (SPIE) Conference Series Vol. 8446, Ground-based and Airborne Instrumentation for Astronomy IV. p. 84462C, doi:10.1117/12.925511

Reddy B. E., Lambert D. L., Allende Prieto C., 2006, MNRAS, 367, 1329

Rice M., et al., 2022, AJ, 164, 104

Ricker G. R., et al., 2015, Journal of Astronomical Telescopes, Instruments, and Systems, 1, 014003

Rieke M. J., Kelly D., Horner S., 2005, in Heaney J. B., Burriesci L. G., eds, Society of Photo-Optical Instrumentation Engineers (SPIE) Conference Series Vol. 5904, Cryogenic Optical Systems and Instruments XI. pp 1–8, doi:10.1117/12.615554

Rieke G. H., et al., 2015, PASP, 127, 584

Rieke M. J., et al., 2023, PASP, 135, 028001

Rodel T., Bayliss D., Gill S., Hawthorn F., 2024, MNRAS,

Rogers J. G., Owen J. E., 2021, MNRAS, 503, 1526

Rosenthal L. J., et al., 2021, ApJS, 255, 8

Rossiter R. A., 1924, ApJ, 60, 15

Rousset G., et al., 2003, in Wizinowich P. L., Bonaccini D., eds, Society of Photo-Optical Instrumentation Engineers (SPIE) Conference Series Vol. 4839, Adaptive Optical System Technologies II. pp 140–149, doi:10.1117/12.459332

Rustamkulov Z., et al., 2023, Nature, 614, 659

Sackett P. D., 1999, in Mariotti J. M., Alloin D., eds, NATO Advanced Study Institute (ASI) Series C Vol. 532, Planets Outside the Solar System: Theory and Observations. p. 189 (arXiv:astro-ph/9811269), doi:10.48550/arXiv.astro-ph/9811269

Safronov V. S., 1972, Evolution of the protoplanetary cloud and formation of the earth and planets.. IPST

Sahlmann J., Lazorenko P. F., Ségransan D., Martín E. L., Queloz D., Mayor M., Udry S., 2013, A&A, 556, A133

Salmon S. J. A. J., Van Grootel V., Buldgen G., Dupret M. A., Eggenberger P., 2021, A&A, 646, A7

Salvatier J., Wiecki T. V., Fonnesbeck C., 2016, PeerJ Computer Science, 2, e55

Sánchez-Blázquez P., et al., 2006, MNRAS, 371, 703

Sanchis-Ojeda R., Rappaport S., Winn J. N., Levine A., Kotson M. C., Latham D. W., Buchhave L. A., 2013, ApJ, 774, 54

Santerne A., Fressin F., Díaz R. F., Figueira P., Almenara J. M., Santos N. C., 2013, A&A, 557, A139

Santerne A., et al., 2018, Nature Astronomy, 2, 393

Santos N. C., et al., 2013, A&A, 556, A150

Savitzky A., Golay M. J. E., 1964, Analytical Chemistry, 36, 1627

Scargle J. D., 1982, ApJ, 263, 835

Schaffenroth V., Pelisoli I., Barlow B. N., Geier S., Kupfer T., 2022, A&A, 666, A182

Schanche N., et al., 2020, MNRAS, 499, 428

Schlecker M., et al., 2020, AJ, 160, 275

Schlichting H. E., Sari R., Yalinewich A., 2015, Icarus, 247, 81

Scott N. J., et al., 2021, Frontiers in Astronomy and Space Sciences, 8, 138

Scuflaire R., Théado S., Montalbán J., Miglio A., Bourge P.-O., Godart M., Thoul A., Noels A., 2008, Ap&SS, 316, 83

Seabroke G. M., et al., 2021, A&A, 653, A160

Seager S., Mallén-Ornelas G., 2003, ApJ, 585, 1038

Shu F. H., Adams F. C., Lizano S., 1987, ARA&A, 25, 23

Singh V., et al., 2024, A&A, 683, A1

Skrutskie M. F., et al., 2006, AJ, 131, 1163

Smith J. C., et al., 2012, PASP, 124, 1000

Smith A. M. S., et al., 2020, Astronomische Nachrichten, 341, 273

Sneden C. A., 1973, PhD thesis, THE UNIVERSITY OF TEXAS AT AUSTIN.

Snellen I. A. G., Covino E., 2007, MNRAS, 375, 307

Sousa S. G., 2014, GeoPlanet: Earth and Planetary Sciences, p. 297–310

Sousa S. G., Santos N. C., Israelian G., Mayor M., Monteiro M. J. P. F. G., 2007, A&A, 469, 783

Sousa S. G., Santos N. C., Adibekyan V., Delgado-Mena E., Israelian G., 2015, A&A, 577, A67

Sousa S. G., et al., 2021, A&A, 656, A53

Southworth J., 2011, MNRAS, 417, 2166

Sozzetti A., et al., 2023, A&A, 677, L15

Spergel D., et al., 2015, arXiv e-prints, p. arXiv:1503.03757

Spyratos P., et al., 2021, MNRAS, 506, 2853

Stark M. A., Wade R. A., 2003, AJ, 126, 1455

Stassun K. G., Torres G., 2021, ApJ, 907, L33

Stassun K. G., et al., 2019, AJ, 158, 138

Stevens D. J., Gaudi B. S., 2013, PASP, 125, 933

Stotesbury I., et al., 2022, in Coyle L. E., Matsuura S., Perrin M. D., eds, Society of Photo-Optical Instrumentation Engineers (SPIE) Conference Series Vol. 12180, Space Telescopes and Instrumentation 2022: Optical, Infrared, and Millimeter Wave. p. 1218033 (arXiv:2209.03337), doi:10.1117/12.2641373

Strøm P., 2016, The Exoplanet Transit Method, https://www.paulanthonywilson.com/exoplanets/exoplanet-detection-techniques/the-exoplanet-transit-method/

Stumpe M. C., et al., 2012, PASP, 124, 985

Stumpe M. C., Smith J. C., Catanzarite J. H., Van Cleve J. E., Jenkins J. M., Twicken J. D., Girouard F. R., 2014, PASP, 126, 100

Swain M. R., et al., 2021, AJ, 161, 213

Swerdlow N. M., 1998, The Babylonian Theory of the Planets. Journal for the History of Astronomy

Szabó G. M., Kiss L. L., 2011, ApJ, 727, L44

Temple L. Y., et al., 2018, MNRAS, 480, 5307

Temple L. Y., et al., 2019, MNRAS, 490, 2467

Teske J., et al., 2021, ApJS, 256, 33

Thiabaud A., Marboeuf U., Alibert Y., Cabral N., Leya I., Mezger K., 2014, Astronomy and Astrophysics, 562, A27

Thompson S. J., et al., 2016, in Evans C. J., Simard L., Takami H., eds, Society of Photo-Optical Instrumentation Engineers (SPIE) Conference Series Vol. 9908, Ground-based and Airborne Instrumentation for Astronomy VI. p. 99086F (arXiv:1608.04611), doi:10.1117/12.2232111

Thuillier A., Van Grootel V., Dévora-Pajares M., Pozuelos F. J., Charpinet S., Siess L., 2022, A&A, 664, A113

Tokovinin A., 2018, PASP, 130, 035002

Torres G., et al., 2011, ApJ, 727, 24

Traub W. A., 2012, ApJ, 745, 20

Tremaine S., Dong S., 2012, AJ, 143, 94

Triaud A. H. M. J., 2018, in Deeg H. J., Belmonte J. A., eds, , Handbook of Exoplanets. Springer International Publishing AG, p. 2, doi:10.1007/978-3-319-55333-7˙2

Tu L., Johnstone C. P., Güdel M., Lammer H., 2015, A&A, 577, L3

Twicken J. D., et al., 2018, PASP, 130, 064502

Twicken J., et al., 2019, in American Astronomical Society Meeting Abstracts #233. p. 140.03

Udry S., et al., 2007, A&A, 469, L43

Ulmer-Moll S., et al., 2022, A&A, 666, A46

Ulmer-Moll S., et al., 2023, A&A, 674, A43

Van Eylen V., Agentoft C., Lundkvist M. S., Kjeldsen H., Owen J. E., Fulton B. J., Petigura E., Snellen I., 2018, MNRAS, 479, 4786

Van Eylen V., et al., 2019, AJ, 157, 61

Van Eylen V., et al., 2021, MNRAS, 507, 2154

Van Grootel V., et al., 2021, A&A, 650, A205

Villanueva Steven J., Dragomir D., Gaudi B. S., 2019, AJ, 157, 84

Vogt S. S., Penrod G. D., 1988, in Instrumentation for Ground-Based Optical Astronomy. p. 68

Vogt S. S., et al., 2014, PASP, 126, 359

Vos J., Vučković M., Chen X., Han Z., Boudreaux T., Barlow B. N., Østensen R., Németh P., 2019, MNRAS, 482, 4592

Wallack N. L., et al., 2024, arXiv e-prints, p. arXiv:2404.01264

Waltham N., 2010, ISSI Scientific Reports Series, 9, 391

Wang S., et al., 2021a, AJ, 162, 50

Wang M.-T., Liu H.-G., Zhu J., Zhou J.-L., 2021b, AJ, 162, 258

Watson A. J., Donahue T. M., Walker J. C. G., 1981, Icarus, 48, 150

Watson C. A., de Mooij E. J. W., Steeghs D., Marsh T. R., Brogi M., Gibson N. P., Matthews S., 2019, MNRAS, 490, 1991

Weiss L. M., et al., 2020, AJ, 159, 242

Werner K., Dreizler S., 1999, Journal of Computational and Applied Mathematics, 109, 65

Werner K., Deetjen J. L., Dreizler S., Nagel T., Rauch T., Schuh S. L., 2003, in Hubeny I., Mihalas D., Werner K., eds, Astronomical Society of the Pacific Conference Series Vol. 288, Stellar Atmosphere Modeling. p. 31 (arXiv:astro-ph/0209535), doi:10.48550/arXiv.astro-ph/0209535

West R. G., et al., 2019, MNRAS, 486, 5094

Wheatley P. J., et al., 2018, MNRAS, 475, 4476

Williams J. P., Cieza L. A., 2011, ARA&A, 49, 67

Wilson J., et al., 2020, MNRAS, 497, 5155

Wilson T. G., et al., 2022, MNRAS,

Winn J. N., 2010, MNRAS, p. arXiv:1001.2010

Winn J. N., 2014, Transits and Occultations (arXiv:1001.2010)

Wittenmyer R., et al., 2018, in American Astronomical Society Meeting Abstracts #231. p. 128.01

Wright E. L., et al., 2010, AJ, 140, 1868

Wright N. J., Drake J. J., Mamajek E. E., Henry G. W., 2011, ApJ, 743, 48

Wright N. J., Newton E. R., Williams P. K. G., Drake J. J., Yadav R. K., 2018, MNRAS, 479, 2351

Wyatt M. C., Kral Q., Sinclair C. A., 2020, MNRAS, 491, 782

Xue Q., Bean J. L., Zhang M., Welbanks L., Lunine J., August P., 2024, ApJ, 963, L5

Yahalomi D. A., Angus R., Spergel D. N., Foreman-Mackey D., 2023, AJ, 166, 258

Youdin A. N., 2011, ApJ, 742, 38

Youdin A. N., Goodman J., 2005, ApJ, 620, 459

Young A. T., et al., 1991, PASP, 103, 221

Zechmeister M., Kürster M., 2009, A&A, 496, 577

Zeng L., Sasselov D. D., Jacobsen S. B., 2016, ApJ, 819, 127

Zeng L., et al., 2019, Proceedings of the National Academy of Science, 116, 9723

Ziegler C., Tokovinin A., Briceño C., Mang J., Law N., Mann A. W., 2020, AJ, 159, 19

Zolotov M. Y., 2007, Geophys. Res. Lett., 34, L23203